


3-13-2017

# Engineered Nanocomposite Materials for Microwave/Millimeter-Wave Applications of Fused Deposition Modeling

Juan De Dios Castro

*University of South Florida, juandedioscastro@gmail.com*

Follow this and additional works at: <http://scholarcommons.usf.edu/etd>

 Part of the [Electromagnetics and Photonics Commons](#), and the [Materials Science and Engineering Commons](#)

## Scholar Commons Citation

Castro, Juan De Dios, "Engineered Nanocomposite Materials for Microwave/Millimeter-Wave Applications of Fused Deposition Modeling" (2017). *Graduate Theses and Dissertations*.  
<http://scholarcommons.usf.edu/etd/6643>

This Dissertation is brought to you for free and open access by the Graduate School at Scholar Commons. It has been accepted for inclusion in Graduate Theses and Dissertations by an authorized administrator of Scholar Commons. For more information, please contact [scholarcommons@usf.edu](mailto:scholarcommons@usf.edu).

Engineered Nanocomposite Materials for Microwave/Millimeter-Wave Applications of  
Fused Deposition Modeling

by

Juan De Dios Castro

A dissertation submitted in partial fulfillment  
of the requirements for the degree of  
Doctor of Philosophy  
Department of Electrical Engineering  
College of Engineering  
University of South Florida

Major Professor: Jing Wang, Ph.D.  
Thomas M. Weller, Ph.D.  
Andrew Hoff, Ph.D.  
Nathan Crane, Ph.D.  
Hariharan Srikanth, Ph.D.

Date of Approval:  
March 13, 2017

Keywords: 3-D printing, additive manufacturing (AM), antennas, dielectrics, predictive models

Copyright © 2017, Juan De Dios Castro

**DEDICATION**

*To my son Isaac*

## ACKNOWLEDGMENTS

My special recognition to CONACYT (The Mexican National Council for Science and Technology) for providing funding for my doctoral degree. I want to express my appreciation to my advisor and major professor Dr. Jing Wang, first for accepting me to be part of his research group in fall 2012, second for his academic coaching and mentoring for me to become a better scholar and professional in my field of study during this period of my life, and lastly for all the recommendations and opportunities that He has shared with me.

Also, I'd like to thank Dr. Thomas Weller for his guidance and academic advice and providing me research appointments for two years when I mostly need them. Similarly, I'd like to thank Dr. Andrew Hoff for being my mentor as a graduate teaching assistant (GTA) for about three years, it was an invaluable experience learning semiconductor processing under his supervision, first as a student, later as GTA. Also, I'd like to thank Dr. Bernard Batson for his support and care about my progress even before I started this journey, always following my progress and looking for opportunities for me. Special thanks to my colleagues Eduardo Rojas-Nastrucci, who help me in many aspects of my work in particular 3D-printing training for FDM and deposition of conductive traces by micro-dispensing, and Dr. Maria Cordoba-Erazo for the near-field microwave microscopy (NFMM) measurements in two of the composites presented in this dissertation.

I'd like to thank all the research peers from the RF-MEMS Transducers Laboratory (including the ones that graduated already), and the research assistants from the WAMI Center at USF that I have met in this last five years of my journey. Special thanks to the research assistants that have used some of the composite materials from this work, we have published together some



peer reviewed conference proceedings papers; Mohamed Abdin, Denise Lugo, Anthony Ross, and Ramiro Ramirez.

I would like to thank the staff at the NREC, especially to Jay Bieber for his SEM and EDS training and recommendations related to characterization of materials. Dr. Yusuf Emirov for the AFM and TEM training, Rich Everly for the metrology, photolithography, and DRIE training, and Robert Tufts for the XRD training and for leading the NREC facility.

Last but not least, I like to express my gratitude to my family for their love, to my son Isaac for being my *inspiration*, my mother, Maria Castro, and my sister Maria de Jesus Bojorquez Castro for always giving me words of support when I need them and for always be there for me. I am grateful for the moral support received from my brothers, Martin and Joel.

This work has been supported by the National Science Foundation under the ECCS-1232183 grant, ARMY #W911NF-13-1-0109 grant, 94388 RF Nanomaterials, and Transducers Foundation, and CONACYT (the Mexican National Council for Science and Technology) under the CVU #259947 grant.

## TABLE OF CONTENTS

LIST OF TABLES	v
LIST OF FIGURES	vii
ABSTRACT	xiv
CHAPTER 1: INTRODUCTION	1
1.1 Overview	1
1.2 Dissertation Organization	3
1.3 Contributions	4
CHAPTER 2: BACKGROUND AND LITERATURE REVIEW	7
2.1 Overview of Direct Digital Manufacturing (DDM)	7
2.1.1 Fused Deposition Modeling (FDM)	7
2.1.2 Direct-Print Additive Manufacturing (Micro-Dispensing Technique)	8
2.2 DDM in the RF/microwave Community	9
2.3 High-Dielectric Materials in Electronic Applications	12
2.4 Fundamental Characteristics of High- <i>k</i> Composites	14
2.4.1 Capacitance and Electric Energy Storage of Materials	14
2.4.2 Polarization and Relaxation in Dielectric Materials	15
2.4.3 Dielectric Strength of Polymer Matrix Composites (PMC)	17
2.5 Functional Composite Materials in Microwave Applications	18
2.6 Expanding the Materials Options for 3D-Printed Microwave Applications	21
2.7 Motivation	22
2.7.1 Comparison of High-Performance FDM Microwave Composites and Thermoplastics	23
CHAPTER 3: ENHANCEMENT OF MICROWAVE PROPERTIES IN COMPOSITE MATERIALS	25
3.1 Note to Reader	25
3.2 Introduction	25
3.3 Experimental Procedure	27
3.4 Fabrication Process of Polymer Matrix Composites	28
3.4.1 Polymer and Ceramic Materials	28
3.4.2 Preparation of Composite Materials and Specimens	29
3.5 Characterization of Bulk Ceramic Materials	30
3.5.1 XRD Analysis	30
3.5.2 Energy Dispersive Spectroscopy (EDS) Analysis	32
3.6 Characterization of Polymer-Ceramic Composites	35

3.6.1	SEM Analysis	35
3.6.2	Near-Field Microwave Microscopy (NFMM) Analysis	37
3.6.3	Extraction of the Microwave Dielectric Properties	40
3.6.3.1	Cavity Perturbation Technique	40
3.7	Theoretical Models for Effective Dielectric Permittivity of Polymer-Matrix Composites	43
3.7.1	Raleigh Model	44
3.7.2	Hanai-Bruggeman Model	44
3.7.3	Volume-fraction Average Model	45
3.7.4	Maxwell Model	45
3.7.5	Maxwell-Garnett Model	45
3.7.6	Jaysundere-Smith Model	48
3.8	Measured Dielectric Properties of Polymer-Matrix Composites	48
3.9	Theoretical Model Prediction of Dielectric Loss ( $\tan \delta_d$ ) in PMCs	52
3.10	Results and Discussions	54
3.11	Conclusion	57
<b>CHAPTER 4: FLEXIBLE EM COMPOSITES AND THEIR APPLICATION TO K-BAND ANTENNAS</b>		61
4.1	Note to Reader	61
4.2	Introduction	61
4.3	Experimental Procedure	62
4.4	Preparation and Characterization PDMS-Ceramic Composites	62
4.4.1	Ceramics Sintering Process	62
4.4.2	XRD, EDS, and SEM Analysis	63
4.4.3	Preparation of Polymer-Ceramic Composites	66
4.5	Characterization of DPAM-Printed Antennas	74
4.5.1	Design of a 19.6 GHz Edge-Fed Microstrip Patch Antenna with PDMS-MgCaTiO <sub>2</sub> Composites	74
4.5.2	Challenges with Direct Print Additive Manufacturing (Micro-Dispensing) Technology together with Composite Materials	75
4.5.3	Characterization of a 19.6 GHz Edge-Fed Patch Antenna Printed over a PDMS-MgCaTiO <sub>2</sub> Substrate	77
4.6	Stress and Strain RF Testing Analysis of a 4.2 GHz Flexible Patch Antenna Based on a 37 vol. % PDMS-MgCaTiO <sub>2</sub> Composite Material	81
4.7	Conclusion	85
<b>CHAPTER 5: CERAMIC-THERMOPLASTIC COMPOSITES FOR FDM</b>		87
5.1	Note to Reader	87
5.2	Introduction	87
5.3	Experimental Procedure	88
5.4	Fabrication of Thermoplastic Composites	88
5.4.1	Choice of Thermoplastic Matrix and Ceramic Fillers	88
5.4.2	Sintered Ceramics Processing	89
5.4.3	FDM Feedstock Hot Melt Compounding Process	90
5.4.4	Particle Size Analysis of Sintered High- <i>k</i> Ceramic Fillers	92

5.4.5	FDM 3D-Printing Process of Ceramic-Thermoplastic Composites	95
5.4.6	Models for Effective Permittivity	99
5.4.7	Model Prediction of the Dielectric Loss Tangent in FDM Composites	104
5.4.8	Thin-Sheet Specimen Dielectric Characterization	105
5.5	Measured Properties of FDM-Printed Samples	107
5.5.1	Measured Dielectric Properties of Pure Thermoplastics and Ceramic-Thermoplastic Composite Materials	107
5.5.2	Comparison of Dielectric Properties of EM Composites vs. Prior Works	110
5.5.3	Dielectric Properties of Thermoplastic Composites in Comparison with State-of-the-Art RF Laminates	111
5.5.4	Repeatability Assessment of Cavity Resonator Measurements in FDM Composites	111
5.5.5	Effect of Fillers Sintering Temperature on FDM Composites	113
5.6	Conclusion	115
<b>CHAPTER 6: DIRECT DIGITAL MANUFACTURING OF KU-BAND ANTENNAS BASED ON FDM-READY CERAMIC-THERMOPLASTIC COMPOSITES</b>		117
6.1	Note to Reader	117
6.2	Microwave Performance Assessment of FDM Composites	117
6.2.1	3D-printed Edge-Fed Microstrip Patch Antennas	117
6.2.2	Surface Treatment Recommendations for FDM Composites	120
6.2.3	Edge-Fed Patch Antennas Performance	122
6.3	Conclusion	129
<b>CHAPTER 7: MILLIMETER-WAVE PERFORMANCE AND THERMAL PROPERTIES ASSESSMENT OF FDM-COMPATIBLE COMPOSITES</b>		130
7.1	Note to Reader	130
7.2	Introduction	130
7.3	Measured Properties of 3D-printed Samples	131
7.3.1	Millimeter-Wave Performance Assessment	131
7.3.2	Thermal Assessment of Pure Thermoplastics and Ceramic-Thermoplastic Composites	137
7.4	Conclusion	140
<b>CHAPTER 8: CONCLUSIONS AND FUTURE WORK</b>		142
8.1	Future Work and Recommendations	142
8.2	Conclusions	143
8.3	Acknowledgments for Sponsors and Facilities	145
<b>REFERENCES</b>		147
<b>APPENDICES</b>		155
Appendix A: Copyright Permissions		156

ABOUT THE AUTHOR

END PAGE

## LIST OF TABLES

Table 2.1	Bulk DC conductivity of CB028 silver paste	9
Table 2.2	Mechanisms that contribute to the displacement of charges in materials [27]	13
Table 3.1	The fundamental properties of ceramic fillers and sintering conditions	28
Table 3.2	Element weight fractions based on EDS of $MgCaTiO_2$ at two sintering conditions	33
Table 3.3	Average particle sizes and lattice parameters of $MgCaTiO_2$ measured by SEM and XRD	34
Table 3.4	Average particle sizes and lattice parameters of $TiO_2$ measured by SEM and XRD	34
Table 3.5	Element weight fractions based on EDS of $TiO_2$ at different sintering conditions	35
Table 3.6	Measured EM properties of polymer-ceramic composites with fillers sintered at different conditions	55
Table 3.7	Comparison of measured EM properties between this work and prior reports up to K-band	60
Table 4.1	Summary of the studied sintering conditions	63
Table 4.2	Lattice parameters of $Ba_{0.55}Sr_{0.45}TiO_3$ measured by XRD	65
Table 4.3	Element weight fractions based on EDS of $Ba_{0.55}Sr_{0.45}TiO_3$ at different sintering conditions	65
Table 4.4	The key properties of ceramic fillers and sintering conditions in this chapter's materials	72
Table 4.5	Comparison of measured dielectric and loss properties of polymer-ceramic composites	72

Table 4.6	Comparison of measured EM properties vs. those reported by prior works up to K-band	73
Table 4.7	Antennas dimensions	77
Table 4.8	Performance comparison of edge-fed patch antenna designs	79
Table 5.1	Vendor-specified dielectric properties of ceramic fillers	88
Table 5.2	Sintering conditions and densities of ceramic fillers	89
Table 5.3	Properties of FDM-compatible materials from this work compared with other works	101
Table 5.4	Measured EM dielectric properties of microwave materials up to the Ku-band	116
Table 6.1	Key antenna dimensions	118
Table 6.2	Edge-fed patch antennas performance comparison	122
Table 7.1	Comparison of measured EM properties of composite materials vs. prior works in the mm-wave spectrum up to V-band	136
Table 7.2	Measured thermal properties of FDM materials tested in this dissertation with a TMA Q400 instrument	141

## LIST OF FIGURES

Figure 2.1	Conceptual illustration of a typical FDM or micro-dispensing printing process	9
Figure 2.2	(a) 2.4 Bluetooth/Wi-Fi planar inverted “F” antenna, photograph courtesy of Deffenbaugh <i>et al.</i> [6] © IMAPS 2013	10
Figure 2.3	Miniaturized 2.45 GHz balun using high-k composites	11
Figure 2.4	Phased array antenna (PAA) unit cell fabricated with direct digital manufacturing (DDM)	12
Figure 2.5	Comparison of measured dielectric permittivity up to 69 GHz of both a pure COP (ZEONEX® RS420) and a 30 vol. % COP-MgCaTiO <sub>2</sub> EM composites, which are compared with commercial microwave laminates from Rogers Corporation [27]	23
Figure 2.6	Comparison of measured dielectric loss properties up to 69 GHz of both a pure COP (ZEONEX® RS420) and a 30 vol. % COP-MgCaTiO <sub>2</sub> EM composites with commercial microwave laminates from Rogers Corporation [27]	24
Figure 3.1	Measured XRD patterns of MgCaTiO <sub>2</sub> ceramic powders after different sintering processes	31
Figure 3.2	Measured XRD patterns of TiO <sub>2</sub> ceramic powder after different processes	32
Figure 3.3	(a) Tested energy dispersive spectroscopy (EDS) spectrum of MgCaTiO <sub>2</sub> ceramic powders sintered at 1100°C	33
Figure 3.4	(a) Tested energy dispersive spectroscopy (EDS) spectrum of TiO <sub>2</sub> ceramic powders sintered at 1100°C	35
Figure 3.5	SEM analysis of MgCaTiO <sub>2</sub> samples sintered at 1100°C, showing (a) a zoom-out view photo of MgCaTiO <sub>2</sub> agglomerates	36
Figure 3.6	SEM analysis of TiO <sub>2</sub> samples sintered at 1100°C, showing (a) a zoom-out view photo of TiO <sub>2</sub> agglomerates	37



Figure 3.7	36 vol. % PDMS-MgCaTiO <sub>2</sub> composites with fillers sintered at 1100°C: (a) NFMM surface topography	39
Figure 3.8	Ideal arrangements of two-phase PMCs	46
Figure 3.9	Distribution of particles in a PMC	47
Figure 3.10	Comparison between the measured dielectric permittivities and predicted dielectric permittivities given by the models including Raleigh (Equation (3.20)), Hanai-Bruggeman (Equation (3.21)) and Maxwell (Equation (3.23)) models, by using the vendor-provided properties of unsintered raw powders and measured properties of PDMS	49
Figure 3.11	Comparison of the model-predicted permittivity of PDMS-based composites embedded with different fillers at various volume ratios based on Equations (3.20)-(3.23)	51
Figure 3.12	(a) Comparison of measured properties for the four types of composites vs. predictions by the Hanai-Bruggeman's model (Equation (3.21))	52
Figure 3.13	Comparison between the measured dielectric losses ( $\tan \delta_d$ ) with the losses predicted by the Raju model based on Equation (3.31) by using the properties of unsintered raw powders and measured properties of PDMS	53
Figure 3.14	Measured dielectric properties of PDMS and PDMS-ceramic thin-sheet samples with 36 vol. % MgCaTiO <sub>2</sub> fillers sintered at different temperatures	55
Figure 3.15	Measured dielectric properties of PDMS and PDMS-ceramic thin-sheet samples with 38 vol. % TiO <sub>2</sub> fillers sintered at different temperatures	56
Figure 3.16	Comparison of measured EM properties of PDMS-ceramic composite samples with commercial RF and microwave laminates (i.e., FR-4 and TMM10i <sup>®</sup> )	57
Figure 4.1	Measured x-ray diffraction (XRD) patterns of Ba <sub>0.55</sub> Sr <sub>0.45</sub> TiO <sub>3</sub> ceramic powders after different processes	64
Figure 4.2	(a) Tested energy dispersive spectroscopy (EDS) spectrum of Ba <sub>0.55</sub> Sr <sub>0.45</sub> TiO <sub>3</sub> ceramic powders sintered at 1100°C	66
Figure 4.3	SEM photos PDMS composite samples	67

Figure 4.4	SEM photos the MgCaTiO <sub>2</sub> particles under different sintering conditions	68
Figure 4.5	Measured EM properties of PDMS-MgCaTiO <sub>2</sub> composites with 37% fillers sintered at 1100°C or 1500°C	69
Figure 4.6	Measured EM properties of the PDMS-Ba <sub>0.55</sub> Sr <sub>0.45</sub> TiO <sub>3</sub> composites with 39 vol. % fillers sintered at 1100°C and 1340°C	70
Figure 4.7	High-frequency measured dielectric properties of the PDMS-Ba <sub>0.55</sub> Sr <sub>0.45</sub> TiO <sub>3</sub> composites with 39 vol. % and 49 vol. % fillers sintered at 1340°C, as well as PDMS-MgCaTiO <sub>2</sub> composites with 49 % fillers sintered at 1100°C	70
Figure 4.8	Schematic-view scanned AFM surface profiles of PDMS based composites	71
Figure 4.9	Schematic diagram of a DPAM-printed rectangular edge-fed patch antenna by using a 37 vol. % PDMS-MgCaTiO <sub>2</sub> EM composite material	76
Figure 4.10	Design and implementation of the edge-fed microstrip patch antennas showing (a) EM simulated current distribution in the patch antenna with the critical dimensions specified by ADS Momentum	76
Figure 4.11	DPAM-printed 19.6 GHz edge-fed patch antennas printed with different setups	77
Figure 4.12	Comparison between measured and simulated return losses for the printed 19.6 GHz edge-fed patch antenna along with a reference device implemented with a Rogers RT/duroid® 5880 laminate board and others mentioned in Table 4.8	78
Figure 4.13	Comparison between gain vs. frequency for all the antennas	79
Figure 4.14	EM simulation result of the 19.6 GHz edge-fed patch antennas by using ANSYS Electronics Desktop 18 (HFSS 2017), showing the radiation patterns comparison for all the antenna designs	80
Figure 4.15	Evaluation of a microstrip patch antenna built over a foldable 37 vol. % PDMS-MgCaTiO <sub>2</sub> composite substrate with 4.2 GHz nominal frequency under stress and bend tests	82
Figure 4.16	Measured return loss of a flexible 4.2 GHz 37 vol. % PDMS-MgCaTiO <sub>2</sub> patch antenna at different bending angles	83

Figure 4.17	Comparison of measured antenna gain vs. frequency between 4.2 GHz (unbent) patch antenna designed over pure PDMS material and a patch antenna built over a 37 vol. % PDMS-MgCaTiO <sub>2</sub> composite substrate with unsintered fillers	83
Figure 4.18	Normalized measured vs. simulated radiation patterns the 4.2 GHz (unbent) patch antennas in (a) H-plane and (b) E-Plane	84
Figure 5.1	SEM photos of two generations of newly developed ceramic-thermoplastic filaments, by using different ball milling times and with fillers sintered at 1100°C and 1200°C for three hours	91
Figure 5.2	SEM photos of two generations of newly developed ceramic-thermoplastic filaments based on a 30 vol. % COP-TiO <sub>2</sub> , by using different ball milling times and with fillers sintered at 1100°C and 1200°C for three hours	93
Figure 5.3	Size distribution by number/percentage (%) of 1200°C sintered TiO <sub>2</sub> particles post-processed by different high-energy ball milling times	94
Figure 5.4	SEM surface view photos of 3D-printed specimens: including (a) an FDM printed 30 vol. % COP-TiO <sub>2</sub> thin-sheet with filters sintered 1100°C	96
Figure 5.5	Energy dispersive spectroscopy (EDS) mapping taken over a 24 μm <sup>2</sup> area of the FDM-printed EM composite made of 30 vol. % COP-MgCaTiO <sub>2</sub> with fillers sintered at 1200°C	97
Figure 5.6	Scanned 2D surface profiles of FDM 3D-printed thin-sheet samples made of 30 vol. % COP-MgCaTiO <sub>2</sub> composites under different processing conditions	98
Figure 5.7	AFM Schematic-view scanned (bottom side) surface profiles of (a) a 25 vol. % COP-MgCaTiO <sub>2</sub> thin-sheet specimen [50] © IMAPS 2015	99
Figure 5.8	Comparison of model-predicted permittivity of COP-based composites embedded with different fillers at varied volume fractions based on Equations (3.20)-(3.23)	102
Figure 5.9	The effective permittivity predicted by the models based on Equations (3.20), (3.21), (3.23)	103
Figure 5.10	Comparison of the model-predicted and measured dielectric loss tangents for two types of composites	105
Figure 5.11	RF dielectric/loss properties characterization setup based upon the cavity perturbation technique for 3D-printed 310 μm-thick specimens	106

Figure 5.12	Loaded and unloaded FDM-printed samples and filaments using pure COP and COP composites	106
Figure 5.13	Measured dielectric properties of three versions of cyclo-olefin polymer, such as ZEONEX <sup>®</sup> RS420, ZEONEX <sup>®</sup> RS420-LDS and ZEONOR <sup>®</sup> 1420R, compared to Cycolac <sup>™</sup> MG47 ABS	108
Figure 5.14	Comparison of measured high-frequency dielectric and loss properties of pure COP (ZEONEX <sup>®</sup> RS420) versus other FDM thermoplastics and a low-loss RF laminate (RT/duroid <sup>®</sup> 5880)	108
Figure 5.15	Comparison of the measured dielectric properties of ZEONEX <sup>®</sup> RS420 COP-based composites loaded with high- <i>k</i> fillers sintered at 1100°C versus ABS composites with fillers sintered at 1340°C and other composites	109
Figure 5.16	Comparison of measured and model-estimated permittivity by the Maxwell and Hanai-Bruggeman models in Equation (3.23) and Equation (3.21)	110
Figure 5.17	Assessment of measured properties of newly developed 30 vol. % COP-TiO <sub>2</sub> composites with fillers sintered at 1100°C and high-end RF laminates	111
Figure 5.18	(a) Measured dielectric permittivity (with mean value and error bar specified) of an FDM-printed thin-sheet specimen composed of 30 vol. % COP-TiO <sub>2</sub> composites loaded with 1100°C sintered and re-pulverized fillers	112
Figure 5.19	Assessment of measured dielectric properties of 30 vol. % COP-TiO <sub>2</sub> composites with two different sintering conditions for the TiO <sub>2</sub> ceramic fillers at 1100°C and 1200°C	114
Figure 5.20	Assessment of measured dielectric properties of 30 vol. % COP-TiO <sub>2</sub> composites vs. other state-of-the-art microwave materials	115
Figure 6.1	(a) Schematic diagram of a 3D-printed rectangular edge-fed patch by using a 25 vol. % COP-MgCaTiO <sub>2</sub> EM composite material	118
Figure 6.2	Top-view image of additive manufactured 16.5 GHz antennas over COP and RT/duroid <sup>®</sup> 5870 substrates (left) as well as 17.2 GHz/16.7 GHz antennas over 25 vol. % COP-MgCaTiO <sub>2</sub> and RT/duroid <sup>®</sup> 5870 substrates (right)	119

Figure 6.3	Antenna return loss characterization setup for a 16.5GHz antenna manufactured by a DDM process with a 360 $\mu\text{m}$ -thick pure COP substrate	119
Figure 6.4	SEM photos of micro-dispensed silver paste (CB028)	121
Figure 6.5	Comparison of the measured and simulated $S_{11}$ of the 17.2 GHz antenna DDM-printed based on COP loaded with $\text{MgCaTiO}_2$ fillers and a reference antenna at 16.7 GHz DPAM-printed over Rogers RT/duroid <sup>®</sup> 5870 laminate	123
Figure 6.6	The measured and simulated $S_{11}$ of the 16.5 GHz antennas based on DDM-printed COP substrate, which is compared with a reference DPAM-printed antenna over a Rogers RT/duroid <sup>®</sup> 5870 laminate at 16.4 GHz	123
Figure 6.7	Edge-fed patch antennas in an anechoic chamber during antenna pattern measurements	124
Figure 6.8	Measured gain vs. frequency for 17.2 GHz antenna DDM-printed on a COP- $\text{MgCaTiO}_2$ composite substrate and a 16.7 GHz reference antenna DPAM-printed over an RT/duroid <sup>®</sup> 5870 substrate	125
Figure 6.9	Measured and simulated gain vs. frequency for antennas DDM-printed on pure (unloaded) COP at 16.5 GHz, which are compared with a 16.4 GHz reference design DPAM-printed over a Rogers RT/duroid <sup>®</sup> 5870 substrate	125
Figure 6.10	Measured (normalized) radiation patterns of the DDM-printed 17.2 GHz antenna by COP- $\text{MgCaTiO}_2$ composites, which is compared with a reference DPAM-printed antenna over a Rogers RT/duroid <sup>®</sup> 5870 laminate core at 16.7 GHz	127
Figure 6.11	Measured (normalized) radiation patterns of the DDM-printed 16.5 GHz antenna composed of pure (unloaded) COP, which is compared with a 16.4 GHz reference antenna DPAM-printed over a Rogers RT/duroid <sup>®</sup> 5870 laminate core	128
Figure 7.1	SEM photos of 30 vol. % COP- $\text{MgCaTiO}_2$ composite FDM-printed samples	131
Figure 7.2	Comparison of measured dielectric and loss properties up to 69 GHz of both a pure COP (ZEONEX <sup>®</sup> RS420) and a 30 vol. % COP- $\text{MgCaTiO}_2$ EM composites based FDM-printed cylindrical specimens	132

Figure 7.3	Comparison of measured dielectric permittivity up to 69 GHz of both a pure COP (ZEONEX <sup>®</sup> RS420) and a 30 vol. % COP-MgCaTiO <sub>2</sub> EM composites with commercial microwave laminates from Rogers Corporation [27]	134
Figure 7.4	Comparison of measured dielectric loss properties up to 69 GHz of both a pure COP (ZEONEX <sup>®</sup> RS420) and a 30 vol. % COP-MgCaTiO <sub>2</sub> EM composites with commercial microwave laminates from Rogers Corporation [27]	135
Figure 7.5	Comparison of measured CTEs of 3D-printed pure (unloaded) thermoplastics	139
Figure 7.6	Comparison of measured CTEs of 3D-printed three variations of COP and COP-ceramic based composites	139

## ABSTRACT

A variety of high-permittivity (high- $k$ ) and low-loss ceramic-thermoplastic composite materials as fused deposition modeling (FDM) feedstock, based on cyclo-olefin polymer (COP) embedded with sintered ceramic fillers, have been developed and investigated for direct digital manufacturing (DDM) of microwave components. The composites presented in this dissertation use a high-temperature sintering process up to 1500°C to further enhance the dielectric properties of the ceramic fillers. The electromagnetic (EM) properties of these newly developed FDM composites were characterized up to the Ku-band by using the cavity perturbation technique. Several models for prediction of the effective relative dielectric permittivity of composites based on the filler loading volume fraction have been evaluated, among which Hanai-Bruggeman and Maxwell models have shown the best accuracy with less than 2% and 5% discrepancies, respectively.

The 30 vol. % COP-TiO<sub>2</sub> FDM-ready composites with fillers sintered at 1200°C have exhibited a relative permittivity ( $\epsilon_r$ ) of 4.78 and a dielectric loss tangent ( $\tan \delta_d$ ) lower than 0.0012 at 17 GHz. Meanwhile, the 30 vol. % COP-MgCaTiO<sub>2</sub> composites with fillers sintered at 1200°C have exhibited an  $\epsilon_r$  of 4.82 and a  $\tan \delta_d$  lower than 0.0018. The DDM approach combines FDM of the engineered EM composites and micro-dispensing for deposition of conductive traces to fabricate by 3D-printing edge-fed patch antennas operating at 17.2 GHz and 16.5 GHz. These antennas were demonstrated by employing a 25 vol. % COP-MgCaTiO<sub>2</sub> composite FDM filament with the fillers sintered at 1100°C and a pure COP filament, which were both prepared and extruded following the process described in this dissertation. The low dielectric loss of the 25 vol.

% COP-MgCaTiO<sub>2</sub> composite material ( $\tan \delta_d$  lower than 0.0018) has been leveraged to achieve a peak realized gain of 6 dBi. Also, the high-permittivity ( $\epsilon_r$  of 4.74), which corresponds to an index of refraction of 2.17, results in a patch area miniaturization of 50% when compared with an antenna designed and DPAM-printed over a Rogers RT/duroid<sup>®</sup> 5870 laminate core through micro-dispensing of CB028 silver paste. This reference antenna exhibited a measured peak realized gain of 6.27 dBi that is comparable.

Also, two low-loss FDM-ready composite materials for DDM technologies are presented and characterized at V-band mm-wave frequencies. Pure COP thermoplastic exhibits a relative permittivity  $\epsilon_r$  of 2.1 and a dielectric loss tangent  $\tan \delta_d$  below 0.0011 at 69 GHz, whereas 30 vol. % COP-MgCaTiO<sub>2</sub> composites with fillers sintered at 1200°C exhibit a  $\epsilon_r$  of 4.88 and a  $\tan \delta_d$  below 0.0070 at 66 GHz. To the best of my knowledge, these EM properties (combination of high- $k$  and low-loss) are superior to other 3D-printable microwave materials reported by the scientific microwave community and are on par with materials developed for high-performance microwave laminates by RF/microwave industry as shown in Chapter 5 and Chapter 7 and summarized in Table 5.4 and Table 7.1. Meanwhile, the linear coefficient of thermal expansion (CTE) from -25°C to 100°C of the reinforced 30 vol. % COP-MgCaTiO<sub>2</sub> composite with fillers sintered at 1200°C is 64.42 ppm/°C, which is about 20 ppm/°C lower when compared with pure ABS and 10 ppm/°C lower as compared to high-temperature polyetherimide (PEI) ULTEM<sup>™</sup> 9085 resin from Stratasys, Ltd. The CTE at 20°C of the same composite material is 84.8 ppm/°C which is about 20 ppm/°C lower when compared with pure ABS that is widely used by the research community for 3D printed RF/microwave devices by FDM. The electromagnetic (EM) composites with tailored EM properties studied by this work have a great potential for enabling the next generation of high-



performance 3D-printed RF/microwave devices and antennas operating at the Ku-band, K-band, and mm-wave frequencies.

## CHAPTER 1 : INTRODUCTION

### 1.1 Overview

Recently, 3D Additive Manufacturing (AM) has received tremendous attention from both research communities and industries in several scientific disciplines due to its great potential as a versatile and accurate rapid prototyping technology [1]-[3]. An ever-increasing number of wireless devices have been demonstrated by employing additive manufacturing (AM) techniques in the last few years, such as stereolithography (SL) [4], fused deposition modeling (FDM) [1]-[3] and [5]-[10], electrochemical fabrication (EFAB) [11], laser direct structuring of molded interconnect device (LDS-MID) technology [12], [13]. Other approaches include a combination of several techniques for device miniaturization (e.g., FDM, photolithography for patterning conductive layers in liquid crystal polymer (LCP) commercial high-end laminates, and the use of high- $k$  polymer matrix composites (PMCs)) [14], and formation of thermoplastic or polymer structures to be used as substrates and packaging [2]. For the deposition of conductive traces and interconnects, technologies such as micro-dispensing, ink-jet printing, aerosol jet printing and selective laser structuring are some of the available approaches [2]. As compared to conventional processes, 3D AM of antennas or other microwave components provides additional design freedom by taking advantage of the complete three-dimensional volume that can be exploited for miniaturization.

The AM rapid market growth is estimated to be over \$8 billion by 2023. Therefore AM technologies are expected to become a powerful enabler for the current and next generation of microwave devices in the internet of things (IoT) era. Nevertheless, the reported development of

advanced FDM-compatible microwave composite materials has been lacking. Most of the FDM-produced RF/microwave devices reported so far [1]-[3], [5]-[9], [15] and [16] are based on pure (unloaded) thermoplastics (e.g., acrylonitrile butadiene styrene (ABS), polycarbonate (PC), polyetherimide (PEI) also known as ULTEM™ resin, etc.). These materials in most of the cases exhibit either low glass-transition temperature ( $T_g$ ) or high dielectric losses at high frequencies, thus limiting their applications to low-power or low-performance microwave devices, respectively.

This work combines several disciplines and techniques (i.e., materials science, 3D-printing, and RF/microwave engineering). A generic methodology to develop FDM-compatible high-permittivity and low-loss ceramic-thermoplastic composites based on cyclo-olefin polymer (COP) loaded with a selected volume fraction of sintered high- $k$  ceramic micro-fillers has been investigated for additive manufacturing of high-performance microwave devices. The effective dielectric and loss properties of the newly developed composites were evaluated up to the Ku-band (17 GHz) or K-band (20 GHz) through cavity resonator measurements. In some cases, the dielectric/loss properties were measured up to V-band (69 GHz) by circular cavity measurements.

For manufacturing of device prototypes, a direct digital manufacturing (DDM) approach was used following the method reported in [1], [2]. Edge-fed patch antennas operating at 17.2 GHz and 16.5 GHz were fabricated by combining FDM and direct print additive manufacturing (DPAM) also known as micro-dispensing for the deposition of conductive traces using CB series screen printable ink materials (e.g., CB028 by DuPont) over the newly developed electromagnetic (EM) composites printed by FDM. These antennas employ an in-house prepared 25 vol. % COP-MgCaTiO<sub>2</sub> composite FDM filament with the fillers sintered at 1100°C and a pure (unloaded) COP filament, which were both prepared and extruded following the process described in this dissertation (c.f. Chapter 5 and Chapter 6). The low dielectric loss of the 25 vol. % COP-

MgCaTiO<sub>2</sub> composite material has been leveraged to achieve a peak realized gain of 6 dBi. Also, a patch area miniaturization of 50% was achieved when compared with an antenna designed and DPAM-printed over a Rogers RT/duroid® 5870 laminate core through micro-dispensing of CB028 silver paste. This reference antenna exhibited a measured peak realized gain of 6.27 dBi.

In this dissertation, two types of newly developed composite materials were characterized up to the V-band (69 GHz) frequencies by using a circular cavity resonator. As compared to ABS, polylactic acid (PLA), polypropylene (PP) and polycarbonate (PC), pure COP and filler-reinforced COP composites offer higher  $T_g$ , better chemical inertness to solvents and strong acids, and superior dielectric/loss properties. In particular, it exhibits low dielectric loss tangent ( $\tan \delta_d$  lower than 0.0011 and  $\tan \delta_d$  lower than 0.0070) up to V-band frequencies for unloaded and ceramic-loaded specimens, respectively. Such attributes offer an exceptional performance potential for wireless systems operating in unique hostile or harsh environments, such as satellite systems in space, aerospace and automotive applications, etc.

## 1.2 Dissertation Organization

This dissertation is organized into eight chapters. The first chapter presents an introduction and overview of the forecasted additive manufacturing market and its potential impacts to wireless communications, followed by the reported progress in microwave devices by the microwave community by using AM technologies. Then the focus is steered towards the FDM technology while describing the main findings of this dissertation research. Chapter 2 provides a background and literature review of DDM with a primary focus on FDM and their application to RF/microwave devices. The motivation of this work is elaborated that is to address the lack of high-permittivity and low-loss 3D-printable materials that severely hinders the ability for AM to be employed for manufacturing RF and microwave electronics in a middle to high-volume manufacturing scale.

Chapter 3 presents a generic methodology to enhance the microwave dielectric properties of polymer-ceramic EM composites with  $\text{MgCaTiO}_2$  and  $\text{TiO}_2$  micro-fillers through a high-temperature sintering process. A new kind of high-permittivity and low-loss EM composites based on sintered  $\text{Ba}_{0.55}\text{Sr}_{0.45}\text{TiO}_3$  and  $\text{MgCaTiO}_2$  micro-fillers for additive manufacturing and their application to 3D-printed K-band antennas are presented in chapter 4. Chapter 5 introduced the preparation and dielectric modeling of ceramic-thermoplastic composites in the form of FDM feedstock materials. Ceramic-thermoplastic composites for FDM and their application to fully 3D-printed antennas operating in the Ku-band are then presented in Chapter 6. Chapter 7 covers millimeter-wave characterization and thermal analysis of ceramic-thermoplastic composites for FDM process. Chapter 8 presents conclusion and viable directions for future research work related to engineered composite materials for 3D-printed microwave components.

### 1.3 Contributions

- To the best of my knowledge, fully 3D-printed microwave devices by a DDM process operating in the Ku-band employing a new kind of engineered EM COP-based composites were published for the first time by this dissertation work [10], [17].
- A new class of FDM-ready, high- $k$  and low-loss feedstock filament materials has been prepared and characterized up to 70 GHz.
- Assessment of several models for prediction of the effective dielectric permittivity of composites by filler loading volume fraction has been evaluated, among which Hanai-Bruggeman and Maxwell models have shown the best accuracy up to 40% filler volume fraction. Also, the preliminary model prediction of the dielectric loss in the composite materials is explored in this dissertation.

- Moreover, several newly developed COP-based electromagnetic (EM) composites are amongst the best of their class on high-permittivity and low-loss (i.e.,  $\epsilon_r \approx 5$  and  $\tan \delta_d$  less than 0.0012) up to the Ku-band. These FDM-ready feedstock composites possess better properties, particularly in terms of dielectric losses than some state-of-the-art microwave laminates, (e.g., Rogers RO4003<sup>®</sup>, TMM3<sup>®</sup>, and isola Tachyon<sup>®</sup>, and isola I-Tera<sup>®</sup> MT). Also, these properties approach the lowest dielectric losses of high-end microwave laminates exhibited by Rogers RT/duroid<sup>®</sup> 5880/5870, ARLON CLTE-XT<sup>™</sup>, and AD250C<sup>™</sup> (see Table 5.4 and Figure 5.17).
- Several Composite materials with dielectric losses on par with the state-of-art Rogers high-frequency microwave laminates have been developed. In particular,  $\epsilon_r$  of 4.56 and  $\tan \delta_d$  lower than 0.0014 have been realized, which are 2x and 3x better than those of ABS (a widely used thermoplastic materials for additive manufacturing), respectively.
- Two composite materials characterized at the mm-wave frequencies up to the V-band (69 GHz). In particular, pure (unloaded) COP thermoplastic exhibits a relative permittivity of 2.1 and a loss tangent below 0.0011 at 69 GHz, whereas 30 vol. % COP-MgCaTiO<sub>2</sub> composites with fillers sintered at 1200°C show a relative permittivity of 4.88 and a loss tangent below 0.0070 at 66 GHz.
- Fully additive manufactured Ku-band 17 GHz patch antennas have been successfully demonstrated by using 25 vol. % COP-MgCaTiO<sub>2</sub> composites and silver paste, showing a 16 dB return loss and a peak gain of 6 dBi. It is 50% smaller than a reference design built with Rogers RT/duroid<sup>®</sup> 5870 microwave laminate core with a similar gain.

- This new class of high- $k$ , low-loss composite materials has shown some promising attributes for enabling the next generation of high-performance 3D-printed RF and microwave devices such as antennas operating in the Ku-band, K-band and the mm-wave frequencies.
- The CTE at 20°C of the 30 vol. % COP-MgCaTiO<sub>2</sub> composites with fillers sintered at 1200°C is 84.8 ppm/°C, which is about 20 ppm/°C lower when compared with the ABS that is widely used by the research community for 3D printed RF/microwave devices by FDM [1]-[3], [6]-[9].
- Pure COP ZEONOR® (1420R) exhibited a dielectric permittivity  $\epsilon_r$  of 2.15 and a dielectric loss tangent  $\tan \delta_d$  lower than 0.0016 (as shown in Table 5.3 and Figure 5.13), and a  $T_g$  of 126°C. This type of COP has exhibited the lower linear CTE of 62 ppm/°C (from -25°C to 100°C) and the lowest CTE of 61.4 ppm/°C (at 20°C) amongst the three variations of 3D-printed COPs, which are better than most of the thermoplastics shown in Table 7.2, also very close to the thermal performance of high-temperature ULTEM™ 9085 resin and PPSF/PPSU materials from Stratasys, Ltd. Hence, it is an excellent candidate as a thermoplastic matrix for the next generation of FDM-ready EM composites based on COP polymer matrix.

## CHAPTER 2 : BACKGROUND AND LITERATURE REVIEW

### 2.1 Overview of Direct Digital Manufacturing (DDM)

The typical DDM process is a manufacturing methodology to develop systems with the least amount of human interaction and tooling as possible. This process integrates multi-material to fabricate functional parts by 3D-printing techniques. 3D-printing is a method to manufacture a part in a line-by-line and layer-by-layer fashion combining several materials and technologies [1]. In this dissertation, fused deposition modeling (FDM) of pure thermoplastics as shown in Table 5.3 or engineered EM composites as shown in Table 5.4 and Table 7.1 followed by the deposition of conductive traces by using a printable silver paste (i.e., CB028 from DuPont) through the micro-dispensing technique are investigated. Another multi-material approaches successfully explored by the research community is the combination of FDM and electroplating as reported by D’Auria *et al.* [18], and polymer poly-jetting with inkjet printing by Kimionis *et al.* [19].

#### 2.1.1 Fused Deposition Modeling (FDM)

Fused deposition modeling (FDM) are trademarks of Stratasys, Ltd. FDM technology was patented in 1992 by Scott Crump, founder of Stratasys, Inc. The patent is entitled “*Apparatus and method for creating three-dimensional objects*” [20], followed by some improved and revised versions of the technology and processes as reported in [21], [22]. FDM is also known as fused filament fabrication (FFF) in the “RepRap” project giving a phrase legally unconstrained in its use [2]. In some cases, it is known as Plastic Jet Printing (PJP). The FDM or FFF technology uses a filament feedstock material, pellets or powder-like material. The process starts by melting the material by passing it through a heated section in the 3D printer. The molten material is then



pressed through a small heated nozzle or tip with the desired diameter and expelled onto the surface of the printed sample [1].

FDM technology is often used for fast prototyping with the primary goal to decrease the design cycle in a typical R&D process by combining a rapid manufacturing process where several iterations can be tried at a very low cost until the desired design is achieved by exploring a high-volume manufacturing process. Typical FDM materials include PLA, ABS, polyphenylsulfone (PPSF), PC, PEI also known as ULTEM™ resin, and others [23], the 3D-printing process by FDM is shown in Figure 2.1. These materials in most of the cases exhibit either low  $T_g$  or high dielectric loss at high frequencies, hence limiting their applications to low-power or low-performance microwave devices, respectively.

### **2.1.2 Direct-Print Additive Manufacturing (Micro-Dispensing Technique)**

Direct print additive manufacturing (DPAM) also known as micro-dispensing is a process that works similarly to FDM, where pressure is used to push material through a nozzle with the desired diameter as shown in Figure 2.1 [23]. Typically conductors, resistors, and dielectrics can be printed through micro-dispensing by mixing chosen materials in solvent suspension [1], [24]. However, the common challenges with the deposition of conductive traces by using slurry type pastes, such as a printable silver paste (CB028), are the required post-process heating to achieve a decent conductivity [2], [8] by following a vendor-recommended curing process. Table 2.1 depicts a summary of the bulk DC conductivity of CB028 measured using a four point probe and van der Pauw method under different curing temperatures [2]. The roughness was measured by using a profiler Dektak D-150 (Veeco, Plainview, NY), along with compatible materials based on the previous works [2], [17], [25]. The measured roughness is reported in Table 2.1, and the  $T_g$  are reported in Table 5.3.

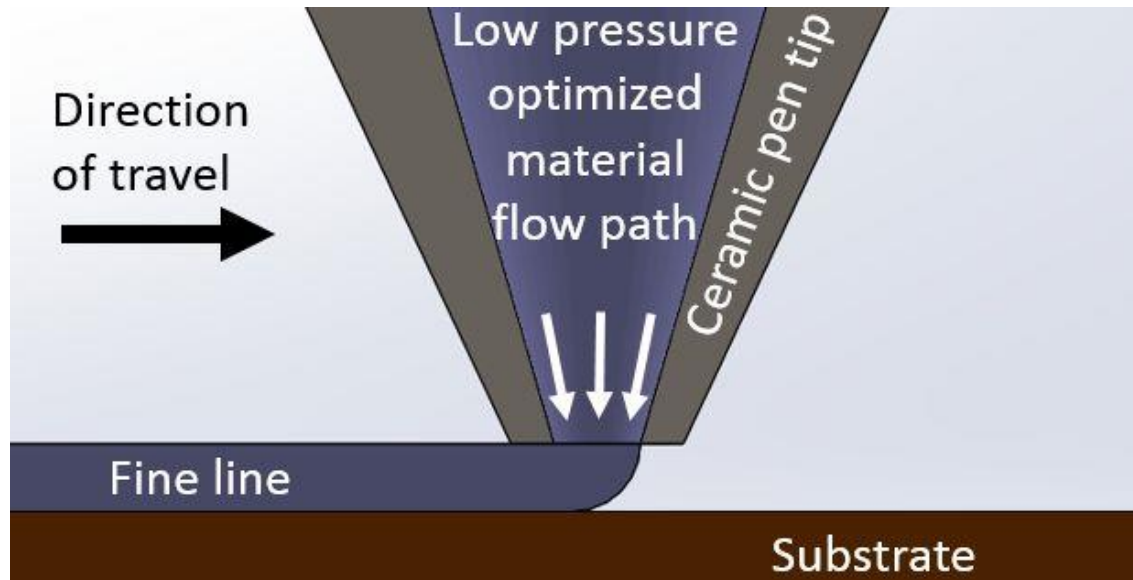


Figure 2.1 – Conceptual illustration of a typical FDM or micro-dispensing printing process. Image courtesy of Church *et al.* [1] © IEEE 2017. See permission in Appendix A.

Table 2.1 – Bulk DC conductivity of CB028 silver paste

Cure Temp. (°C)	Conductivity (S/m), [2]	Compatible Materials, [2], [17]	Roughness (Ra), [25]
60	1.75e6	PLA,PP	3.68 μm
90	2.62e6	ABS,PC-ABS,COP	
130	3.94e6	COP, PC	
160	4.63e6	PEI, PPSF/PPSU	

## 2.2 DDM in the RF/microwave Community

The main goal of DDM processes for microwave applications is to develop structural microwave electronics by combining several techniques (e.g., FDM, micro-dispensing, pick-and-place, milling, laser-machining, micro-machining, etc.) preferably with the least amount of human interaction and tooling as possible. Hence, ideal strategies should avoid micro-machining as much as possible, due to its subtractive-manufacturing nature that typically involves several processes (e.g., chemicals, sacrificial layers (waste), masks, etc.). By combining several DDM techniques and AM systems, it is possible to fabricate non-planar or multilayer microwave structures that would be difficult to be accomplished by using conventional micro-machining processes along

with planar microwave laminates or semiconductor substrates. Some non-planar devices fabricated by DDM techniques in prior works are shown in Figure 2.2 (b), Figure 2.3, and Figure 2.4.

One of the first fully 3D-printed microwave devices by using a DDM process that combines FDM and micro-dispensing was a 2.4 Bluetooth/Wi-Fi planar inverted “F” antenna reported in 2013 by Deffenbaugh [6]. This work uses ABS as dielectric material and silver paste (CB028) for the conductive traces, and the DDM produced antenna is shown in Figure 2.2(a). On the other hand, the potential of AM technologies in a non-planar microwave device can be appreciated more easily with the periodic spiral antenna (PSA) shown in Figure 2.2(b) reported by O’Brien *et al.* [15], [16]. This antenna was fabricated by using a Fortus 400mc FDM system from Stratasys, Ltd., to create a volumetrically optimized substrate based on high-temperature ULTEM™ resin material with good dielectric properties ( $\epsilon_r = 2.75$ ,  $\tan \delta_d = 0.004$ ) [15].

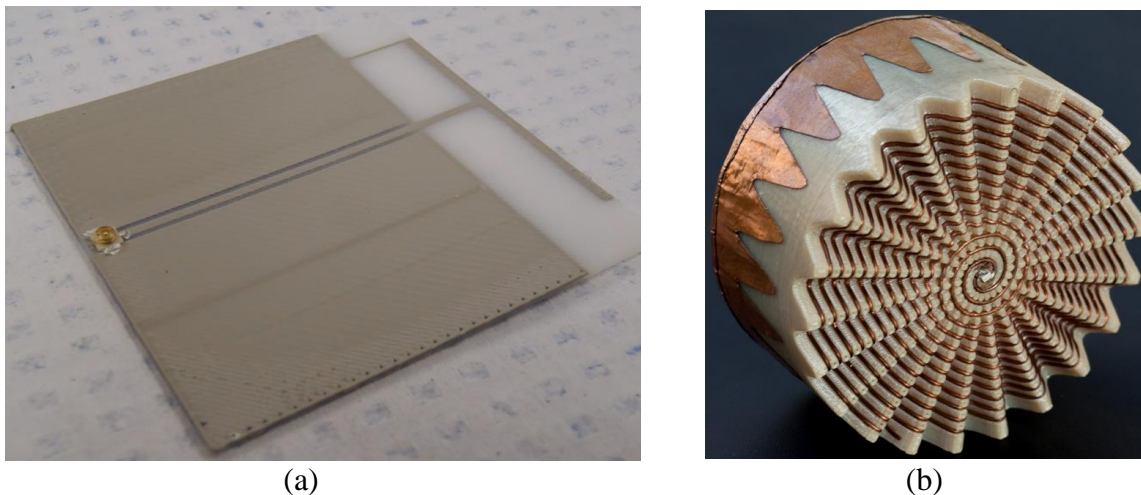


Figure 2.2 – (a) 2.4 Bluetooth/Wi-Fi planar inverted “F” antenna, photograph courtesy of Deffenbaugh *et al.* [6] © IMAPS 2013. (b) 3D-printed periodic spiral antenna (PSA), photograph courtesy of O’Brien *et al.* [15] © IEEE 2015. See permissions in Appendix A.

In 2015, Abdin *et al.* reported a miniaturized 2.45 GHz 3D-printed balun fabricated by combining AM techniques along with UV lithography. The device uses a high- $k$  polymer-ceramic composites deposited and molded manually over an FDM-printed ABS substrate, followed by a

layer of liquid crystal polymer (LCP) ULTRALAM<sup>®</sup> 3850HT from Rogers Corp., which is patterned by a photolithography process to form the conductive layers. The final layer uses a second layer of the molded high- $k$  polymer-ceramic composites based on PDMS-MgCaTiO<sub>2</sub> as shown in Figure 2.3(a). In this work, about 60% of miniaturization in size was reported by this methodology. However, the high- $k$  composites employed was not 3D-printed due to the incompatibility with AM techniques (e.g., FDM or micro-dispensing, etc.). The miniaturized 2.45 GHz balun is shown in Figure 2.3(b) [14].

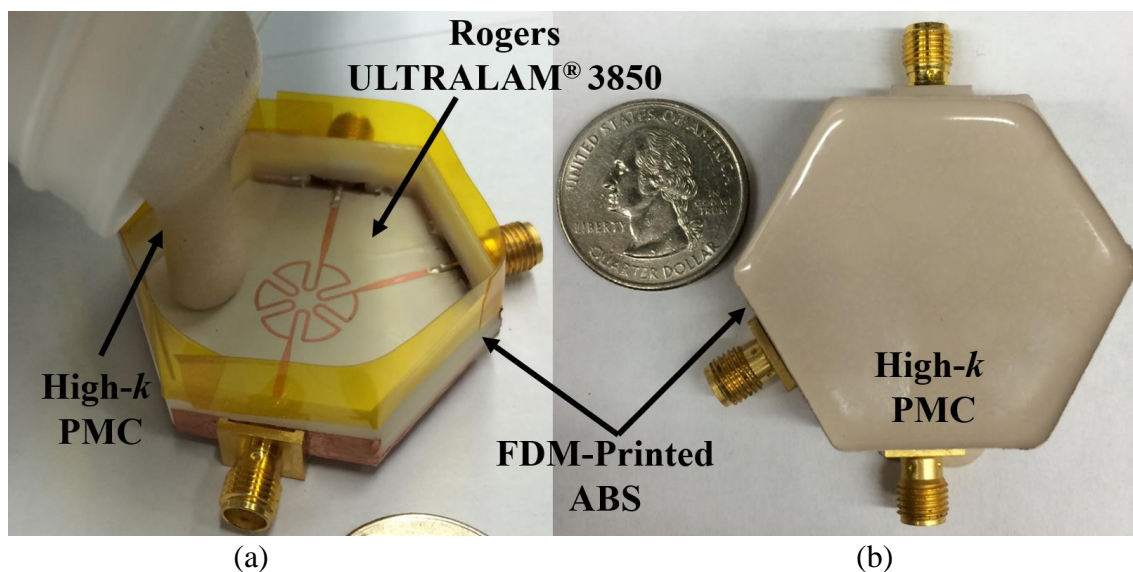


Figure 2.3 –Miniaturized 2.45 GHz balun using high- $k$  composites. Combining: (a) 3D-printing ABS by FDM, photolithography for patterning metal layers, and molding of high- $k$  composites. (b) Miniaturized 2.45 GHz balun. Photographs courtesy of Abdin *et al.* [14] © IEEE 2015. See permissions in Appendix A.

Similarly, In 2015, Ketterl *et al.* reported an entirely 3D-printed RF front end with a 2.45 GHz phased array antenna unit cell [2], implemented by a multi-material micro-dispensing and FDM approach using ABS. Despite this recent success, the two main drawbacks of employing ABS as the core of high-performance microwave devices remain. One is related to its relatively low  $T_g$  of about 105°C, which limits its use to low-power applications. The other is related to the poor chemical inertness of ABS, which could result in susceptibility to failures in harsh

environments. Figure 2.4 depicts the fully 3D-printed RF Front-end by using a DDM process that is combined with FDM to print several layers of ABS and conductive traces through alternating of FDM and micro-dispensing processes.

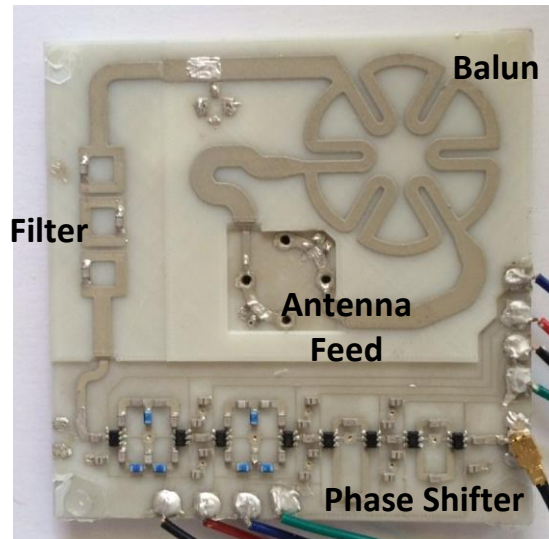


Figure 2.4 –Phased array antenna (PAA) unit cell fabricated with direct digital manufacturing (DDM). The front-end consists of a phase shifter, band-pass filter, amplifier module, balun and antenna (on the bottom of the stack). The unit cell dimensions are 6 cm in length and width, with a height of 5.2 mm. Photograph courtesy of Church *et al.* [1] © IEEE 2017 and Ketterl *et al.* [2] © IEEE 2015. See permissions in Appendix A.

### 2.3 High-Dielectric Materials in Electronic Applications

High-permittivity materials (also known as high- $k$  dielectric materials) can store more electric energy than a dielectric material with lower permittivity as shown in Equations (2.1) and (2.2). Therefore, a high- $k$  material is capable of improving the efficiency of electronic devices. There are several applications of high- $k$  materials (e.g., aerospace, underwater navigation, and surveillance, etc.). Also, they are used for biomedical imaging, imaging microphones, and so on [26], along with use in passive components such as capacitors. Additionally, they are widely used in microwave applications such as high-end microwave laminates or printed circuit boards (PCBs).

Some ceramics with high stiffness and excellent thermal stability also have the desired high- $k$  properties. However, their high density, brittleness, as well as challenging and costly

processing conditions hinder their wide use as high- $k$  dielectrics in some practical applications. Due to the mechanical flexibility and tunable properties, polymer matrix composites (PMC) are a very attractive option for electronic applications. Nevertheless, typically organic polymers exhibit quite low dielectric permittivity of 2-3, in very rare cases their relative permittivity can go beyond 10 [26]. And this is the main reason why engineered composite materials play a significant role in microwave applications, and it will be discussed further in the following chapters.

Some strategies to engineer PMC with well-tailored EM properties have been explored in the last years [26], such as random composites of polymers, field structured composites, and synthesis of new polymers. In particular, to raise the dielectric permittivity, the addition of high- $k$  fillers to form polymer-ceramic composites with the fillers ranging from metals, ceramics, carbon-based materials, and organic fillers (e.g., conductive oligomer and conductive polymer matrices) have shown some great promises [26]. In this dissertation, ceramic-polymer composites prepared by adding sintered high- $k$  ceramic fillers in a strategically-chosen polymer host matrix have been systematically investigated, which are detailed in the following chapters.

Table 2.2 – Mechanisms that contribute to the displacement of charges in materials [27]

Frequency (Hz)	Mechanisms
< about $10^3$	Ion migration can occur
up to $10^{11}$	Rotation of polar entities typically occur
up to $10^{14}$	Molecules can respond to an electric field by bond vibration
above $10^{14}$	Only electrons of an atom are sufficiently mobile to respond

The dielectric constant or relative permittivity ( $k$  or  $\epsilon_r$ ) of a certain material or PMC is the tendency of a material to polarize under an electric field. The dielectric constant of a medium arises from the interaction of the electric field with the polar elements (sites of charge displacement) of the material itself. The higher the polarity of the sites, and the higher the density of the sites, the



higher the dielectric constant typically is for a certain material as elaborated by Horn [27]. The conventional mechanisms that contribute to the displacement of charges in a material vary with frequency as shown in Table 2.2. Hence, as frequency increases the dielectric constant of a material tends to decrease depending on its composition as explained by Horn [27].

The dielectric loss or loss tangent ( $\tan \delta_d$  or  $\epsilon_r''/\epsilon_r'$ ) is the ratio of the apparent power consumed by a material to the real power consumed. Typically, the dielectric loss is reduced when the time it takes for a dipole moment of a molecule reaches equilibrium with the electric field rapidly. Usually, the dielectric loss arises from the molecular and atomic friction caused by the charge displacement during the polarization process [27]. Ideally, a lossless material would switch polarization in synchronization with the applied electric field. Dielectric loss tangent ( $\tan \delta_d$ ) may increase or decrease by frequency depending on the properties of the material. The dielectric loss often increases by frequency, and it is one of the most critical material parameters that needs to be engineered as low as possible at high frequencies for high-performance microwave applications.

## 2.4 Fundamental Characteristics of High- $k$ Composites

### 2.4.1 Capacitance and Electric Energy Storage of Materials

A capacitor is made of two conductive electrodes (plates) separated by a dielectric material. When a potential (V) is applied between these electrodes, the capacitor can store electric charge (Q) in coulombs given by Equation (2.1):

$$Q = CV \quad (2.1)$$

where C is the capacitance in farads (F). Also, the capacitance of a capacitor with parallel plate electrodes is given by Equation (2.2):

$$C = \epsilon_0 \epsilon_r \frac{A}{d} \quad (2.2)$$

where  $\epsilon_0$  is the dielectric permittivity of vacuum 8.85418 pF/m,  $\epsilon_r$  is the relative permittivity of the dielectric material,  $A$  is the area of overlap of the two parallel plate electrodes in  $m^2$ , and  $d$  is the separation between the parallel plate electrodes in m.

## 2.4.2 Polarization and Relaxation in Dielectric Materials

As explained in Table 2.2 the permittivity of materials depends on the frequency of the applied electric field, and generally, the frequency dependence reveals the possible existence of dispersive behaviors over the electromagnetic spectrum [26]. Dielectric relaxation is the temporary delay in the dielectric permittivity of a material usually caused by the time delay in molecular polarization under a changing electric field in a dielectric medium. The relaxation can be described in terms of permittivity as a function of frequency, which can be outlined by the Debye Equation (2.7). The complex permittivity of a material as a function of frequency is given by Equation (2.3):

$$\epsilon^*(\omega) = \epsilon'(\omega) + j\epsilon''(\omega) \quad (2.3)$$

where  $\omega$  is the angular frequency  $\omega=2\pi f$ , and  $\epsilon'(\omega)$  is the real part of the dielectric permittivity, which represents the contribution to the polarization responsible for the energy storage in the material. The  $\epsilon''(\omega)$  is the imaginary part, known as the loss factor, typically shows the dissipative effects with a finite value higher than zero in dispersive regions [26]. The dissipation behavior (dielectric loss or loss tangent) can be expressed by dielectric loss tangent given by Equation (2.4):

$$\tan \delta(\omega)_d = \frac{\epsilon''(\omega)}{\epsilon'(\omega)} \quad (2.4)$$

In a homogeneous material, such as a PMC, the polarization and  $\epsilon''(\omega)$  result from several contributions. As per Dang *et al.* [26], the individual contribution to  $\epsilon''(\omega)$  can be added up to give the effective relative complex permittivity ( $\epsilon^*_{eff}$ ) expressed by Equation (2.5):

$$\epsilon^*_{eff}(\omega) = \epsilon^*(\omega) + \sum_i \epsilon^*_{MW,i}(\omega) + j\left(\frac{\sigma_{DC}}{\omega\epsilon_0}\right) \quad (2.5)$$



where  $\varepsilon^*(\omega)$  is the permittivity of all components,  $\varepsilon^*_{MW,i}(\omega)$  is the permittivity of interfaces, and  $\sigma_{DC}$  is the DC electrical conductivity. Equation (2.5) can be simplified to Equation (2.6):

$$\varepsilon^*_{eff}(\omega) = \left( \varepsilon'(\omega) + \sum_i \varepsilon'_{MW,i}(\omega) \right) + j \left( \varepsilon''(\omega) + \sum_i \varepsilon''_{MW,i}(\omega) + \frac{\sigma_{DC}}{\omega \varepsilon_0} \right) \quad (2.6)$$

where  $\varepsilon'_{MW,i}$  accounts for the  $i$ th interfacial contribution. As per Dang *et al.* all the dispersive phenomena related with the intrinsic polarization are considered by  $\varepsilon^*(\omega)$  in Equation (2.5). In the presence of multiple intrinsic relaxations,  $\varepsilon^*(\omega)$  can be expressed as a superposition of individual contributions. Each of these relaxation processes is either orientational or interfacial. In the case of a material based on identical and non-interacting dipoles whose relaxation is characterized by a unique time constant  $\tau$  (also known as dipole relaxation time), Debye derived a relaxation function for the complex permittivity in the dispersion region [26], [60]. The Debye model in the frequency domain is given by Equation (2.7) reported by Dang *et al.* [26]:

$$\varepsilon^*(\omega) = \varepsilon_\infty + \frac{\varepsilon_s - \varepsilon_\infty}{1 + j\omega\tau} \quad (2.7)$$

where  $\varepsilon_s$  and  $\varepsilon_\infty$  are the static low-frequency (relaxed) and the high-frequency (unrelaxed) values of permittivity, respectively. Equation (2.7) can be rewritten to show the real part given by Equation (2.8):

$$\varepsilon'(\omega) = \varepsilon_\infty + \frac{\varepsilon_s - \varepsilon_\infty}{1 + \omega^2\tau^2} \quad (2.8)$$

While the Equation (2.7) can be rewritten showing the imaginary part given by Equation (2.9):

$$\varepsilon''(\omega) = \frac{(\varepsilon_s - \varepsilon_\infty)\omega\tau}{1 + \omega^2\tau^2} \quad (2.9)$$

In general, the Debye model tends to fail when describing the relaxation phenomena in complex systems. Havriliak-Negami model proposed a more accurate model by phenomenological approach [26], [29], [60] given by Equation (2.10), which includes the possibility of distribution

of different time constants through the introduction in Equation (2.8) of two shape parameters  $\alpha$  and  $\beta$  [26] as shown in Equation (2.10):

$$\varepsilon''(\omega) = \varepsilon_{\infty} + \frac{(\varepsilon_s - \varepsilon_{\infty})}{[1 + (j\omega\tau)^{1-\alpha}]^{\beta}} \quad (0 < \alpha < 1, 0 < \beta < 1) \quad (2.10)$$

It is worthwhile mentioning that the dielectric losses in materials not only dissipate energy but also deteriorate the insulation properties of materials. The power density (W) dissipated into the dielectric medium is a function of electric field given by Equation (2.11):

$$W \approx \omega |\vec{E}|^2 \varepsilon''_{eff}(\omega) \quad (2.11)$$

### 2.4.3 Dielectric Strength of Polymer Matrix Composites (PMC)

In 2012, Dang *et al.* [26] reported several relationships to estimate the dielectric strength in PMCs. Since high- $k$  PMCs are typically used to store electric energy, the material dielectric strength is an important parameter that should be taken into account during engineering composites for electronic applications. The maximum energy storage density ( $W_{max}$ ) in  $Jm^{-3}$  is calculated by Equation (2.12):

$$W_{max} \approx \frac{1}{2} \varepsilon_0 \varepsilon_r E_{break}^2 \quad (2.12)$$

where  $E_{break}$  is the material dielectric strength. Considering a homogenous material and elastic body at low strains, the nominal breakdown field of the materials is given by Equation (2.13):

$$E_{break} = \frac{V_{break}}{t} = e^{-1/2} \sqrt{\frac{Y}{2\varepsilon_0 \varepsilon_r}} \cong 0.6 \sqrt{\frac{Y}{2\varepsilon_0 \varepsilon_r'}} \quad (2.13)$$

where  $Y$  is the elastic modulus, and  $\varepsilon_r$  is the relative dielectric permittivity of the material,  $\varepsilon_0$  is the permittivity of vacuum,  $V_{break}$  is the breakdown voltage of the sample with thickness  $t$  at rest. It is observed that by increasing the relative dielectric permittivity in a composite material, the dielectric strength tends to decrease. Equation (2.13) provides a good approximation [26]. Another

model is based on local field theory of dielectric media, which considers a material exposed to an electric field  $\vec{E}$ . As a result, the local electric field ( $E_{\text{local}}$ ), which is also known as the Lorentz local field, is induced given by Equation (2.14). It is the field that acts on an individual polarizable unit (e.g., molecule or atom) [26].

$$E_{\text{local}} = \frac{\varepsilon' + 2}{3} \vec{E} \quad (2.14)$$

where  $\varepsilon'$  is the relative permittivity of the material adjacent to the local polarizable unit (not including the unit itself). Another relationship that takes into account the relative permittivity and dielectric strength of the polymer matrix ( $\varepsilon_m'$ ,  $E_{\text{break-matrix}}$ ), as well as these properties of the final composites ( $\varepsilon_c$ ,  $E_{\text{break-composite}}$ ) is given by Equation (2.15). It typically provides a good property estimation [26].

$$\frac{\varepsilon_m' + 2}{3} E_{\text{break,matrix}} = \frac{\varepsilon_c' + 2}{3} E_{\text{break,composite}} \quad (2.15)$$

## 2.5 Functional Composite Materials in Microwave Applications

Preparation of PMC materials comprised of low-loss polymers loaded with high-permittivity ceramic particles is a very useful technique to raise the dielectric permittivity and explore miniaturization of microwave components by increasing the index of refraction in microwave materials given by Equation (2.16). In particular, dielectric ceramics have been widely used for microwave applications as the key element of dielectric resonators and filters [30]-[31].

Due to the ease of processing, excellent compatibility with additive manufacturing and their versatile properties (e.g., thermal, mechanical and electromagnetic), low-cost polymer composites have emerged as a promising functional material for microwave device applications [32]. For instance, antenna miniaturization has been demonstrated by using composite materials with evenly dispersed high-permeability [32]-[37] or high-permittivity ceramic fillers [38]-[42], as

well as mosaics of two dielectric materials [43]-[46]. The latter composites are arranged according to a particular design known as “textured dielectrics” in the microwave community, which employs spatially variant dielectric composites [43] with the index of refraction  $n$  and also the miniaturization factor is given by Equation (2.16):

$$n = \sqrt{\mu_r \varepsilon_r} \quad (2.16)$$

Similarly, the zero-order antenna bandwidth over a magneto-dielectric substrate with thickness  $t$  can be approximated by Equation (2.17) as reported by Mosallaei *et al.* [37]:

$$BW \approx \frac{96 \sqrt{\frac{\mu_r}{\varepsilon_r}} \frac{t}{\lambda_0}}{\sqrt{2} [4 + 17 \sqrt{\mu_r \varepsilon_r}]} \quad (2.17)$$

The well-known Equation (2.18) gives the wavelength of a signal propagating through a medium.

$$\lambda_g = \frac{\lambda_0}{\sqrt{\mu_r \varepsilon_r}} = \frac{c_0}{f \sqrt{\mu_r \varepsilon_r}} \quad (2.18)$$

where  $\lambda_g$ ,  $\lambda_0$ ,  $c_0$ ,  $\mu_r$ , and  $\varepsilon_r$  are the wavelength in the material, the wavelength in vacuum, the speed of light in free-space, relative permeability and relative dielectric permittivity, respectively [32], [33].

In 2006, Koulouridis *et al.* reported characteristics of several high-permittivity flexible polymer-ceramic composites by loading Polydimethylsiloxane (PDMS) (Dow Corning, Midland, MI) with ceramic powders, which were supplied by (Trans-Tech, Inc., Adamstown, MD and Ferro corp., Cleveland, OH). They reported PDMS-BT-BaTiO<sub>3</sub> composites with measured dielectric properties of  $\varepsilon_r$  of 20 and  $\tan \delta_d$  lower than 0.04 as well as PDMS-MgCaTiO<sub>2</sub> and PDMS-BiBaNdTi composites with measured  $\varepsilon_r$  of about 8.5 and  $\tan \delta_d$  lower than 0.009 [39]. Nonetheless, these composites were only characterized up to 1 GHz, which renders uncertainties for applications

beyond the ultra-high-frequency (UHF) range given the fact that dielectric properties of EM composite materials are frequency dependent.

The work reported by Koulouridis *et al.* in 2006 has allowed the microwave community to exploit this approach in the last decade and develop new methodologies for microwave composite materials. This method has been widely explored more recently as reported by Cure [41], by Shi *et al.* [42], our group [38], [40] and some variations by Koulouridis *et al.* [39]. Tunable magneto-dielectric composites have been reported previously by Morales *et al.* by using PDMS embedded with chemically synthesized  $\text{Fe}_3\text{O}_4$  nanoparticles [34], [35], [36]. Antenna miniaturization has been achieved by using composite materials with embedded high-permittivity [17], [10], [38]-[42] and [49] or high-permeability [32]-[37] particle fillers.

In 2013, Cure *et al.* reported a newly developed RF planar substrate that is composed of PDMS with embedded  $\text{NdTiO}_3$  ceramic powders at different loading concentrations. Specifically, 20 vol. % PDMS- $\text{NdTiO}_3$  composites were built into a 4 GHz microstrip patch antenna which exhibited a gain of 3 dBi along with a 5.8% bandwidth and a 42% size reduction [41]. Nonetheless, all composites above were filled with unsintered micro-fillers and were only characterized up to 1 GHz. In 2014, Shi *et al.* reported the fabrication of a PDMS- $\text{SrTiO}_3$  composite sample with tested  $\epsilon_r$  of 8.40 and  $\tan \delta_d$  of 0.017 up to 10 GHz [42]. In July 2015, Zhang *et al.* reported a high- $k$  and low-loss composite material based on Bisphenol-A cyanate ester resin (BADCy) and  $\text{Ni}_{0.5}\text{Ti}_{0.5}\text{NbO}_4$  fillers sintered at  $700^\circ\text{C}$  with measured  $\epsilon_r$  of 22.79 and  $\tan \delta_d$  of about 0.00417 up to 9 GHz [47]. This work shows great potential for its applications in high EM frequencies. Despite this recent success, these molded rigid composites are only suited as a direct substitute of planar printed circuit boards (PCBs). In 2014, the temperature dependence of dielectric properties (at frequencies from 100 Hz to 1 MHz) for  $0.94\text{MgTiO}_3\text{-}0.06\text{Ca}_{0.8}\text{Sr}_{0.2}\text{TiO}_3$  (MT-CST) ceramics

sintered at 1300°C for four hours was reported by Zhang *et al.* These ceramics were prepared by the conventional solid-state reaction process [48]. In 2015, we published a study of ceramic-thermoplastic composites based on cyclo-olefin polymer (COP) with sintered ceramic fillers well suited for FDM. In particular, 25 vol. % COP- MgCaTiO<sub>2</sub> have exhibited  $\epsilon_r$  of 4.74 and  $\tan \delta_d$  lower than 0.0018 up to 17 GHz, while 25 vol. % COP-Ba<sub>0.55</sub>Sr<sub>0.45</sub>TiO<sub>3</sub> have exhibited  $\epsilon_r$  of 4.88 and  $\tan \delta_d$  lower than 0.0071 at frequencies up to 10 GHz [17], [49].

## 2.6 Expanding the Materials Options for 3D-Printed Microwave Applications

Currently, the microwave community is exploring engineered composite materials that are compatible with AM 3D-printing technologies, such as FDM, due to the great potential as enabler methodology for the next generation of wireless devices in the Internet of Things (IoT) era. In particular, the work reported by Grant *et al.* [73], by Isakov *et al.* [74], by Castles *et al.* [75], by Arbaoui *et al.* [81] and by Castro *et al.* in this dissertation work [10], [17], [49], [50] are focused on EM composites for microwave applications by using FDM as a chosen 3D-printing technology.

In 2015, Isakov *et al.* reported three types of composite materials with high dielectric permittivity of about seven based on ABS loaded with BaTiO<sub>3</sub> or Ba<sub>0.64</sub>Sr<sub>0.36</sub>TiO<sub>3</sub> micro-fillers [74]. However, these 3D-printed ABS-composites by a FDM process has a relatively low  $T_g$  of about 100°C as listed in Table 5.3 and they exhibit a high dielectric loss tangent greater than 0.034, which is worse than the dielectric losses of even low-performance FR-4 laminates. Due to the high dielectric losses of the bulk BaTiO<sub>3</sub> or Ba<sub>0.64</sub>Sr<sub>0.36</sub>TiO<sub>3</sub> ceramic powders, the composites based on these two types of fillers are anticipated to exhibit high dielectric losses as reported in [40], [49], and [79].

Similarly, Castles *et al.* also reported a composite material with a dielectric permittivity of 8.72 along with a high dielectric loss tangent of 0.0273 [75], which is worse than that of the FR-4

laminates, thus hindering its applications for high gain antennas or high-performance microwave devices. On the other hand, Isakov *et al.* [74] reported another type of composite material based on Polypropylene (PP) loaded with  $\text{CaTiO}_3$  with a  $\epsilon_r$  of 5 and a fairly low dielectric loss tangent  $\tan \delta_d$  of 0.0051. Despite the decent dielectric properties, the loss is still noticeably higher than that of state-of-the-art microwave laminates that typically exhibit dielectric loss tangents lower than 0.003. Also, the  $T_g$  of PP is about  $-14^\circ\text{C}$  and the melting temperature is  $176^\circ\text{C}$  as shown in Table 5.3, which are too low for lots of practical device applications.

## 2.7 Motivation

In the last five years, several RF/microwave devices have been successfully demonstrated by using 3D AM technologies as reported in [2]-[9], which makes AM a promising enabler for the next generation of high-frequency devices and systems. However, there are important challenges to be overcome to adopt the AM technology for microwave device applications. In particular, the lack of functional EM materials, such as high-permittivity and low-loss 3D printable materials, severely hinders the ability for AM to be employed for manufacturing RF/microwave electronics at high frequencies (e.g., Ku, K, and V bands). Also, the lack of high-conductivity printable inks for DPAM is another key challenge that is currently being investigated and addressed by some researchers in the microwave community.

The primary goal of this dissertation is to develop a generic methodology for preparation of EM composites with well-tailored EM properties for fully 3D-printed and high-performance RF/microwave devices fabricated by DDM processes, by using FDM and micro-dispensing for the deposition of ceramic-thermoplastic composites and conductive traces, respectively. It is worthwhile mentioning that some of the EM composites might be compatible with other 3D-printing technologies or planar processes such as high-frequency microwave laminates.

### 2.7.1 Comparison of High-Performance FDM Microwave Composites and Thermoplastics

Figure 2.5 and Figure 2.6 show the measured dielectric permittivity and dielectric loss up to the V-band frequencies (69 GHz) for 3D-printed specimens by using pure COP and 30 vol. % COP-MgCaTiO<sub>2</sub> composites, which are compared with other materials shown in Table 7.1. The EM properties are compared with other FDM materials reported by the scientific community and commercial microwave laminate materials from Rogers Corporation and a material for LDS-MID technology from LPKF Laser and Electronics AG (LPKF).

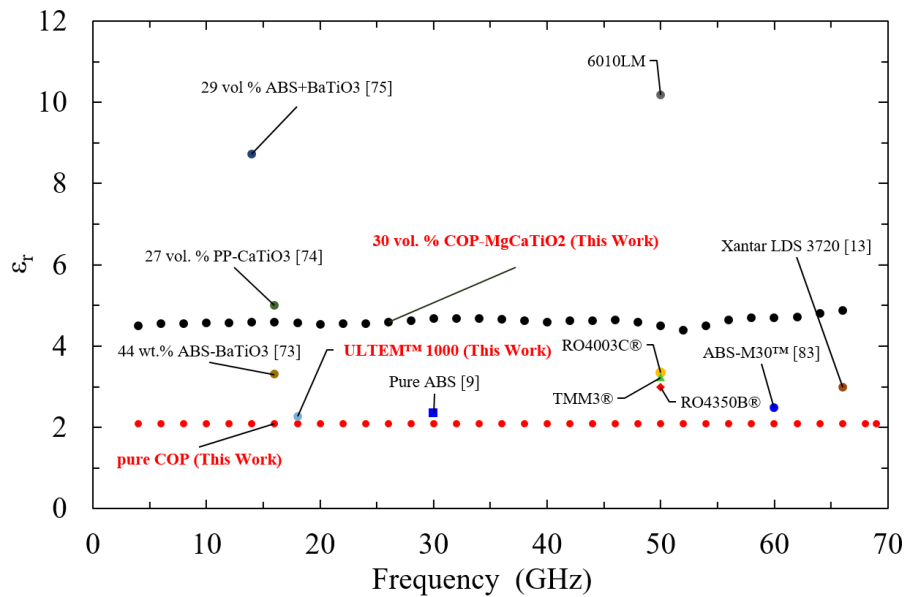


Figure 2.5 – Comparison of measured dielectric permittivity up to 69 GHz of both a pure COP (ZEONEX® RS420) and a 30 vol. % COP-MgCaTiO<sub>2</sub> EM composites, which are compared with commercial microwave laminates from Rogers Corporation [27]. Results from other previously reported works summarized in Table 7.1

As observed in Figure 2.5, despite excellent progress in development of high-*k* materials for FDM-based on ABS and PP as reported previously by Grant *et al.* [73], by Isakov *et al.* [74], by Castles *et al.* [75], the dielectric losses of these composites are still significantly higher as compared to commercial high-end microwave laminates from Rogers Corporation [27]. As a figure of merit, 30 vol. % COP-MgCaTiO<sub>2</sub> EM composites with fillers sintered at 1200°C exhibited an



excellent balance of high-permittivity and low dielectric loss when it is compared with results by prior works [73], [74], and [75]. Moreover, the FDM-ready composites exhibit better dielectric properties than pure ABS-M30™ characterized at 60 GHz reported by Bisognin *et al.* [83], which are almost on par with some high-end microwave laminates, as seen in Figure 2.5 and Figure 2.6 [27].

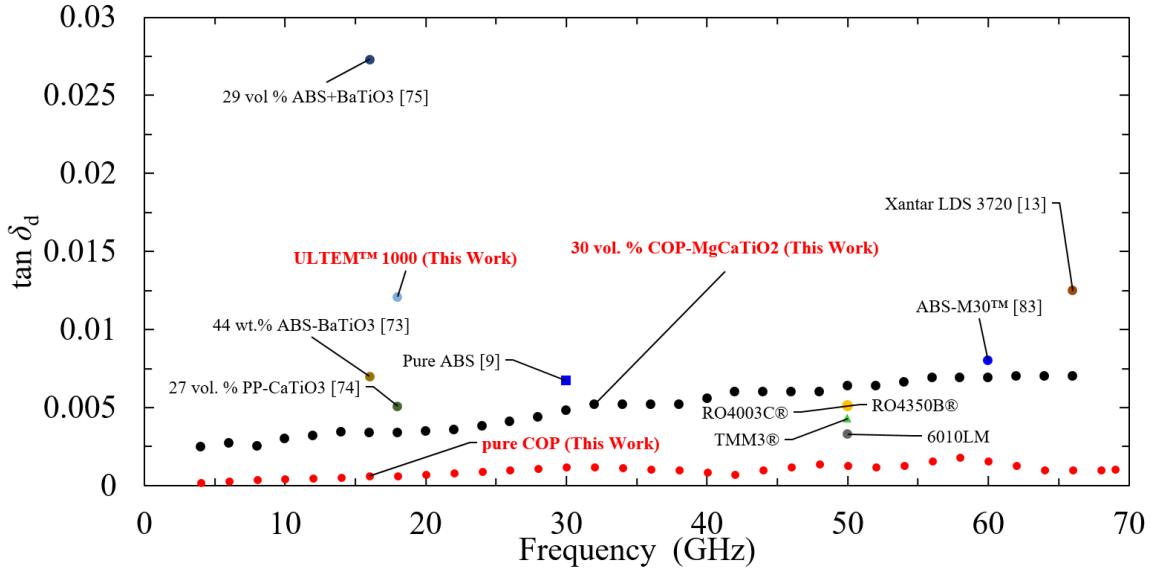


Figure 2.6 – Comparison of measured dielectric loss properties up to 69 GHz of both a pure COP (ZEONEX® RS420) and a 30 vol. % COP-MgCaTiO<sub>2</sub> EM composites with commercial microwave laminates from Rogers Corporation [27]. Results from other materials are shown in Table 7.1.

## CHAPTER 3 :

### ENHANCEMENT OF MICROWAVE PROPERTIES IN COMPOSITE MATERIALS

#### 3.1 Note to Reader

Portions of this chapter, including figures have been submitted to peer-review in the Journal of American Ceramic Society [76].

#### 3.2 Introduction

One of the key goals of this chapter is to evaluate the impact of a high-temperature sintering process as an effective enhancing strategy on the resultant dielectric and loss properties (i.e., relative permittivity  $\epsilon_r$  and dielectric loss tangent  $\tan \delta_d$ ) of EM composite materials composed of Polydimethylsiloxane (PDMS) loaded with sintered MgCaTiO<sub>2</sub> and TiO<sub>2</sub> ceramic fillers. Five types of flexible high-permittivity and low-loss polymer-ceramic EM composite materials based on PDMS elastomer host-matrix reinforced by MgCaTiO<sub>2</sub> and TiO<sub>2</sub> microfillers are rigorously investigated and presented. The ceramic fillers are analyzed with x-ray diffraction (XRD), energy dispersive spectroscopy (EDS) and scanning electron microscope (SEM) for morphology and crystallinity before and after a high-temperature sintering process steps. All the EM composites were loaded with ceramic fillers sintered at temperatures up to 1500°C with concentrations as high as 49% by volume. The TiO<sub>2</sub> and MgCaTiO<sub>2</sub> based composites were characterized up to 17 GHz by the cavity resonator method and at 5 GHz using a custom-built near-field microwave microscopy (NFMM) system. For frequencies up to 17 GHz, the 36 vol. % PDMS-MgCaTiO<sub>2</sub> composites with 1100°C sintered fillers have exhibited a stable  $\epsilon_r$  of 10.27 and  $\tan \delta_d$  lower than 0.021, which correspond to an enhancement of 20% in relative permittivity and 29% in dielectric

loss tangent when compared to the specimen loaded with unsintered raw ceramic powders. Furthermore the 36 vol. % PDMS-MgCaTiO<sub>2</sub> composites with 1500°C sintered fillers have exhibited a stable  $\epsilon_r$  of 9.93 and loss tangent ( $\tan \delta_d$ ) lower than 0.021 for frequencies up to 17 GHz, which correspond to an enhancement of 16.41% in relative permittivity and 28% in dielectric loss tangent. Evidently, there is an optimum sintering temperature for improving the effective dielectric and loss properties of MgCaTiO<sub>2</sub> microfillers. The 49 vol. % PDMS-MgCaTiO<sub>2</sub> composites with 1100°C sintered fillers have exhibited a  $\epsilon_r$  of 16.33 and loss tangent ( $\tan \delta_d$ ) lower than 0.021 at 19 GHz. Similarly, 38 vol. % PDMS-TiO<sub>2</sub> sample with particles sintered at 1100°C has exhibited a dielectric permittivity of  $\epsilon_r$  of 9.73 and slightly a higher loss tangent ( $\tan \delta_d$  lower than 0.031) at frequencies up to 17 GHz, which suggests an enhancement of 9.8% in relative permittivity but a 27% increase of the dielectric loss tangent as compared to those of specimen loaded with unsintered raw TiO<sub>2</sub> powders. This indicates that an optimal sintering condition/temperature exists.

Meanwhile, 38 vol. % PDMS-TiO<sub>2</sub> composites with fillers sintered at 1500°C have shown a stable  $\epsilon_r$  of 8.3 and loss tangent ( $\tan \delta_d$ ) lower than 0.025 at frequencies up to 17 GHz, which suggests a slight decrease of 7% in relative permittivity and a 3% increase of the dielectric loss tangent. The uniform dispersion of sintered ceramic high-*k* microfillers has effectively increased the effective permittivity for all the samples compared to that of pure PDMS host matrix. Meanwhile, the inclusion of the ceramic powders after the sintering process, in particular, has significantly decreased the dielectric losses of the MgCaTiO<sub>2</sub> based composite samples up to 30%. The near-field microwave microscopy (NFMM) analysis revealed that the MgCaTiO<sub>2</sub> ceramic particles are more uniformly distributed than the TiO<sub>2</sub> particles over an area of 50  $\mu\text{m}$   $\times$  50  $\mu\text{m}$ , which might contribute to the superior improvements in the dielectric and loss properties.

### 3.3 Experimental Procedure

In this chapter three sintering temperatures up to the ceramics' melting points reported in Table 3.1 are evaluated to find the best sintering conditions to enhance the effective dielectric and loss properties at microwave frequencies in composite materials based on PDMS. For this purpose, polymer-ceramic composite samples were prepared with MgCaTiO<sub>2</sub> or TiO<sub>2</sub> fillers under “as-is” unsintered condition or sintered at 1100°C and 1500°C for 3 hours. The high-temperature sintering process is a critical step for enhancing the dielectric and loss properties of the ceramic powders. The assessment of dielectric properties was carried out via cavity resonators based on the cavity perturbation theory [57]-[59]. A 0.5 mm-thick molded thin-sheet specimen composed of different volume concentrations of MgCaTiO<sub>2</sub> or TiO<sub>2</sub> ceramic fillers (sintered at 1100°C or 1500°C for three hours) loaded PDMS composites were prepared and characterized. The 36 vol. % PDMS-MgCaTiO<sub>2</sub> composite molded specimen has exhibited a measured  $\epsilon_r$  of 10.27 and loss tangent  $\tan \delta_d$  lower than 0.021 between 0.4 GHz and 17 GHz. Furthermore, a PDMS-MgCaTiO<sub>2</sub> composite sample loaded with 49 vol. % MgCaTiO<sub>2</sub> has exhibited a measured  $\epsilon_r$  of 16.33 and a loss tangent  $\tan \delta_d$  lower than 0.021 between 0.4 GHz and 20 GHz. Similarly 38 vol. % PDMS-TiO<sub>2</sub> sample with particles sintered at 1100°C has exhibited a dielectric permittivity of  $\epsilon_r$  of 9.73 and a loss tangent ( $\tan \delta_d$  lower than 0.031) at frequencies up to 17 GHz. Meanwhile, a 38 vol. % PDMS-TiO<sub>2</sub> composite sample with TiO<sub>2</sub> microfillers sintered at 1500°C has shown  $\epsilon_r$  of 8.3 and  $\tan \delta_d$  lower than 0.025 between 0.4 GHz and 17 GHz. Moreover, the flexibility of the high- $k$  composite substrates seems to be well suited for future RF/microwave device prototypes that conform to uneven or curved surfaces for applications up to the Ku-band and K-band frequencies.

In this study, the best EM characteristics were achieved for composite specimens filled with either MgCaTiO<sub>2</sub> or TiO<sub>2</sub> particles, which were sintered at 1100°C for three hours, indicating

20% and 10% increases of the relative permittivities, respectively, and a 29% reduction of the dielectric losses for MgCaTiO<sub>2</sub> loaded samples. However, a 27% increase in the dielectric losses was observed for the TiO<sub>2</sub> loaded composites (as seen in Table 3.6). In my prior study of PDMS-MgCaTiO<sub>2</sub> using a different batch of MgCaTiO<sub>2</sub> ceramic powders, we have demonstrated a 51% increases of the relative permittivity and 38% decrease in the relative dielectric loss by employing a three hours sintering process at 1100°C in the air [49], [50].

### 3.4 Fabrication Process of Polymer Matrix Composites

#### 3.4.1 Polymer and Ceramic Materials

Sylgard<sup>®</sup> 184 (Dow Corning, Midland, MI), based on polydimethylsiloxane (PDMS) is a two-component silicone elastomer (silicone base resin and cross-linking/curing agent) with measured  $\epsilon_r$  of 2.5 and  $\tan \delta_d$  lower than 0.024 up to 17 GHz [38]. Due to the good dielectric properties, rapid and versatile curing process (e.g., room temperature and heated curing). Furthermore, the high transparency that allows easy inspection of components, which supports the typical applications of Sylgard<sup>®</sup> 184 silicone elastomer for the protection of electrical/electronic devices, such as LED lighting encapsulation, sensors, connectors, adhesive/encapsulant for solar cells, etc.

Table 3.1 – The fundamental properties of ceramic fillers and sintering conditions

Ceramic Powder <sup>†</sup>	Max. Temp. (°C)	Groups	Dielectric Properties @ 6 GHz		Absolute Density (g/cc)	Particle Size (µm) <sup>‡</sup>	Melting Point (°C)
			$\epsilon_r$ <sup>§</sup>	$\tan \delta_d$			
MgCaTiO <sub>2</sub> (MCT-140)	1500/3 hours	II-IV-VI	127	0.00117	3.90	2.26	>1450
TiO <sub>2</sub> (D-100)	1500/3 hours	IV-VI	96	0.00038	3.98	6.90	>1500

<sup>†</sup>Obtained from Trans-Tech, Inc.

<sup>‡</sup> Particle size measured by SEM characterization.

<sup>§</sup> Permittivity for MgCaTiO<sub>2</sub> and TiO<sub>2</sub> tested at 6 GHz reported by Trans-Tech, Inc.

Both MgCaTiO<sub>2</sub> and TiO<sub>2</sub> ceramic powders utilized in this study, which are intentionally agglomerated into 50-100 μm spherical granules for improved powder flow and compaction, are acquired from Trans-Tech, Inc. [53]. The important dielectric properties at 6 GHz and sintering conditions for the aforementioned ceramic particles are summarized in Table 3.1.

### 3.4.2 Preparation of Composite Materials and Specimens

For the high-temperature sintering process, zirconia trays are used together with two sintering furnaces both operating in air. One is an Omegalux LMF-3550 box furnace (Omega Engineering, Stamford, CT) that works up to 1100°C and the other is a KSL 1700X box furnace (MTI Corporation, Richmond, CA) that operates up to 1700°C. The applied sintering conditions are described in Table 3.1. After the sintering process, the densified and crystallized ceramic powders are re-pulverized using a MM 400 high-energy ball mill (Retsch, Haan, Germany) to obtain an average particle size of ~50 μm or smaller as shown in Figure 3.5(d) in order to allow more uniform dispersion of the high-*k* particle fillers in the polymer-ceramic composites.

The preparation of PDMS-ceramic particle composites starts with mixing of the two components of the PDMS silicone elastomer in a 10:1 ratio between the resin and curing agent, using an ARE-310 planetary centrifugal mixer (THINKY, Tokyo, Japan) at 2000 rpm for 2 minutes, followed by a 30 second deaerating step (also known as “degassing”) at 2200 rpm for removing any trapped air bubbles [40]. The second phase is to determine the volume ratio between the sintered ceramic fillers and the host polymer based on the measured tapped powder density reported in Table 3.3 and Table 3.4. The ARE-310 planetary centrifugal mixer is used again to mix the ceramic powders and the host elastomer (PDMS) at the desired volume concentration to ensure a homogenous dispersion. The resultant polymer-ceramic composites are then poured into the custom-designed hot compression molds followed by a degassing step at 22 in-Hg using an

Isotemp 281A vacuum oven (Fisher Scientific, Waltham, MA) to remove the air bubbles. A degassing time of more than two hours is needed for samples with high filler loading ratio beyond 30% in volume, including purging steps every 10 minutes. The sample is then compression molded and cured at 100°C for one hour.

### 3.5 Characterization of Bulk Ceramic Materials

#### 3.5.1 XRD Analysis

The X-ray diffraction (XRD) analysis was performed by using a X'Pert Pro diffractometer (Panalytical, Almelo, Netherlands) to evaluate the phase composition and purity before and after the sintering processes at the different temperatures shown in Table 3.3. These XRD analyses were carried out to study the effects of the various sintering processes on the morphology, composition, and crystal structure of the ceramic microfillers. It was observed that the sintering process slightly modified the chemical composition of the compound powders of MgCaTiO<sub>2</sub> and TiO<sub>2</sub> as shown by the XRD patterns in Figure 3.1 and Figure 3.2, respectively, as well as the semi-quantitative analysis results from the energy dispersive spectroscopy (EDS) in Table 3.2 and Table 3.5, respectively. Figure 3.1 presents the XRD patterns for MgCaTiO<sub>2</sub> before and after a three hours sintering step at 1100°C or 1500°C, while the corresponding lattice parameters are reported in Table 3.3. Similarly, Figure 3.2 shows the XRD patterns for TiO<sub>2</sub> samples before and after a sintering step at 1100°C or 1500°C, while the corresponding lattice parameters are given in Table 3.4. No major differences in the d-spacings [Å] in the corresponding peaks measured with the X-Ray spectra for MgCaTiO<sub>2</sub> and TiO<sub>2</sub> ceramics were observed as shown in Figure 3.1 and Figure 3.2, respectively. However, changes were observed in the peak intensity along the (012) and (213) crystal orientations for MgCaTiO<sub>2</sub> samples. Similarly, variations were observed in the peak intensity along (110), (101) and (211) the crystal orientations for TiO<sub>2</sub> samples.

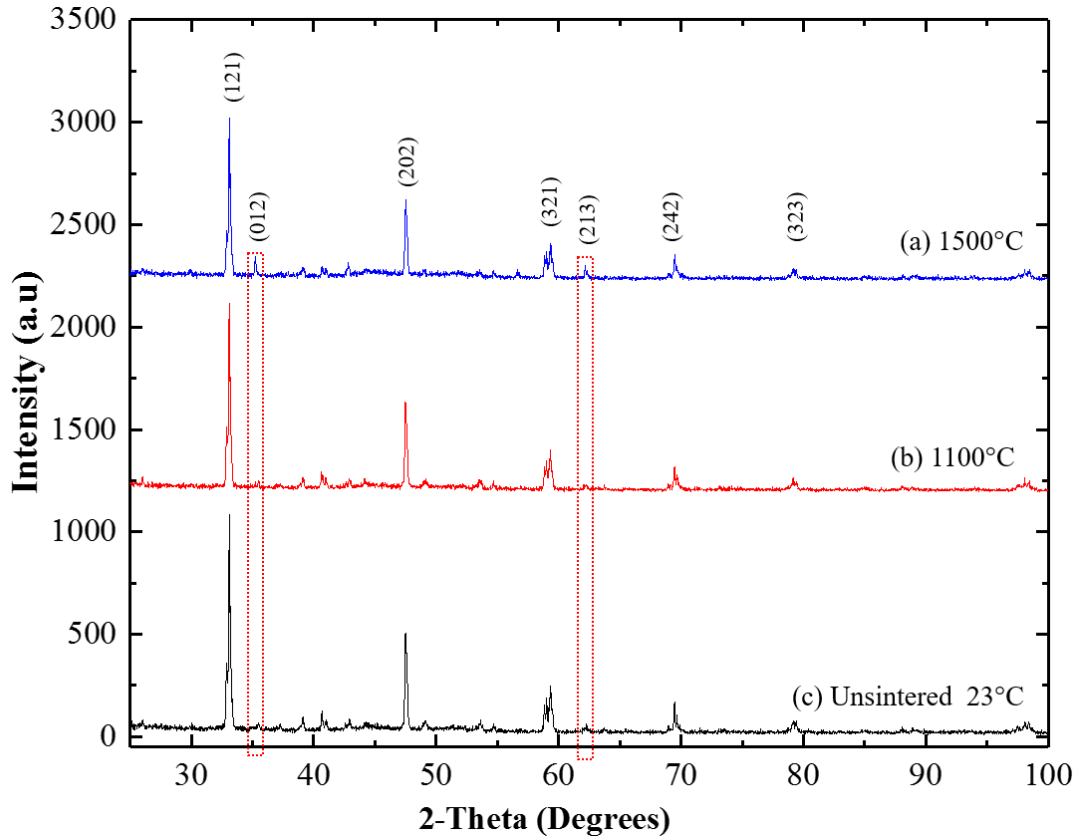


Figure 3.1 – Measured XRD patterns of MgCaTiO<sub>2</sub> ceramic powders after different sintering processes. (a) A sample after a three hours sintering process at 1500°C. (b) A sample after three hours sintering process at 1100°C. (c) Unsintered raw powders.

Table 3.3 and Table 3.4 summarize the average particle agglomerate size, average individual particle size, and lattice parameters for MgCaTiO<sub>2</sub> and TiO<sub>2</sub> ceramic particles, respectively, which were processed under different sintering conditions. As shown, the measured average agglomerate sizes for both samples were noticeably reduced after the 1100°C sintering process as compared to those of unsintered raw powders and the 1500°C sintered samples. This implies that both raw powders were effectively densified at 1100°C. Whereas a sintering process at 1500°C might have caused a major morphology, density, and composition transformation, due to the proximity to the melting point of both ceramics (shown in Table 3.1) that might have induced a crystalline state gas-solid reaction in air. As seen in Table 3.3, no significant differences were



observed in the average cell volumes for MgCaTiO<sub>2</sub> due to the applied sintering conditions. On the contrary, the sintering process at 1500°C have resulted in densification and enlargement of the TiO<sub>2</sub> particle unit cell as shown Table 3.4.

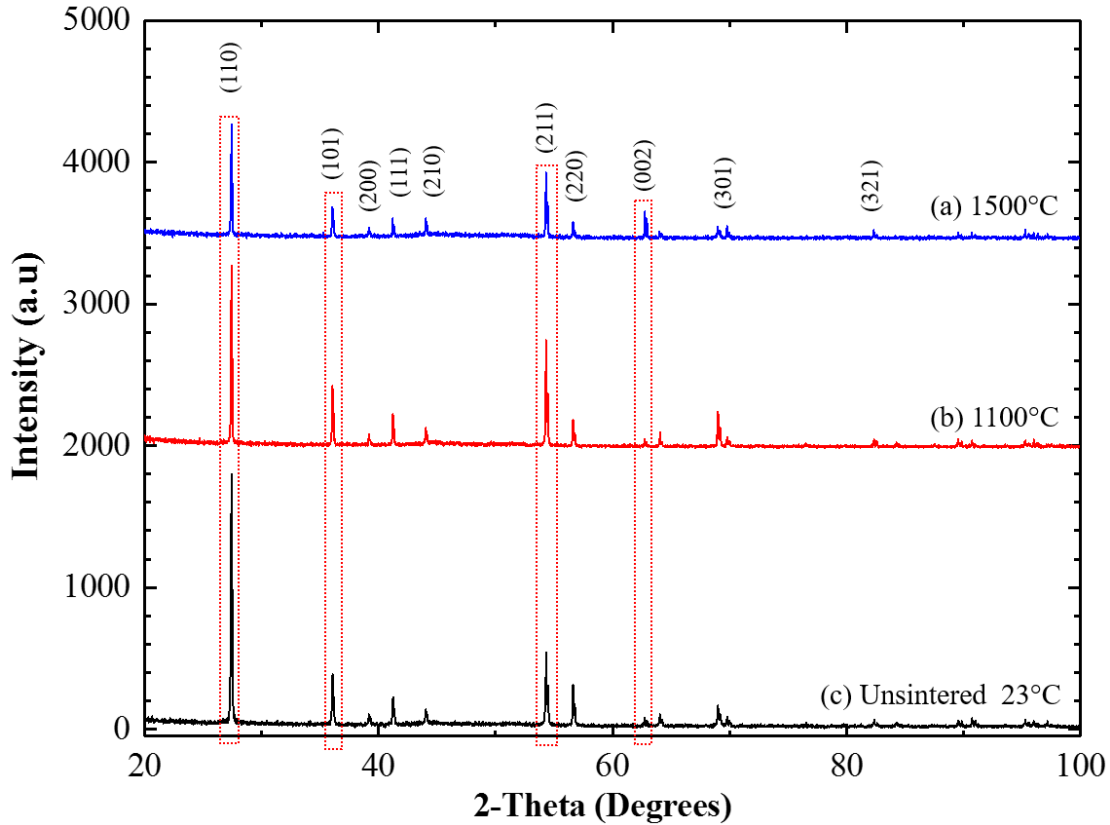


Figure 3.2 – Measured XRD patterns of TiO<sub>2</sub> ceramic powder after different processes. (a) A sample after three hours 1500°C sintering process. (b) A sample after a three hours 1100°C sintering process. (c) Unsintered raw powders.

### 3.5.2 Energy Dispersive Spectroscopy (EDS) Analysis

The elemental analysis was performed by EDS, using an S-800 field emission scanning electron microscope (FE-SEM) (Hitachi Ltd., Tokyo, Japan), which is equipped with an EDS system (EDAX Inc., Mahwah, NJ). The EDS analysis clearly shows how the elements reacted under the different applied sintering temperatures and conditions. Table 3.2 provides semi-quantitative elemental composition analysis for MgCaTiO<sub>2</sub> microfillers, while the corresponding EDS spectrum is shown in Figure 3.3. Moreover, Table 3.5 provides a semi-quantitative elemental

composition analysis for  $\text{TiO}_2$  particles, while the corresponding EDS spectrum is shown in Figure 3.4. Both ceramic materials were processed under various sintering conditions in air. Ti and O are the elements, which have shown more noticeable changes in the wt. % concentrations by the chemical reaction during the high-temperature sintering process.

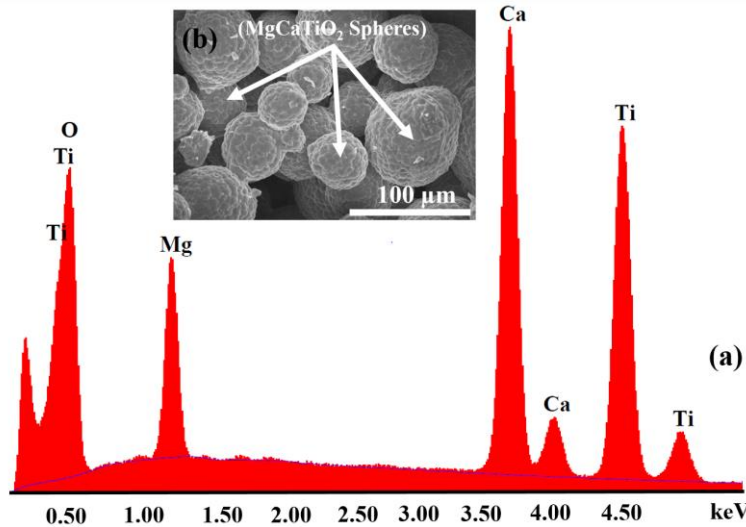


Figure 3.3 – (a) Tested energy dispersive spectroscopy (EDS) spectrum of  $\text{MgCaTiO}_2$  ceramic powders sintered at  $1100^\circ\text{C}$ . (b) SEM photo of  $\text{MgCaTiO}_2$  fillers after a  $1500^\circ\text{C}$  sintering process.

Table 3.2 – Element weight fractions based on EDS of  $\text{MgCaTiO}_2$  at two sintering conditions

Element	Unsintered $23^\circ\text{C}^\dagger$	$1100^\circ\text{C}$	$1500^\circ\text{C}$
O	18.52	20.59	40.64
Mg	4.23	4.27	5.17
Ca	30.19	30.21	27.34
Ti	47.07	44.94	26.86
<b>Total →</b>	100.00	100.00	100.00

<sup>†</sup> Raw samples received from Trans-Tech, Inc. at room temperature under unsintered condition.

Table 3.3 – Average particle sizes and lattice parameters of MgCaTiO<sub>2</sub> measured by SEM and XRD

Sintering Temp (°C)	Tapped Density (g/cc) <sup>§</sup>	Average Agglomerate Size (µm) <sup>†</sup>	Average Particle Size (µm) <sup>‡</sup>	a (Å)	b (Å)	c (Å)	V (Å <sup>3</sup> )	Crystal Structure
1500	2.3241	58.93	3.63	5.3829	7.6453	5.4458	224.12	Orthorhombic
1100	2.1722	35.37	2.97	5.3829	7.6453	5.4458	224.12	
Unsintered	2.1434	57.32	2.26	5.3829	7.6453	5.4458	224.12	

<sup>†</sup> Average agglomerate sphere sizes of MgCaTiO<sub>2</sub> samples were measured using SEM images.

<sup>‡</sup> Average particle size of spherical agglomerates was measured by using SEM images.

<sup>§</sup> Measured tapped density after mass and volume measurement determined a 2-5 min ball milling process.

Table 3.4 – Average particle sizes and lattice parameters of TiO<sub>2</sub> measured by SEM and XRD

Sintering Temp (°C)	Tapped Density (g/cc) <sup>§</sup>	Average Agglomerate Size (µm) <sup>†</sup>	Average Particle Size (µm) <sup>‡</sup>	a (Å)	b (Å)	c (Å)	V (Å <sup>3</sup> )	Crystal Structure
1500	2.1993	49.71	15.5	4.5940	4.5940	2.9590	62.45	Tetragonal
1100	2.0973	43.56	6.67	4.5933	4.5933	2.9580	62.41	
Unsintered	1.8871	49.35	6.77	4.5933	4.5933	2.9580	62.41	

<sup>†</sup> Average agglomerate sphere sizes of TiO<sub>2</sub> samples were measured using SEM images.

<sup>‡</sup> Average particle size among spherical agglomerates was measured using SEM images.

<sup>§</sup> Measured tapped density after a 2-5 min ball milling process was determined by mass and volume measurement.

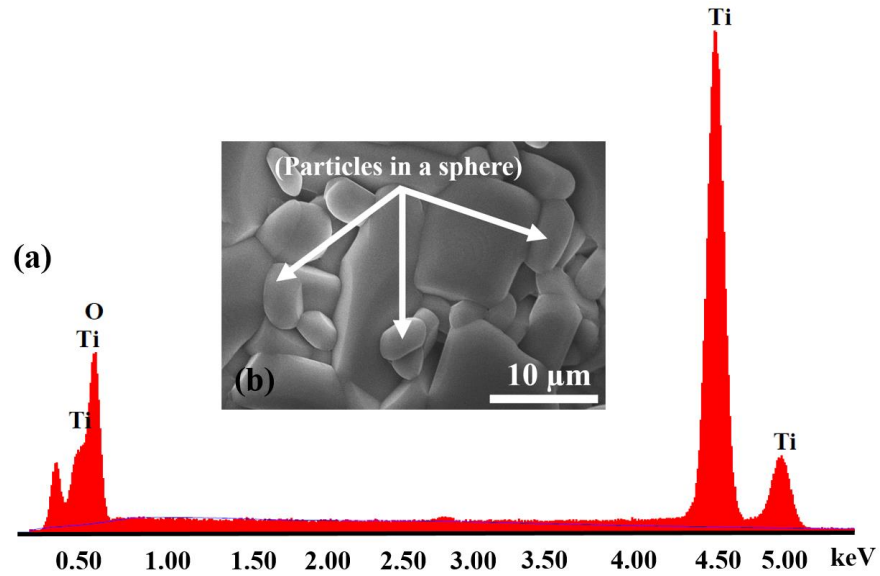


Figure 3.4 – (a) Tested energy dispersive spectroscopy (EDS) spectrum of  $\text{TiO}_2$  ceramic powders sintered at  $1100^\circ\text{C}$ . (b) SEM photo of  $\text{MgCaTiO}_2$  fillers after an  $1100^\circ\text{C}$  sintering process.

Table 3.5 – Element weight fractions based on EDS of  $\text{TiO}_2$  at different sintering conditions

Element	Unsintered	$23^\circ\text{C}^\dagger$	$1100^\circ\text{C}$	$1500^\circ\text{C}$
O	18.41	15.83	48.78	
Ti	81.59	84.17	51.22	
<b>Total</b> →	100.00	100.00	100.00	

<sup>†</sup> Raw samples received from Trans-Tech, Inc. at room temperature under unsintered condition.

### 3.6 Characterization of Polymer-Ceramic Composites

#### 3.6.1 SEM Analysis

The SEM analysis was performed using a SU-70 scanning electron microscope (Hitachi, Ltd, Tokyo, Japan). Figure 3.5(a) and Figure 3.5(b) present the SEM images of  $\text{MgCaTiO}_2$  particles after an  $1100^\circ\text{C}$  sintering process, while Figure 3.5(c) and Figure 3.5(d) show the SEM pictures of the PDMS- $\text{MgCaTiO}_2$  polymer composites with the sintered and re-pulverized ceramic fillers. Figure 3(d) has shown an excellent particle size distribution of about  $5\ \mu\text{m}$ . The composites show excellent particle-to-polymer and particle-to-particle interfaces without noticeable agglomeration of particles.

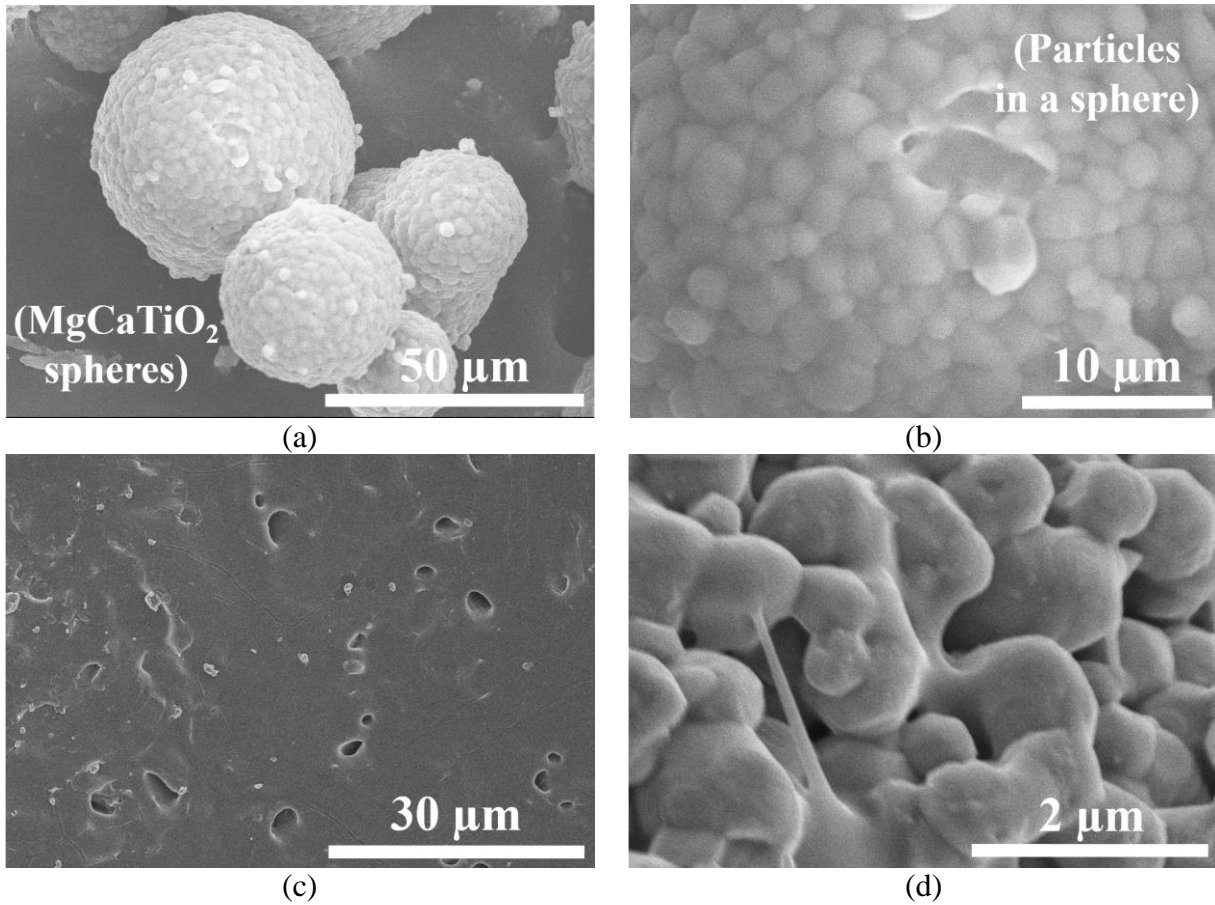


Figure 3.5 – SEM analysis of  $\text{MgCaTiO}_2$  samples sintered at  $1100^\circ\text{C}$ , showing (a) a zoom-out view photo of  $\text{MgCaTiO}_2$  agglomerates. (b) A zoom-in view photo of agglomerated  $\text{MgCaTiO}_2$  particles. (c) A surface-view photo of 36 vol. % PDMS- $\text{MgCaTiO}_2$  composites. (d) A cross-sectional view photo of 36 vol. % PDMS- $\text{MgCaTiO}_2$  composites.

Figure 3.6(a) and (b) present the SEM images of  $\text{TiO}_2$  particles after an  $1100^\circ\text{C}$  sintering process, while Figure 3.6(c) and Figure 3.6(d) show the SEM pictures of the PDMS- $\text{TiO}_2$  polymer composites with the sintered and re-pulverized ceramic fillers. Figure 3.6(d) depicts the  $\text{TiO}_2$  agglomerate sphere embedded in the silicone elastomer polymer matrix. The SEM images also indicate great particle-to-polymer and particle-to-particle interfaces without noticeable agglomeration of particles.

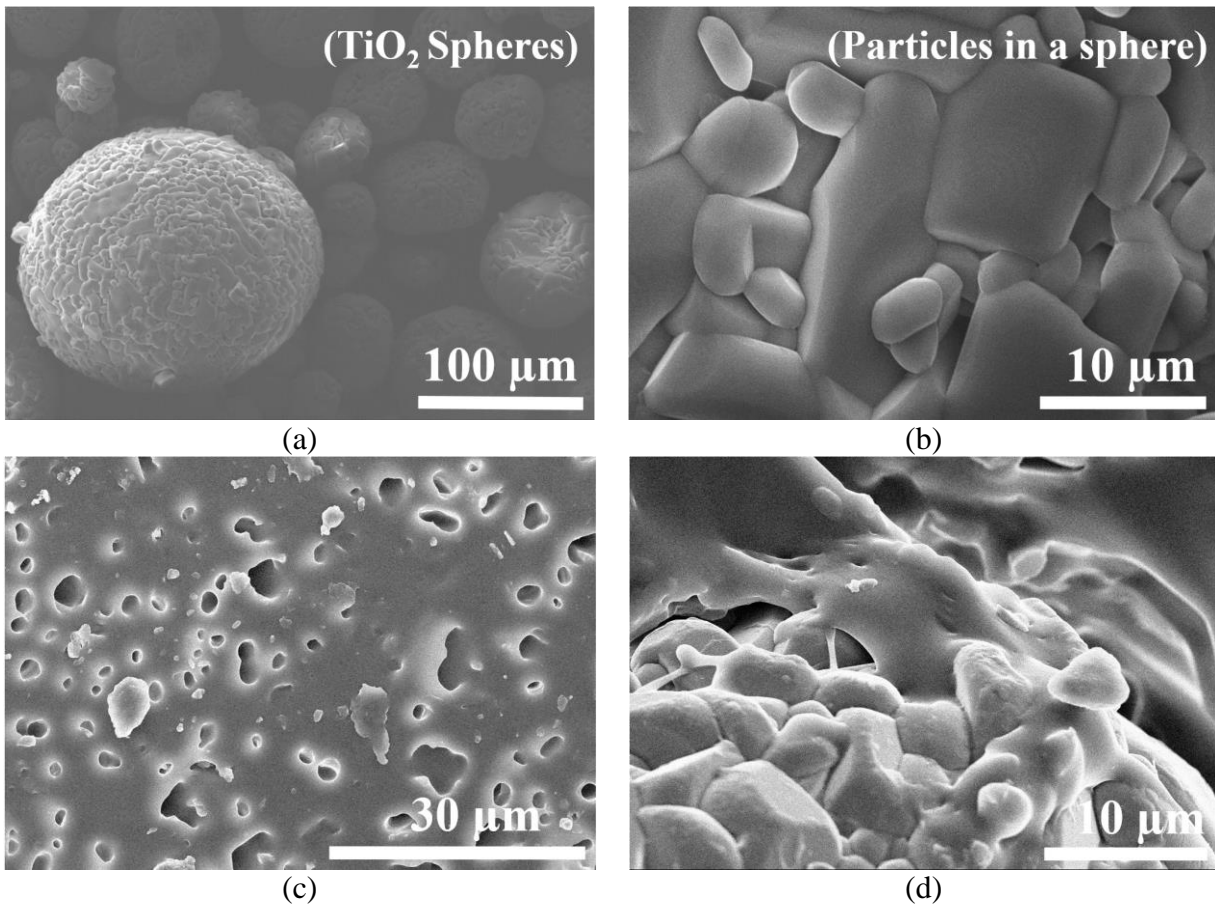


Figure 3.6 – SEM analysis of TiO<sub>2</sub> samples sintered at 1100°C, showing (a) a zoom-out view photo of TiO<sub>2</sub> agglomerates. (b) A zoom-in view photo of agglomerated TiO<sub>2</sub> particles. (c) A surface-view photo of 38 vol. % PDMS-TiO<sub>2</sub> composites. (d) A cross-sectional view photo of 38 vol. % PDMS-TiO<sub>2</sub> composites.

### 3.6.2 Near-Field Microwave Microscopy (NFMM) Analysis

Localized characterization of insulating single crystals [51], thin films [52] and ceramics [53] has been performed through near-field microwave microscopy (NFMM). NFMM is a non-destructive tool that measures the EM properties of a sample with a spatial resolution that is determined by the microscope probe tip size. In a resonant NFMM, the sample under test is positioned near the microscope probe tip, affecting the resonance frequency ( $F_r$ ) and quality factor ( $Q$ ) of the microwave probe. These changes in  $F_r$  and  $Q$  can be correlated with the electromagnetic properties of the sample using calibration [54] and theoretical methods [55]. In 2004, Zhang *et al.*



presented  $F_r$  images of  $\text{LaAlO}_3$  and  $\text{TiO}_2$  single crystals and yttria-stabilized zirconia (YSZ) polycrystalline ceramic. These images demonstrated the influence of microstructural features, such as strain and grain boundaries, on the local dielectric behavior of the samples [51]. In 2006, Wing *et al.* observed different phases of the polished  $\text{CaTiO}_3$ - $\text{MgTiO}_3$ - $\text{Mg}_2\text{TiO}_4$  system from the measured  $F_r$  images [53]. In this work, NFMM is used to study the localized distribution of ceramic particles (sintered at  $1100^\circ\text{C}$ ) for 38 vol. % PDMS- $\text{TiO}_2$  and 36 vol. % PDMS- $\text{MgCaTiO}_2$  thin-sheet specimens. Localized and non-destructive characterization of the ceramic composites through NFMM is of interest not only for the understanding the spatial distribution and improvement of sintering conditions but also for the study of the use of these materials in microwave and millimeter wave applications.

The schematic diagram of the 5.0 GHz coaxial transmission line resonator-based NFMM employed in this work was previously reported [56]. To operate the NFMM in non-contact mode and to map  $F_r$ ,  $Q$ , and surface topography simultaneously, the NFMM employs a quartz tuning fork-based distance following feedback system. NFMM measurements were performed at a tip-sample distance of 100 nm. The tungsten probe tip used has a radius of 10  $\mu\text{m}$ .

Figure 3.7(a), Figure 3.7(d), Figure 3.7(b), and Figure 3.7(e) show the measured topography and  $F_r$  of 36 vol. % PDMS- $\text{MgCaTiO}_2$  and 38 vol. % PDMS- $\text{TiO}_2$ , respectively. From these images, it can be observed that there is no evident correlation between topography and  $F_r$ , which indicates that the measured changes in  $F_r$  result from changes in the material properties (permittivity) rather than topography artifacts. The correlation coefficients between surface topography and  $F_r$  images are computed to be  $\rho=0.11$  and  $\rho=0.27$  for 36 vol. % PDMS- $\text{MgCaTiO}_2$  and 38 vol. % PDMS- $\text{TiO}_2$ , respectively.

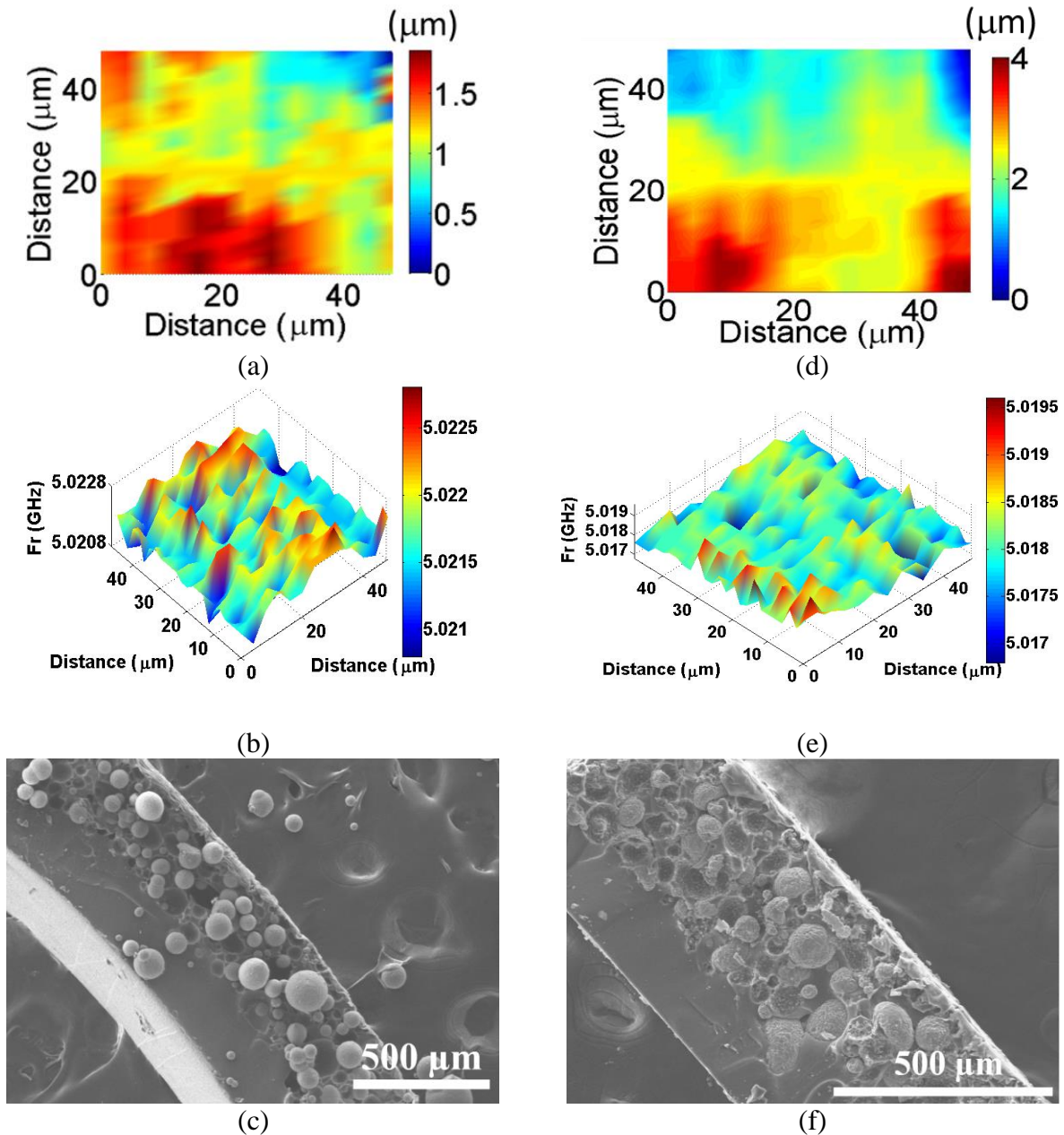


Figure 3.7 – 36 vol. % PDMS-MgCaTiO<sub>2</sub> composites with fillers sintered at 1100°C: (a) NFMM surface topography. (b) NFMM  $F_r$ . (c) Cross-sectional SEM image. Similarly, 38 vol. % PDMS-TiO<sub>2</sub> composites with fillers sintered at 1100°C: (d) NFMM surface topography. (e) NFMM  $F_r$ . (f) Cross-sectional SEM image.

These results confirm that the correlation is negligible. Additionally, from Figure 3.7(b) and Figure 3.7(e), it can be observed that  $F_r$  is not constant over the 50  $\mu\text{m} \times 50 \mu\text{m}$  area but varies by about 1.5 MHz (36 vol. % PDMS-MgCaTiO<sub>2</sub>) and 2 MHz (38 vol. % PDMS-TiO<sub>2</sub>), which



could be due to non-uniform ceramic particle distribution. This is confirmed by the cross-sectional SEM images of the samples presented in Figure 3.7(c) and Figure 3.7(f). The standard deviation of the  $Fr$  was computed to be 401 KHz and 366 KHz for 36 vol. % PDMS-MgCaTiO<sub>2</sub> and 38 vol. % PDMS-TiO<sub>2</sub> specimens, respectively, indicating that the ceramic particles are more uniformly distributed in 36 vol. % PDMS-MgCaTiO<sub>2</sub> than in 38 vol. % PDSM-TiO<sub>2</sub> thin-sheet samples for these particularly studied regions.

### 3.6.3 Extraction of the Microwave Dielectric Properties

#### 3.6.3.1 Cavity Perturbation Technique

The determination of the dielectric constant of an unknown material by using cavity resonators measuring the shift in resonant frequency and  $Q$  factor caused by the dielectric sample perturbing the cavity has been demonstrated previously by Che *et al.* [58] and Pozar [59]. This methodology is typically used to extract the dielectric properties (permittivity and dielectric loss) in microwave materials in a range of frequencies. The effect of the perturbations on the cavity performance is typically calculated by using approximations. The technique is known as the *perturbational method* [59], which assumes that the actual fields of a cavity with an inserted thin-sheet material are not significantly different.

Pozar derived the relationships considering a cavity of volume  $V_0$  perturbed by a change in permittivity ( $\Delta\epsilon$ ), or change in permeability ( $\Delta\mu$ ) due to partial filling of the cavity by the material under test [59].  $\bar{E}_0, \bar{H}_0$  are the fields of the original cavity, and  $\bar{E}, \bar{H}$  are the fields of the perturbed cavity, then Maxwell's curls equations are rewritten as follows:

$$\nabla \times \bar{E}_0 = -j\omega_0\mu\bar{H}_0, \quad (3.1)$$

$$\nabla \times \bar{H}_0 = j\omega_0\epsilon\bar{E}_0, \quad (3.2)$$

$$\nabla \times \bar{E} = -j\omega(\mu + \Delta\mu)\bar{H}, \quad (3.3)$$

$$\nabla \times \bar{H} = j\omega(\varepsilon + \Delta\varepsilon)\bar{E}, \quad (3.4)$$

where  $\bar{H}$  is the magnetic field in (A/m), and  $\bar{E}$  is the electric field in (V/m),  $\omega_0$  is the resonant frequency of the original cavity, and  $\omega$  is the resonant frequency of the perturbed cavity. By multiplying (3.1) by  $\bar{H}$ , and multiplying (3.4) by  $\bar{E}_0^*$ , the following expressions can be derived:

$$\bar{H} \cdot \nabla \times \bar{E}_0^* = j\omega_0\mu\bar{H} \cdot \bar{H}_0^*, \quad (3.5)$$

$$\bar{E}_0^* \cdot \nabla \times \bar{H} = j\omega(\varepsilon + \Delta\varepsilon)\bar{E}_0^* \cdot \bar{E}, \quad (3.6)$$

Subtracting (3.5) from (3.6) and using the vector identity, Equation (3.7) can be derived:

$$\nabla \cdot (\bar{A} \times \bar{B}) = \bar{B} \cdot \nabla \times \bar{A} - \bar{A} \cdot \nabla \times \bar{B} \quad (3.7)$$

Resulting in Equation (3.8):

$$\nabla \cdot (\bar{E}_0^* \times \bar{H}) = j\omega_0\mu\bar{H} \cdot \bar{H}_0^* - j\omega(\varepsilon + \Delta\varepsilon)\bar{E}_0^* \cdot \bar{E} \quad (3.8)$$

Now multiplying (3.2) by  $\bar{E}$  and multiplying (3.3) by  $\bar{H}_0^*$ , the following equations are given:

$$\bar{E} \cdot \nabla \times \bar{H}_0^* = -j\omega_0\varepsilon\bar{E}_0^* \cdot \bar{E}, \quad (3.9)$$

$$\bar{H}_0^* \cdot \nabla \times \bar{E} = -j\omega(\mu + \Delta\mu)\bar{H}_0^* \cdot \bar{H}, \quad (3.10)$$

Subtracting (3.9) from (3.10) and using the vector, identity Equation (3.7), Equation (3.11) can be obtained:

$$\nabla \cdot (\bar{E} \times \bar{H}_0^*) = -j\omega(\mu + \Delta\mu)\bar{H}_0^* \cdot \bar{H} + j\omega_0\varepsilon\bar{E}_0^* \cdot \bar{E}, \quad (3.11)$$

Adding (3.8) and (3.11), and integrating over the volume  $V_0$  and using the divergence theorem, the left part is volume integral, and the right part is surface integral, as shown by Equation (3.12):

$$\begin{aligned} \int_{V_0} \nabla \cdot (\bar{E}_0^* \times \bar{H} + \bar{E} \times \bar{H}_0^*) dv &= \oint_{S_0} (\bar{E}_0^* \times \bar{H} + \bar{E} \times \bar{H}_0^*) \cdot ds = 0 \\ &= j \int_{V_0} \{[\omega_0\varepsilon - \omega(\varepsilon + \Delta\varepsilon)]\bar{E}_0^* \cdot \bar{E} + [\omega_0\mu - \omega(\mu + \Delta\mu)]\bar{H}_0^* \cdot \bar{H}\} dv, \end{aligned} \quad (3.12)$$

Since the  $\hat{n} \times \bar{E} = 0$  on  $S_0$ , hence the surface integral is zero, then equation can be rewritten as Equation (3.13):

$$\frac{\omega - \omega_0}{\omega} = \frac{-\int_{V_0} (\Delta\varepsilon \bar{E} \cdot \bar{E}_0^* + \Delta\mu \bar{H} \cdot \bar{H}_0^*) dv}{\int_{V_0} (\varepsilon \bar{E} \cdot \bar{E}_0^* + \mu \bar{H} \cdot \bar{H}_0^*) dv} \quad (3.13)$$

Equation (3.13) is an exact equation for the change in resonant frequency due to material perturbation, however, it is not usable since typically the exact fields  $\bar{E}$  and  $\bar{H}$  in the perturbed cavity are unknown. And by assuming that  $\Delta\varepsilon$  and  $\Delta\mu$  are small enough that the perturbed fields  $\bar{E}$ , and  $\bar{H}$  are approximately the same with original fields  $\bar{E}_0$  and  $\bar{H}_0$ , while substituting  $\omega$  in the denominator by  $\omega_0$ , the fractional change in resonant frequency is given by Equation (3.14):

$$\frac{\omega - \omega_0}{\omega_0} \approx \frac{-\int_{V_0} (\Delta\varepsilon |\bar{E}_0|^2 + \Delta\mu |\bar{H}_0|^2) dv}{\int_{V_0} (\varepsilon |\bar{E}_0|^2 + \mu |\bar{H}_0|^2) dv} \quad (3.14)$$

The complex permittivity of a material can be expressed as Equation (3.15):

$$\varepsilon_r = \varepsilon_r' + j\varepsilon_r'' \quad (3.15)$$

where  $\varepsilon_r'$  and  $\varepsilon_r''$  are the real and imaginary parts of the complex permittivity, the real part is the relative dielectric permittivity, and the imaginary part is the dielectric loss factor [26].

Then the equations to calculate the complex permittivity are given by (3.16) and (3.17) as reported by Che *et al.* [58].

$$\varepsilon_r' - 1 = \left( \frac{f_0 - f_s}{f_s} \right) \left( \frac{V_0}{2V_s} \right) \quad (3.16)$$

$$\varepsilon_r'' = \left( \frac{1}{Q_s} - \frac{1}{Q_0} \right) \left( \frac{V_0}{4V_s} \right) \quad (3.17)$$

where  $f_s$  and  $f_0$  are the resonant frequencies with and without a specimen in the cavity;  $Q_s$  and  $Q_0$  are the quality factors ( $Q$ ) of the cavity with and without the inserted thin-sheet sample; and  $V_s$  and  $V_0$  are the volumes of sample and cavity, respectively [58].

Once the complex permittivity of the material under test is calculated, we can then determine the effective conductivity  $\sigma_e$  and dielectric loss tangent  $\tan \delta_d$  as shown below:

$$\sigma_e = \omega \varepsilon'' = 2\pi f \varepsilon_0 \varepsilon_r'' \quad (3.18)$$

$$\tan \delta_d = \frac{\varepsilon_r''}{\varepsilon_r'} \quad (3.19)$$

The microwave dielectric characteristics of several types of multilayer dielectric resonators fabricated by employing MgTiO<sub>3</sub>-CaTiO<sub>3</sub> powders synthesized by a solid-state reaction process characterized using a finite-element analysis with transverse electric (TE<sub>013</sub>) resonant mode has been reported previously by Li *et al.* [31]. These resonators were built by stacking different types of ceramic powders. However, the dielectric properties of these layered resonators were characterized only at 6.9 GHz, which also renders uncertainties for any applications at higher GHz frequencies beyond the C-band [31].

In this work, the microwave dielectric properties of PDMS-ceramic composite substrates at microwave frequencies were characterized by using Equations (3.16)-(3.19) and using an 8720ES 20 GHz network analyzer (Keysight Technologies, Santa Rosa, CA) and two different commercial thin dielectric sheet cavity resonators 125HC and 015 fixtures (Damaskos, Inc., Concordville, PA). The model 125HC test fixture that works in the transverse electromagnetic (TEM) mode is designed for the low-frequency band of 0.4 to 4.4 GHz, while the model 015 test fixture that works in the transverse electric (TE) mode covers the high-frequency band of 6.2 to 19.4 GHz, which corresponds to K-band frequencies.

### 3.7 Theoretical Models for Effective Dielectric Permittivity of Polymer-Matrix Composites

In this section, different models reported in [26], [60]-[69] are applied to the PMCs to predict the relative dielectric permittivity and to evaluate their accuracy by comparing the model predictions with measured data. These models are based on mixing rules to estimate the effective

permittivity of PMCs made of two phases. In the following models, the  $\epsilon_{eff}$  is the permittivity of the mixture (composite),  $\epsilon_1$  is the permittivity of the matrix material 1 (polymer or thermoplastic matrix),  $\epsilon_2$  is the permittivity of the filler particles (ceramic fillers),  $\varphi_1$  is the volume fraction of the polymer matrix, and  $\varphi_2$  is the volume fraction of the filler particles. Most of these models consider an isotropic matrix filled with spheroids as shown in Figure 3.8(c) [26], except for the volume-fraction average model that considers a parallel arrangement of the phases in the PMC as shown in Figure 3.8(b) [64], [69].

### 3.7.1 Raleigh Model

In 2003 and 2016, Raju reported several models to predict the permittivity of composite materials [63]. One of the most common analyses of the dielectric permittivity of two-component mixtures is based on the Raleigh model, which assume cylindrical particles mixed in a medium with effective permittivity given by Equation (3.20):

$$\frac{\epsilon_{eff} - \epsilon_1}{\epsilon_{eff} + \epsilon_1} = \frac{\varphi_2(\epsilon_2 - \epsilon_1)}{\epsilon_2 + \epsilon_1} \quad (3.20)$$

### 3.7.2 Hanai-Bruggeman Model

A widely-used model for the relative permittivity of EM composites is the Bruggeman model [60], which was also derived by Hanai [61]. Hence it is referred as the Hanai-Bruggeman model [62]. Some advantages of this model are that it considers constituent particles may be very close to each other or agglomerate, which is given by Equation (3.21):

$$\frac{\epsilon_2 - \epsilon_{eff}}{\epsilon_2 - \epsilon_1} \left( \frac{\epsilon_1}{\epsilon_{eff}} \right)^{\frac{1}{3}} = 1 - \varphi_2 \quad (3.21)$$

Hanai-Bruggeman model is expected to predict accurately for volume fractions of particles  $\varphi_2$  up to about 50%, with the assumption that the distributed particles in the PMC do not form a percolative path throughout the medium [26].

### 3.7.3 Volume-fraction Average Model

In 2009, Barber *et al.* reported this theoretical model that have been developed to predict the effective dielectric permittivity of polymer composites based on the volume loading fraction of the high- $k$  ceramic fillers [64]. The volume-fraction model (also known as parallel mixing model) is a relatively straightforward but inaccurate model [63], [69] that tends to overestimate effective relative permittivity of polymer composites that is given by Equation (3.22):

$$\varepsilon_{eff} = \varphi_1 \varepsilon_1 + \varphi_2 \varepsilon_2 \quad (3.22)$$

Several prior studies involving experimental data [65]-[66] and theory [67]-[68] disapproved the trend predicted by this simple volume-fraction model as shown in Equation (3.22).

### 3.7.4 Maxwell Model

Barber *et al.* also reported the Maxwell model based on mean-field theory [64]. This model also reported by Yoon *et al.* [69] presents a more realistic way to estimate the effective permittivity in polymer composites systems, and the model is given by Equation (3.23):

$$\varepsilon_{eff} = \varepsilon_1 \frac{\varepsilon_2 + 2\varepsilon_1 - 2(1-\varphi_1)(\varepsilon_1 - \varepsilon_2)}{\varepsilon_2 + 2\varepsilon_1 + (1-\varphi_1)(\varepsilon_1 - \varepsilon_2)} \quad (3.23)$$

The Maxwell model of Equation (3.23) is based on a mean field approximation of a single spherical inclusion surrounded by a continuous matrix of the polymer [69].

### 3.7.5 Maxwell-Garnett Model

In 2012 Dang *et al.* reported several models for the prediction of effective permittivity in PMCs, including the Maxwell-Garnett model [26]. For two-phase composites the lower effective permittivity is calculated by the series model shown in Figure 3.8(a), which is given by Equation (3.24):

$$\varepsilon_{eff,min} = \frac{\varepsilon_1 \varepsilon_2}{\varepsilon_1 \varphi_2 + \varepsilon_2 \varphi_1} \quad (3.24)$$

while the upper effective dielectric permittivity is calculated by the parallel model shown in Figure 3.8(b) which is given by Equation (3.25):

$$\epsilon_{eff,max} = \varphi_1\epsilon_1 + \varphi_2\epsilon_2 \quad (3.25)$$

The effective dielectric permittivity  $\epsilon_{eff}$  of a PMC system must fall within these two limits  $\epsilon_{eff,min}$  by Equation (3.24) and  $\epsilon_{eff,max}$  by Equation (3.25), which is known as Wagner theoretical limits or Wagner theoretical schemes given by Equation (3.26) [26], [28].

$$\epsilon_{eff,min} \leq \epsilon_{eff} \leq \epsilon_{eff,max} \quad (3.26)$$

It can be described by mixing models with series and parallel configurations, similar to practical composites with a homogenous dispersion of spheroid particles, as shown in Figure 3.8(c).

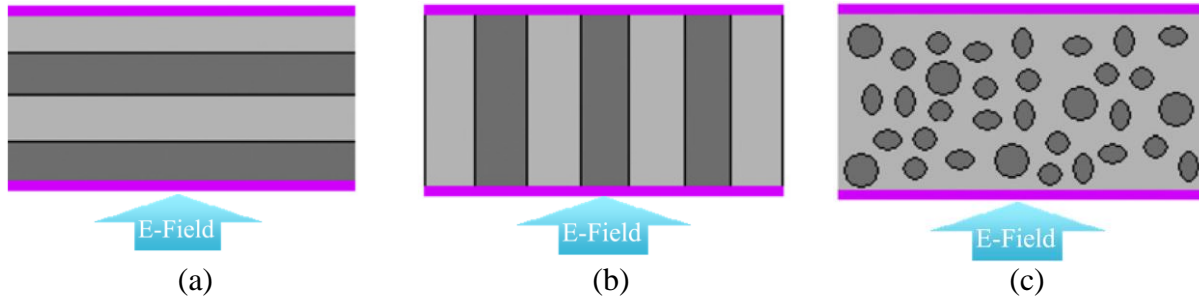


Figure 3.8 – Ideal arrangements of two-phase PMCs. (a) Series model. (b) Parallel model. (c) Mixing model. Particles in a matrix, purple lines denotes the electrodes and the corresponding electric field. Images courtesy of Dang *et al.* [26] © ELSEVIER 2012. See permission in Appendix A.

Other models have been developed to predict the effective dielectric permittivity based on the previous Equations (3.24) - Equation (3.26), such as the Sillars or Landzu-Lifshitz model which is given by Equation (3.27) [26]:

$$\epsilon_{eff} = \epsilon_1 \left[ 1 + \frac{3\varphi_2(\epsilon_2 - \epsilon_1)}{2\epsilon_1 + \epsilon_2} \right] \quad (3.27)$$

However Landzu-Lifshitz model is accurate only for low volume fractions of filler, limited by the values of conductivity of the fillers and polymer matrix, typically fillers must have a higher

electrical resistivity than that of the polymer matrix for the model to be accurate. Therefore a more precise model known as the Maxwell-Garnet model is developed that is given by Equation (3.28) [26]:

$$\varepsilon_{eff} = \varepsilon_1 \left[ 1 + \frac{3\varphi_2(\varepsilon_2 - \varepsilon_1)}{(1 - \varphi_2)(\varepsilon_2 - \varepsilon_1) + 3\varepsilon_1} \right] \quad (3.28)$$

Maxwell-Garnet model given by Equation (3.28) considers spherical fillers dispersed in a medium and this model does not consider the resistivity of the filler or matrix, which is an advantage when compared with Landzu-Lifshitz model. In some references, Maxwell-Garnet model is expressed in other forms, and it is referred with other names (e.g., Maxwell-Wagner, Rayleigh, Lorentz-Lorenz or Kernner-Böttcher) [26]. For instance, another expression for the Maxwell-Garnet model is given by Equation (3.29):

$$\frac{\varepsilon_{eff} - \varepsilon_1}{\varepsilon_{eff} + 2\varepsilon_1} = \varphi_2 \left[ \frac{(\varepsilon_2 - \varepsilon_1)}{\varepsilon_2 + 2\varepsilon_1} \right] \quad (3.29)$$

However Maxwell-Garnet model Equation (3.29) is applicable only to spherical particles [26].

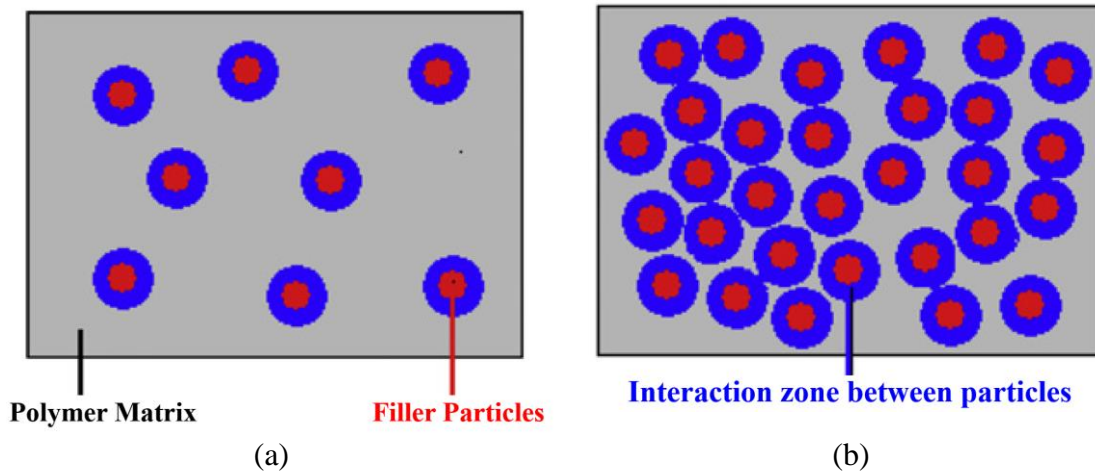


Figure 3.9 – Distribution of particles in a PMC. (a) A low concentration of fillers. (b) High-concentration of fillers. Images courtesy of Dang *et al.* [26] © ELSEVIER 2012. See permission in Appendix A.



Maxwell-Garnet model is only valid for low filler concentrations as shown in Figure 3.9(a). Since the interaction between filler particles is relatively weak, it is typically neglected by this model.

### 3.7.6 Jaysundere-Smith Model

At higher concentration of particles, the interaction of them is more significant due to the closer distance between them as depicted in Figure 3.9(b) for PMCs with a higher concentration of fillers, in particular, nanosized filler particles. By taking into account, the interaction between filler particles, Jaysundere-Smith model calculated the electric field with a dielectric sphere embedded in a continuous dielectric medium while considering the polarization of contiguous particles, which is given by Equation (3.30) [26]:

$$\epsilon_{eff} = \frac{\epsilon_1 \varphi_1 + \epsilon_2 \varphi_2 \frac{3\epsilon_1}{(2\epsilon_1 + \epsilon_2)} \left[ 1 + 3\varphi_2 \frac{(\epsilon_2 - \epsilon_1)}{2\epsilon_1 + \epsilon_2} \right]}{\varphi_1 + \varphi_2 \frac{3\epsilon_1}{(2\epsilon_1 + \epsilon_2)} \left[ 1 + 3\varphi_2 \frac{(\epsilon_2 - \epsilon_1)}{2\epsilon_1 + \epsilon_2} \right]} \quad (3.30)$$

### 3.8 Measured Dielectric Properties of Polymer-Matrix Composites

The properties of polydimethylsiloxane (PDMS) silicone elastomer were measured, revealing  $\epsilon_r$  of 2.5 and  $\tan \delta_d$  lower than 0.024 at 17 GHz [40]. At the same time, the dielectric properties of MgCaTiO<sub>2</sub> and TiO<sub>2</sub> ceramic powders were characterized at 6 GHz with reported  $\epsilon_r$  of 127.26 and  $\tan \delta_d$  lower than 0.0017 for MgCaTiO<sub>2</sub> along with  $\epsilon_r$  of 95.76 and  $\tan \delta_d$  lower than 0.00038 for TiO<sub>2</sub> raw samples, respectively. Figure 3.10 depicts the comparison between the measured dielectric permittivity compared with the predicted results based on three models (i.e., Equations (3.20), (3.21) and (3.23)) including Raleigh, Hanai-Bruggeman, and Maxwell models. The volume-fraction average model is omitted in Figure 3.10 due to its significant discrepancy. For this study, samples at different concentrations were prepared to evaluate the accuracy of these models, including 36 vol. % and 20 vol. % PDMS-MgCaTiO<sub>2</sub> composites, and 38 vol. % and 20

vol. % PDMS-TiO<sub>2</sub> composites, which all have been loaded with well-dispersed and unsintered raw powders.

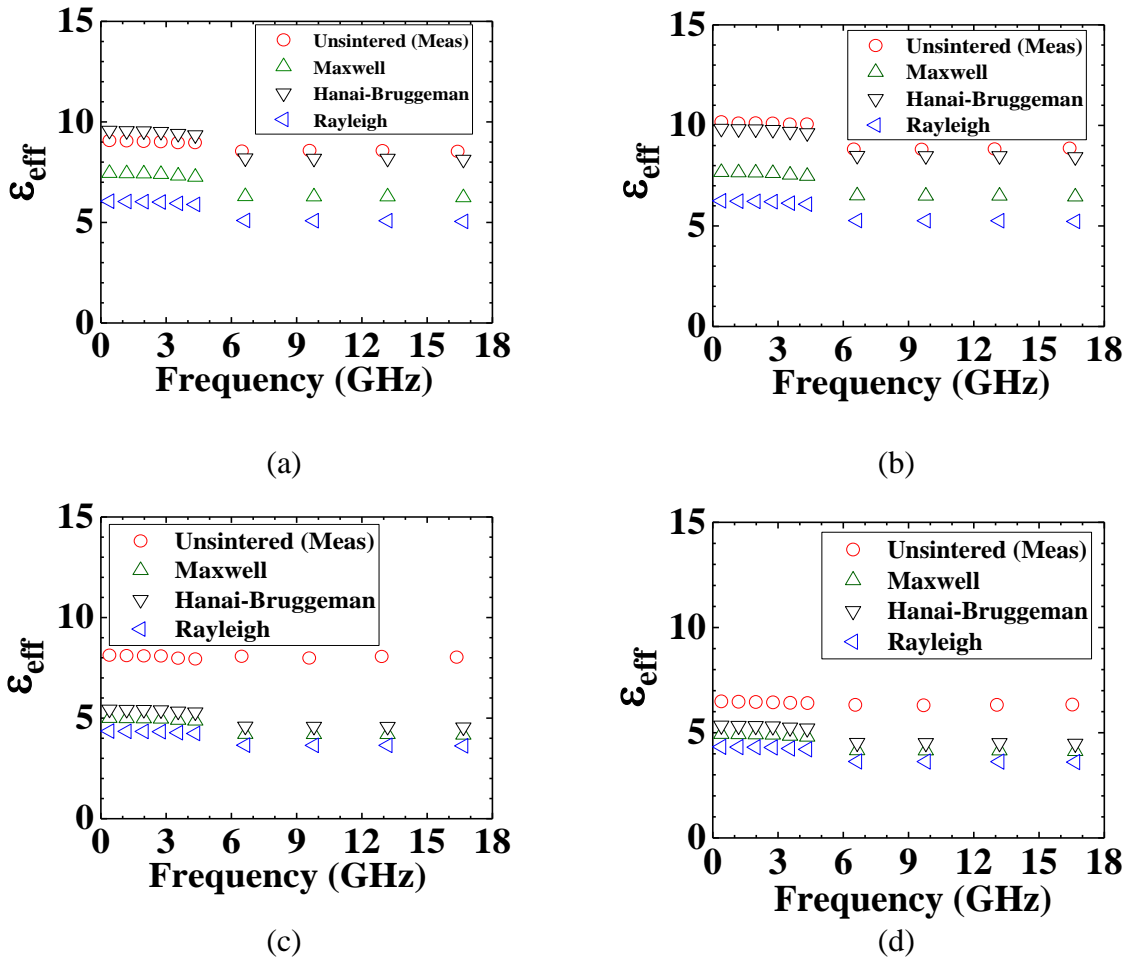


Figure 3.10 – Comparison between the measured dielectric permittivities and predicted dielectric permittivities given by the models including Raleigh (Equation (3.20)), Hanai-Bruggeman (Equation (3.21)) and Maxwell (Equation (3.23)) models, by using the vendor-provided properties of unsintered raw powders and measured properties of PDMS. (a) A 36 vol. % PDMS-MgCaTiO<sub>2</sub> composite sample. (b) A 38 vol. % PDMS-TiO<sub>2</sub> composite sample (c) A 20 vol. % PDMS-MgCaTiO<sub>2</sub> composite sample; (d) a 20 vol. % PDMS-TiO<sub>2</sub> composite sample.

The most accurate prediction of dielectric permittivity in this study for high volume loading concentrations was found to be the Hanai-Bruggeman model (i.e., Equation (3.21)), resulting in a 1.5% discrepancy for a 36 vol. % PDMS-MgCaTiO<sub>2</sub> specimen and a 3.6% deviation for a 38 vol. % PDMS-TiO<sub>2</sub> sample, as shown in Figure 3.10(a) and Figure 3.10(b), respectively. Meanwhile,

it leads to a 37.1% discrepancy for a 20 vol. % PDMS-MgCaTiO<sub>2</sub> specimen and a 10.6% deviation for a 20 vol. % PDMS-TiO<sub>2</sub> sample, as shown in Figure 3.10(c) and Figure 3.10(d), respectively. As shown in Figure 3.10, it is observed that the Hanai-Bruggeman's model based on Equation (3.21) provides reasonable effective permittivity prediction of two-component polymer-ceramic composites with 36 % to 38 % filler loading volume fractions while exhibiting lower accuracy for samples with 20 vol. % fractions loadings. Note that the measured frequency-dependent complex permittivity of an unfilled PDMS specimen has been adopted as the properties of the polymer matrix for all the models, which leads to the similar frequency-dependent model behaviors as shown in Figure 3.14.

Figure 3.11 shows the effective permittivity prediction by four of the exploited models at different filler loading volume fractions, including volume-fraction, Maxwell, Hanai-Bruggeman, and Rayleigh models, which are compared to the measured permittivity at 6 GHz for composites loaded with unsintered ceramic fillers at different volume fractions. Figure 3.11(a) shows the model predictions vs. the tested effective permittivity for 20 vol. % and 36 vol. % PDMS-MgCaTiO<sub>2</sub> composites, while Figure 3.11(b) shows the model predictions vs. tested effective permittivity for 20 vol. % and 38 vol. % PDMS-TiO<sub>2</sub> composites.

Figure 3.12(a) presents the comparison of the measured properties of the four types of composites versus predictions by Hanai-Bruggeman's model, while Figure 3.12(b) shows the measured properties for the four types of composites versus predictions by Maxwell's model.

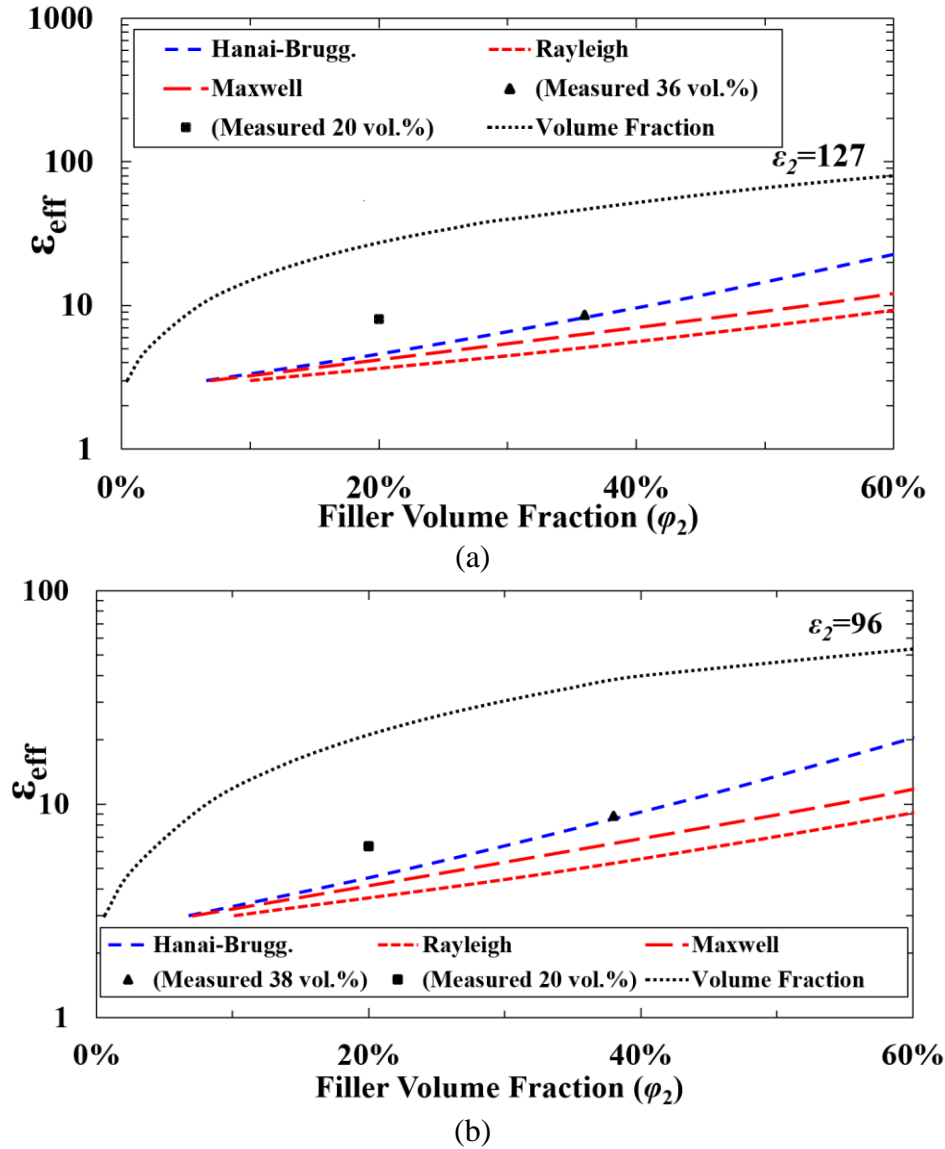


Figure 3.11 – Comparison of the model-predicted permittivity of PDMS-based composites embedded with different fillers at various volume ratios based on Equations (3.20)-(3.23). (a) 20 vol. % and 36 vol. % PDMS-MgCaTiO<sub>2</sub> composites. (b) 20 vol. % and 38 vol. % PDMS-TiO<sub>2</sub> composites. Model predictions are compared with the measured results at 6 GHz for PDMS-based composites loaded with high-temperature sintered fillers of different volume concentrations.

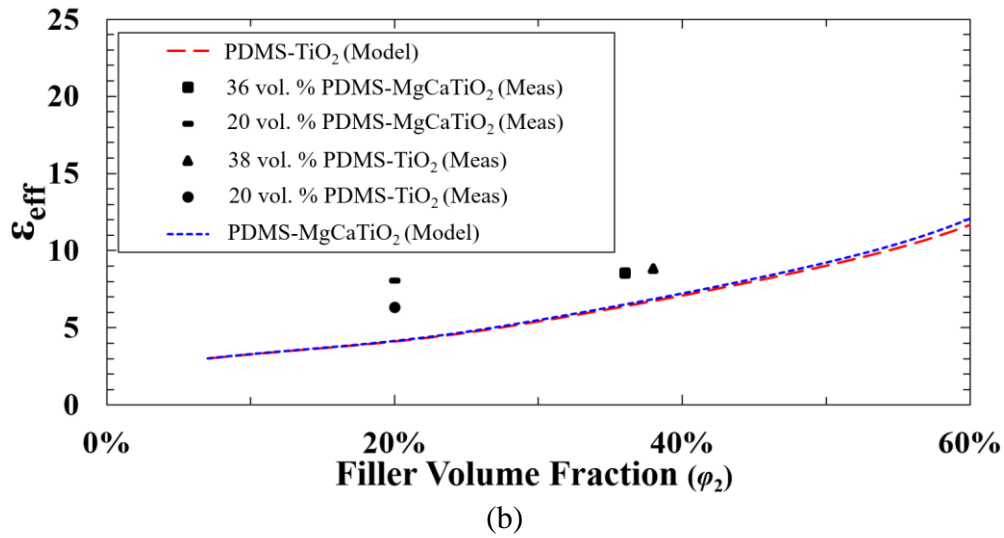
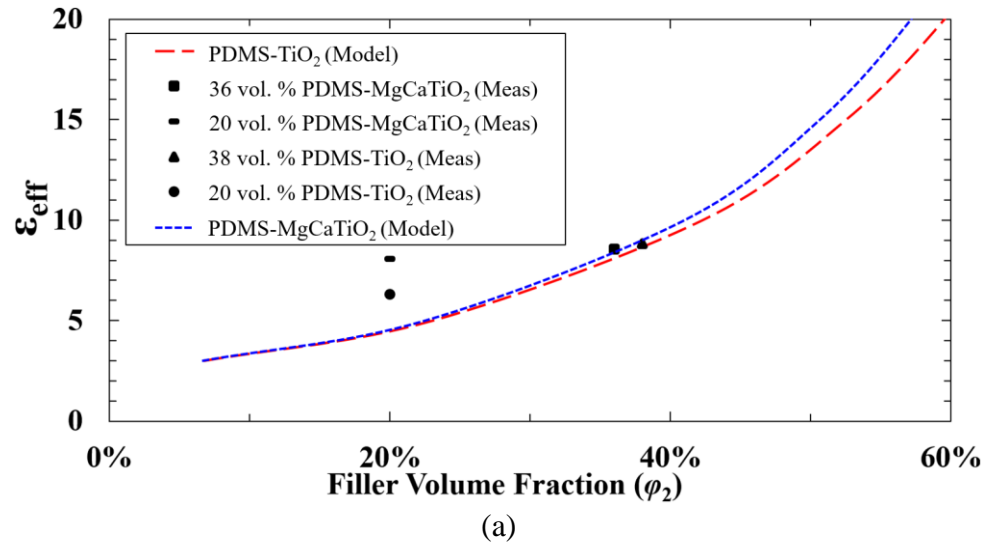


Figure 3.12 – (a) Comparison of measured properties for the four types of composites vs. predictions by the Hanai-Bruggeman's model (Equation (3.21)). (b) Measured properties for the four types of composites vs. predictions by Maxwell's model (Equation (3.23)). Model predictions are compared with the measured results at 6 GHz for PDMS-based composites loaded with high-temperature sintered fillers of different volume concentrations.

### 3.9 Theoretical Model Prediction of Dielectric Loss ( $\tan \delta_d$ ) in PMCs

The dissipation factor also is known as dielectric loss tangent ( $\tan \delta_d$ ) of a mixture of two components with corresponding dissipation factors (loss tangents)  $\tan \delta_{d1}$  and  $\tan \delta_{d2}$ , as per Raju [63] is given by Equation (3.31).

$$\tan \delta_d = \frac{\varphi_2 \varepsilon_1' \tan \delta_{d2} + \varphi_1 \varepsilon_2' \tan \delta_{d1} (1 + \tan^2 \delta_{d2})}{\varphi_2 \varepsilon_1' + \varphi_1 \varepsilon_2' (1 + \tan^2 \delta_{d2})} \quad (3.31)$$

where  $\tan \delta_d$  is the dielectric loss tangent of the composite material,  $\tan \delta_{d1}$  is the dielectric loss tangent of the polymer matrix,  $\tan \delta_{d2}$  is the dielectric loss tangent of the ceramic fillers,  $\varepsilon_1'$  is the permittivity of the polymer matrix,  $\varepsilon_2'$  is the permittivity of the filler particles,  $\varphi_1$  is the volume fraction of the matrix, and  $\varphi_2$  is the volume fraction of the filler particles.

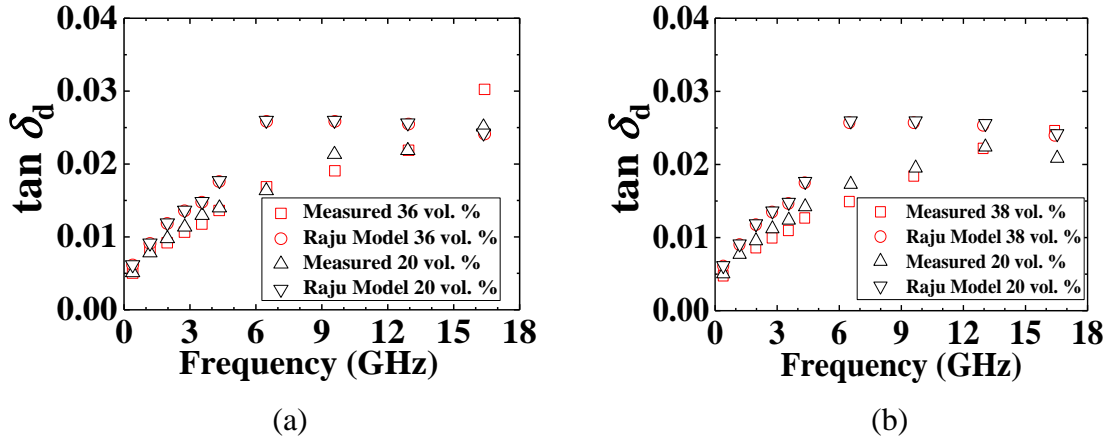


Figure 3.13 – Comparison between the measured dielectric losses ( $\tan \delta_d$ ) with the losses predicted by the Raju model based on Equation (3.31) by using the properties of unsintered raw powders and measured properties of PDMS. (a) 36 vol. % and 20 vol. % PDMS-MgCaTiO<sub>2</sub> composites. (b) 38 vol. % and 20 vol. % PDMS-TiO<sub>2</sub> composites.

Figure 3.13 depicts the comparison between the measured and predicted dielectric loss tangent by the Raju model based on Equation (3.31) of the four kinds of polymer-ceramic composites using the properties of unsintered ceramic fillers. The model predictions from 0.4 GHz to 17 GHz have shown a 19% and 20% discrepancies for the 36 vol. % and 20 vol. % PDMS-MgCaTiO<sub>2</sub> composite samples, respectively. Similarly, a slightly higher 26% and 25% of deviation for 38 vol. % and 20 vol. % PDMS-TiO<sub>2</sub> composite specimens have been observed. The measured frequency-dependent permittivity and loss tangent of PDMS matrix was used in this study as the baseline properties of the polymer matrix, which has led to frequency-dependent loss characteristics by the model predictions.

### 3.10 Results and Discussions

The impact of a high-temperature sintering process under different conditions on the resultant dielectric and loss properties (i.e., permittivity  $\epsilon_r$  and loss tangent  $\tan \delta_d$ ) of PDMS-ceramic composite materials has been evaluated. There is a saturation limit regarding the amount of homogeneously dispersed ceramics fillers due to the resultant defects, such as “air voids”, which are too hard to remove by the degassing step due to the high viscosity. The 1100°C sintering process has significantly improved the dielectric and loss properties for both PDMS-MgCaTiO<sub>2</sub> and PDMS-TiO<sub>2</sub> composites as compared to those of PDMS composite specimens loaded with unsintered corresponding ceramic powders. As shown in Table 3.6, significant improvements of about 20% increase in permittivity and 29% decrease in dielectric loss tangent were observed at 17 GHz for the composite sample with MgCaTiO<sub>2</sub> fillers sintered at 1100°C; whereas more subtle changes of about 10% increase in permittivity was observed (at 17 GHz) for the sample with TiO<sub>2</sub> fillers sintered at 1100°C along with a 27% increase of the dielectric loss tangent. Furthermore, Figure 3.14 and Figure 3.15 present the measured EM characteristics up to 17 GHz of PDMS-MgCaTiO<sub>2</sub> based composites and PDMS-TiO<sub>2</sub> based composites sintered at the different conditions, respectively.

In this study, it was observed that both ceramic fillers became harder to re-pulverize after the sintering process at 1500°C. The measured tapped densities for these ceramic powders sintered at 1500°C were higher than the other samples as shown in Table 3.3 and Table 3.4. The excessive solidification prevents the desired sub-50  $\mu\text{m}$  particle size distribution to be realized during the subsequent ball milling step. Thus, some spherical agglomerates bigger than 50  $\mu\text{m}$  were observed during the SEM analysis of the polymer-ceramic composite samples loaded with fillers sintered at 1500°C, which could lead to slightly increased losses due to the effects of porosity, grain size,

grain boundary, and defects [48]. Piagai *et al.* have successfully demonstrated finer particles of  $Mg_{0.95}Ca_{0.05}TiO_3$  of about  $0.1 \mu m$  by using an alkoxide precursor method [70], which could help to reduce further the microwave dielectric losses caused by agglomeration of particles within polymer-ceramics composites.

Table 3.6 – Measured EM properties of polymer-ceramic composites with fillers sintered at different conditions

Ceramic Powder	Sintering Conditions	Volume Ratio (%)	$\epsilon_r$		$\tan \delta_d$		Improvement	
			Raw Sample	Sintered Sample	Raw Sample	Sintered Sample	$\epsilon_r$ (%)	$\tan \delta_d$ (%)
MgCaTiO <sub>2</sub>	1100°C/ 3 hours	36	8.53	10.26	0.0302	0.0214	20.28	29.13
MgCaTiO <sub>2</sub>	1500°C/ 3 hours	36	8.53	9.93	0.0302	0.0218	16.41	27.81
TiO <sub>2</sub>	1100°C/ 3 hours	38	8.86	9.73	0.0246	0.0313	9.82	-27.23
TiO <sub>2</sub>	1500°C/ 3 hours	38	8.86	8.28	0.0246	0.0254	-6.55	-3.25

Note: The comparison is based on permittivity  $\epsilon_r$  and loss tangent  $\tan \delta_d$  measured at 16.5 GHz.

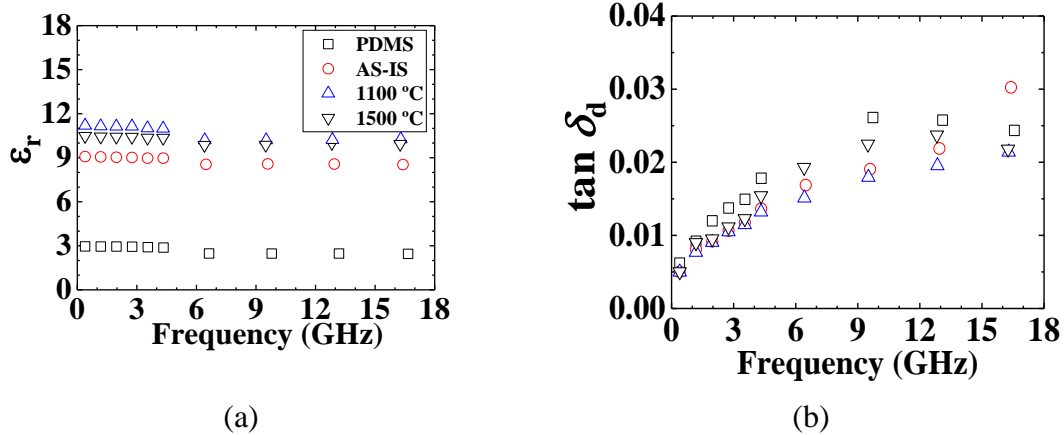


Figure 3.14 – Measured dielectric properties of PDMS and PDMS-ceramic thin-sheet samples with 36 vol. % MgCaTiO<sub>2</sub> fillers sintered at different temperatures. (a) Measured permittivities. (b) Measured dielectric loss tangents.

In our experiments, it was observed that the primary source of the dielectric losses of the two types of polymer-ceramic composites could be ascribed to the dielectric loss of the PDMS polymer host matrix as shown in Figure 3.14 and Figure 3.15. As shown in Figure 3.16, the best



balance between high-permittivity and low-loss at high-frequency region was achieved with the 36 vol. % and 49 vol. % PDMS-MgCaTiO<sub>2</sub> composite specimens. Composite materials with MgCaTiO<sub>2</sub> and TiO<sub>2</sub> fillers have shown nearly frequency-independent permittivities. At the same time, loss tangents slightly lower than that of pure PDMS have been realized as opposed to prior works [38]-[42] as shown in Table 3.7. Evidently, the incorporation of low-loss and high-*k* ceramic fillers not only effectively increases the permittivity but also in most of the cases slightly lowers the overall effective dielectric loss.

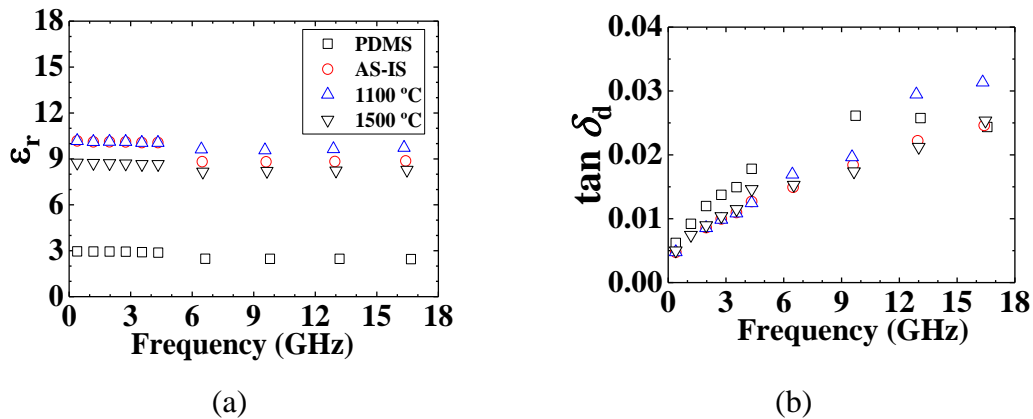


Figure 3.15 – Measured dielectric properties of PDMS and PDMS-ceramic thin-sheet samples with 38 vol. % TiO<sub>2</sub> fillers sintered at different temperatures. (a) Measured permittivities. (b) Measured dielectric loss tangents.

As shown in Figure 3.16, the measured dielectric permittivity and loss tangent of the 36 vol. % and 49 vol. % PDMS-MgCaTiO<sub>2</sub> composites are superior to those of widely-used “FR-4” epoxy microwave laminates with woven fiberglass enforcement at frequencies up to 20 GHz and 8 GHz, respectively. In fact, these results are no longer far behind the characteristics of some commercial rigid high-end microwave laminates such as TMM13i<sup>®</sup> from Rogers Corporation, which are composed of hydrocarbon thermoset polymer loaded with BaTiO microfillers and the RT/duroid<sup>®</sup> 6010LM laminate, which consist of ceramic-PTFE composites based on TiO<sub>2</sub> microfillers, respectively [71], [72]. Therefore, this new class of mass-producible high-*k*, low-loss,

and compliant polymer composite materials has already shown some promising attributes for enabling the next generation of 3D conformal or flexible RF and microwave devices [38], [49]. It is worthwhile mentioning that the dielectric loss of the PDMS elastomer host matrix has predominantly limited the best achievable loss properties, which is going to be mitigated through our ongoing work by replacing PDMS with other thermoset or thermoplastic polymers with a substantially lower dielectric loss tangent, such as cyclo-olefin polymer (COP), as discussed in the following chapters of this dissertation.

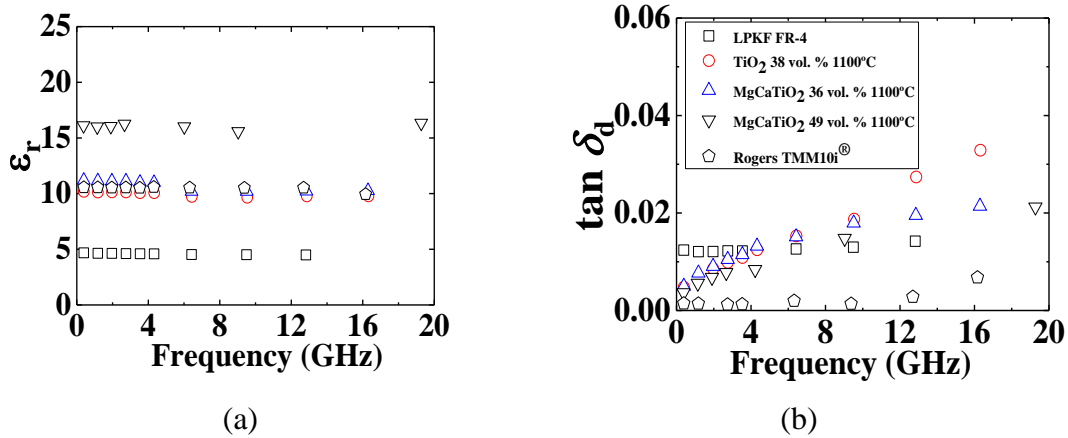


Figure 3.16 – Comparison of measured EM properties of PDMS-ceramic composite samples with commercial RF and microwave laminates (i.e., FR-4 and TMM10i®). (a) Measured permittivities. (b) Measured loss tangents.

### 3.11 Conclusion

Five flexible high- $k$  and low-loss polymer-ceramic EM composites based on MgCaTiO<sub>2</sub> and TiO<sub>2</sub> dielectric micro-fillers have been investigated, with a particular focus on the employment of high-temperature sintering processes to enhance the microwave dielectric and loss properties further. A 36 vol. % PDMS-MgCaTiO<sub>2</sub> substrate with fillers sintered at 1100°C has exhibited very stable  $\epsilon_r$  of 10.27 and a  $\tan \delta_d$  lower than 0.021 at frequencies up to 17 GHz. These results correspond to a 20% increase in relative permittivity and a 29% decrease in dielectric loss tangent when compared with the specimen loaded with “as-is” unsintered raw powders. Similarly, the 36

vol. % PDMS-MgCaTiO<sub>2</sub> composites with 1500°C sintered fillers have exhibited a stable  $\epsilon_r$  of 9.93 and  $\tan \delta_d$  lower than 0.021 at frequencies up to 17 GHz. These results correspond to an enhancement of 16% regarding relative permittivity and a 28% decrease in dielectric loss tangent when compared with the specimen loaded with the same concentration of unsintered raw powders. Moreover the 49 vol. % loaded PDMS-MgCaTiO<sub>2</sub> composite thin-sheet specimen with particles sintered at 1100°C has exhibited a dielectric permittivity  $\epsilon_r$  of 16.33 and a low  $\tan \delta_d$  lower than 0.021 at frequencies up to 19 GHz. On the contrary, 38 vol. % PDMS-TiO<sub>2</sub> sample with particles sintered at 1100°C has exhibited a  $\epsilon_r$  of 9.73 and slightly higher  $\tan \delta_d$  lower than 0.031 at frequencies up to 17 GHz, which suggests an enhancement of 10% in relative permittivity along with a 27% increase of the dielectric loss tangent as compared to those of specimen loaded with unsintered raw powders. Meanwhile, a 38 vol. % PDMS-TiO<sub>2</sub> sample with particles sintered at 1500°C has exhibited a very stable  $\epsilon_r$  of 8.28 and a  $\tan \delta_d$  lower than 0.025 at frequencies up to 17 GHz, which suggests a 7% decrease of in the relative permittivity and a 3% increase of the dielectric loss tangent. Localized characterization of the ceramic composites was performed using a custom-built near-field microwave microscopy (NFMM) tool operating at 5 GHz. NFMM images revealed the non-uniform distribution of the MgCaTiO<sub>2</sub> and TiO<sub>2</sub> ceramic particles in the host matrix. It was found that over an area of 50  $\mu\text{m} \times 50 \mu\text{m}$ , less particle filler dispersion uniformity is achieved for PDMS-TiO<sub>2</sub> composites as compared to that of PDMS-MgCaTiO<sub>2</sub> composites. It is worthwhile mentioning that the measured microwave dielectric properties of both composite elastomer substrates are superior to that of the widely-used FR-4 printed circuit boards with respect to both higher relative permittivity and similar dielectric losses. These new classes of high- $k$ , low-loss, and compliant polymer-ceramic composite materials has already shown some

promising attributes for enabling the next generation of 3D conformal or flexible RF and microwave devices up to the Ku and K-bands.

Table 3.7 – Comparison of measured EM properties between this work and prior reports up to K-band

Composite or Commercial Laminates	Year	Flexible	Vol (%)	Freq. (GHz)	$\epsilon_r$	$\tan \delta_d$	Reference
MgCaTiO <sub>2</sub> / PDMS	2006	Yes	25	1	8.5	0.0090	[39]
BT-BaTiO <sub>3</sub> / PDMS	2006	Yes	25	1	20	0.0400	[39]
PDMS- NdTiO <sub>3</sub> (sintered 960°C)	2015	Yes	25	17	9.22	0.0250	[40]
PDMS- NdTiO <sub>3</sub>	2013	Yes	30	1	9.5	0.0090	[41]
PDMS-SrTiO <sub>3</sub>	2014	Yes	31.2	10	8.40	0.0170	[42]
BADCy/Ni <sub>0.5</sub> Ti <sub>0.5</sub> NbO <sub>4</sub>	2015	No	N/A	9	22.79	0.0042	[47]
COP-Ba <sub>0.55</sub> Sr <sub>0.45</sub> TiO <sub>3</sub> (sintered 1340°C) FDM <sup>†</sup>	2015	No	25	10	4.88	0.0071	[49]-[50]
COP-MgCaTiO <sub>2</sub> (sintered 1200°C) FDM <sup>†</sup>	2015	No	30	17	4.82	0.0018	[17]
PDMS-TiO <sub>2</sub> (sintered 1100°C)			38	17	9.73	0.0313	
PDMS-TiO <sub>2</sub> (sintered 1500°C)			38	17	8.28	0.0254	<b>This Work</b>
PDMS-MgCaTiO <sub>2</sub> (sintered 1100°C)	2015	Yes	36	17	10.27	0.0214	
PDMS-MgCaTiO <sub>2</sub> (sintered 1100°C)			49	20	16.33	0.0212	
PDMS-MgCaTiO <sub>2</sub> (sintered 1500°C)			36	17	9.93	0.0218	
FR-4	2015	No	N/A	12	4.5	0.0142	LPKF
ROGERS TMM13i <sup>®</sup>					12.85	0.0019	
ROGERS TMM10i <sup>®</sup>					9.80	0.0020	ROGERS Corp.
ROGERS RT/duroid <sup>®</sup> 6010LM	2015	No	N/A	10	10.2	0.0023	
ROGERS RO3010 <sup>®</sup>					10.2	0.0022	
isola Tachyon <sup>®</sup>				10	3.02	0.0021	
isola I-Tera <sup>®</sup> MT	2015	No	N/A	10	3.45	0.0031	isola Group
isola Astra <sup>®</sup> MT				2	3.0	0.0017	

Note: Comparison based on the values of  $\epsilon_r$  and  $\tan \delta_d$  at the maximum characterization frequency reported in literature or datasheets (for ROGERS, and isola laminates). <sup>†</sup>Samples by FDM.

## CHAPTER 4 :

### FLEXIBLE EM COMPOSITES AND THEIR APPLICATION TO K-BAND ANTENNAS

#### 4.1 Note to Reader

Portions of this chapter, including figures have been previously published in [38], [40], [49], and [50], which have been reproduced with permission from IEEE Microwave Theory and Techniques Society, and from the International Microelectronics Assembly and Packaging Society and Microelectronics Foundation. Permissions are included in Appendix A.

#### 4.2 Introduction

In this chapter, four types of high-permittivity and low-loss EM composites based on a Polydimethylsiloxane (PDMS) reinforced by  $\text{Ba}_{0.55}\text{Sr}_{0.45}\text{TiO}_3$  or  $\text{MgCaTiO}_2$  micro-particle fillers with volume loading concentration up to 49 vol. % have been prepared and characterized up to 20 GHz using cavity resonators. These high- $k$  ceramic powders were sintered at temperatures up to  $1500^\circ\text{C}$  to further enhance their dielectric properties. The 49 vol. % loaded PDMS- $\text{Ba}_{0.55}\text{Sr}_{0.45}\text{TiO}_3$  composites loaded with  $1340^\circ\text{C}$  sintered fillers have exhibited a dielectric permittivity  $\epsilon_r$  of 23.51 and a dielectric loss tangent  $\tan \delta_d$  less than 0.047 at frequencies up to 20 GHz. Meanwhile the 39 vol. % loaded PDMS- $\text{Ba}_{0.55}\text{Sr}_{0.45}\text{TiO}_3$  composites with  $1340^\circ\text{C}$  sintered fillers have an  $\epsilon_r$  of 15.02 and a  $\tan \delta_d$  less than 0.042 at frequencies up to 16 GHz. On the other hand, the 37 vol. % loaded PDMS- $\text{MgCaTiO}_2$  composites with  $1100^\circ\text{C}$  sintered fillers have an  $\epsilon_r$  of 12.19 and a  $\tan \delta_d$  less than 0.021 at frequencies up to 20 GHz. The 49 vol. % loaded PDMS- $\text{MgCaTiO}_2$  composite specimen has a measured  $\epsilon_r$  of 16.33 and a  $\tan \delta_d$  less than 0.021 between 0.4 and 20 GHz. As a demonstration of a device prototype, a 19.6 GHz microstrip patch antenna was printed by

employing a molded PDMS-MgCaTiO<sub>2</sub> composite substrate and micro-dispensed silver paste (CB028) to form the conductive layer, which has achieved 20 dB return loss and about 10% bandwidth. Evidently, these newly developed polymer-ceramic composites are well suited for applications up to the K-band and are amenable to be adopted to 3D printing technologies.

### 4.3 Experimental Procedure

In this chapter, the systematic sample preparation approach discussed in Chapter 3 has been adopted to develop high-*k* and low-loss polymer-ceramic composites based on different ceramic fillers sintered under different conditions. Four types of polymer-ceramic composites were prepared by homogeneous dispersion of high-*k* titanate fillers, such as MgCaTiO<sub>2</sub> from Trans-Tech Inc. and Ba<sub>0.55</sub>Sr<sub>0.45</sub>TiO<sub>3</sub> from Ferro Corporation with particle loading concentration up to 49 vol. %. The measured material properties are shown in Table 4.4.

This chapter reports an assessment of applications of PDMS-ceramic composites to fabricate flexible substrates for the implementation of microstrip edge-fed patch antennas operating at 19.6 GHz. Note that the batch of MgCaTiO<sub>2</sub> (MCT-140) material used in this study is different than the material used and reported in Chapter 3. In particular, different bulk dielectric properties have been observed as shown in Table 4.4.

### 4.4 Preparation and Characterization PDMS-Ceramic Composites

#### 4.4.1 Ceramics Sintering Process

For the high-temperature sintering process, zirconia trays are used together with two sintering furnaces both in air. One is an Omegalux LMF-3550 box furnace (Omega Engineering, Stamford, CT) that works up to 1100°C and the other is a KSL 1700X box furnace (MTI Corporation, Richmond, CA) that operates up to 1700°C. The applied sintering conditions are described in Table 4.1. These temperatures were strategically selected to evaluate how the ceramic

powders behave under different sintering conditions, including room temperature (unsintered), an intermediate temperature of 1100°C and a temperature close to the ceramic's melting point of 1500°C and 1340°C for MgCaTiO<sub>2</sub> and Ba<sub>0.55</sub>Sr<sub>0.45</sub>TiO<sub>3</sub>, respectively.

Table 4.1 – Summary of the studied sintering conditions

<b>Ceramic Material</b>	<b>Max Applied Temperature (°C)</b>	<b>Sintering Time (hours)</b>	<b>Measured Tapped Density (g/cm<sup>3</sup>)</b>
Ba <sub>0.55</sub> Sr <sub>0.45</sub> TiO <sub>3</sub>	Unsintered	N/A	1.37
	1100	3	1.45
	1340	2	3.14
MgCaTiO <sub>2</sub>	Unsintered	N/A	2.14
	1100	3	2.17
	1500	3	2.32

After the sintering process, the densified and crystallized powders are re-pulverized using a MM 400 ball mill (Retsch, Haan, Germany) for 5 minutes to obtain an average particle size of 5 µm or less as seen in Figure 4.3(b) to avoid filler dispersion inhomogeneity due to the particle agglomeration in the polymer-ceramic composites. The tapped densities of the ceramic powders were determined after the sintering and ball milling processes as shown in Table 4.1.

#### 4.4.2 XRD, EDS, and SEM Analysis

The ceramic particles were analyzed using a X'Pert Pro X-ray diffractometer (Panalytical, Almelo, Netherlands) to study the effects of the sintering process on the crystallographic structure. The XRD analysis was performed before and after the sintering operations. A previous XRD study for the MgCaTiO<sub>2</sub> ceramic powders was conducted as shown in Figure 3.1 indicating the peaks with significant compositional changes by the sintering conditions. Figure 4.1 depicts the XRD patterns for the Ba<sub>0.55</sub>Sr<sub>0.45</sub>TiO<sub>3</sub> ceramic powders, showing the peaks with significant changes caused by the sintering conditions.



Differences in the d-spacings [ $\text{\AA}$ ] in the corresponding peaks measured with the X-Ray spectra for  $\text{Ba}_{0.55}\text{Sr}_{0.45}\text{TiO}_3$  ceramic were observed after the sintering conditions ( $1100^\circ\text{C}$  and  $1340^\circ\text{C}$ ) compared with the unsintered material at room temperature (unsintered) as shown in Table 4.2. As observed, the unit volume cell shrinks which suggests densification. The peaks with significant changes in intensity are along the (110) and (211) crystal orientations as shown in Figure 4.1. The elemental analysis was performed by using an S-800 field emission scanning electron microscope (FE-SEM) (Hitachi Ltd., Tokyo, Japan), which is equipped with an EDS system (EDAX Inc., Mahwah, NJ). The EDS analysis clearly shows how each element reacted under the different sintering temperatures applied. For  $\text{MgCaTiO}_2$  powders, the  $\text{TiO}$  molecules showed significant changes as depicted in Figure 3.3 and discussed in Chapter 3.

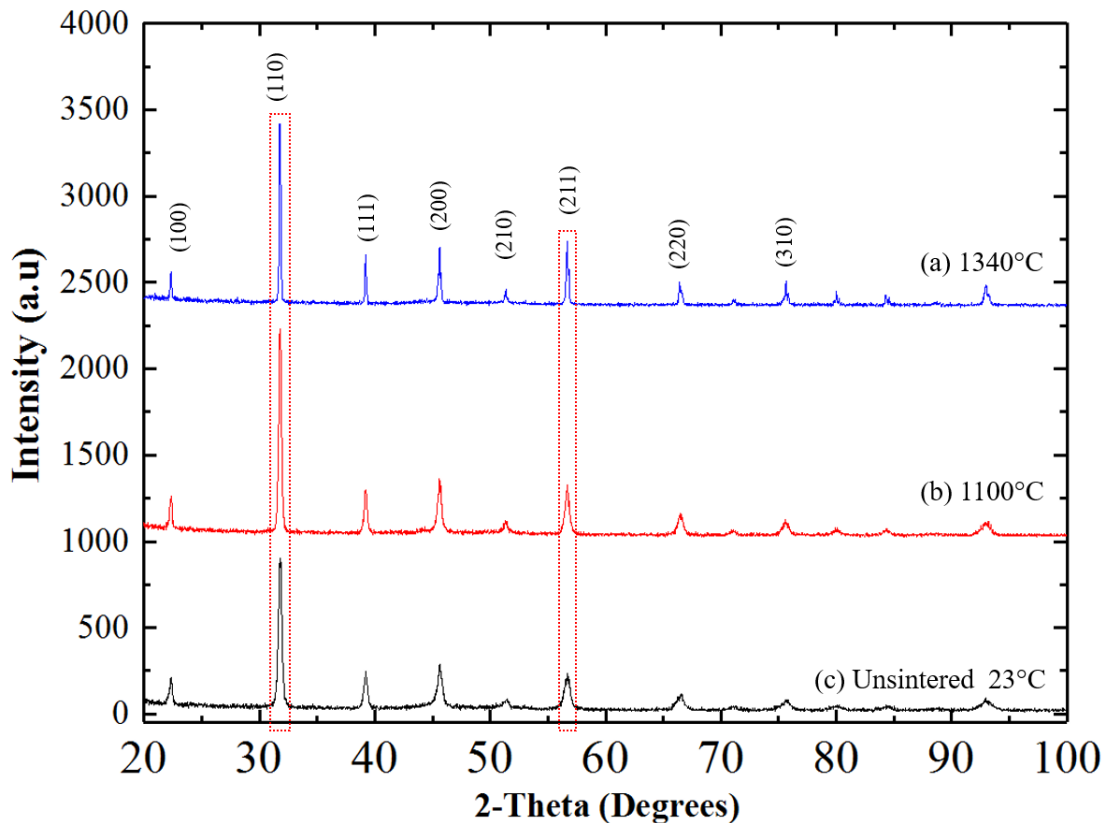


Figure 4.1 – Measured x-ray diffraction (XRD) patterns of  $\text{Ba}_{0.55}\text{Sr}_{0.45}\text{TiO}_3$  ceramic powders after different processes. (a) A sample after a two hour sintering process at  $1340^\circ\text{C}$ . (b) A sample after a three hour sintering process at  $1100^\circ\text{C}$ . (c) Unsintered raw powders.

Table 4.2 –Lattice parameters of Ba<sub>0.55</sub>Sr<sub>0.45</sub>TiO<sub>3</sub> measured by XRD

Sintering Temp (°C)	Tapped Density (g/cc) <sup>§</sup>	a (Å)	b (Å)	c (Å)	V (Å <sup>3</sup> )	Crystal Structure
1340	3.1372	3.9724	3.9724	3.9703	62.65	Tetragonal
1100	1.4452	3.9724	3.9724	3.9703	62.65	
Unsintered	1.3682	3.9771	3.9771	3.9883	63.08	

§ Measured tapped density after a 2-5 min ball milling process was determined by mass and volume measurement.

Similarly, the BaTiO molecule exhibited major transformation for the sintered Ba<sub>0.55</sub>Sr<sub>0.45</sub>TiO<sub>3</sub> powders as summarized in Table 4.3 that provides a semi-quantitative elemental composition analysis for Ba<sub>0.55</sub>Sr<sub>0.45</sub>TiO<sub>3</sub> ceramic fillers. The corresponding EDS spectrum of Ba<sub>0.55</sub>Sr<sub>0.45</sub>TiO<sub>3</sub> powders sintered at 1100°C is shown in Figure 4.2. The characterization results also indicate a 56% and a 51% increase of the relative permittivity due to the sintering process conditions (i.e., 1340°C for two hours and 1100°C for three hours for Ba<sub>0.55</sub>Sr<sub>0.45</sub>TiO<sub>3</sub> and MgCaTiO<sub>2</sub> powders, respectively) as shown in Figure 4.6 and Figure 4.5, respectively.

Table 4.3 – Element weight fractions based on EDS of Ba<sub>0.55</sub>Sr<sub>0.45</sub>TiO<sub>3</sub> at different sintering conditions

Element	Unsintered	23°C <sup>†</sup>	1100°C	1340°C
O	0	0	0	11.57
Ba	6.41		5	44.19
Sr	31.47		31.89	20.96
Ti	62.12		63.11	23.26
<b>Total →</b>	100.00		100.00	100.00

<sup>†</sup> Raw samples received from Ferro Corporation at room temperature under unsintered condition.

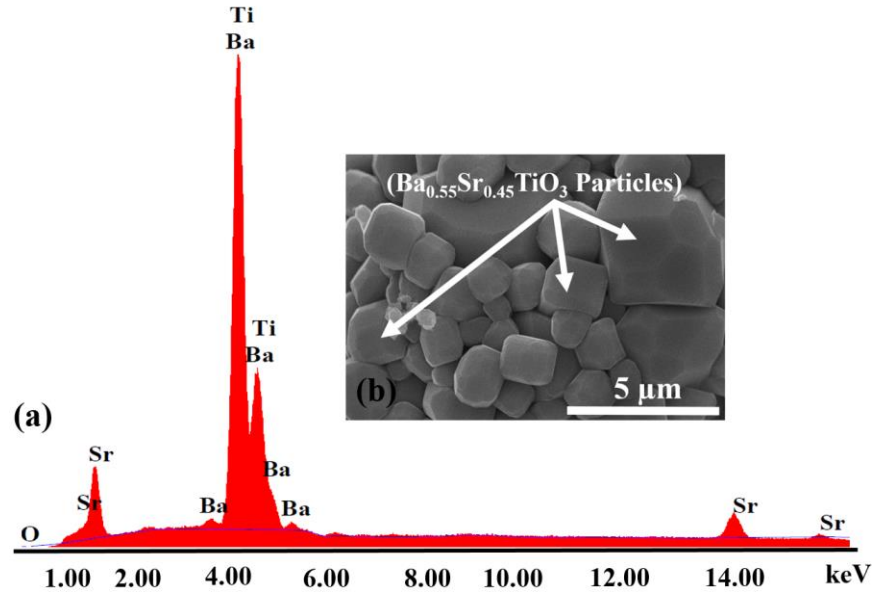


Figure 4.2 – (a) Tested energy dispersive spectroscopy (EDS) spectrum of  $\text{Ba}_{0.55}\text{Sr}_{0.45}\text{TiO}_3$  ceramic powders sintered at  $1100^\circ\text{C}$ . (b) SEM photo of  $\text{Ba}_{0.55}\text{Sr}_{0.45}\text{TiO}_3$  spheres after a  $1340^\circ\text{C}$  sintering process.

#### 4.4.3 Preparation of Polymer-Ceramic Composites

The development of PDMS-ceramic composites starts with mixing of the two components of the PDMS in a 10:1 ratio using a THINKY ARE-310 planetary centrifugal mixer for 2 minutes at 2000 rpm followed by a 30 second deaerating step (also known as “degassing”) at 2200 rpm for removing any trapped air bubbles [40]. The second phase is to determine the volume ratio between the sintered ceramic fillers and the host polymer based on the measured tapped powder density shown in Table 4.1. The ARE-310 planetary centrifugal mixer is used again to mix ceramic powders and the PDMS host elastomer at the desired volume concentration to ensure a homogenous dispersion.

The resultant polymer-ceramic composites are then poured into a custom-designed hot compression mold followed by a careful degassing step at 22 in-Hg to remove the air bubbles by using an Isotemp 281A vacuum oven (Fisher Scientific, Waltham, MA, USA). A degassing time of more than two hours along with purging steps, every 10 minutes is needed for samples with

high filler loading beyond 30% in volume. The sample is then compression molded and cured at 100°C for one hour. The high-temperature sintering process is a critical step for enhancing the dielectric and loss properties of the ceramic powders as shown in Table 4.5.

The SEM analysis was performed using a SU-70 scanning electron microscope (Hitachi, Ltd, Tokyo, Japan). Figure 4.3(a) show the top-view SEM photo of 49 vol. % PDMS- $\text{Ba}_{0.55}\text{Sr}_{0.45}\text{TiO}_3$  by volume with powders sintered at 1340°C. Figure 4.3(b) cross-sectional view SEM photo of PDMS- $\text{Ba}_{0.55}\text{Sr}_{0.45}\text{TiO}_3$  composites with filler loading of 39 vol. %. Figure 4.4(a), Figure 4.4(b) and Figure 4.4(c) present the SEM images of  $\text{MgCaTiO}_2$  particles, which are unsintered, sintered at 1100°C, and sintered at 1500°C, respectively. Figure 4.4(d) show the SEM image of the PDMS- $\text{MgCaTiO}_2$  polymer composites with ceramic fillers sintered at the 1100°C and re-pulverized. As shown in Figure 4.4(d), an excellent particle size distribution of about 5  $\mu\text{m}$  has been achieved. The composites show excellent particle-to-polymer and particle-to-particle interfaces without noticeable agglomeration of particles.

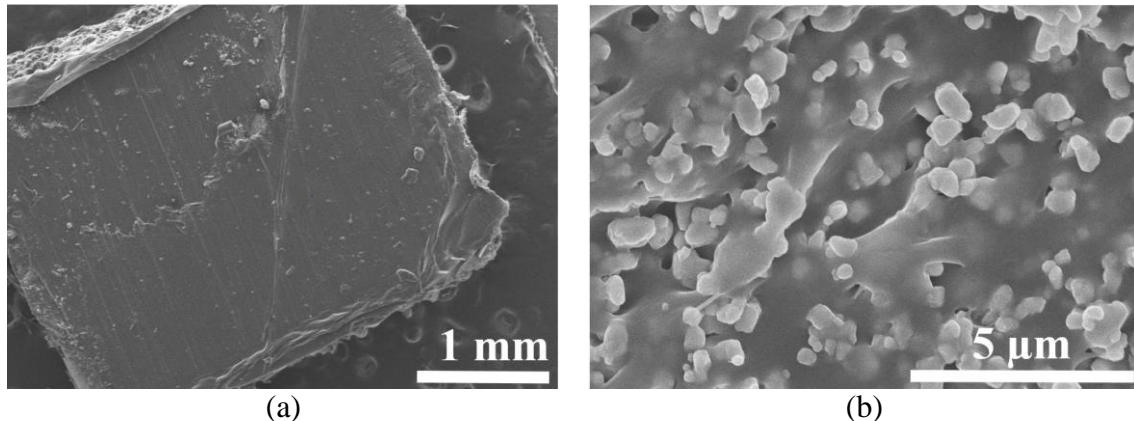


Figure 4.3 – SEM photos PDMS composite samples. (a) Top-view SEM photo of 49 vol. % PDMS- $\text{Ba}_{0.55}\text{Sr}_{0.45}\text{TiO}_3$  by volume with powders sintered at 1340°C. (b) Cross-sectional view SEM photo of PDMS- $\text{Ba}_{0.55}\text{Sr}_{0.45}\text{TiO}_3$  composites with filler loading of 39 vol. %.

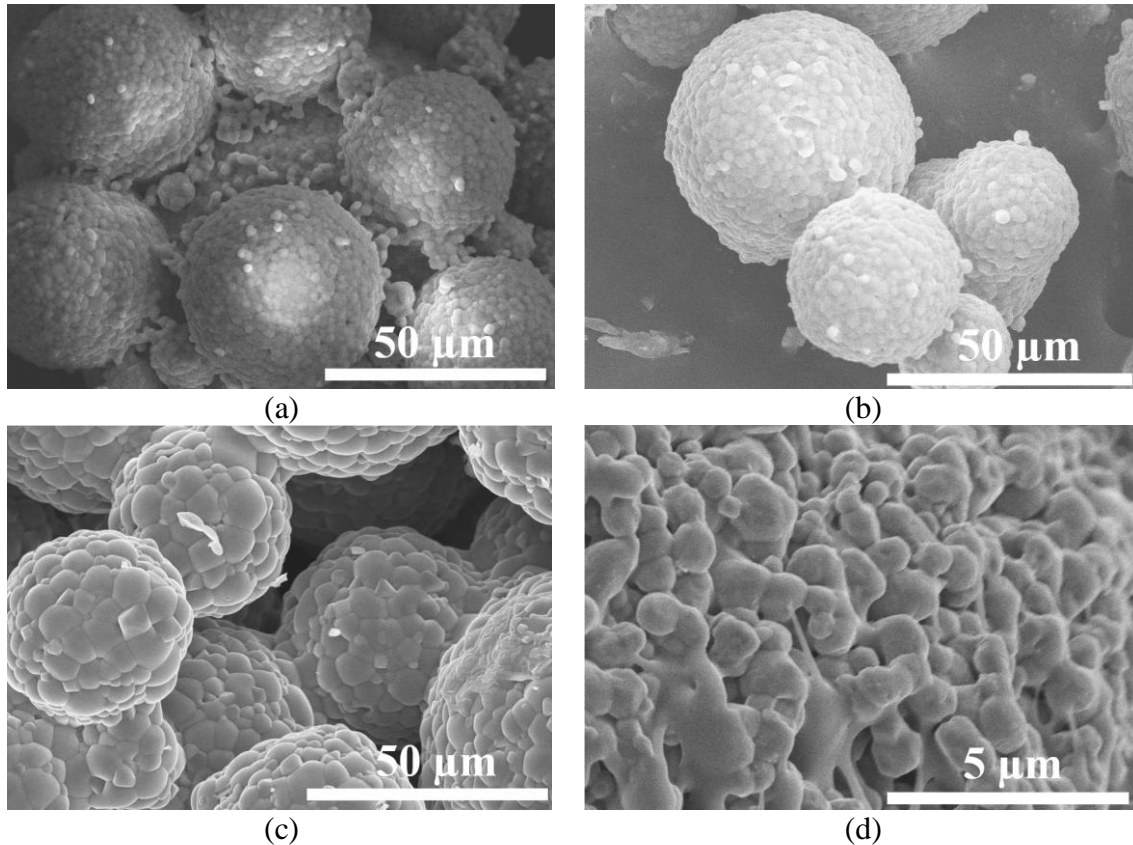


Figure 4.4 – SEM photos the  $\text{MgCaTiO}_2$  particles under different sintering conditions. (a) Unsintered. (b) Sintered at  $1100^\circ\text{C}$ ; (c) Sintered at  $1500^\circ\text{C}$ . (d) Cross-sectional view photo of the corresponding PDMS- $\text{MgCaTiO}_2$  composites at 37 vol. % particle volume concentration after the  $1100^\circ\text{C}$  sintering process.

The assessment of dielectric properties of the PDMS-ceramic composites was carried out using cavity resonators based on the cavity perturbation theory [57]-[59] by using Equation (3.15) - Equation (3.19) as detailed in Chapter 3. A 0.7 mm-thick molded PDMS- $\text{MgCaTiO}_2$  thin-sheet was prepared with a particular volume concentration of loaded ceramic fillers previously sintered at  $1100^\circ\text{C}$  for three hours. The molded specimen composed of 37 vol. % PDMS- $\text{MgCaTiO}_2$  composites have shown a measured  $\epsilon_r$  of 12.19 and  $\tan \delta_d$  lower than 0.021 between 0.4 GHz and 20 GHz; while a 49% loaded PDMS- $\text{MgCaTiO}_2$  composite specimen has a  $\epsilon_r$  of 16.33 and a  $\tan \delta_d$  lower than 0.021 at the same frequency range.

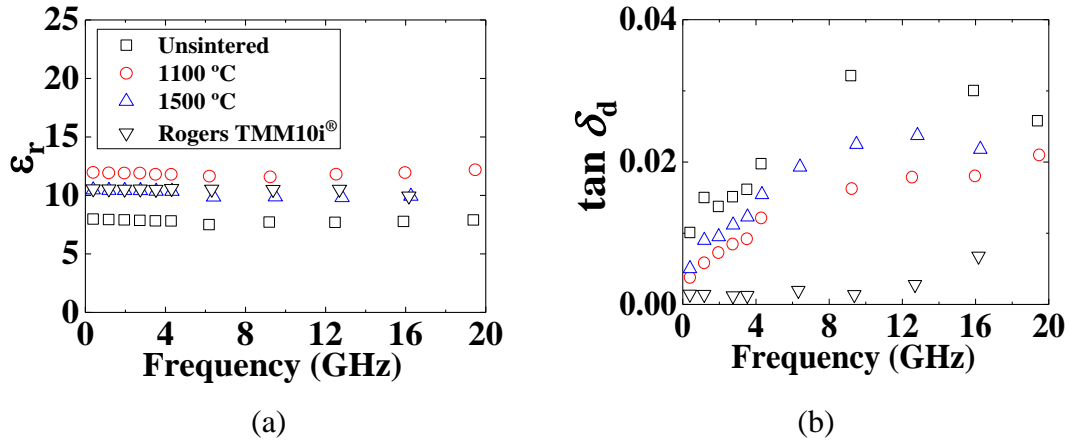


Figure 4.5 – Measured EM properties of PDMS-MgCaTiO<sub>2</sub> composites with 37% fillers sintered at 1100°C or 1500°C. (a) Relative permittivity. (b) Dielectric loss tangent, which were both plotted versus frequencies and sintering temperatures while compared with a measured properties of a Rogers TMM10i<sup>®</sup> thermoset laminate.

As shown in Figure 4.5, the measured relative permittivities and dielectric losses of 37 vol. % PDMS-MgCaTiO<sub>2</sub> composites with fillers sintered at 1100°C and 1500°C were compared with a sample filled with unsintered raw powders. As observed, this MgCaTiO<sub>2</sub> composite material exhibited greater enhanced properties after an 1100°C sintering process rather than a 1500°C sintering process. Nevertheless, there is an improvement regarding increased permittivity and reduced dielectric losses under both sintering conditions. Similarly, Figure 4.6 presents the measured permittivity of 39 vol. % PDMS-Ba<sub>0.55</sub>Sr<sub>0.45</sub>TiO<sub>3</sub> composites with the fillers sintered at 1100°C and 1340°C. Due to the high-temperature sintering, the relative dielectric permittivities were improved by up to 51% and 56% while the dielectric losses were reduced by 38% and 33% for MgCaTiO<sub>2</sub> and Ba<sub>0.55</sub>Sr<sub>0.45</sub>TiO<sub>3</sub> loaded PDMS composites, respectively, as summarized in Table 4.5. Figure 4.7 depicts the high-frequency performance of the PDMS-Ba<sub>0.55</sub>Sr<sub>0.45</sub>TiO<sub>3</sub> composites loaded with 39 vol. % and 49 vol. % fillers sintered at 1340°C for two hours.

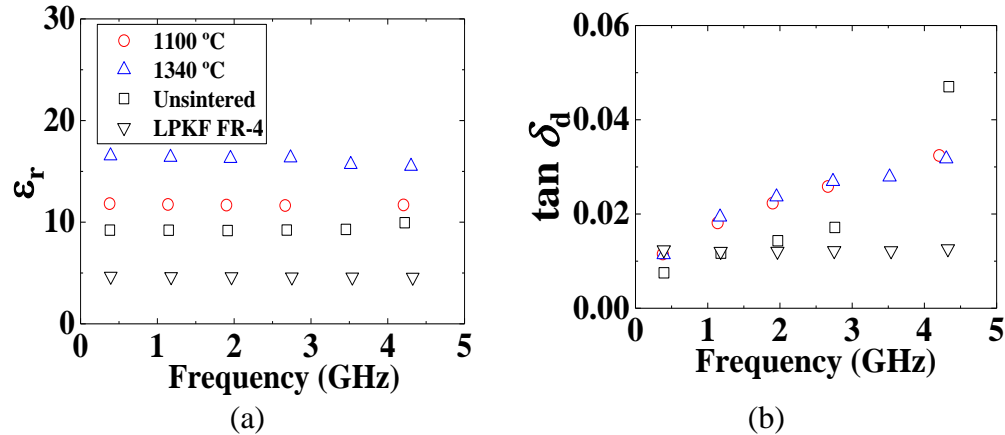


Figure 4.6 – Measured EM properties of the PDMS- $\text{Ba}_{0.55}\text{Sr}_{0.45}\text{TiO}_3$  composites with 39 vol. % fillers sintered at 1100°C and 1340°C. (a) Permittivity. (b) Dielectric loss, which were both plotted versus frequencies and sintering temperatures while compared with measured properties of an LPKF FR-4 laminate.

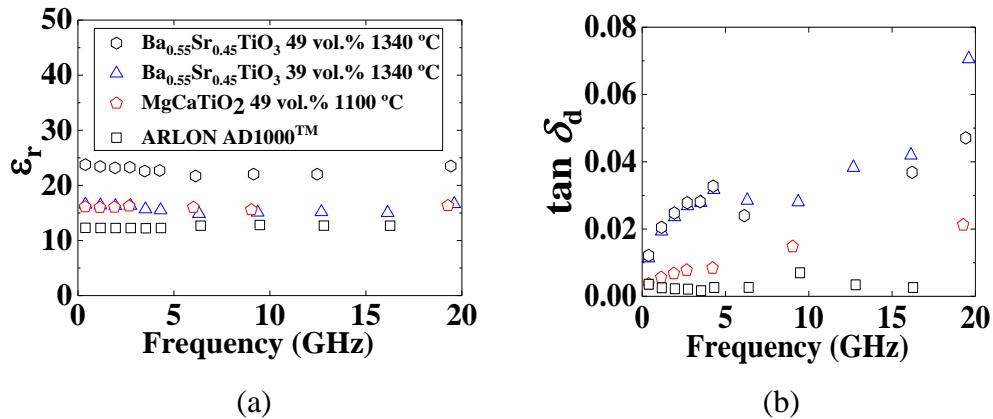


Figure 4.7 – High-frequency measured dielectric properties of the PDMS- $\text{Ba}_{0.55}\text{Sr}_{0.45}\text{TiO}_3$  composites with 39 vol. % and 49 vol. % fillers sintered at 1340°C, as well as PDMS- $\text{MgCaTiO}_2$  composites with 49 % fillers sintered at 1100°C. (a) Permittivity. (b) Dielectric loss tangent that was plotted vs. frequencies and compared with a measured ARLON AD1000™ woven glass reinforced laminate.

Both composite materials have shown fairly frequency-independent high dielectric permittivity and slightly lower loss tangent as compared to prior works [39]-[42], which is summarized in Table 4.6.



The measured dielectric and loss properties of the both composite elastomer substrates at microwave frequencies are superior to that of the widely-used FR4 printed circuit boards regarding relative permittivity and dielectric losses. While almost approaching the properties of some rigid, high-performance commercial microwave laminates such as TMM10i<sup>®</sup>, TMM13i<sup>®</sup>, RO3010 and RT/duroid<sup>®</sup> 6010LM from Rogers Corporation and the AD1000<sup>™</sup> from ARLON electronic materials (now ARLON is merged with Rogers Corporation after the acquisition in 2015). Figure 4.8 shows the 3D schematic-view surface profiles of molded thin-sheet samples taken by a Dimension 3100 atomic force microscope (AFM) tool. Figure 4.8(a) presents the AFM-scanned profile of a 49 vol. % PDMS-Ba<sub>0.55</sub>Sr<sub>0.45</sub>TiO<sub>3</sub> thin-sheet specimen with an average roughness value of 1.5 μm over a 10 μm × 10 μm area. Whereas Figure 4.8(b) depicts the AFM-scanned profile of a 37 vol. % PDMS-MgCaTiO<sub>2</sub> thin-sheet specimen with a mean roughness of about 623 nm across a 5 μm × 5 μm area.

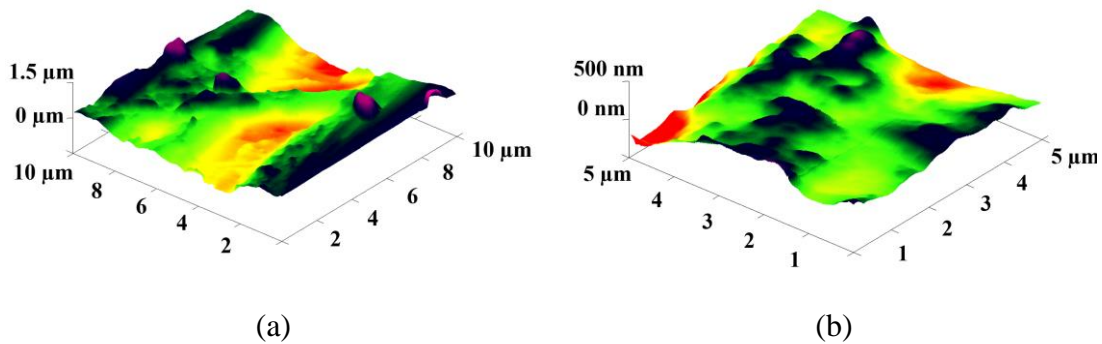


Figure 4.8 – Schematic-view scanned AFM surface profiles of PDMS based composites. (a) A 49 vol. % PDMS-Ba<sub>0.55</sub>Sr<sub>0.45</sub>TiO<sub>3</sub> thin-sheet specimen. (b) A 37 vol. % PDMS-MgCaTiO<sub>2</sub> thin-sheet specimen.



Table 4.4 – The key properties of ceramic fillers and sintering conditions in this chapter's materials

Ceramic Material	Max. Temp. (°C)	Groups	Dielectric Properties		Absolute Density (g/cc)	Particle Size (µm) <sup>‡</sup>	Melting Point (°C)
			$\epsilon_r$	$\tan \delta_d$			
MgCaTiO <sub>2</sub> (MCT-140) <sup>†</sup>	1500/ 3 hours	II-IV-VI	148	0.0012	3.85	2.26	>1450
Ba <sub>0.55</sub> Sr <sub>0.45</sub> TiO <sub>3</sub> <sup>§</sup>	1340/ 2 hours	II-IV-VI	2367	0.0019	5.70	0.87	>1340

<sup>†</sup>Obtained from Trans-Tech, Inc., Dielectric Properties at 6 GHz

<sup>‡</sup>Particle size measured in a sphere during SEM characterization

<sup>§</sup>Obtained from Ferro Corporation., Dielectric Properties at 1 kHz

Table 4.5 – Comparison of measured dielectric and loss properties of polymer-ceramic composites

Ceramic Powder	Firing Temperature (°C)	Volume Ratio	Firing Time (hours)	$\epsilon_r$		$\tan \delta_d$		Improvement	
				Raw Sample	Sintered Sample	Raw Sample	Sintered Sample	$\epsilon_r$ (%)	$\tan \delta_d$ (%)
Ba <sub>0.55</sub> Sr <sub>0.45</sub> TiO <sub>3</sub>	1100	39%	3	9.94	11.69	0.0470	0.0324	17.61	31.06
Ba <sub>0.55</sub> Sr <sub>0.45</sub> TiO <sub>3</sub>	1340	39%	2	9.94	15.50	0.0470	0.0317	55.94	32.55
MgCaTiO <sub>2</sub>	1100	37%	3	7.82	11.80	0.0197	0.0122	51.00	38.07
MgCaTiO <sub>2</sub>	1500	37%	3	7.82	10.35	0.0197	0.0154	32.37	21.69

Note: The permittivity  $\epsilon_r$  and  $\tan \delta_d$  were measured at 4.3 GHz. Raw samples are unsintered samples.

Table 4.6 – Comparison of measured EM properties vs. those reported by prior works up to K-band

Composites or Commercial Laminates	Year	Flexible	vol. (%)	Freq. (GHz)	$\epsilon_r$	$\tan \delta_d$	Reference
MgCaTiO <sub>2</sub> / PDMS	2006	Yes	25	1	8.5	0.0090	[39]
BT-BaTiO <sub>3</sub> / PDMS	2006	Yes	25	1	20	0.0400	[39]
PDMS- NdTiO <sub>3</sub>	2013	Yes	30	1	9.5	0.0090	[41]
PDMS-SrTiO <sub>3</sub>	2014	Yes	31.2	10	8.40	0.0170	[42]
PDMS-Ba <sub>0.55</sub> Sr <sub>0.45</sub> TiO <sub>3</sub> (sintered 1340°C) <sup>‡</sup>			39	16	15.02	0.0419	
PDMS-Ba <sub>0.55</sub> Sr <sub>0.45</sub> TiO <sub>3</sub> (sintered 1340°C) <sup>‡</sup>	2015	Yes	49	20	23.51	0.0471	<b>This Work</b>
PDMS-MgCaTiO <sub>2</sub> (sintered 1100°C) <sup>‡</sup>			37	20	12.19	0.0210	
PDMS-MgCaTiO <sub>2</sub> (sintered 1100°C) <sup>‡</sup>			49	20	16.33	0.0212	
FR-4	2015	No	N/A	12	4.5	0.0142	LPKF
Tachyon <sup>®</sup>	2015	No	N/A	10	3.02	0.0021	isola
I-Tera <sup>®</sup> MT	2015	No	N/A	10	3.45	0.0031	Group
AD1000 <sup>™</sup>	2015	No	N/A	10	10.20	0.0023	ARLON
TC600 <sup>™</sup>	2015	No	N/A	10	6.15	0.0020	Electronic Materials
TMM13i <sup>®</sup>					12.85	0.0019	
TMM10i <sup>®</sup>					9.80	0.0020	
RT/duroid <sup>®</sup> 6010LM	2015	No	N/A	10	10.2	0.0023	Rogers Corp.
RO3010 <sup>®</sup>					10.2	0.0022	
TMM3 <sup>®</sup>					3.45	0.0020	
RT/duroid <sup>®</sup> 5880					2.2	0.0009	

Note: The comparison is based on the values of permittivity and dielectric loss at the maximum characterization frequency reported in literature or vendor-provided datasheets.

## 4.5 Characterization of DPAM-Printed Antennas

### 4.5.1 Design of a 19.6 GHz Edge-Fed Microstrip Patch Antenna with PDMS-MgCaTiO<sub>2</sub>

#### Composites

The key aim to design and implement an edge-fed patch antenna prototype at 19.6 GHz was to demonstrate the EM properties and device capabilities up to K-band (18-27 GHz) of the 37 vol. % PDMS-MgCaTiO<sub>2</sub> composites. During the antenna design process, the edge-fed microstrip patch was selected to avoid the need for ultra-small inset feeds, the dimensions for the rectangular patch were determined using equations reported by Balanis [80] in Equations (4.1) - (4.6), and the dielectric properties reported in Figure 4.5.

Since the waves travel in both the composite substrate and the air; the effective dielectric constant  $\epsilon_{reff}$  is used to account for the effect of the fringing field and wave propagation through a microstrip line as shown in Equation (4.1).

$$\epsilon_{reff} = \frac{\epsilon_r + 1}{2} + \frac{\epsilon_r - 1}{2} \left[ 1 + 12 \frac{h}{W_p} \right]^{-1/2} \quad (4.1)$$
$$\frac{W_p}{h} > 1$$

where  $h$  is the substrate thickness, and  $W_p$  is the patch width.

The normalized patch antenna feedline extension length can be approximated by using the following Equation (4.2):

$$\frac{\Delta L}{h} = 0.412 \frac{(\epsilon_{reff} + 0.3) \left( \frac{W_p}{h} + 0.264 \right)}{(\epsilon_{reff} - 0.258) \left( \frac{W_p}{h} + 0.8 \right)} \quad (4.2)$$

The effective patch length is given by Equation (4.3):

$$L_{eff} = L + 2\Delta L = \frac{\lambda g}{2} \quad (4.3)$$

For an efficient radiator, the practical patch width that leads to a good radiation efficiency is given by Equation (4.4):

$$Wp = \frac{1}{2f_r \sqrt{\mu_0 \epsilon_0} \sqrt{\epsilon_r + 1}} = \frac{c_0}{2f_r} \sqrt{\frac{2}{\epsilon_r + 1}} \quad (4.4)$$

where  $c_0$  is the free-space velocity of light, and the actual length of the patch is determined by Equation (4.5):

$$Lp = \frac{1}{2f_r \sqrt{\epsilon_{reff}} \sqrt{\mu_0 \epsilon_0}} - 2\Delta L \quad (4.5)$$

The actual length of the patch is reduced to Equation (4.6):

$$Lp = \frac{\lambda_g}{2} - 2\Delta L \quad (4.6)$$

The calculated dimensions are shown in Figure 4.10(a), whereas the three printed antennas are also presented in Figure 4.10(b) and Figure 4.11.

#### 4.5.2 Challenges with Direct Print Additive Manufacturing (Micro-Dispensing) Technology together with Composite Materials

The main challenges observed with direct print additive manufacturing (DPAM) also known as (Micro-Dispensing) by employing a silver paste as a conductive layer are delamination issues between the silver paste (CB028) printed over the flexible substrate without a proper surface treatment. Another challenge is the reproducibility of the feature sizes below 250  $\mu\text{m}$ , as shown in Figure 4.11, which typically can be improved with longer setups allowing better precision and repeatability in the feature sizes. 250  $\mu\text{m}$ -wide printed microstrip lines have been realized. It is possible to achieve 100  $\mu\text{m}$  feature size with a longer setup time. The conductivity of the layer formed by micro-dispensed silver paste (CB028) dried at 90°C is 2.62e6 (S/m) [2], and the typical

measured average roughness is  $3.68 \mu\text{m}$  [25]. The key antenna geometry and dimensions are given in Figure 4.9 and Table 4.7, respectively.

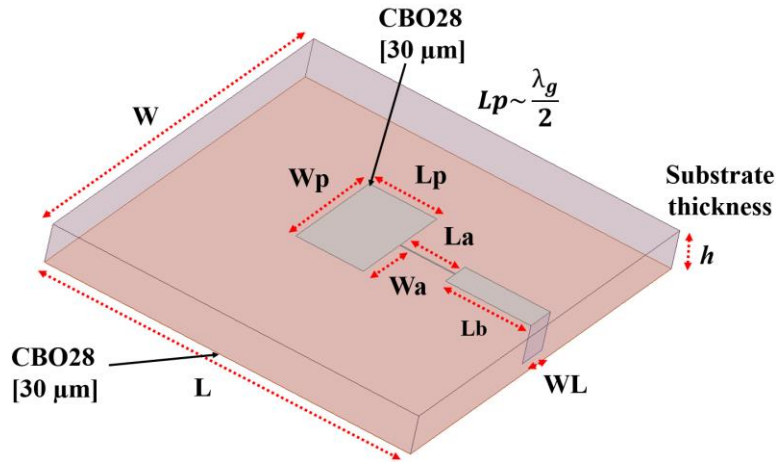


Figure 4.9 – Schematic diagram of a DPAM-printed rectangular edge-fed patch antenna by using a 37 vol. % PDMS-MgCaTiO<sub>2</sub> EM composite material. Critical dimensions and geometry of the edge-fed patch antennas.

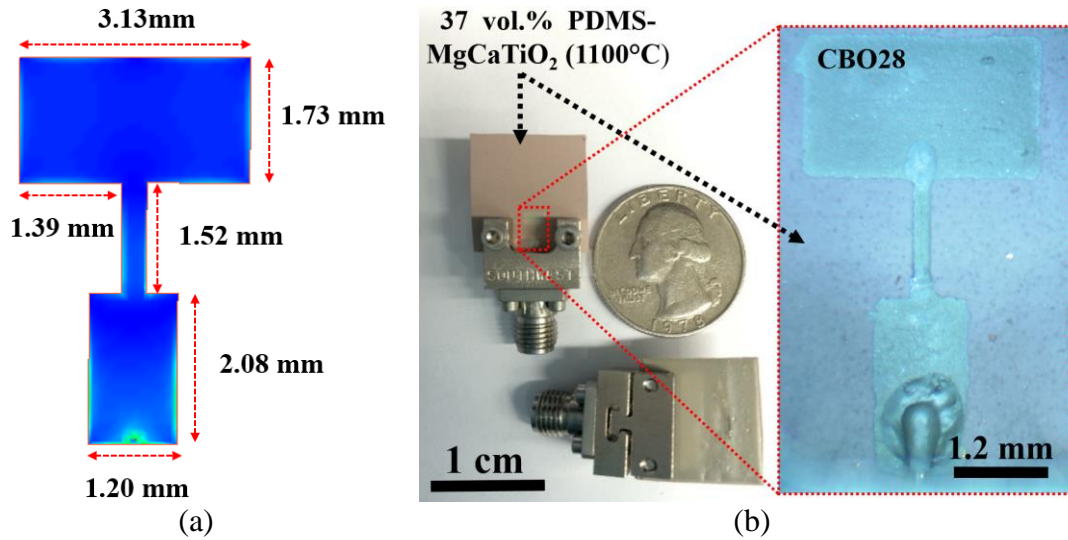


Figure 4.10 – Design and implementation of the edge-fed microstrip patch antennas showing (a) EM simulated current distribution in the patch antenna with the critical dimensions specified by ADS Momentum. (b) Photos of printed edge-fed patch antennas.

Table 4.7 – Antennas dimensions\*

Substrate Material	W	L	Wp	Lp	WL	Wa	La	Lb
Rogers RT/5880	14	20.30	6.00	4.50	2.77	2.46	2.82	4.59
Rogers TMM10i <sup>®</sup>	9.9	9.70	2.98	1.84	0.86	1.46	1.44	2.25
LPKF FR-4	12	14.44	4.39	3.01	1.69	1.99	2.07	3.29
PDMS-MgCaTiO <sub>2</sub>	9.4	8.62	3.13	1.73	1.20	1.39	1.29	2.08

\*All dimensions are given in mm.

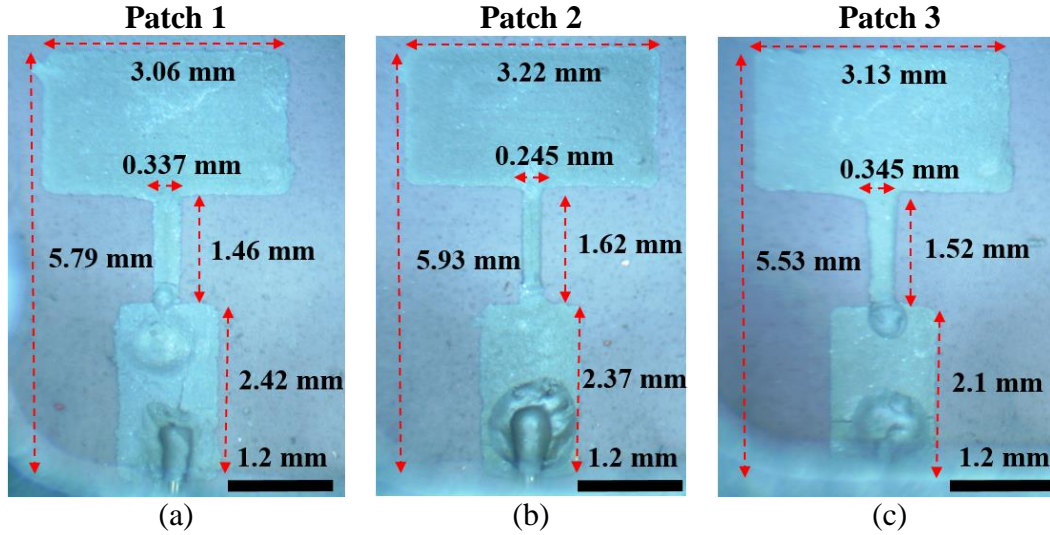


Figure 4.11 – DPAM-printed 19.6 GHz edge-fed patch antennas printed with different setups. (a) Top-view photo of a device with a 337  $\mu\text{m}$  line resolution. (b) Top-view photo of a device with a 245  $\mu\text{m}$  line resolution. (c) A printed antenna with a defect due to some delamination issues at the curing process.

#### 4.5.3 Characterization of a 19.6 GHz Edge-Fed Patch Antenna Printed over a PDMS-MgCaTiO<sub>2</sub> Substrate

The microwave performance of the newly developed high- $k$  composite materials at the K-band was evaluated with an edge-fed microstrip patch antenna designed at 19.6 GHz using aforementioned Equations (4.1)-(4.6) and simulated with ANSYS<sup>®</sup> Electromagnetics Suite 18 (HFSS 2017) by using  $2.62 \times 10^6$  (S/m) as conductivity of the printed silver ink. The molded 0.9 mm-thick 37 vol. % PDMS-MgCaTiO<sub>2</sub> composite substrate has rendered a  $\epsilon_r$  of 12.19 and  $\tan \delta_d$  lower than 0.021. The silver ink pattern was printed by micro-dispensing by using a tabletop 3Dn 3D-

printer (nScript, Orlando, FL) which is equipped with a SmartPump™ that utilizes a pressure pump with a high-precision computer actuated valve and a nozzle. The front-side patch antenna pattern and ground plane were printed using CB028 silver paste, with a pressure of 12 psi, a speed of 20 mm/s and a printer tip inner diameter of 125 μm.

Figure 4.11 shows three patch antennas printed over compression molded (9.4 mm × 8.62 mm × 0.9 mm) 37 vol. % PDMS-MgCaTiO<sub>2</sub> composite thin-sheet with fillers sintered at 1100°C. The molded substrates have been granted identical EM characteristics to those characterized thin-sheet samples as shown in Figure 4.5.

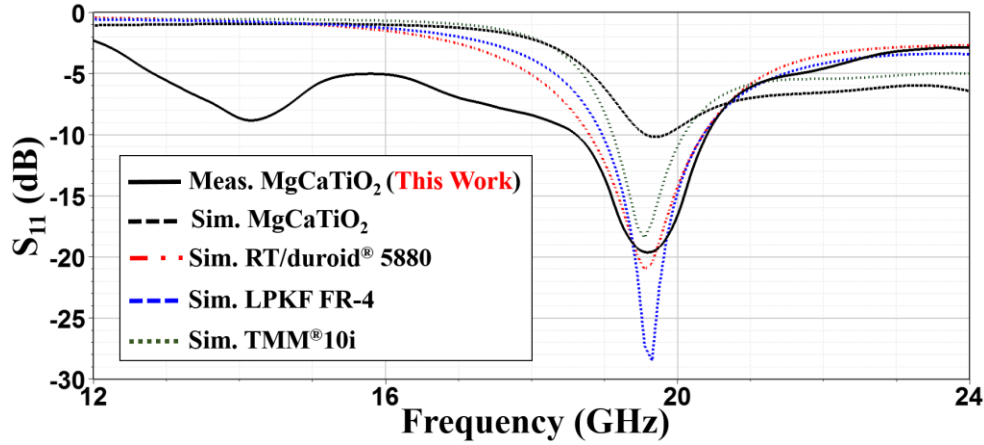


Figure 4.12 – Comparison between measured and simulated return losses for the printed 19.6 GHz edge-fed patch antenna along with a reference device implemented with a Rogers RT/duroid® 5880 laminate board and others mentioned in Table 4.8.

The DPAM-printed patch antenna exhibited a measured return loss of 20 dB along with a 10% bandwidth and a simulated gain of 2.43 dBi and 62% of radiation efficiency. The simulated vs. measured results are presented in Figure 4.12. All the antennas were simulated with ANSYS® Electromagnetics Suite 18 (HFSS 2017) using 30 μm thick CB028 silver paste with an assumed conductivity of 2.62e6 (S/m). Also, the measured dielectric properties of these commercial substrates, shown in Figure 3.16, Figure 4.5, and Figure 5.14, extracted by using the cavity



perturbation technique as explained in the previous chapter up to the K-band by using Equations (3.15)-(3.19) have been used herein.

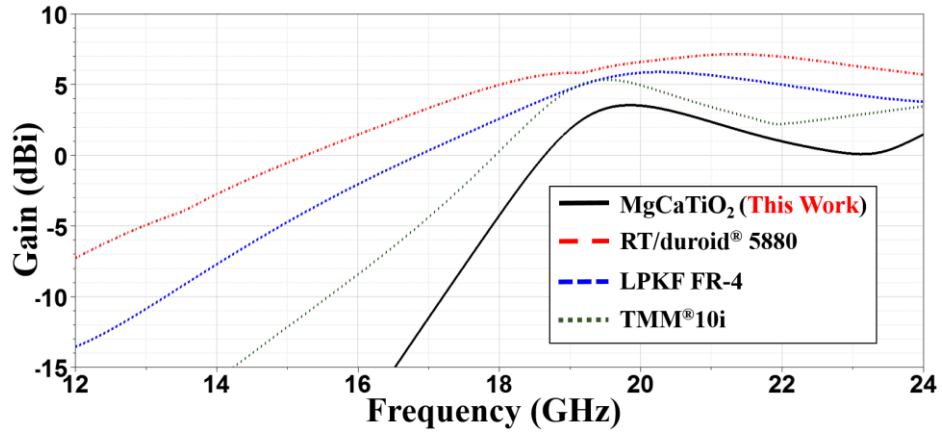


Figure 4.13 –Comparison between gain vs. frequency for all the antennas.

Despite that, the highest size reduction was achieved with the 37 vol. % PDMS-MgCaTiO<sub>2</sub> composite amongst all the antennas shown in Table 4.8 due to the higher index of refraction. The DPAM-printed patch antenna presents 62% radiation efficiency and 2.43 dBi of peak realized gain and about 80% size reduction when compared with a counterpart made of Rogers RT/duroid<sup>®</sup> 5880. This reference design exhibits 94% of radiation efficiency, and 4.27 dBi of peak realized gain due to the lower losses of the Rogers RT/duroid<sup>®</sup> 5880 laminate core material. Figure 4.13 depicts the comparison of the peak realized gain vs. frequency for all the designed antennas.

Table 4.8 – Performance comparison of edge-fed patch antenna designs

Material	Rogers (RT/duroid <sup>®</sup> 5880)	LPKF (FR-4)	Rogers (TMM10i <sup>®</sup> )	PDMS- MgCaTiO <sub>2</sub> 37 vol. % (1100°C)
Freq. (GHz)	19.6	19.6	19.6	19.6
Substrate thickness “h” (mm)	0.9	0.9	0.9	0.9
Radiator Area (mm <sup>2</sup> )	26.64	13.21	5.48	5.41
Size Reduction (%)	--	50.41	79.43	79.67
Peak Realized Gain (dBi)	4.27	3.59	3.41	2.43
Peak Directivity (dB)	4.58	4.73	4.40	4.33
Efficiency (%)	93.94	76.03	78.68	62.17

EM Simulations with ANSYS Electronics Desktop 18 (HFSS 2017)



As observed in Figure 4.13 the peak realized antenna gain is superior in all the commercial substrates due to the lower dielectric losses of these commercial materials as compared to the dielectric loss of the PDMS-based composites.

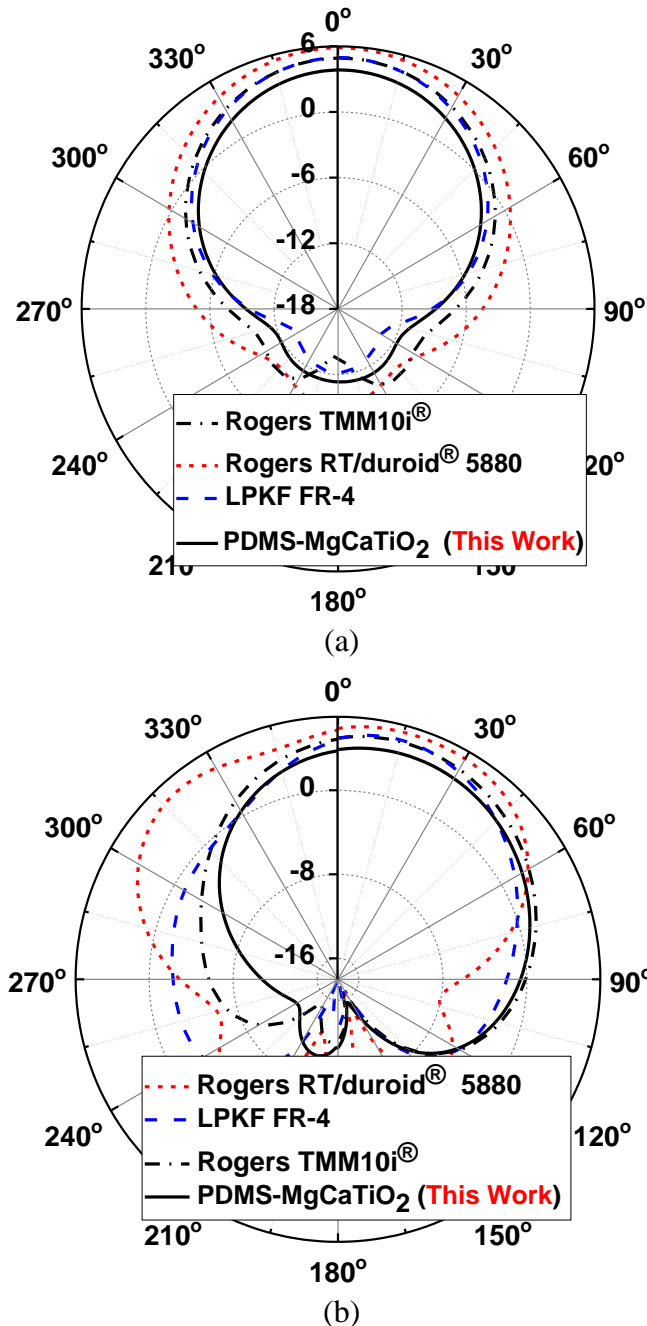


Figure 4.14 – EM simulation result of the 19.6 GHz edge-fed patch antennas by using ANSYS Electronics Desktop 18 (HFSS 2017), showing the radiation patterns comparison for all the antenna designs. (a) H-plane. (b) E-Plane.

Figure 3.15 shows the dielectric losses of the PDMS matrix, which hinders the maximum peak realized gain in the DPAM-printed antenna over PDMS-ceramic based composite substrate. Moreover, due to incompatibility issues with the fused deposition modeling (FDM) process of PDMS-based composites, cyclo-olefin polymer (COP), a low-loss amorphous thermoplastic matrix, have been strategically chosen for the ceramic-thermoplastic composites studied in the subsequent chapters.

Figure 4.14 shows the radiation patterns simulated by using HFSS 2017. As expected, the antennas based on the commercial materials present better radiation characteristics (higher gain) in both E-plane and H-plane, due to their lower dielectric losses as compared to the 37 vol. % PDMS-MgCaTiO<sub>2</sub> composites as summarized in Table 4.8.

#### **4.6 Stress and Strain RF Testing Analysis of a 4.2 GHz Flexible Patch Antenna Based on a 37 vol. % PDMS-MgCaTiO<sub>2</sub> Composite Material**

The mechanical and electrical performance characteristics of a 37 vol. % PDMS-MgCaTiO<sub>2</sub> based substrate using unsintered fillers was first evaluated to test the flexibility of the EM composite material. The testing is performed when the antenna it is exposed to stress and strain, the antenna was designed and fabricated to operate at 4.2 GHz by using Equations (4.1) - (4.6) along with the measured dielectric properties reported in Figure 4.5. A 18 µm-thick of copper tape were used for implementation of the antenna patch and the ground plane over a 1.52 mm-thick 37 vol. % PDMS-MgCaTiO<sub>2</sub> EM composite substrate loaded with unsintered fillers.

Figure 4.15 presents the evaluation of a patch antenna built on top of the PDMS-MgCaTiO<sub>2</sub> substrate with 4.2 GHz nominal frequency tested under various bending angles by Equation (4.7).

$$\theta \text{ (radians)} = \frac{L}{r} \quad (4.7)$$

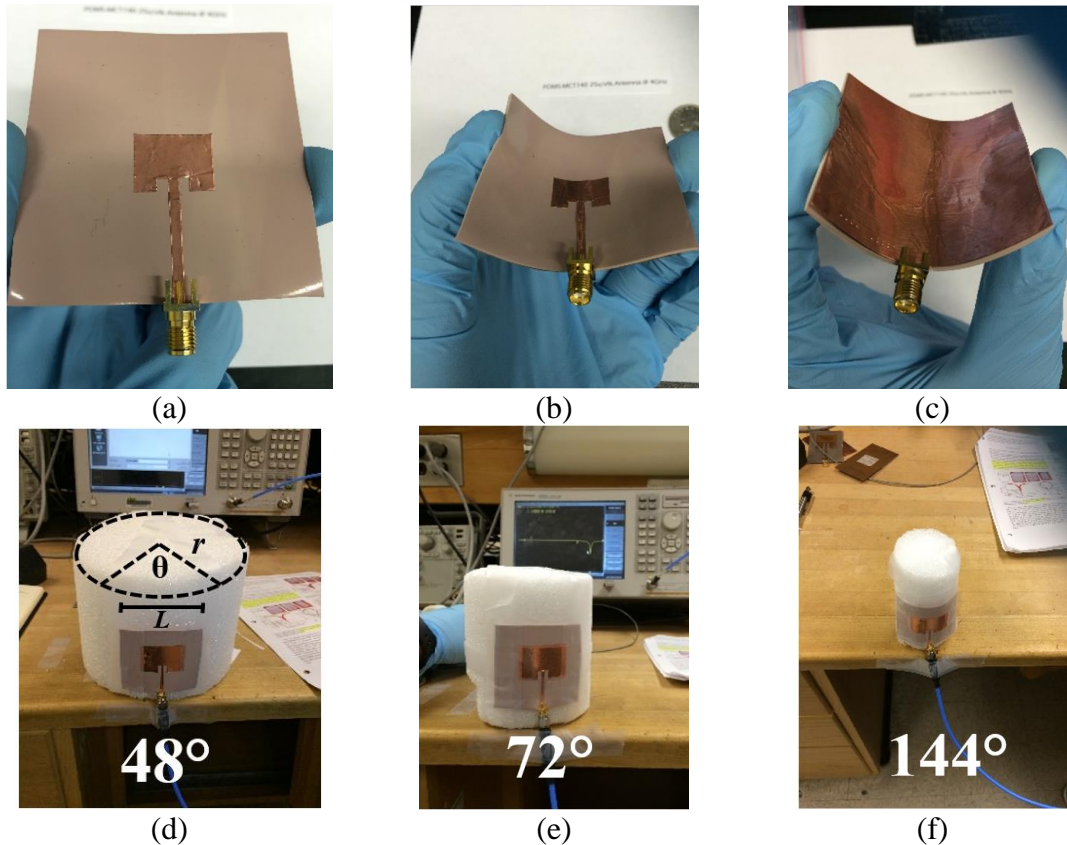


Figure 4.15 – Evaluation of a microstrip patch antenna built over a foldable 37 vol. % PDMS-MgCaTiO<sub>2</sub> composite substrate with 4.2 GHz nominal frequency under stress and bend tests. (a) Unbent antenna. (b) Antenna bent with a positive curvature. (c) Antenna bent with negative curvature. (d) Antenna testing under 48° bending angle. (e) Antenna testing under 72° bending angle. (f) Antenna testing under 144° bending angle.

As expected, the antenna demonstrates a deformation in the ground and top metallization layers, which in turns results in a change of the port impedance together with a shift in the resonance frequency under different bending angles as seen in Figure 4.16. Nevertheless, the flexibility of the high- $k$  composite substrate seems to be well suited for future device developments to conform to an uneven or curved surface.

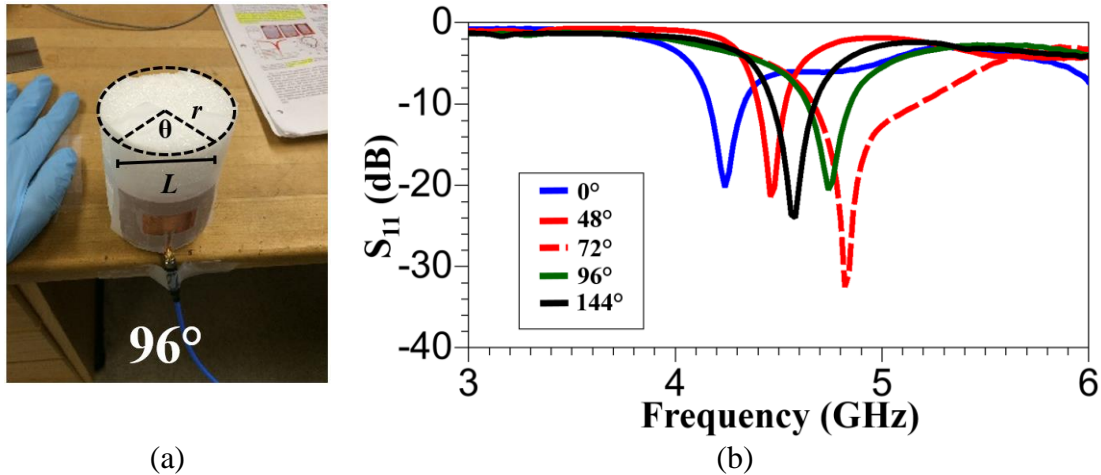


Figure 4.16 – Measured return loss of a flexible 4.2 GHz 37 vol. % PDMS-MgCaTiO<sub>2</sub> patch antenna at different bending angles. (a) Antenna under 96° bending angle. (b) Return losses under the applied bending angles of 0°, 48°, 72°, 96°, and 144°.

As observed in Figure 4.17, the peak realized antenna gain is slightly superior in the 37 vol. % PDMS-MgCaTiO<sub>2</sub> composite substrate when compared with a counterpart antenna designed using pure PDMS material as a substrate due to the lower dielectric losses of the 37 vol. % PDMS-MgCaTiO<sub>2</sub> EM composites.

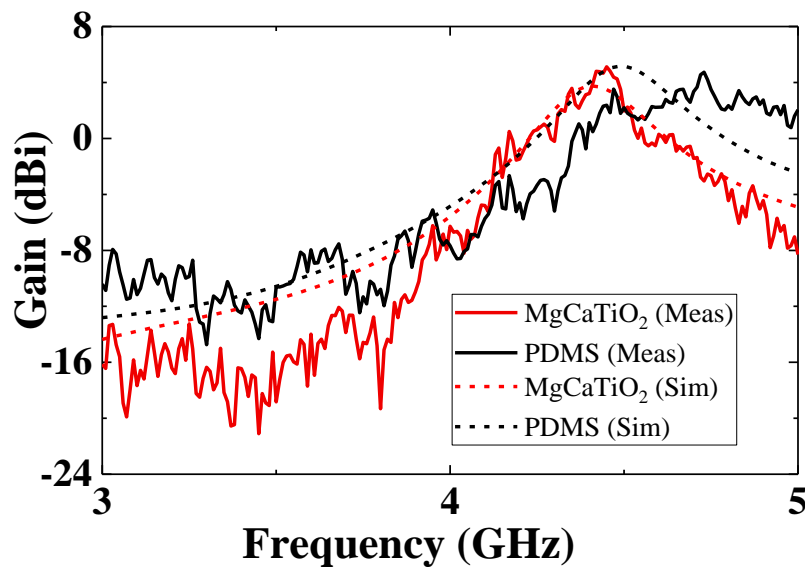


Figure 4.17 – Comparison of measured antenna gain vs. frequency between 4.2 GHz (unbent) patch antenna designed over pure PDMS material and a patch antenna built over a 37 vol. % PDMS-MgCaTiO<sub>2</sub> composite substrate with unsintered fillers.

The dielectric properties of the pure PDMS are shown in Figure 3.15, whereas the measured EM properties of 37 vol. % PDMS-MgCaTiO<sub>2</sub> composites are shown in Figure 4.5. The high-permittivity of the loaded antenna  $\epsilon_r$  of 8.96 (with a refractive index  $n$  of 2.99) is 64 % smaller when compared with the pure PDMS antenna  $\epsilon_r$  of 2.87 (with a refractive index  $n$  of 1.69).

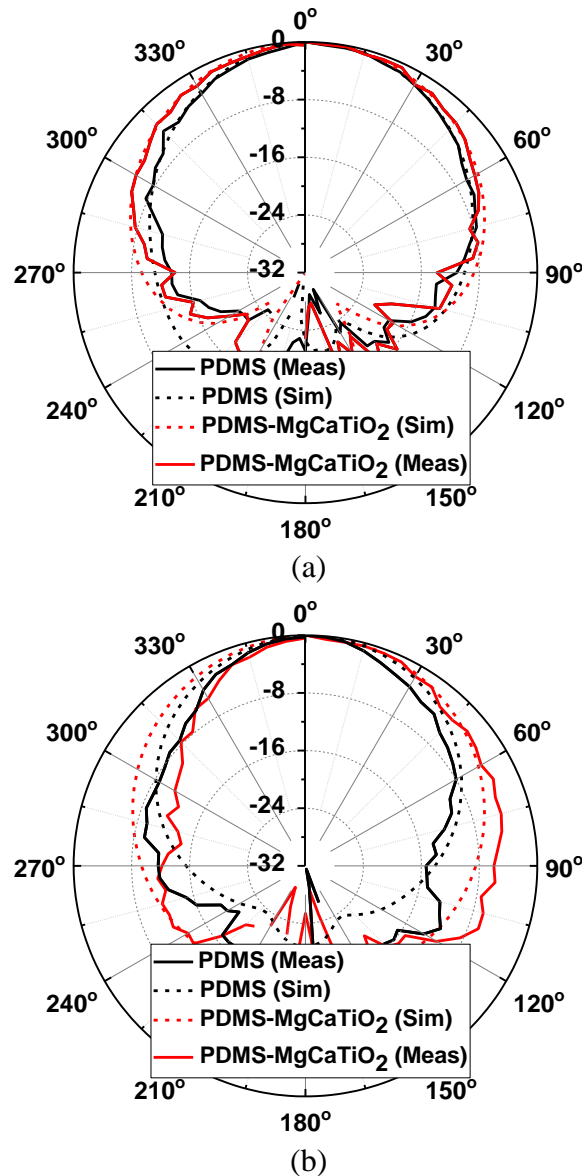


Figure 4.18 – Normalized measured vs. simulated radiation patterns the 4.2 GHz (unbent) patch antennas in (a) H-plane and (b) E-Plane.

The radiation patterns and gain vs. frequency measurements were conducted using an anechoic chamber of dimensions 3.66 m × 7.32 m × 3.66 m (length, width, and height). Figure

4.18 shows the comparison between the measured and simulated normalized H-plane and E-plane radiation patterns for the 4.2 GHz antenna based on 37 vol. % PDMS-MgCaTiO<sub>2</sub> composites that are compared with a pure PDMS antenna. Figure 4.18(a) depicts an excellent agreement in the H-plane characteristics for both antennas. Both antennas exhibit small back lobes which agree with the EM simulations. Figure 4.18(a) shows the comparison between the simulated and measured E-plane radiation patterns, which also agrees with the EM simulations.

#### 4.7 Conclusion

Four different high- $k$  and low-loss polymer-ceramic EM composite materials have been developed by employing a high-temperature sintering process up to 1500°C to further enhance the dielectric and loss properties. 39 vol. % PDMS-Ba<sub>0.55</sub>Sr<sub>0.45</sub>TiO<sub>3</sub> composites loaded with 1340°C sintered fillers have shown a dielectric permittivity ( $\epsilon_r$ ) of 15.02 and a  $\tan \delta_d$  less than 0.042 at frequencies up to 16 GHz. Similarly, 49 vol. % loaded PDMS-Ba<sub>0.55</sub>Sr<sub>0.45</sub>TiO<sub>3</sub> sample has exhibited very stable  $\epsilon_r$  of 23.51 and a  $\tan \delta_d$  lower than 0.047 at frequencies up to 20 GHz. 37 vol. % loaded PDMS-MgCaTiO<sub>2</sub> substrate has shown very stable dielectric permittivity ( $\epsilon_r$ ) of 12.19 and a  $\tan \delta_d$  lower than 0.021 at frequencies up to 20 GHz. Also, a 19.6 GHz patch antenna was successfully demonstrated by 3D printing over a 37 vol. % PDMS-MgCaTiO<sub>2</sub> composite substrate to form the metallization layer by using a CB028 silver paste from DuPont. The printed patch antenna exhibited a measured return loss of 20 dB along with a 10% bandwidth and a simulated gain of 3 dBi and 71% of efficiency. The antenna size is reduced by 80% when compared with a counterpart design based on Rogers RT/duroid® 5880 material. The printed antenna was rigorously compared with reference designs implemented using several state-of-the-art commercial laminates. This new class of mass-producible high- $k$ , low-loss, and bendable polymer composite

materials has already shown some promising attributes for enabling the next generation of 3D conformal RF and microwave devices.

## CHAPTER 5 :

### CERAMIC-THERMOPLASTIC COMPOSITES FOR FDM

#### 5.1 Note to Reader

Portions of this chapter, including figures, have been previously published in [10], [17], [49], and [50], and they have been reproduced with permissions from IEEE Microwave Theory and Techniques Society, the International Microelectronics Assembly and Packaging Society and Microelectronics Foundation. Permissions are included in Appendix A.

#### 5.2 Introduction

A new kind of high-permittivity (high- $k$ ) and low-loss composite material for FDM technology based on a COP thermoplastic matrix embedded with sintered ceramic fillers was developed and characterized up to Ku-band. FDM printed samples made of 30 vol. % COP-MgCaTiO<sub>2</sub> composites, with filler particles sintered at 1200°C, show a  $\epsilon_r$  of 4.82 and a  $\tan \delta_d$  below 0.0018. Meanwhile, 3D-printed samples composed of 25 vol. % COP-Ba<sub>0.55</sub>Sr<sub>0.45</sub>TiO<sub>3</sub> with particles sintered at 1340°C exhibit a  $\epsilon_r$  of 4.92 and a  $\tan \delta_d$  lower than 0.0114. Also, 30 vol. % COP-TiO<sub>2</sub> specimens with filler particles sintered at 1200°C exhibit a  $\epsilon_r$  of 4.78 and a  $\tan \delta_d$  lower than 0.0012, whereas ABS-Ba<sub>0.55</sub>Sr<sub>0.45</sub>TiO<sub>3</sub> specimens with a 6% volume fraction loading of microparticle fillers sintered at 1340°C have demonstrated a  $\epsilon_r$  of 3.98 and a  $\tan \delta_d$  less than 0.0086. Edge-fed microstrip patch antennas operating at 17 GHz were fabricated by a direct digital manufacturing (DDM) approach that combines FDM of EM composites and micro-dispensing for deposition of conductive traces and compared with reference designs implemented using commercial microwave laminates regarding antenna size and performance. Evidently, the newly



developed ceramic-thermoplastic composites are well suited for microwave device applications up to Ku-band and can be adapted to 3D printing technologies.

### 5.3 Experimental Procedure

A detailed analysis is performed to show the dielectric and other physical properties of the low-loss thermoplastics employed for the preparation of microwave EM composites that are compared with other FDM compatible materials reported by the research community in recent years. Aside from the description of the material preparation, an assessment of model predictions of dielectric properties is conducted in Section 5.4.6, and Section 5.4.7. Four models of relative permittivity and one for dielectric loss tangent have been explored. A comparison of the microwave performance up to 17 GHz is presented between the newly developed ceramic-thermoplastic composites and other EM materials reported by the research community as well as commercial microwave materials and laminates in Section 5.5.3. Finally, the design, simulation and testing of antennas based on direct digital manufacturing (DDM) approach [2] that employs FDM and micro-dispensing processes are detailed in the following Chapter 6. The dielectric properties of the ceramic fillers studied in this work are listed in Table 5.1.

Table 5.1 – Vendor-specified dielectric properties of ceramic fillers

<b>High-<i>k</i> Ceramics</b>	$\epsilon_r$	$\tan \delta_d$	<b>Freq.</b>	<b>Material Supplier</b>
MgCaTiO <sub>2</sub>	127	0.0012	6 GHz	Trans Tech Inc.
TiO <sub>2</sub>	96	0.0004	6 GHz	Trans Tech Inc.
Ba <sub>0.55</sub> Sr <sub>0.45</sub> TiO <sub>3</sub>	2367	0.0900	1 MHz	Ferro Corp.

### 5.4 Fabrication of Thermoplastic Composites

#### 5.4.1 Choice of Thermoplastic Matrix and Ceramic Fillers

COP is a type of amorphous thermoplastic polymer, which is widely used for injection molding and conventional machining of optical components. COP has a melting temperature of

about 230°C and a  $T_g$  of 136°C. Also, it is chemically inert to strong acids and solvents, which is superior to other widely used thermoplastics such as ABS.

Table 5.2 – Sintering conditions and densities of ceramic fillers

<b>Ceramic Micro-Fillers</b>	<b>Temp. (°C)</b>	<b>Firing Time (hours)</b>	<b>Tapped Density (g/cm<sup>3</sup>)</b>
MgCaTiO <sub>2</sub>	1100	3	2.17
MgCaTiO <sub>2</sub>	1200	3	1.85
TiO <sub>2</sub>	1100	3	2.09
TiO <sub>2</sub>	1200	3	2.00
Ba <sub>0.55</sub> Sr <sub>0.45</sub> TiO <sub>3</sub>	1340	2	3.14

More importantly, COP also exhibits excellent EM properties with a permittivity of 2.12 and a low  $\tan \delta_d$  lower than 0.0009 up to 17 GHz, which is on par with that of Rogers RT/duroid® 5880 laminates and very likely the lowest loss among thermoplastics. The densities and sintering conditions for ceramic fillers are given in Table 5.2, while a list of previously reported FDM-compatible thermoplastics in comparison with the thermoplastics explored in this work is presented in Table 5.3.

#### 5.4.2 Sintered Ceramics Processing

The high- $k$  ceramic powders were sintered at temperatures up to 1340°C by using a two different furnaces: a HST 12/400 horizontal split, single zone tube furnace (Carbolite, GERO, UK) that operates up to 1200°C, and a KSL 1700X box furnace (MTI Corporation, Richmond, CA) that operates up to 1700°C, to further enhance their dielectric and loss properties as reported previously in [50] and [76]. This sintering process allows us to achieve the highest  $\epsilon_r$  and lowest  $\tan \delta_d$  with the smallest volume fraction of ceramic fillers required for the final EM composites, hence avoiding feedstock filament brittleness. The used sintering conditions and resultant filler densities are listed in Table 5.2. Figure 5.1 shows the SEM photos by using a SU-70 SEM (Hitachi, Ltd, Tokyo, Japan) of two generations of FDM-ready feedstock composites materials made of COP-

MgCaTiO<sub>2</sub> loaded with 25 vol. % and 30 vol. % ceramic fillers sintered for three hours at 1100°C and 1200°C, respectively. Figure 5.2 shows the SEM photos of two generations of COP-TiO<sub>2</sub> composites loaded with 30 vol. % ceramic fillers sintered for three hours at 1200°C.

### 5.4.3 FDM Feedstock Hot Melt Compounding Process

The measured particle tapped densities are 0.55 g/cm<sup>3</sup> for COP ZEONEX® (RS420), 0.602 g/cm<sup>3</sup> for ABS Cynolac™ (MG47), and 0.61 g/cm<sup>3</sup> for ABS448T. The typically tapped density of the ceramic fillers is about 3 to 5 times higher than the density of the thermoplastics used in this work as listed in Table 5.2, hence 30 vol. % was kept as the highest high-*k* filler volume fraction, thus circumventing possible feedstock filament brittleness and high viscosity of the molten composites during the actual FDM (3D-printing) process.

The 30 vol. % COP-MgCaTiO<sub>2</sub> FDM feedstock filament preparation process starts with the re-pulverization of sintered ceramics using an MM 400 mixer mill (Retsch, Haan, Germany) or an XQM-2 high-energy planetary ball milling instrument (Changsha TENCAN powder technology Co., Ltd., China). In some cases, a sieving process is applied to ensure that the maximum particle sizes are below 40 μm as shown in Figure 5.2(a). The COP or ABS thermoplastic matrixes and sintered ceramic particles are then uniformly pre-blended along with a Solplus™ DP310 hyperdispersant (Lubrizol Corporation, Wickliffe, Ohio) by using an ARE-310 planetary centrifugal mixer (THINKY, Tokyo, Japan). Solplus™ DP310 is a 100% active polymeric dispersant, typically used for improved processing in thermoplastic masterbatch and compounding such as improve pigment/filler dispersion and stability in thermoplastics. The 30 vol. % COP-MgCaTiO<sub>2</sub> formulation was prepared by using 10% wt. of dispersant, 59 % wt. of sintered MgCaTiO<sub>2</sub> particles at 1200°C and 30 % wt. of COP, the corresponding volume fractions formulation are 17 vol. % of a dispersant, 30 vol. % of sintered MgCaTiO<sub>2</sub> particles at 1200°C and

53 vol. % of COP. While the 30 vol. % COP-TiO<sub>2</sub> formulation was prepared by using 11% wt. of dispersant, 61 % wt. of sintered TiO<sub>2</sub> particles at 1200°C and 28 % wt. of COP, the corresponding volume fraction formulation are 19 vol. % of a dispersant, 30 vol. % of sintered TiO<sub>2</sub> at 1200°C particles and 51 vol. % of COP. The hot melt compounding process (extrusion) typically is performed by using the melting temperature of the thermoplastic matrix: about 260°C or about 190°C for COP or ABS, respectively, and using an EX2 filament extruder (Filabot, Barre VT, USA) to produce filaments with a diameter of about 2.0 mm. Figure 5.1(a)(b) depicts the SEM photos of 2 generations of newly developed ceramic-thermoplastic filaments, by using different ball milling times based on sintered MgCaTiO<sub>2</sub> fillers at 1100°C and 1200°C for three hours. Figure 5.1(a) depicts a cross-sectional and zoom-in view photos of a 25 vol. % COP-MgCaTiO<sub>2</sub> 1100°C sample with 5 minutes of ball milling, showing an 80 μm sintered MgCaTiO<sub>2</sub> spheres embedded in the COP matrix. Figure 5.1(b) depicts a 30 vol. % COP-MgCaTiO<sub>2</sub> 1200°C sample with a 24 hour of high-energy milling time, showing significantly improved average particle size distribution of 10 μm.

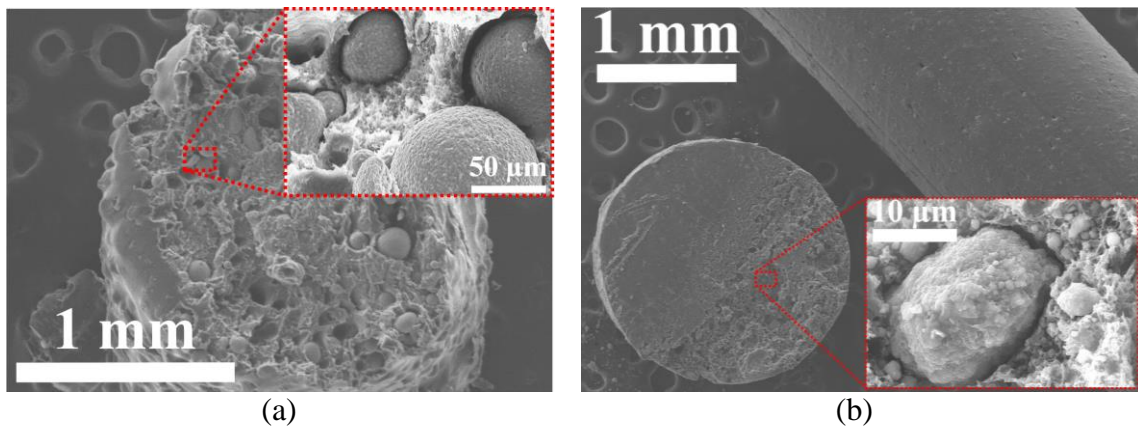


Figure 5.1 – SEM photos of two generations of newly developed ceramic-thermoplastic filaments, by using different ball milling times and with fillers sintered at 1100°C and 1200°C for three hours. Including cross-sectional and zoom-in view photos. (a) A 25 vol. % COP-MgCaTiO<sub>2</sub> 1100°C sample with 5 minutes of ball milling. (b) A 30 vol. % COP-MgCaTiO<sub>2</sub> 1200°C sample with 24 hours of high-energy milling time.

#### 5.4.4 Particle Size Analysis of Sintered High-*k* Ceramic Fillers

The nanoparticle size analysis was performed by using a Zetasizer Nano-S dynamic light scattering system (Malvern Instruments, Malvern, Worcestershire, UK) for re-pulverized TiO<sub>2</sub> particles sintered at 1200°C. The high-energy ball milling process was performed by using an XQM-2 high-energy ball mill (Changsha TENCAN powder technology Co., Ltd., China). The comparison of different high-energy ball milling times vs. size distribution is shown in Figure 5.3. It is worthwhile mentioning that the improved average particle size distribution with a mean particle size of 1300 nm was measured after a 24 hours ball milling process. Hence, 24 hours was kept as a high-energy ball milling time to standardize the particle size distribution as close as possible to 2000 nm (2 μm) with all the ceramic fillers used in this dissertation as shown in Figure 5.3(e). It is important to mention that the achieved particle size distribution and average particle size strongly depends on the type of sintered particles. For instance, an average MgCaTiO<sub>2</sub> particle size of about 18 μm was observed after a 24 hours of ball milling time, as shown in Figure 5.5(a).

Figure 5.2 depicts the SEM photos of 2 generations of newly developed FDM-ready ceramic-thermoplastic filaments based on sintered TiO<sub>2</sub> fillers at 1100°C and 1200°C for three hours, by using different ball milling times. Figure 5.1(a) depicts a cross-sectional and zoom-in view photos of a 30 vol. % COP-TiO<sub>2</sub> 1100°C sample after 5 minutes of ball milling process, followed by filtering with a 50 μm sieve. Figure 5.2(b) presents a 30 vol. % COP-TiO<sub>2</sub> filament with 1200°C sintered fillers treated by a 24 hours of high-energy milling process, showing an average particle size of 1.3 μm.

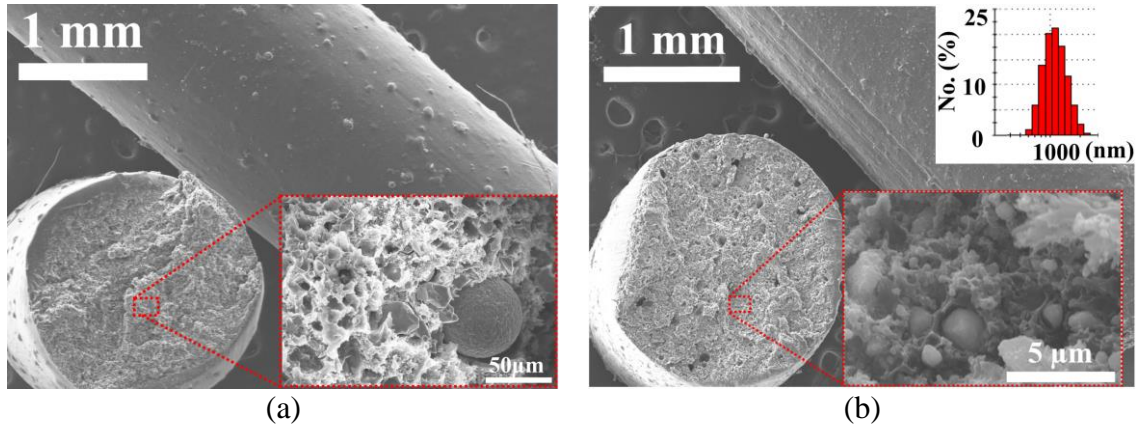
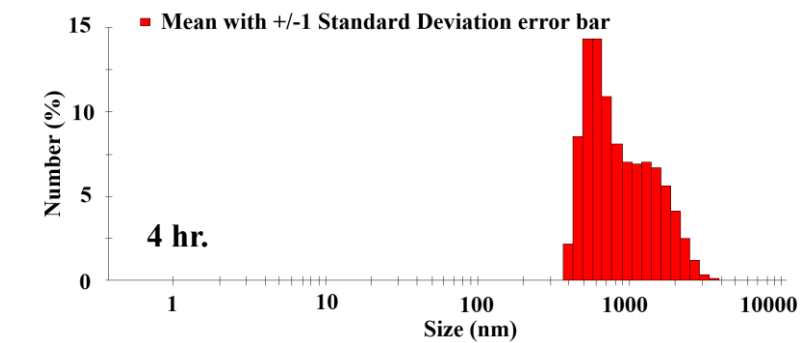
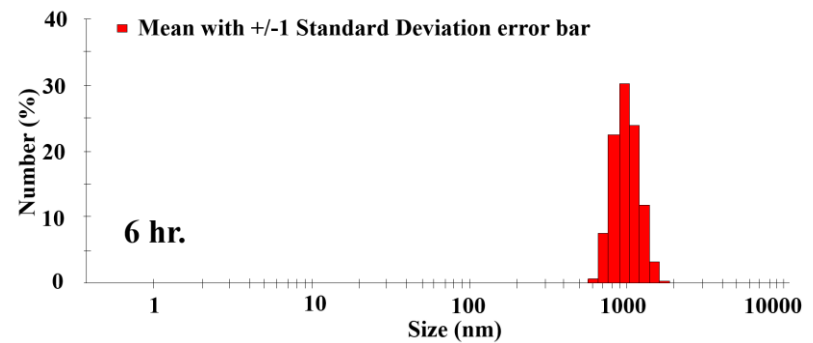


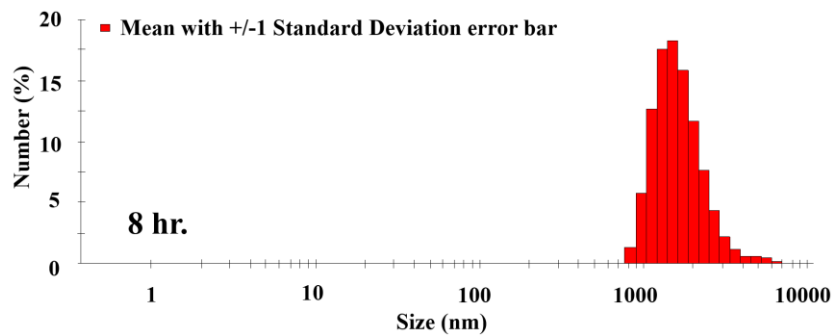
Figure 5.2 – SEM photos of two generations of newly developed ceramic-thermoplastic filaments based on a 30 vol. % COP-TiO<sub>2</sub>, by using different ball milling times and with fillers sintered at 1100°C and 1200°C for three hours. Including cross-sectional and zoom-in view photos. (a) 1100°C sample with 5 minutes of ball milling and a 50 μm sieving process. (b) 1200°C sample with 24 hours of high-energy milling time.



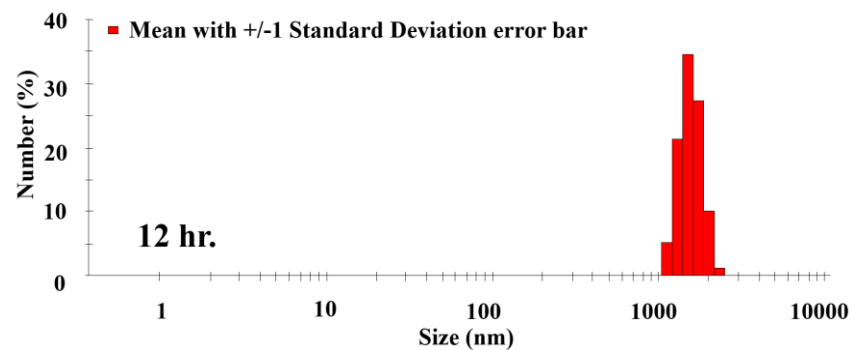
(a)



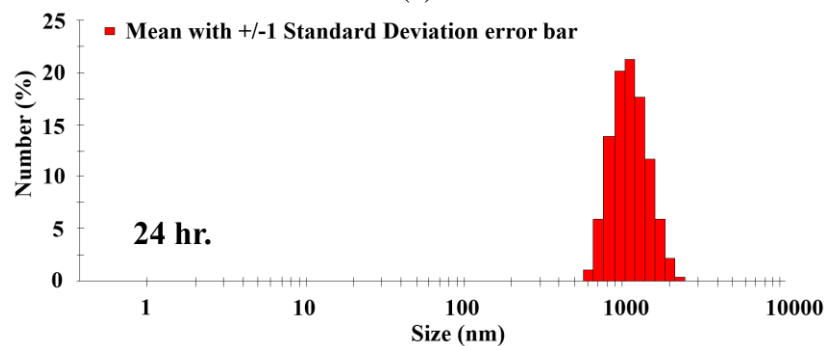
(b)



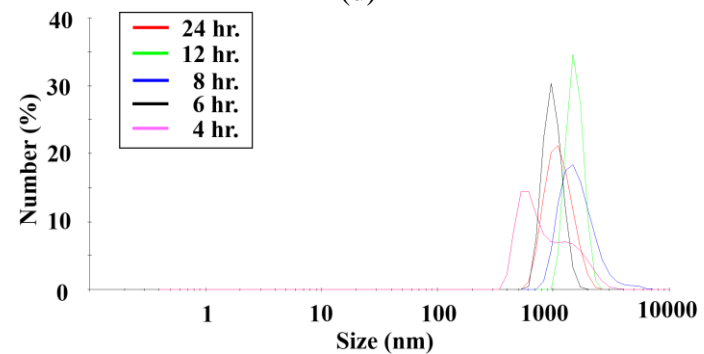
(c)



(d)



(e)



(f)

Figure 5.3 – Size distribution by number/percentage (%) of 1200°C sintered TiO<sub>2</sub> particles post-processed by different high-energy ball milling times. (a) 4 hours. (b) 6 hours. (c) 8 hours. (d) 12 hours. (e) 24 hours. (f) comparison of all milling times.



### 5.4.5 FDM 3D-Printing Process of Ceramic-Thermoplastic Composites

The FDM-ready feedstock composites were 3D-printed by using a tabletop 3Dn 3D-printer (nScript, Orlando, FL) by following a fused deposition modeling (FDM) process. The 3D-printer is equipped with a device known as nFD™, which is driven by a high-precision computer controlled system that allows deposition of thermoplastic composite materials at XYZ coordinated locations. A 1.8 mm diameter FDM feedstock material composed 30 vol. % COP-MgCaTiO<sub>2</sub> with fillers sintered at 1200°C for three hours was 3D-printed by setting the nozzle heater at 290°C and using a nozzle tip known as ceramic nTIPT™ with 325 μm inner diameter and 425 μm outer diameter. The 3D-printer base plate (also called bed) was heated at 170°C. This 3D-printing setting to result in a first layer thickness of 0.2 mm, an extrusion multiplier of 0.9, and a printing speed of 7 mm/s. A printing speed lower than 10 mm/s is recommended to avoid filament feedstock breakage for filler loaded feedstock materials.

Figure 5.4 shows a surface SEM images of a 3D-printed specimen. Figure 5.4(a) shows a sample made of 30 vol. % COP-TiO<sub>2</sub> thermoplastic composites with a measured surface roughness of about 25 μm as shown in Figure 5.6. Figure 5.4(b) presents a specimen made of 25 vol. % COP-MgCaTiO<sub>2</sub> thermoplastic composites showing one of the embedded MgCaTiO<sub>2</sub> microspheres.

Figure 5.5 depicts a cross-sectional EDS mapping study over a 25 μm<sup>2</sup> area of an FDM-printed 30 vol. % COP-MgCaTiO<sub>2</sub> specimen prepared by a metallographic specimen preparation process. The sample was sputter coated with a 20 nm of gold/palladium (Au/Pd) metal alloy. The mapping was performed by using an S-800 field emission scanning electron microscope (FE-SEM) (Hitachi Ltd., Tokyo, Japan) equipped with an EDS system (EDAX Inc., Mahwah, NJ). Figure 5.5(a) was taken by using an SU-70 SEM (Hitachi, Ltd, Tokyo, Japan). As shown, the ceramic particles with an average particle size of 18 μm and some agglomeration in the form of micro-



spheres were observed. Figure 5.5(f) shows the corresponding EDS spectrum of the mapped area through a semi-quantitative analysis of the elements. As seen in Figure 5.5(e) and Figure 5.5(f), Ti molecule shows the highest weight percentage wt. % in the mapped area.

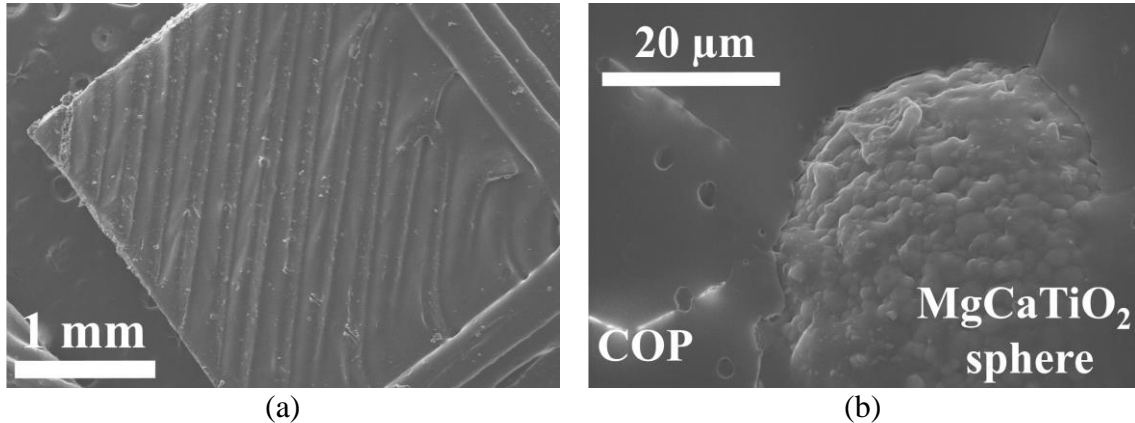


Figure 5.4 – SEM surface view photos of 3D-printed specimens: including (a) an FDM printed 30 vol. % COP-TiO<sub>2</sub> thin-sheet with filters sintered 1100°C. (b) An FDM printed 25 vol. % COP-MgCaTiO<sub>2</sub> thin-sheet with fillers sintered at 1100°C. The relatively large particle agglomerate was found due to the short (<20 mins) of ball milling time.

### 3D-printed 300 $\mu\text{m}$ Substrate

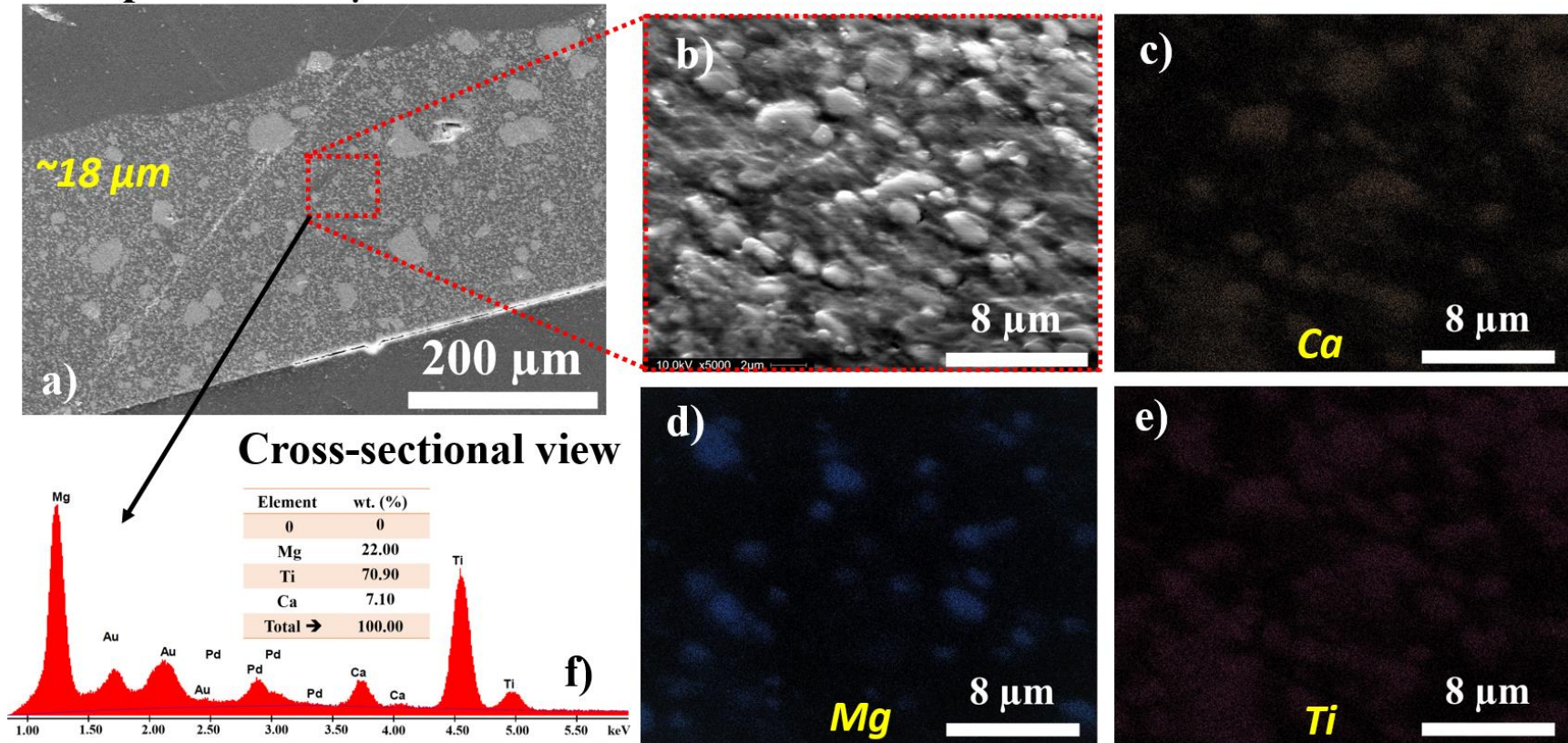


Figure 5.5 – Energy dispersive spectroscopy (EDS) mapping taken over a  $24 \mu\text{m}^2$  area of the FDM-printed EM composite made of 30 vol. % COP-MgCaTiO<sub>2</sub> with fillers sintered at 1200°C. (a) Cross-sectional SEM photo of the 300  $\mu\text{m}$ -thick FDM-printed specimen. (b) Zoom-in view over a  $24 \mu\text{m}^2$  area showing the MgCaTiO<sub>2</sub> grains in the polymer matrix. (c) wt. % the Ca element in the composite. (d) wt. % the Mg element in the composite. (e) wt. % the Ti element in the composite. (f) Corresponding EDS spectrum of scanned area.

Figure 5.6 depicts the 2D surface profile measurements of 3D-printed specimens based on  $\text{TiO}_2$  and  $\text{MgCaTiO}_2$  composites by using a Dektak D-150 profiler (Veeco, Plainview, NY). Figure 5.6 presents the comparison of the measured surface roughness of the two sides of a 3D-printed 30 vol. % COP- $\text{MgCaTiO}_2$  composite thin-sheet specimen. The bottom side, which is in contact with the heated printer bed during the FDM printing process, shows a measured average-step-height (ASH) of  $2.33 \mu\text{m}$ . On the contrary, the top side that is directed printed underneath the FDM nozzle shows a measured roughness or ASH of  $23 \mu\text{m}$ . For a 30 vol. % COP- $\text{TiO}_2$  composite specimen that was hot-compressed by using a heated hydraulic press at  $130^\circ\text{C}$  (slightly above the glass-transition temperature), the roughness or ASH was reduced down to  $1 \mu\text{m}$  or so.

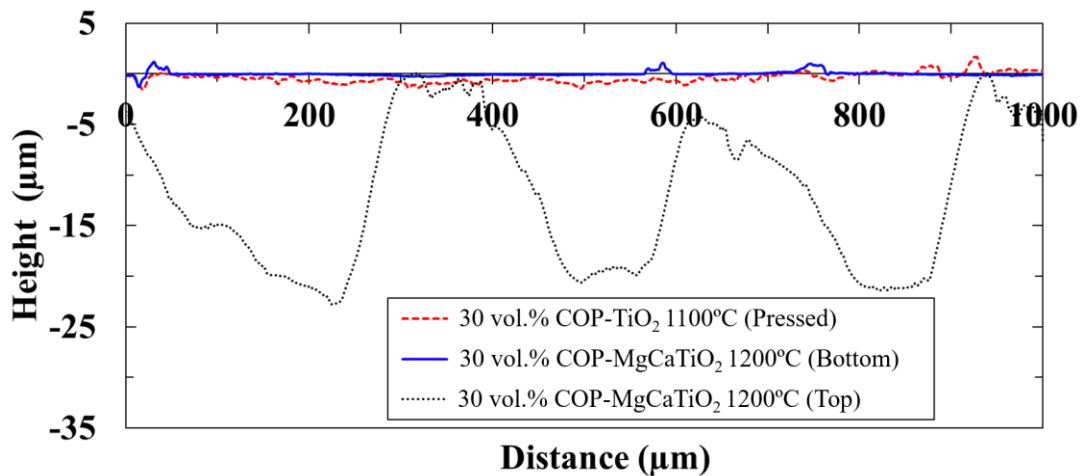


Figure 5.6 – Scanned 2D surface profiles of FDM 3D-printed thin-sheet samples made of 30 vol. % COP- $\text{MgCaTiO}_2$  composites under different processing conditions.

Figure 5.7 shows the 3D schematic-view surface profiles (bottom side) of FDM printed thin-sheet samples taken by a Dimension 3100 atomic force microscope (AFM) instrument. Figure 5.7(a) presents the AFM-scanned profile of a 25 vol. % COP- $\text{MgCaTiO}_2$  composite based thin-sheet specimen with an average roughness value of  $880 \text{ nm}$  over a  $50 \mu\text{m} \times 50 \mu\text{m}$  area for the

bottom side but a much higher average roughness of  $23\ \mu\text{m}$  for the direct printed front side. Figure 5.7(b) depicts an FDM-printed pure (unloaded) COP thin-sheet specimen with a mean roughness of  $440\ \text{nm}$  across a  $50\ \mu\text{m} \times 50\ \mu\text{m}$  area for the bottom side that is in contact with the heated bed and an average roughness of  $25\ \mu\text{m}$  for the printed top side. The average roughness depends on the inner diameter of the FDM nozzle orifice used during the 3D-printing process.

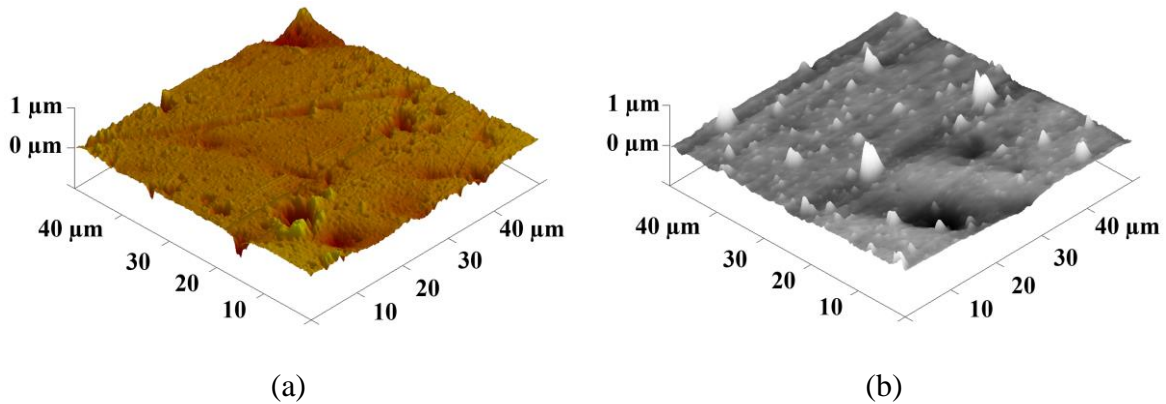


Figure 5.7 – AFM Schematic-view scanned (bottom side) surface profiles<sup>1</sup> of (a) a 25 vol. % COP-MgCaTiO<sub>2</sub> thin-sheet specimen [50] © IMAPS 2015. (b) A pure COP specimen [17], © IEEE 2017. See permissions in Appendix A.

#### 5.4.6 Models for Effective Permittivity

The models described in Chapter 3 were used to evaluate the model prediction accuracy against the measured relative dielectric permittivity for all FDM-ready composites. As depicted in Figure 5.8, the Hanai-Bruggeman model based on Equation (3.21) predicts the dielectric permittivity more accurately than the other models. For instance, the measured dielectric permittivity of 25 vol. % COP-Ba<sub>0.55</sub>Sr<sub>0.45</sub>TiO<sub>3</sub> composites matches well with the model predicted value with less than 2% deviation, while model predictions for 25 vol.% COP-MgCaTiO<sub>2</sub> composites and 30 vol. % COP-TiO<sub>2</sub> composites exhibit discrepancies less than 1% and 6%, respectively.

<sup>1</sup> These AFM images were published in [17], [50]. See permissions in Appendix A.

Meanwhile, the Maxwell model based on Equation (3.23) predicts the permittivities of 25 vol. % COP-Ba<sub>0.55</sub>Sr<sub>0.45</sub>TiO<sub>3</sub> composites, 25 vol. % COP-MgCaTiO<sub>2</sub> composites, and 30 vol. % COP-TiO<sub>2</sub> composites, with less than 4%, 5%, and 1.3% deviation as compared to the measured properties, respectively. On the other hand, the Rayleigh model based on Equation (3.20) leads to slightly less accurate predictions for the 25 vol. % COP-Ba<sub>0.55</sub>Sr<sub>0.45</sub>TiO<sub>3</sub> composites, 25 vol. % COP-MgCaTiO<sub>2</sub> composites, and 30 vol. % COP-TiO<sub>2</sub> composites, with discrepancies of 13%, 13.5%, and 7.2%, respectively, when compared with actual measured properties.

Table 5.3 – Properties of FDM-compatible materials from this work compared with other works<sup>2</sup>

Thermoplastic	Material	Vendor	$T_g$ (°C)	Melting Temp. (°C)	Freq. (GHz)	$\epsilon_r$	$\tan \delta_a$	Ref.
ABS	(ABS)	N/A	N/A	216-260	15	2.65	0.0048	[74]
Polypropylene	(PP)	N/A	-14	176	15	2.25	0.0003	[74]
Polylactic Acid	(PLA)	N/A	60	170	N/A	3.10	0.0100	[77]
ULTEM™ (9085)	(PEI)		186	350-400	MHz	3.00	0.0027	
Polycarbonate	(PC)		161	225	N/A	2.80	0.0005	[78]
ABS-M30™	(ABS)	Stratasys, Ltd.	108	216-260		2.60	0.0048	
Polycarbonate-ABS	(PC-ABS)		125	N/A	N/A	2.90	0.0035	Stratasys, Ltd.
Polyphenylsulfone	(PPSF/PPSU)		230	N/A		3.20	0.0015	
ULTEM™ (1000) ‡	(PEI)	SABIC	217	350-400		2.27	0.0121	
Cyclocac™ (MG47) ‡	(ABS)	SABIC	100	216-260		2.37	0.0055	
ABS448T‡	(ABS)	Star Prime™ Resins	N/A	216-260	17	2.10	0.0077	<b>This Work</b>
ZEONEX® (RS420) ‡						2.12	0.0009	
ZEONOR® (1420R) ‡	(COP)	ZEON Corp.	136	250-300		2.15	0.0016	
ZEONEX® (RS420-LDS) ‡						2.26	0.0011	
ABS White	(ABS)	Ultimachine	100	216-260		2.18	0.0062	

Note: ‡ All the samples were 3D-printed by FDM with in-house prepared feedstock filaments.

<sup>2</sup> ZEONEX® and ZEONOR® are registered trademarks of ZEON CORPORATION. Permissions in Appendix A.



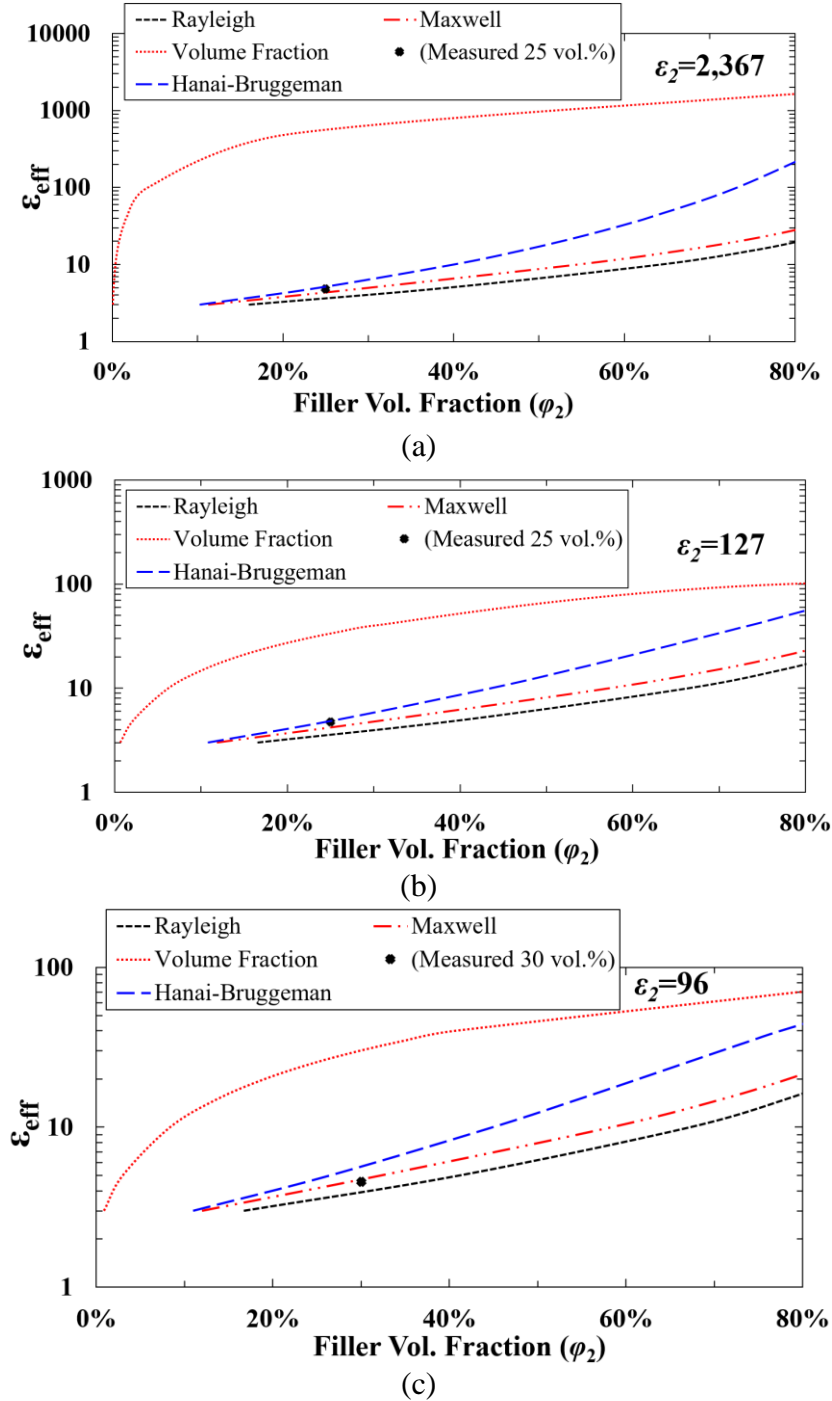


Figure 5.8 – Comparison of model-predicted permittivity of COP-based composites embedded with different fillers at varied volume fractions based on Equations (3.20)-(3.23). (a) COP-Ba<sub>0.55</sub>Sr<sub>0.45</sub>TiO<sub>3</sub> composites with fillers sintered at 1340°C. (b) COP-MgCaTiO<sub>2</sub> composites with fillers sintered at 1100°C. (c) COP-TiO<sub>2</sub> composites with fillers sintered at 1100°C, which are compared with measured properties of the corresponding 25 vol. % and 30 vol. % composites.

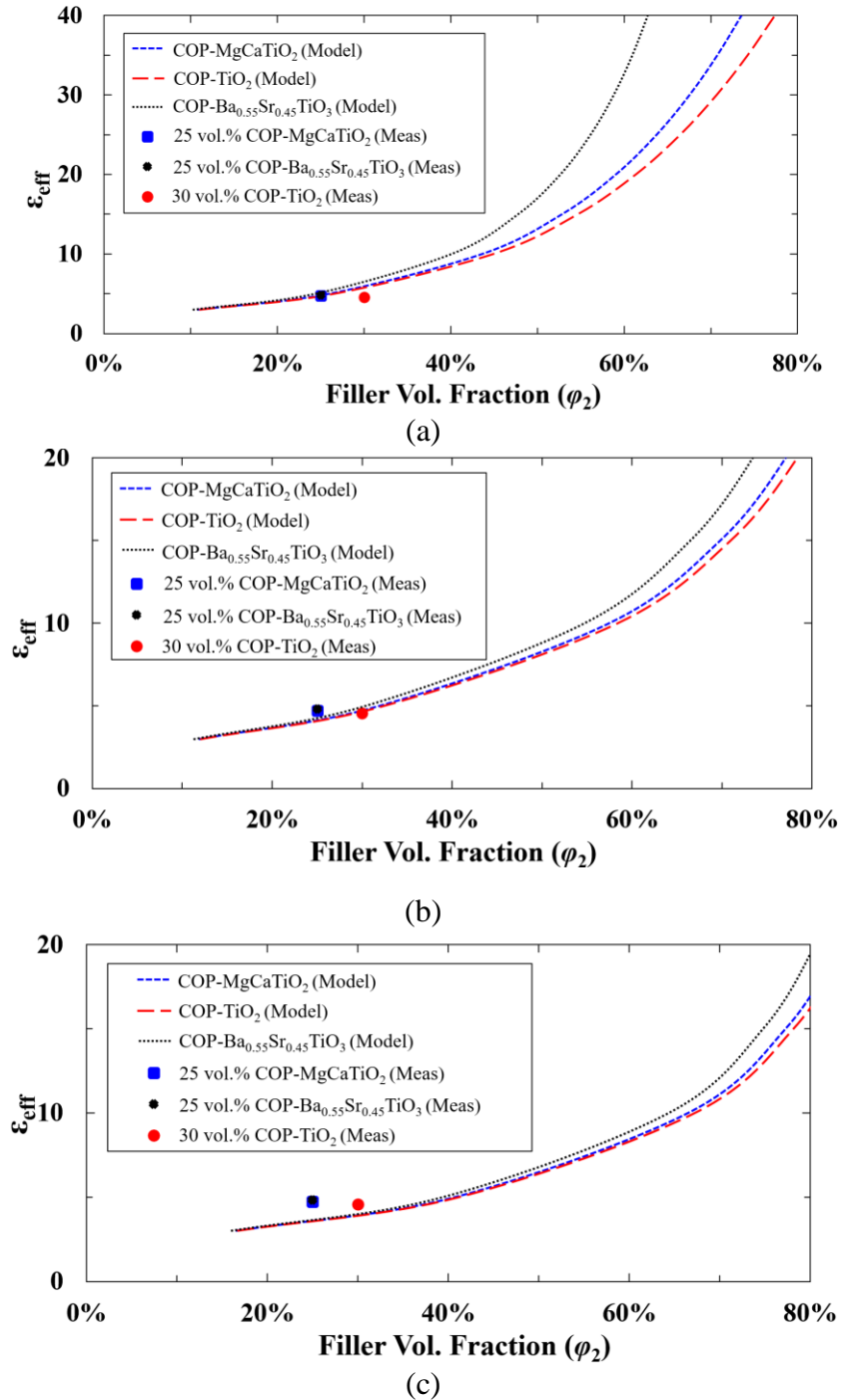


Figure 5.9 – The effective permittivity predicted by the models based on Equations (3.20), (3.21), (3.23). (a) Hanai-Bruggeman model. (b) Maxwell model. (c) Rayleigh model. They are compared with the measured results at 6 GHz for COP-based composites loaded with several sintered ceramic fillers, such as COP-Ba<sub>0.55</sub>Sr<sub>0.45</sub>TiO<sub>3</sub> with fillers sintered at 1340°C, COP-MgCaTiO<sub>2</sub> and COP-TiO<sub>2</sub> composites with ceramic fillers sintered at 1100°C.



As evidenced by Figure 5.8 and Figure 5.9, the Hanai-Bruggeman model Equation (3.21) and Maxwell model Equation (3.23) are well-suited for the prediction of relative dielectric permittivities of EM composites with high- $k$  filler volume ratios between 25 vol. % and 30 vol. %. Hanai-Bruggeman model it is expected to be an accurate model for filler volume fractions  $\varphi_2$  of 50 %, with the limitation that the dispersed inorganic ceramic particles do not form a percolative path throughout the medium as reported by Dang *et al.* [26]. The simple volume fraction model Equation (3.22) is designed for composites made of two media in a parallel combination as reported by Yoon *et al.* [69] and Raju [63]. The volume fraction model based on Equation (3.22) is known to be inaccurate for assessing the relative permittivities of polymer composites with uniformly dispersed ceramic filler particles (Figure 5.1) as also seen in Figure 5.8. Figure 5.9 shows the three most accurate models compared to the measured permittivities for the composites with sintered ceramic fillers at different volume fractions. As depicted in Figure 5.9(a) and Figure 5.9(b), the Hanai-Bruggeman model and Maxwell model both show good accuracy with less than 6% discrepancy when compared with measured properties of the EM composite materials.

#### **5.4.7 Model Prediction of the Dielectric Loss Tangent in FDM Composites**

The dielectric loss tangent ( $\tan \delta_d$ ) is the ratio between the imaginary and real parts of the complex permittivity given by Equation (3.19). The effective dielectric loss tangent of a two component mixture with corresponding loss tangents of  $\tan \delta_{d1}$  and  $\tan \delta_{d2}$  is given by Equation (3.31) reported by Raju [63].

Figure 5.10 shows the comparison between the measured versus model predicted dielectric losses by Equation (3.31) of two types of  $\text{TiO}_2$  and  $\text{MgCaTiO}_2$  based two-component composites. The model predictions show a maximum discrepancy of 45% and 34% for the 25 vol. % COP-

MgCaTiO<sub>2</sub> composites and the 30 vol. % COP-TiO<sub>2</sub> composites, respectively, this can be ascribed to other major loss mechanisms (e.g., dispersion losses) that are not accounted for.

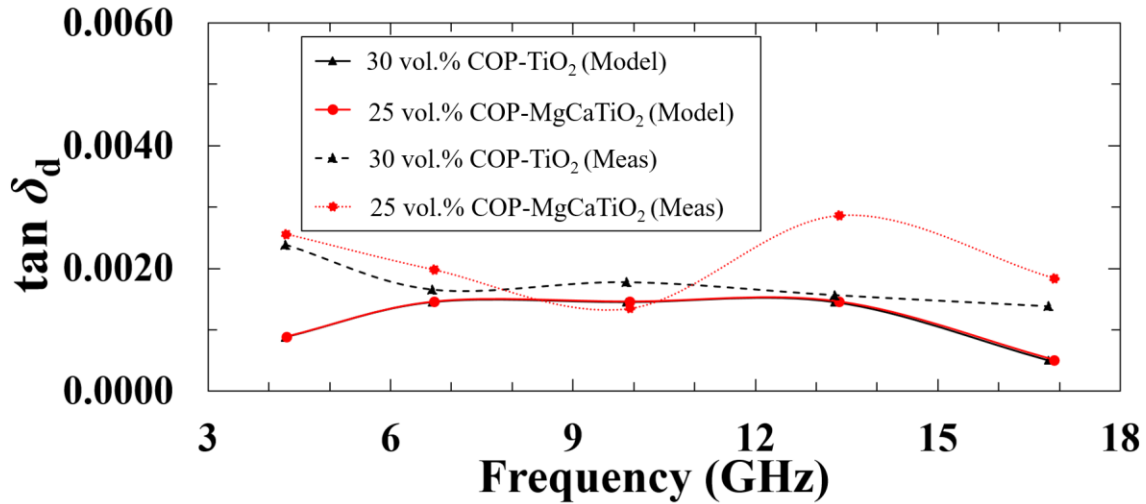


Figure 5.10 – Comparison of the model-predicted and measured dielectric loss tangents for two types of composites. (i.e., 25 vol. % COP-MgCaTiO<sub>2</sub> and 30 vol. % COP-TiO<sub>2</sub>), both composites loaded with ceramic fillers sintered at 1100°C.

#### 5.4.8 Thin-Sheet Specimen Dielectric Characterization

The dielectric properties of 3D-printed thin-sheet specimens composed of COP, ABS, ULTEM™ resin, and a high-*k* filler loaded composites were prepared by an FDM process and assessed at microwave frequencies by using cavity resonator test fixtures from Damaskos Inc. and an 8720ES vector network analyzer from Keysight Technologies. The Damaskos 125HC test fixture operating in the transverse electromagnetic (TEM) mode covers the low-frequency band of 0.4 to 4.4 GHz, while the model 015 test fixture that works in the transverse electric (TE) mode covers the high-frequency band of 6.2 GHz to 19.4 GHz. These cavity resonator testers operate upon the cavity perturbation theory, from which the complex permittivity can be extracted by the resonant frequency shift and variation of *Q* factor of a rectangular cavity due to the impact of an inserted thin-sheet sample. Equation (3.15) - Equation (3.19) are used to calculate the loss tangent

and the complex permittivity [49], [57], [59]. Once the complex permittivity of the material under test is calculated, then the dielectric loss tangent can be determined by using Equation (3.19).

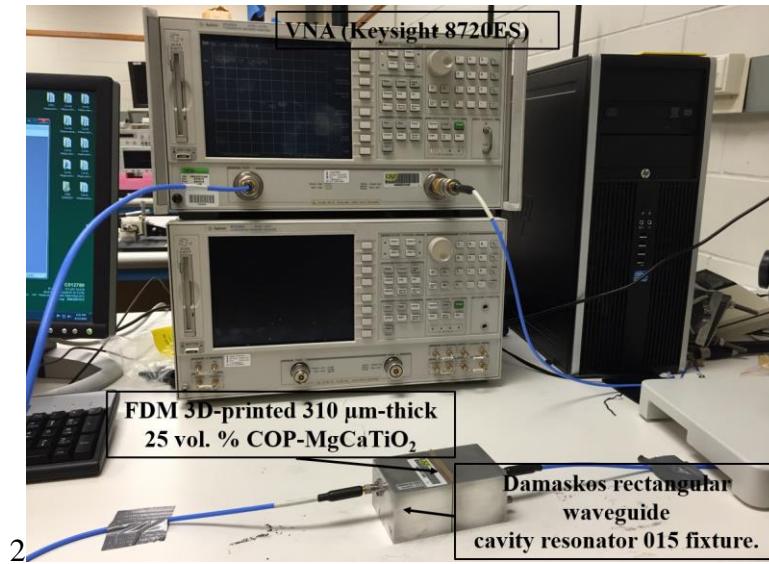


Figure 5.11 – RF dielectric/loss properties characterization setup based upon the cavity perturbation technique for 3D-printed 310 μm-thick specimens.

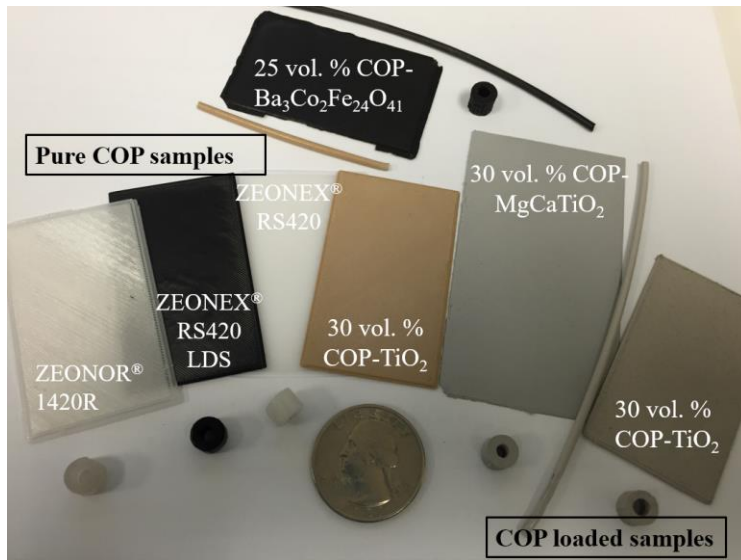


Figure 5.12 – Loaded and unloaded FDM-printed samples and filaments using pure COP and COP composites. Including; ZEONEX® RS420-LDS (black), ZEONOR® 1420R (Clear), ZEONEX® RS420 (white) and COP loaded with sintered fillers, such as TiO<sub>2</sub> (brown) and MgCaTiO<sub>2</sub> fillers (gray), etc.

Figure 5.11 depicts the cavity resonator measurement setup for the extraction of complex permittivity by using a Damaskos 015 cavity resonator based test fixture. Figure 5.12 shows some of the 3D-printed thin-sheet and cylindrical O-ring specimens based on COP (ZEONEX® RS420) loaded with several types of sintered ceramic fillers. The thin-sheet specimens of 5 cm × 3 cm × 0.5 mm are prepared by an FDM process for characterization by the cavity resonator fixtures.

## **5.5 Measured Properties of FDM-Printed Samples**

### **5.5.1 Measured Dielectric Properties of Pure Thermoplastics and Ceramic-Thermoplastic Composite Materials**

Figure 5.13 presents the measured dielectric and loss properties of three types of COP thermoplastics as compared with Cycolac™ MG47 (ABS), which is another widely used FDM-compatible thermoplastic. As observed, the relative permittivities of these COP materials are roughly 2.2 with a very low dielectric loss of 0.0009. Cycolac™ MG47 (ABS) exhibits five times higher dielectric losses. In this study, ZEONEX® RS420 with the lowest dielectric loss was chosen as the base polymer matrix to develop EM composites as FDM-ready feedstock materials.

Figure 5.14 presents the measured EM performance of COP as compared with those widely used FDM thermoplastics and Rogers RT/duroid® 5880 laminate. It is worthwhile mentioning that the intrinsic performance characteristics of COP are on par or better than all other samples.

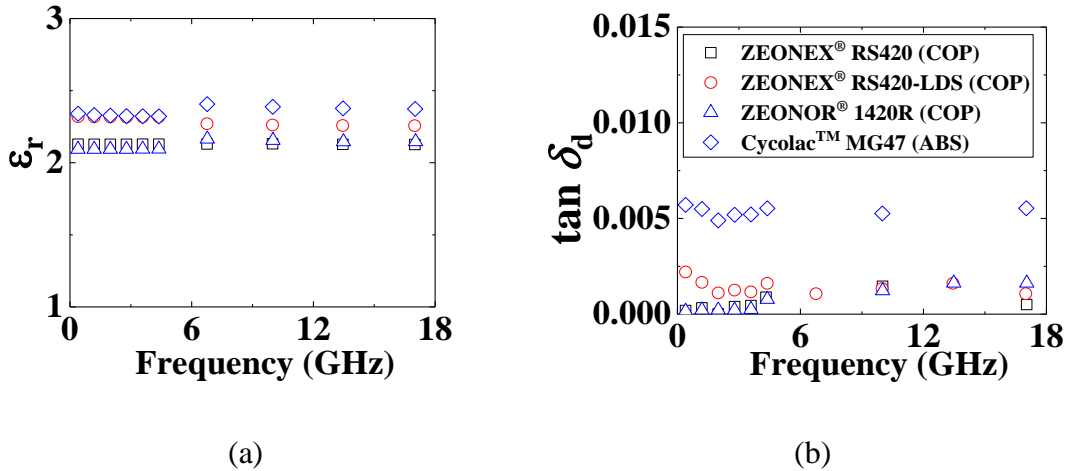


Figure 5.13 – Measured dielectric properties of three versions of cyclo-olefin polymer, such as ZEONEX<sup>®</sup> RS420, ZEONEX<sup>®</sup> RS420-LDS and ZEONOR<sup>®</sup> 1420R, compared to Cyclocac<sup>™</sup> MG47 ABS. (a) Relative dielectric permittivity. (b) Dielectric loss tangent.

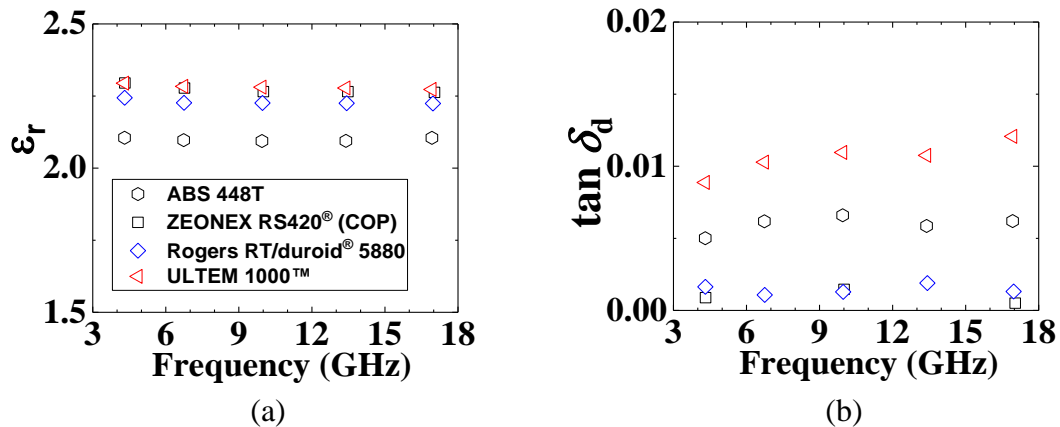


Figure 5.14 – Comparison of measured high-frequency dielectric and loss properties of pure COP (ZEONEX<sup>®</sup> RS420) versus other FDM thermoplastics and a low-loss RF laminate (RT/duroid<sup>®</sup> 5880). (a) Relative permittivity. (b) Dielectric losses.

As depicted in Figure 5.15, 30 vol. % COP-TiO<sub>2</sub> composites with fillers sintered at 1100°C have exhibited a  $\epsilon_r$  of 4.57 and a loss tangent lower than 0.0014 at frequencies up to 17 GHz. Meanwhile, 25 vol. % COP-MgCaTiO<sub>2</sub> composites with MgCaTiO<sub>2</sub> fillers sintered at 1100°C have exhibited a dielectric permittivity  $\epsilon_r$  of 4.74 and a low dielectric loss tangent  $\tan \delta_d$  below 0.0018 as can be seen in Figure 5.15.

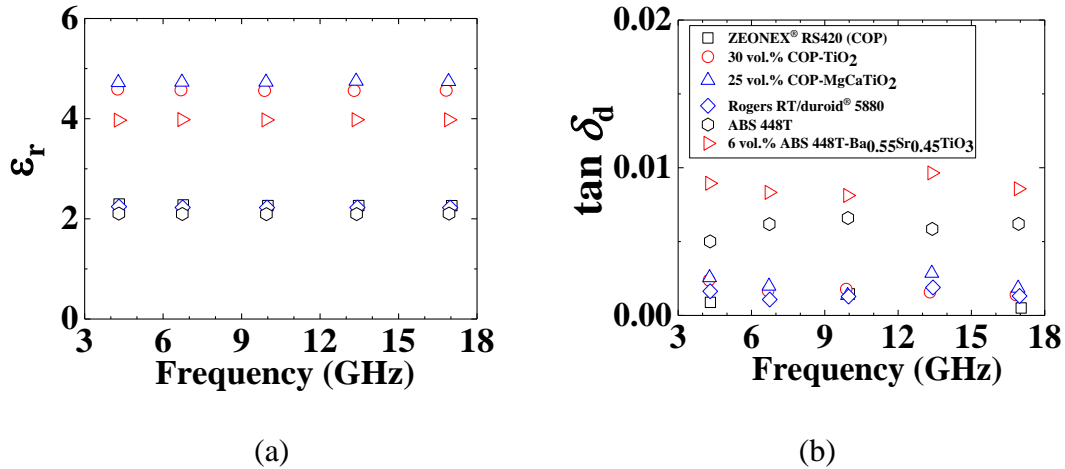


Figure 5.15 – Comparison of the measured dielectric properties of ZEONEX® RS420 COP-based composites loaded with high- $k$  fillers sintered at 1100°C versus ABS composites with fillers sintered at 1340°C and other composites. (a) Relative dielectric permittivity. (b) Dielectric loss tangent.

Figure 5.16 shows a comparison between measured permittivity and model-estimated permittivity over frequency by the Maxwell model based on Equation (3.23), showing less than 7.7%, 7.2% and 6.4% discrepancy for the 30 vol. % COP-TiO<sub>2</sub> composites, the 25 vol. % COP-MgCaTiO<sub>2</sub> composites, and the 25 vol. % COP-Ba<sub>0.55</sub>Sr<sub>0.45</sub>TiO<sub>3</sub> composites, respectively. Meanwhile, Figure 5.16(b) depicts the estimated relative dielectric permittivity by the Hanai-Bruggeman model in Equation (3.21) that shows a much better accuracy with no more than 1% discrepancy for the COP-Ba<sub>0.55</sub>Sr<sub>0.45</sub>TiO<sub>3</sub> composites.

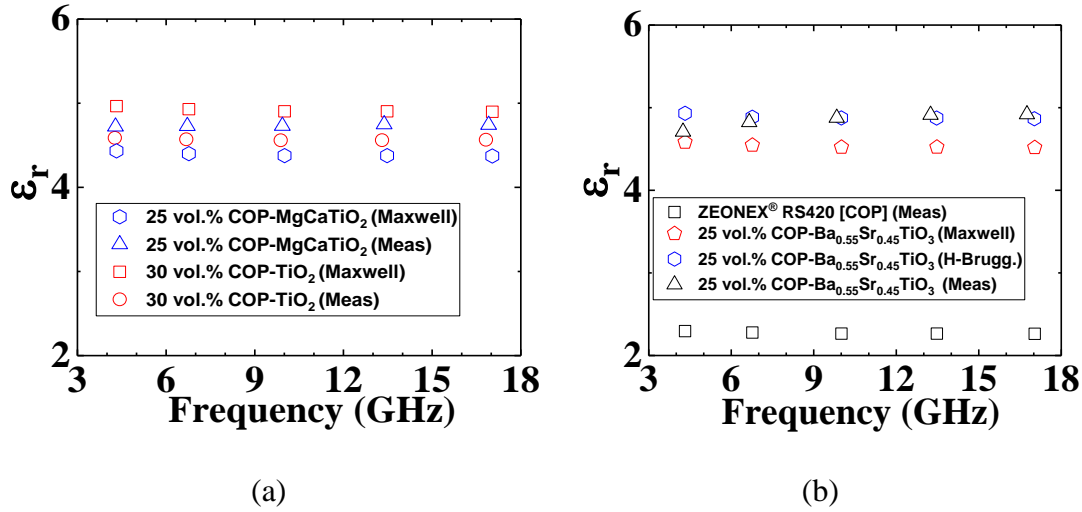


Figure 5.16 – Comparison of measured and model-estimated permittivity by the Maxwell and Hanai-Bruggeman models in Equation (3.23) and Equation (3.21). (a) 25 vol. % COP-MgCaTiO<sub>2</sub> and 30 vol. % COP-TiO<sub>2</sub> composites with fillers sintered at 1100°C. (b) 25 vol. % COP-Ba<sub>0.55</sub>Sr<sub>0.45</sub>TiO<sub>3</sub> composites with fillers sintered at 1340°C.

### 5.5.2 Comparison of Dielectric Properties of EM Composites vs. Prior Works

In 2015, Isakov *et al.* reported three types of composite materials with high dielectric permittivity of about seven based on ABS loaded with BaTiO<sub>3</sub> or Ba<sub>0.64</sub>Sr<sub>0.36</sub>TiO<sub>3</sub> micro-fillers [74]. However, typically 3D-printed ABS by FDM has a relatively low  $T_g$  of about 100°C as listed in Table 5.3 and these composites exhibit a high dielectric loss tangent great than 0.034, which is worse than the dielectric losses of even low-cost FR-4 laminates. Due to the high dielectric losses of the bulk BaTiO<sub>3</sub> or Ba<sub>0.64</sub>Sr<sub>0.36</sub>TiO<sub>3</sub> ceramic powders, the composites based on these two types of fillers are anticipated to exhibit high dielectric losses as reported in [40], [49], [50], and [79].

Similarly, Castles *et al.* also reported a composite material with a dielectric permittivity of 8.72 along with a high dielectric loss tangent of 0.0273 [75], which is worse than that of the FR-4 laminates, thus limiting its applications for high gain antennas or high-performance microwave devices. On the other hand, Isakov *et al.* [74] reported another type of composite based on PP loaded with CaTiO<sub>3</sub> with a  $\epsilon_r$  of 5 and a low  $\tan \delta_d$  of 0.0051. Despite the decent dielectric

properties, the loss is still noticeably higher than that of state-of-the-art microwave laminates that typically exhibit low  $\tan \delta_d$  less than 0.003. Also, the  $T_g$  of PP is about  $-14^\circ\text{C}$  and the melting temperature is  $176^\circ\text{C}$  as shown in Table 5.3, which are too low for practical device applications.

### 5.5.3 Dielectric Properties of Thermoplastic Composites in Comparison with State-of-the-Art RF Laminates

Figure 5.17 shows a comparison of the measured permittivity and loss tangent between the 30 vol. % COP-TiO<sub>2</sub> composites and a few types of high-end commercial RF/microwave laminates. As a figure of merit, the 30 vol. % COP-TiO<sub>2</sub> composites with fillers sintered at  $1100^\circ\text{C}$  have shown higher permittivity values and lower dielectric losses up to 17 GHz (limited by test fixtures) when compared with high-end microwave laminates from Rogers Corp. (Rogers RO4003<sup>®</sup> and Rogers TMM3<sup>®</sup>) and Isola Group. (Isola Tachyon<sup>®</sup> and Isola I-Tera<sup>®</sup> MT).

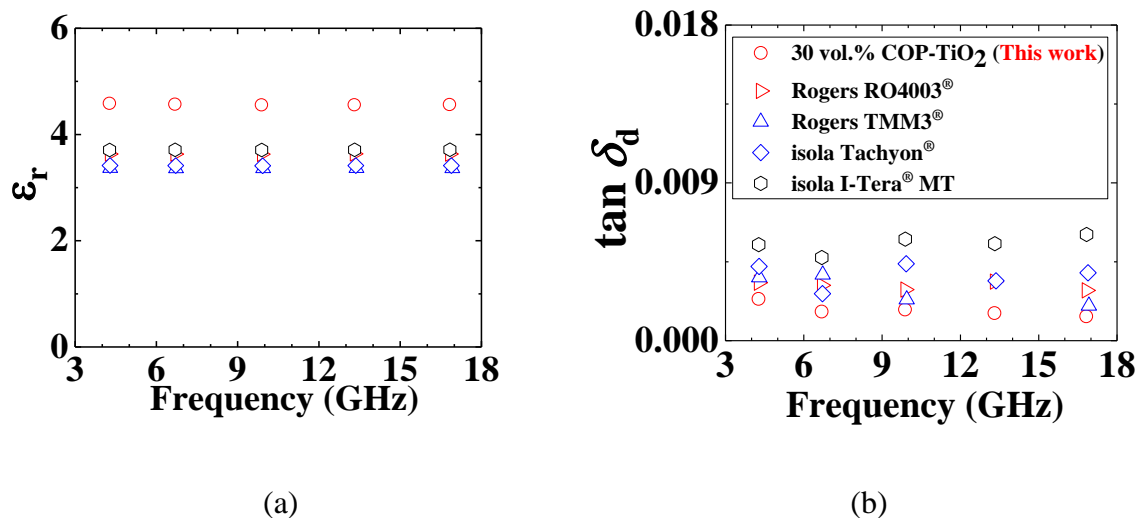


Figure 5.17 – Assessment of measured properties of newly developed 30 vol. % COP-TiO<sub>2</sub> composites with fillers sintered at  $1100^\circ\text{C}$  and high-end RF laminates. (a) Relative dielectric permittivity. (b) Dielectric loss tangent.

### 5.5.4 Repeatability Assessment of Cavity Resonator Measurements in FDM Composites

Figure 5.18 presents dielectric permittivity and loss tangent versus frequency from five separate sample measurements by cavity resonator test fixtures measured following the procedure



in Section 5.4.8 for repeatability assessment of a 420  $\mu\text{m}$ -thick thin-sheet specimen made of 30 vol. % COP-TiO<sub>2</sub> composites loaded with 1100°C sintered and re-pulverized fillers.

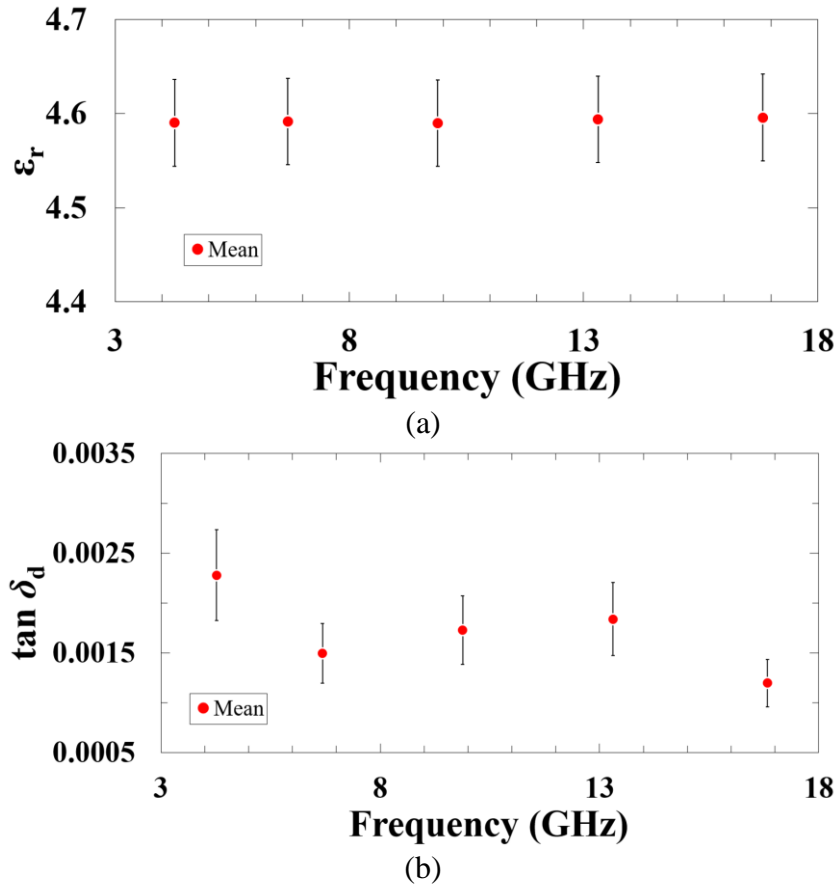


Figure 5.18 – (a) Measured dielectric permittivity (with mean value and error bar specified) of an FDM-printed thin-sheet specimen composed of 30 vol. % COP-TiO<sub>2</sub> composites loaded with 1100°C sintered and re-pulverized fillers. (b) Measured loss tangent of the same sample based on five separate measurements at different spots for repeatability assessment.

The thin-sheet specimen was prepared by an FDM process as described in Section 5.4.3, and Section 5.4.5. Five separate measurements over different spots have been taken by using the cavity resonator test fixture, which exhibited a measured mean permittivity and loss tangent of 4.6 and 0.0014, respectively. Figure 5.18 (a) shows an excellent reproducibility of the relative dielectric permittivity measurements with all the measurements falling inside of the error bars with 2.6 $\sigma$  (99% confidence interval) of accuracy with respect to the mean value, while Figure 5.18 (b)

shows the dissipation factor measurements falling inside of the error bars with  $1.3\sigma$  (80% confidence interval) of accuracy with respect to the measured mean value.

### 5.5.5 Effect of Fillers Sintering Temperature on FDM Composites

Enhancement of dielectric properties by applying a high-temperature sintering process upon the high- $k$  ceramic fillers for EM composite materials has been reported in our previous publications in [50], [76]. The COP-TiO<sub>2</sub> composites were selected due to the low dielectric loss as seen in Table 5.4 to study the effect of the high-temperature sintering process. This study was performed by sintering the TiO<sub>2</sub> micro-particles at 1100°C and 1200°C for three hours in air followed by analysis of the compositional change due to induced reaction within the TiO<sub>2</sub> molecule during high-temperature annealing as studied in Chapter 3 and Chapter 4, which in turn affects the dielectric properties. The fabrication process of the functional feedstock filaments for this study and the 3D printing process was performed as explained in Section 5.4.3 and 5.4.5, respectively, while the dielectric properties of the FDM-printed samples were extracted by the cavity perturbation technique described in Section 3.6.3 and Section 5.4.8 without using any post-FDM process such as hot-compression or polishing. Thus, it was possible to evaluate the effect of the ceramic microfiller annealing conditions on the effective dielectric properties of the as-printed thermoplastic composites prepared by FDM.

The COP composites loaded with TiO<sub>2</sub> particles sintered at 1200°C exhibited (in the whole frequency range) a 6% increase of the relative dielectric permittivity and a 19% increase of the dielectric loss tangent when compared with the COP-TiO<sub>2</sub> composites embedded with TiO<sub>2</sub> fillers sintered at 1100°C, which agrees with the findings reported in Chapter 3 by using a PDMS as a polymer matrix. However, as per the results in Chapter 3 and Chapter 4, other high- $k$  ceramics (e.g., MgCaTiO<sub>2</sub> and Ba<sub>0.55</sub>Sr<sub>0.45</sub>TiO<sub>3</sub>) reacted more positively to result in a simultaneous increase

of dielectric permittivity and a decrease of dielectric loss tangent. Figure 5.19(a) depicts the direct comparison of the dielectric permittivity of the two samples, and Figure 5.19(b) shows the comparison of the dielectric loss properties. Hence, the sintering process should be used as an enhancing strategy depending on the type of ceramic fillers employed in the PMC while taking into account the corresponding trade-off between enhancement of dielectric properties (e.g., changes of both permittivity and dielectric loss). In another word, for some ceramic fillers, it is not possible to improve both dielectric and loss properties at the same time by applying a certain sintering process.

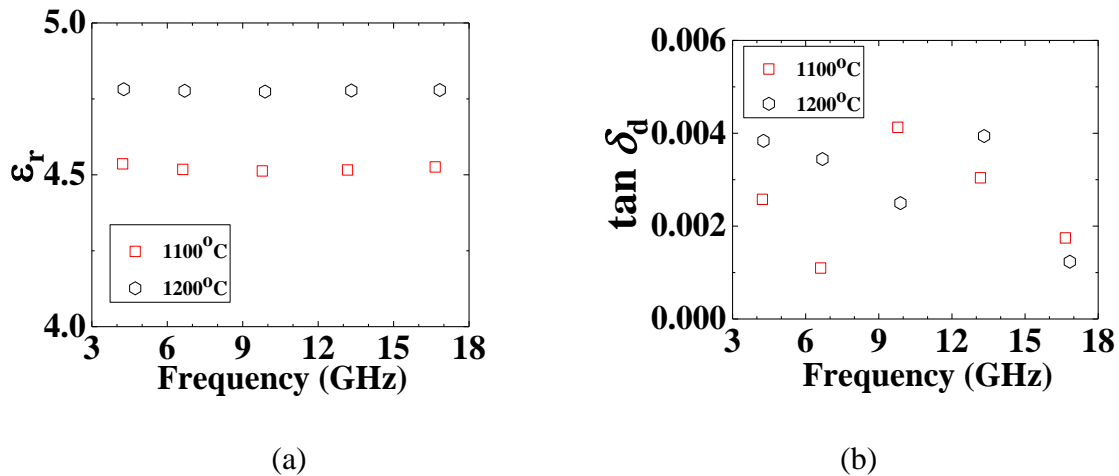


Figure 5.19 – Assessment of measured dielectric properties of 30 vol. % COP-TiO<sub>2</sub> composites with two different sintering conditions for the TiO<sub>2</sub> ceramic fillers at 1100°C and 1200°C. (a) Dielectric permittivity. (b) Dielectric loss tangent.

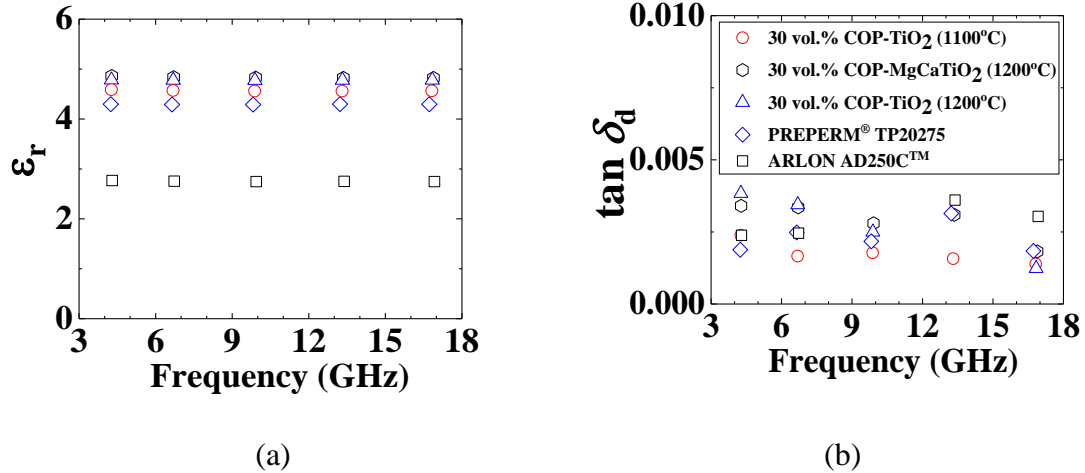


Figure 5.20 – Assessment of measured dielectric properties of 30 vol. % COP-TiO<sub>2</sub> composites vs. other state-of-the-art microwave materials. (a) Dielectric permittivity. (b) Dielectric loss tangent.

## 5.6 Conclusion

A variety of high-permittivity (high- $k$ ) and low-loss ceramic-thermoplastic composite materials as FDM feedstock, based on COP embedded with sintered ceramic fillers, have been developed and investigated for direct digital manufacturing (DDM) of microwave components. The EM properties of these newly developed FDM composites were characterized up to the Ku-band by the cavity perturbation technique. Several models for prediction of the effective relative dielectric permittivity of composites based on the filler loading volume fraction have been evaluated, among which Hanai-Bruggeman and Maxwell models have shown the best accuracy with less than 2% and 5% discrepancies, respectively. The 30 vol. % COP-TiO<sub>2</sub> FDM-ready composites with fillers sintered at 1200°C have exhibited an  $\epsilon_r$  of 4.78 and a  $\tan \delta_d$  lower than 0.0012 at 17 GHz. Meanwhile, the 30 vol. % COP-MgCaTiO<sub>2</sub> composites with fillers sintered at 1200°C have exhibited an  $\epsilon_r$  of 4.82 and a  $\tan \delta_d$  lower than 0.0018.

Table 5.4 – Measured EM dielectric properties of microwave materials up to the Ku-band

Material/Composite	Year	Technology	Filler	Freq. (GHz)	$\epsilon_r$	$\tan \delta_d$	Ref.
ABS-BaTiO <sub>3</sub>	2015	FDM	44 wt. %	15	3.30	0.0070	[73]
ABS-Ba <sub>0.64</sub> Sr <sub>0.36</sub> TiO <sub>3</sub>			30 vol. %		6.70	0.0368	
ABS-BaTiO <sub>3</sub>	2015	FDM	27 vol. %	15	7.00	0.0342	[74]
PP - CaTiO <sub>3</sub>			27 vol. %		5.00	0.0051	
BaTiO <sub>3</sub> /ABS	2016	FDM	29 vol. %	14.13	8.72	0.0273	[75]
PPE (PREPERM <sup>®</sup> TP20275)	2015	FDM	N/A	17	4.42	0.0019	PREMIX
ABS-Ba <sub>0.55</sub> Sr <sub>0.45</sub> TiO <sub>3</sub> (sintered 1340°C) †			6 vol. %		3.98	0.0086	
COP-TiO <sub>2</sub> (sintered 1100°C) ‡			30 vol. %		4.57	0.0014	
COP-TiO <sub>2</sub> (sintered 1200°C) ‡	2016	FDM	30 vol. %	17	4.78	0.0012	<b>This Work</b>
COP-MgCaTiO <sub>2</sub> (sintered 1100°C) ‡			25 vol. %		4.74	0.0018	
COP-MgCaTiO <sub>2</sub> (sintered 1200°C) ‡			30 vol. %		4.82	0.0018	
COP-Ba <sub>0.55</sub> Sr <sub>0.45</sub> TiO <sub>3</sub> (sintered 1340°C) ‡			25 vol. %		4.92	0.0114	
Vectra 840i LDS					3.80	0.0025	
Grilamid 1SVX-50H LDS	2014	LDS-MID	N/A	30	4.00	0.0100	[13]
Xantar LDS 3720					2.90	0.0075	
COP/MgO	2015	Molded Disk	30 vol. %	12	3.83	0.0005	[86]
FR-4	2015	Laminate	N/A	12	4.50	0.0142	LPKF
CLTE-XT <sup>™</sup>	2015	Laminate	N/A	10	2.94	0.0012	ARLON Elect. Materials
AD250C <sup>™</sup>	2015	Laminate	N/A	10	2.50	0.0014	
Tachyon <sup>®</sup>	2015	Laminate	N/A	10	3.02	0.0021	isola
I-Tera <sup>®</sup> MT	2015	Laminate	N/A	10	3.45	0.0031	Group
RO4003C <sup>®</sup>				10	3.55	0.0027	
TMM3 <sup>®</sup>	2015	Laminate	N/A	10	3.45	0.0020	Rogers
RT/duroid <sup>®</sup> 5880				10	2.20	0.0009	Corp.
RT/duroid <sup>®</sup> 5870				10	2.33	0.0012	

Note: †‡ All the samples were 3D-printed by FDM with in-house prepared feedstock filaments. †‡ Filed provisional disclosure. Laser Direct Structureable (LDS)-Molded Interconnect Device (MID), LDS-MID Materials. ARLON, Rogers and isola laminates values were taken from vendors' datasheets.

## CHAPTER 6 :

### DIRECT DIGITAL MANUFACTURING OF KU-BAND ANTENNAS BASED ON FDM-READY CERAMIC-THERMOPLASTIC COMPOSITES

#### 6.1 Note to Reader

Portions of this chapter, including figures, have been previously published in [10] and [17], and they have been reproduced with permissions from IEEE Microwave Theory and Techniques Society. Permissions are included in Appendix A.

#### 6.2 Microwave Performance Assessment of FDM Composites

##### 6.2.1 3D-printed Edge-Fed Microstrip Patch Antennas

Rectangular edge-fed patch antennas were designed for 16.5 GHz and 17.2 GHz. These antennas were manufactured using a 2-step DDM process [2], including the FDM fabrication of a 25 vol. % COP-MgCaTiO<sub>2</sub> composite substrate and a pure COP substrate following the procedure described in Section 5.4.3 and Section 5.4.5. The front-side patch antenna pattern and ground plane were printed using CB028 thick-film silver paste, with a pressure of 12 psi, a speed of 20 mm/s and a printer tip inner diameter of 125 μm. Both steps (FDM and micro-dispensing) were done in a continuous manner using a tabletop-3Dn 3D-printer (nScript, Orlando, FL). Due to the delamination issues of the chosen micro-dispensable silver paste (CB028) on top of the Rogers RT/duroid® 5880 laminate, a 380 μm thick Rogers RT/duroid® 5870 substrate with similar properties was selected to fabricate reference antennas operating at 16.4 GHz and 16.7 GHz, with the purpose of assessing and comparing the microwave material performance.

Table 6.1 – Key antenna dimensions\*

Material / F. (GHz)	W	L	W <sub>p</sub>	L <sub>p</sub>	WL	W <sub>a</sub>	L <sub>a</sub>	L <sub>b</sub>
RT/5870 (16.4)	13.0	23.70	6.80	5.60	1.19	3.18	3.24	5.25
COP (16.5)	12.5	23.99	6.91	5.68	1.09	3.25	3.27	5.31
RT/5870 (16.7)	13.0	23.40	6.80	5.50	1.19	3.18	3.20	5.19
COP-MgCaTiO <sub>2</sub> (17.2)	9.3	16.75	4.97	3.79	0.56	2.42	2.35	3.73

\* All dimensions are given in mm.

The original copper cladding layers were etched away to expose the dielectric core of the RT/duroid® 5870 substrate. The key antenna dimensions and geometry are shown in Figure 6.1(b) and Table 6.1.

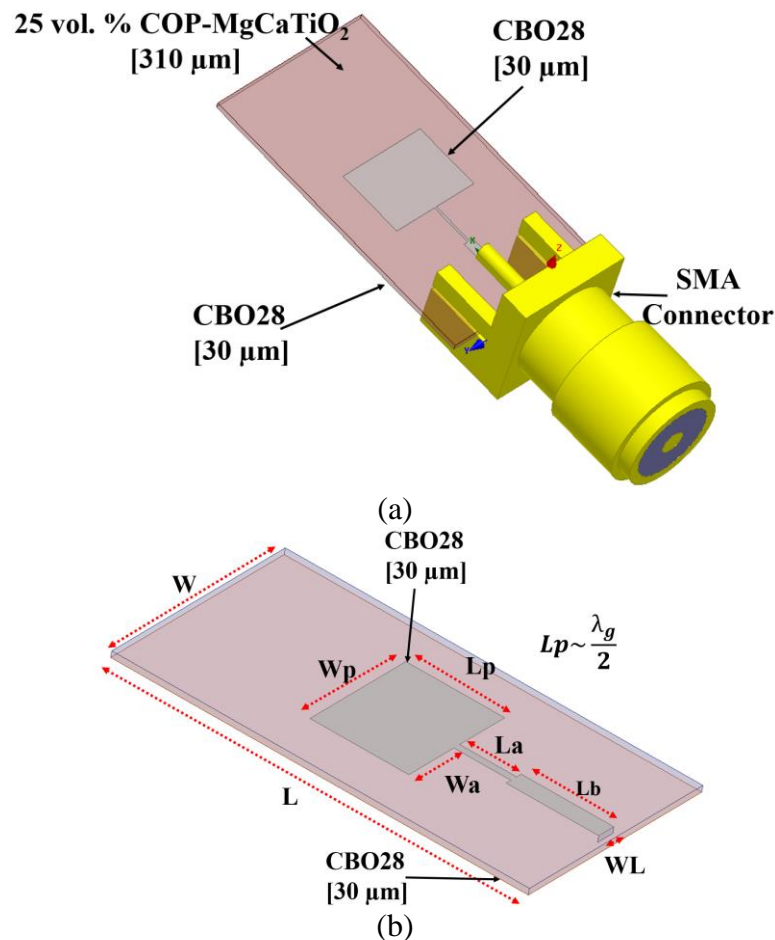


Figure 6.1 – (a) Schematic diagram of a 3D-printed rectangular edge-fed patch by using a 25 vol. % COP-MgCaTiO<sub>2</sub> EM composite material. (b) The critical dimensions and geometry of the patch antenna.



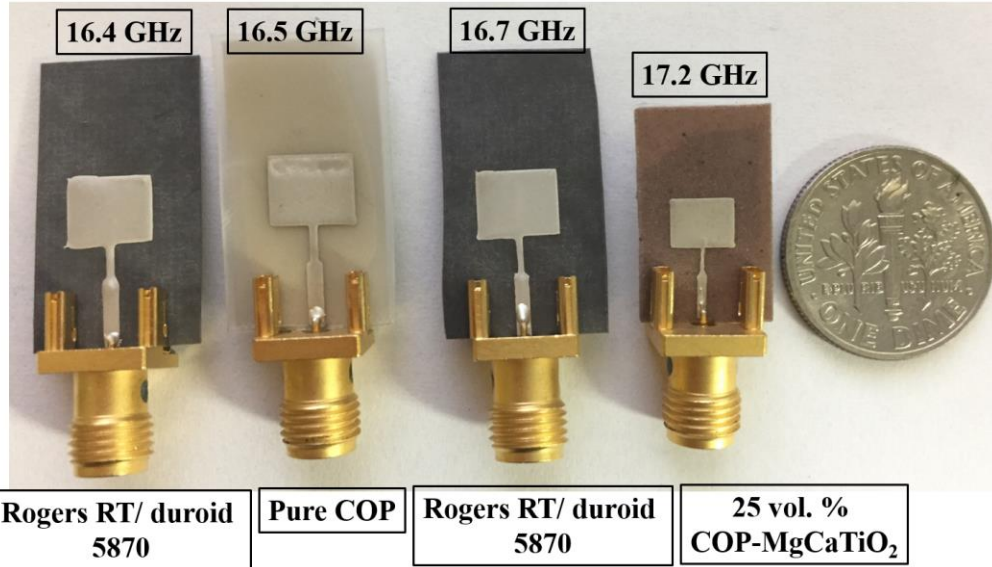


Figure 6.2 – Top-view image of additive manufactured 16.5 GHz antennas over COP and RT/duroid® 5870 substrates (left) as well as 17.2 GHz/16.7 GHz antennas over 25 vol. % COP-MgCaTiO<sub>2</sub> and RT/duroid® 5870 substrates (right). 50% antenna area reduction was achieved using loaded composites.

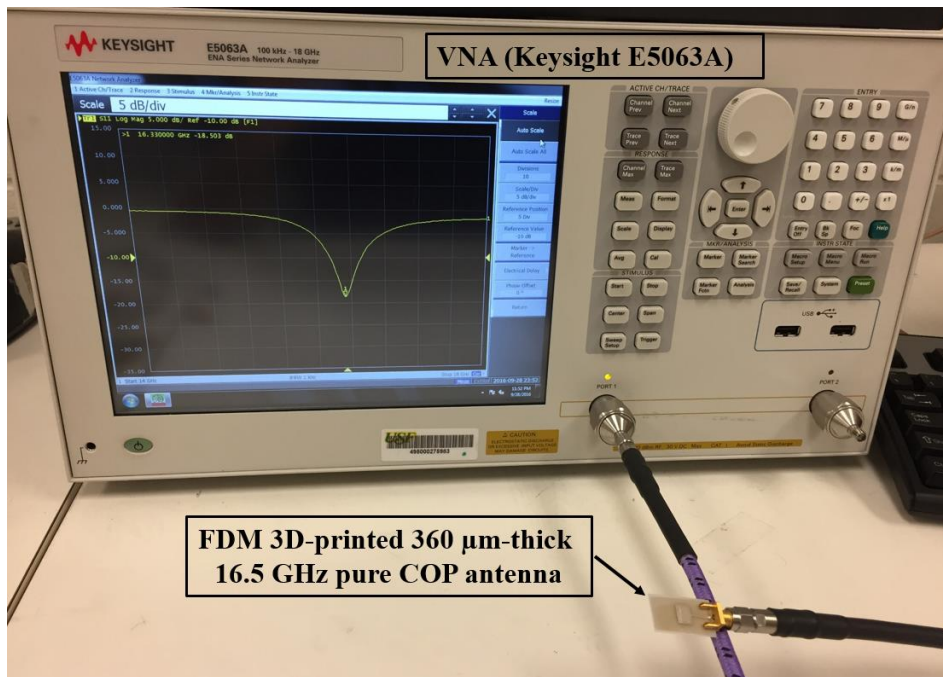


Figure 6.3 – Antenna return loss characterization setup for a 16.5GHz antenna manufactured by a DDM process with a 360 μm-thick pure COP substrate.



The edge-fed microstrip patch antenna configuration was selected to avoid the need for small microstrip inset feeds. The dimensions for the rectangular patch were determined based on the measured dielectric properties listed in Figure 5.15 by using equations reported by Balanis [80] (i.e. Equations (4.1) - (4.6)). Figure 6.2 depicts the size comparison of the 3D-printed antennas as compared with the antennas fabricated on Rogers RT/duroid<sup>®</sup> 5870 core laminate. The return loss of the antennas was measured by an E5063A VNA (Keysight Technologies, Santa Rosa, CA.) using a setup as depicted in Figure 6.3. The EM simulation of the antennas was performed using ANSYS<sup>®</sup> Electromagnetics Suite 18 (HFSS 2017).

### 6.2.2 Surface Treatment Recommendations for FDM Composites

Figure 6.4(a) depicts the cross-sectional SEM photo showing the actual interface between FDM-produced COP thin-sheet and the 30  $\mu\text{m}$ -thick printed metallization layer comprised of micro-dispensed silver paste (CB028). Whereas Figure 6.4(b) presents the 16.5 GHz COP patch antenna feed line, note the typical pattern of a DPAM printed CB028 silver paste, while Figure 6.4(a) shows a top-view SEM photo of the printed layer showing silver flakes of 650 nm on average, DPAM-printed in a 16.5 GHz radiator area in edge-fed patch antenna. Figure 6.4(b) depicts the cross-sectional SEM photo showing the actual interface between the FDM printed COP (ZEONEX<sup>®</sup> RS420) substrate and micro-dispensed silver paste layer. The conductivity of the layer formed by micro-dispensed silver paste (CB028) dried at 110°C is 3.94e6 (S/m) [2], and the typical measured average surface roughness is 3.68  $\mu\text{m}$  [25].

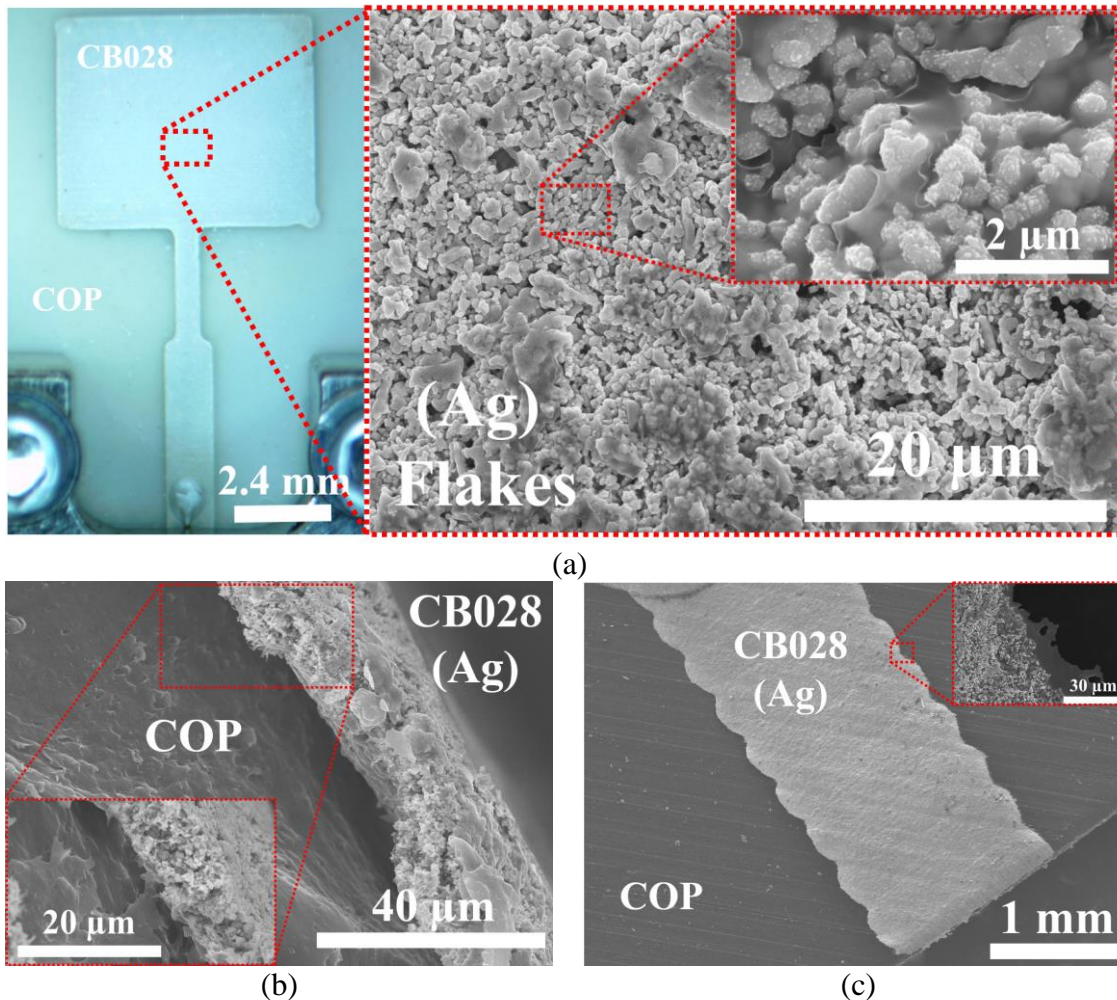


Figure 6.4 – SEM photos of micro-dispensed silver paste (CB028). (a) A top-view photo showing silver flakes of 650 nm on average, in a DPAM printed 16.5 GHz COP patch antenna (radiator area). (b) A cross-sectional SEM photo showing the actual interface between the FDM printed COP (ZEONEX® RS420) substrate and micro-dispensed silver paste layer. (c) Top-view photo of a 16.5 GHz COP patch antenna feed line.

Future works are needed to explore methods that could improve adhesion between the FDM-printed COP and COP loaded EM composites as well as the micro-dispensed silver paste (i.e., CB028) layer followed by the curing/drying process. In some cases, there are some delamination issues between the pure COP or COP-based composite samples and the micro-dispensed metal traces as shown in Figure 6.4(b). Cui *et al.* suggested that introducing groups into polymer chains could be a good strategy to effectively improve the material performance, such as

toughness, adhesion, paintability, and compatibility with other polymers and materials [85]. Hence, one possible solution is to investigate another variation of COP, such as ZEONOR® (1420R), which also exhibited the lower coefficient of thermal expansion (CTE) when compared with all the other types of COP thermoplastics explored in this work. Since for practical electronic/microwave applications, the CTE of the EM composites and the thick-film silver paste (e.g. CB028) should be as close as possible, as explained in Chapter 7. Moreover, some adhesion promoters for cyclic olefin resin compositions has been recommended by Cruce *et al.* [87], which should also be investigated.

### 6.2.3 Edge-Fed Patch Antennas Performance

The measured antenna peak gain, size reduction, and other parameters are given in Table 6.2. The simulations were performed using 3.94e6 S/m as the conductivity of the micro-dispensed CB028 silver paste metallization layer. Figure 6.5 shows a comparison between measured and simulated return losses of the 17.2 GHz and 16.7 GHz antenna designs, indicating a good match between measured and simulated results.

Table 6.2 – Edge-fed patch antennas performance comparison

Material	COP	COP-MgCaTiO <sub>2</sub>	Rogers RT/5870	
Freq. (GHz)	16.5	17.2	16.4	16.7
Substrate thickness (mm)	0.36	0.31	0.38	0.38
Radiator Area (mm <sup>2</sup> )	36.24	18.84	38.08	35.64
Size Reduction vs. RT/5870 (%)	-3	50	--	--
Measured Peak Gain (dBi)	5.70	6.01	5.99	6.27
Simulated Peak Gain (dBi)†	5.47	4.76	5.59	5.65
Micro-dispensing	Yes	Yes	Yes	Yes
FDM	Yes	Yes	No	No

†Simulated peak gain using DC conductivity of CB028 [3.94e6 S/m]

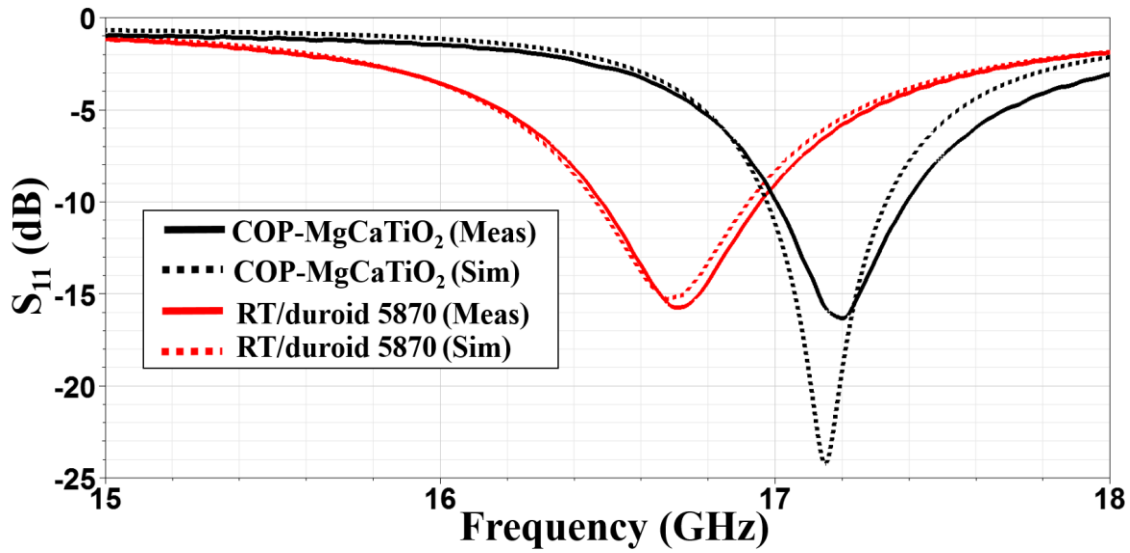


Figure 6.5 – Comparison of the measured and simulated  $S_{11}$  of the 17.2 GHz antenna DDM-printed based on COP loaded with  $MgCaTiO_2$  fillers and a reference antenna at 16.7 GHz DPAM-printed over Rogers RT/duroid<sup>®</sup> 5870 laminate. Copper cladding layer removed, followed by micro-dispensing of silver paste.

For the 17.2 GHz antenna fabricated by a DDM process over a 310  $\mu\text{m}$ -thick 25 vol. % COP- $MgCaTiO_2$  substrate, a measured 10 dB return loss bandwidth of 390 MHz was achieved. For comparison, a 16.7 GHz antenna design over a 380  $\mu\text{m}$ -thick RT/duroid<sup>®</sup> 5870 substrate has shown similar performance with a 480 MHz bandwidth as seen in Figure 6.5.

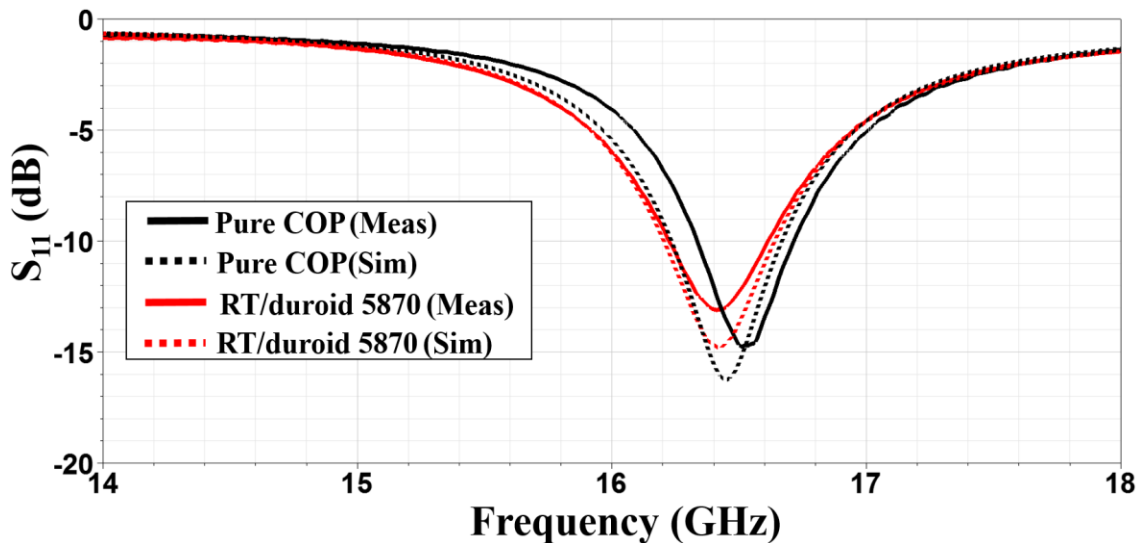


Figure 6.6 – The measured and simulated  $S_{11}$  of the 16.5 GHz antennas based on DDM-printed COP substrate, which is compared with a reference DPAM-printed antenna over a Rogers RT/duroid<sup>®</sup> 5870 laminate at 16.4 GHz.

For the 16.5 GHz patch antenna printed over an FDM-produced 360  $\mu\text{m}$ -thick COP substrate, a measured 390 MHz bandwidth was realized. For comparison, a 16.4 GHz antenna design over an RT/duroid<sup>®</sup> 5870 substrates has shown a measured bandwidth of 390 MHz as seen in Figure 6.6. The radiation patterns and gain vs. frequency measurements were conducted using an anechoic chamber of dimensions 3.66 m  $\times$  7.32 m  $\times$  3.66 m (length, width, and height, respectively) and calibrated using standard gain horns (Com-power AH-118). The antenna test setup is depicted in Figure 6.7. Figure 6.8 presents measured and simulated maximum realized gain versus frequency for the 17.2 GHz COP-MgCaTiO<sub>2</sub> antenna and the 16.7 GHz Rogers RT/duroid<sup>®</sup> 5870 antenna, which have shown good agreement with simulation results. The largest difference between the measured and simulated antenna peak realized gains is less than 1.25 dB as shown in Table 6.2 and Figure 6.8.

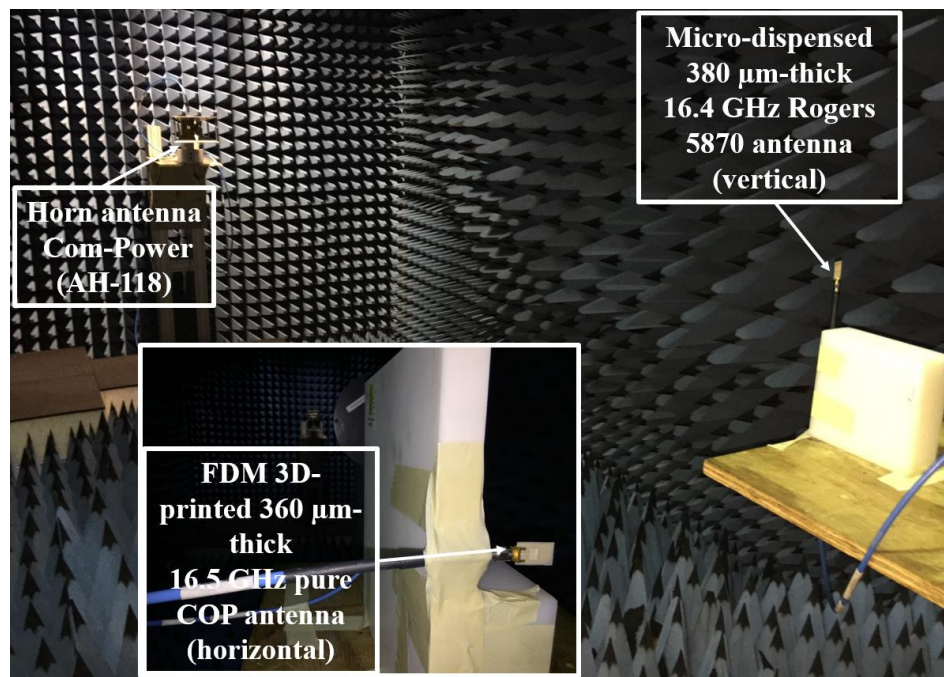


Figure 6.7 – Edge-fed patch antennas in an anechoic chamber during antenna pattern measurements. The center insert shows a front view of the 16.5 GHz 360  $\mu\text{m}$ -thick COP-based antenna in a horizontal position; the antenna shown to the right is a 16.4 GHz Rogers RT/duroid<sup>®</sup> 5870 micro-dispensed antenna.



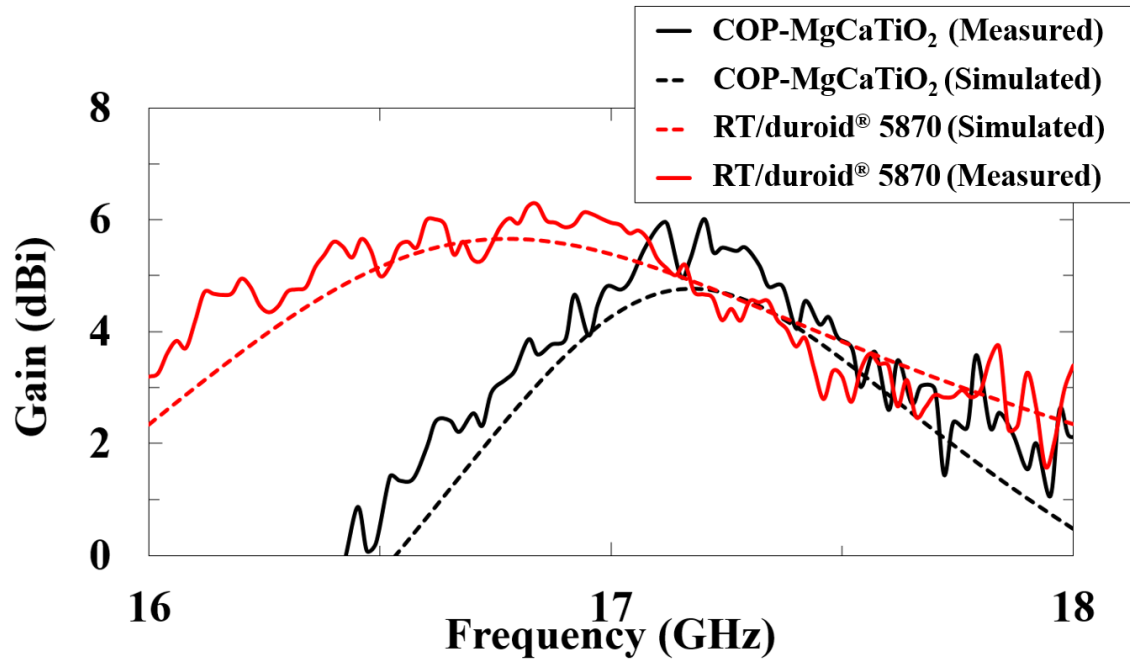


Figure 6.8 – Measured gain vs. frequency for 17.2 GHz antenna DDM-printed on a COP-MgCaTiO<sub>2</sub> composite substrate and a 16.7 GHz reference antenna DPAM-printed over an RT/duroid<sup>®</sup>5870 substrate. Both antennas are compared with simulated results with assumed metal layers (CB028) conductivity of 3.94e6 (S/m).

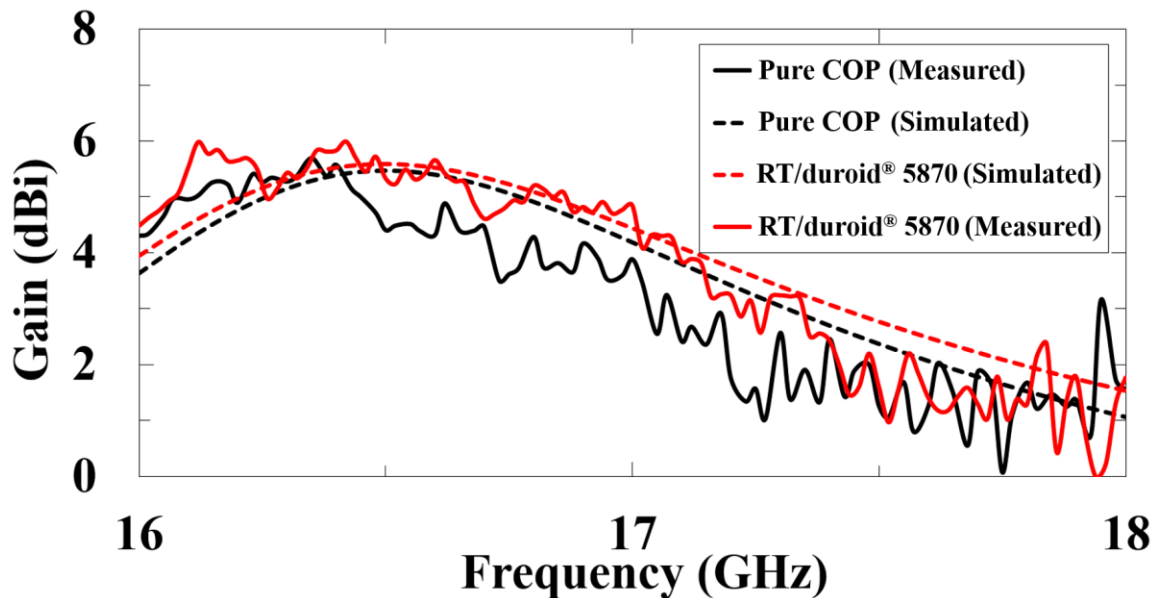
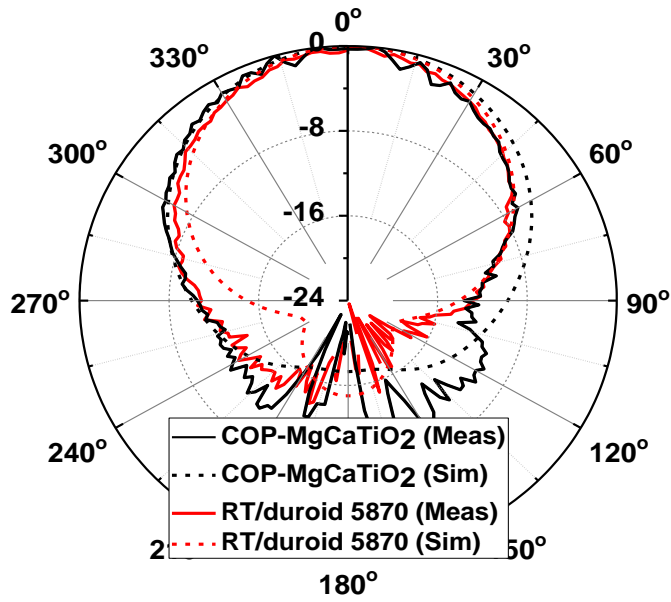


Figure 6.9 – Measured and simulated gain vs. frequency for antennas DDM-printed on pure (unloaded) COP at 16.5 GHz, which are compared with a 16.4 GHz reference design DPAM-printed over a Rogers RT/duroid<sup>®</sup>5870 substrate. Both antennas are compared with simulated results with assumed metal layers (CB028) conductivity of 3.94e6 (S/m).

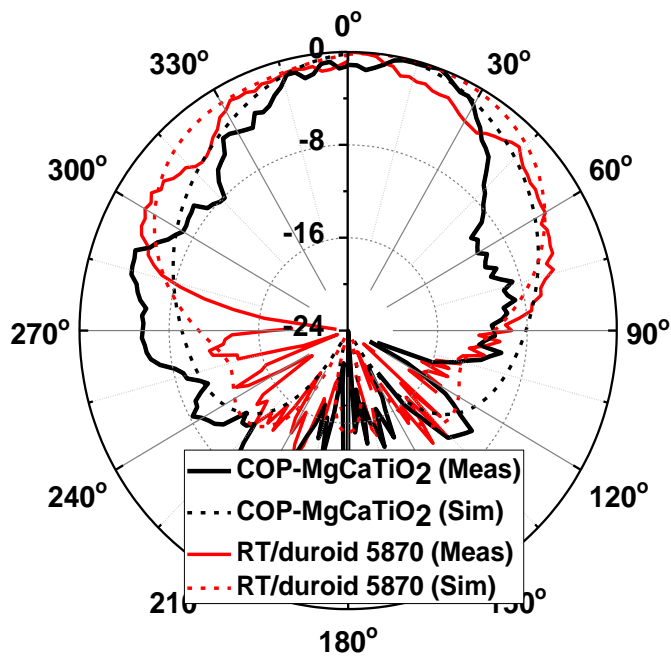
Figure 6.9 presents the measured gain versus frequency for the 16.5 GHz COP-based antenna in comparison with the 16.4 GHz reference antenna design based on a Rogers RT/duroid® 5870 substrate. As shown, the measured and simulated gain versus frequency responses are quite comparable, as the maximum difference of the peak realized gain between the measured and simulated data is only 0.23 dB. For this case, a very close match is achieved, also by assuming a conductivity of  $3.94e6$  (S/m) of CB028 in the device simulations.

As a key figure of merit, very similar measured realized gains have been demonstrated for the fully 3D-printed antennas based on the ceramic-loaded COP composites and pure COP when compared with reference designs printed over Rogers RT/duroid® 5870 core substrates as depicted in Figure 6.8 and Figure 6.9, respectively. The antenna performance is summarized in Table 6.2. Figure 6.10 shows the comparison between the measured and simulated normalized H-plane and E-plane radiation patterns for the fully 3D-printed 17.2 GHz antenna based on 25 vol. % COP-MgCaTiO<sub>2</sub> composites that are compared with a 16.7 GHz Rogers RT/duroid® 5870 antenna. Figure 6.10(a) depicts an excellent agreement in the H-plane characteristics for both antennas. Both antennas exhibit small back lobes which agree with the EM simulations. Figure 6.10(b) shows the comparison between the simulated and measured E-plane radiation patterns. The measured E-plane patterns have some imperfections regarding the symmetry of the main lobes due to the size of the connectors and the size of the patch (radiators). Figure 6.11 shows the measured and simulated H-plane and E-plane normalized radiation patterns for the fully 3D-printed 16.5 GHz antenna based on pure (unloaded) COP material, which is compared with the 16.4 GHz Rogers RT/duroid® 5870 antenna. Figure 6.11(a) depicts a close agreement regarding the main lobe symmetry in the measured and simulated H-plane radiation patterns. Similarly, Figure 6.11(b)

shows some imperfections in the main lobe symmetry in the measured E-plane radiation patterns due to the relatively large size of the connectors and small size of the radiators.



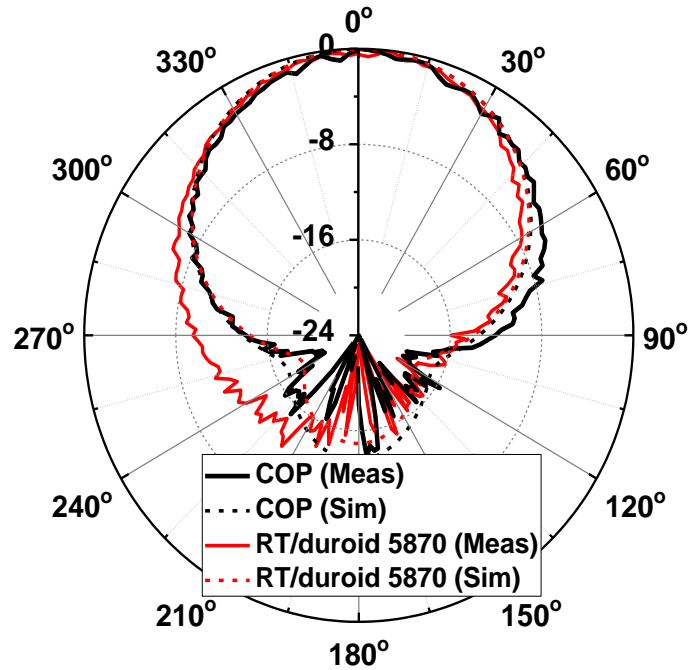
(a)



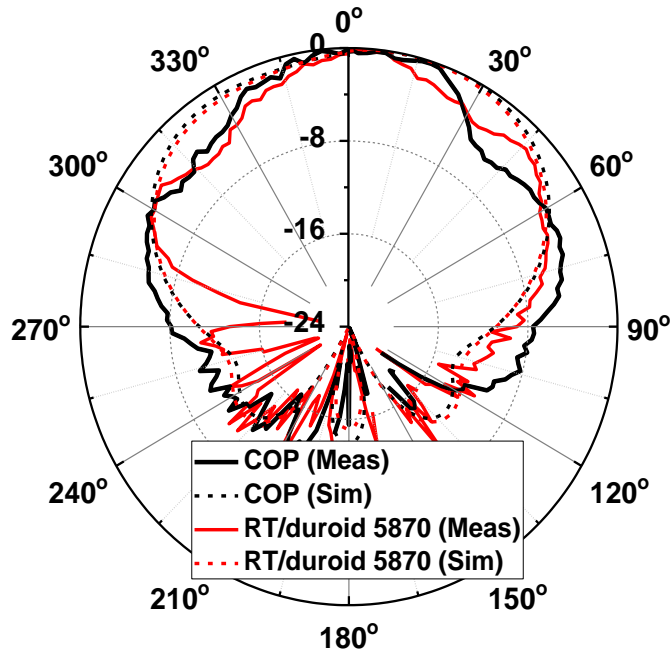
(b)

Figure 6.10 – Measured (normalized) radiation patterns of the DDM-printed 17.2 GHz antenna by COP-MgCaTiO<sub>2</sub> composites, which is compared with a reference DPAM-printed antenna over a Rogers RT/duroid<sup>®</sup> 5870 laminate core at 16.7 GHz. Including radiation patterns for (a) H-Plane. (b) E-Plane.





(a)



(b)

Figure 6.11 – Measured (normalized) radiation patterns of the DDM-printed 16.5 GHz antenna composed of pure (unloaded) COP, which is compared with a 16.4 GHz reference antenna DPAM-printed over a Rogers RT/duroid® 5870 laminate core. Including radiation patterns for (a) H-Plane. (b) E-Plane.

### 6.3 Conclusion

Edge-fed patch antennas operating at 17.2 GHz and 16.5 GHz were manufactured by DDM that employs a 25 vol. % COP-MgCaTiO<sub>2</sub> composite FDM filament with the fillers sintered at 1100°C and a pure COP filament, which were both prepared and extruded following the process described in this dissertation. The low dielectric loss of the 25 vol. % COP-MgCaTiO<sub>2</sub> composite material has been leveraged to achieve a peak realized a gain of 6 dBi. Also, a patch area miniaturization of 50% was achieved when compared with an antenna designed and DPAM-printed over a Rogers RT/duroid® 5870 laminate core through micro-dispensing of CB028 thick-film silver paste. This reference antenna exhibited a measured peak realized gain of 6.27 dBi. The electromagnetic composites with tailored EM properties studied by this work have shown some great potential for the next generation of fully 3D-printed and high-performance RF/microwave devices.

**CHAPTER 7 :**  
**MILLIMETER-WAVE PERFORMANCE AND THERMAL PROPERTIES**  
**ASSESSMENT OF FDM-COMPATIBLE COMPOSITES**

**7.1 Note to Reader**

Portions of this chapter, including figures, are in publication process at the 2017 IEEE AP-S Symposium on Antennas and Propagation and USNC-URSI Radio Science Meeting [82].

**7.2 Introduction**

Characterization of EM composite materials suited for DDM technologies at the mm-wave frequencies up to 69 GHz is presented in this chapter. A COP thermoplastic matrix reinforced by MgCaTiO<sub>2</sub> micro-fillers sintered at 1200°C has been prepared and characterized up to 67 GHz (V-band). Pure COP exhibits a relative permittivity of 2.1 and a loss tangent below 0.0011 up to 69 GHz. Moreover, 30 vol. % COP-MgCaTiO<sub>2</sub> composites show a relative permittivity of 4.88 and a loss tangent below 0.0070 at 66 GHz. The newly characterized composites show the some of the lowest dielectric losses reported for FDM materials that are ideal for microwave applications at mm-wave frequencies as shown in Table 7.1. Evidently, these newly developed polymer-ceramic composites are well suited for applications at the mm-wave frequencies and can be adapted to 3D-printing technologies.

The reported progress in AM-compatible functional mm-wave EM composite materials, specifically those compatible with FDM, has been lacking especially regarding more options other than the standard thermoplastics [2]-[3] such as ABS, Polycarbonate (PC), and polyetherimide (PEI) also known as ULTEM™ resin. To the best of my knowledge, this work reports FDM-ready

COP-based composites characterized at mm-wave frequencies up to 69 GHz (V-band) for the first time. Moreover, an excellent balance between relative dielectric permittivity value of 4.88 and a low-dielectric-loss tangent  $\tan \delta_d$  lower than 0.0070 at 66 GHz for a newly developed COP-ceramic based FDM compatible has been reported, which shows better dielectric characteristics than most of the pure thermoplastics, such as ABS Cyclic™ (MG47), and ULTEM™ (1000) [10], [17].

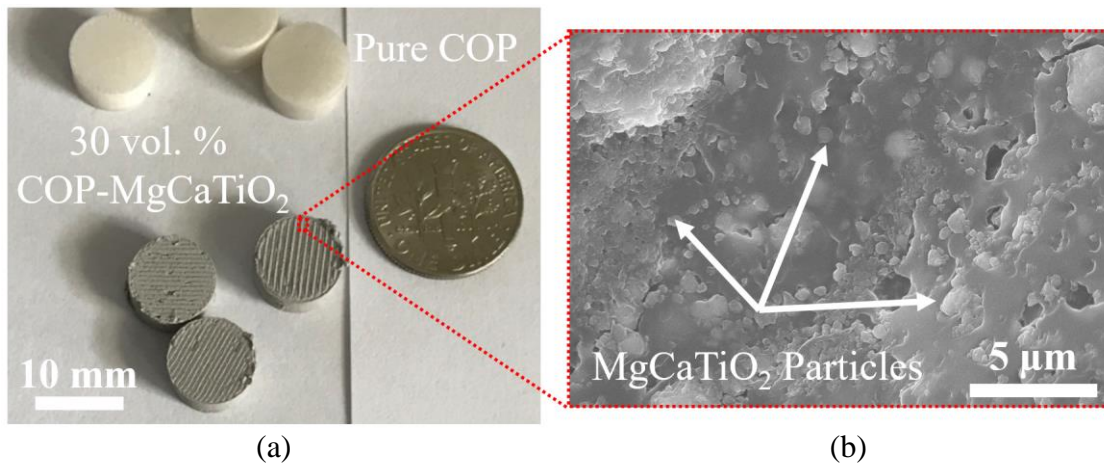


Figure 7.1 – SEM photos of 30 vol. % COP-MgCaTiO<sub>2</sub> composite FDM-printed samples. (a) Surface view. (b) Zoom-in view of showing the sintered MgCaTiO<sub>2</sub> ceramic particles, note the isotropic distribution of the ceramic particles.

Figure 7.1(b) depicts the SEM photos of one of the 30 vol. % COP-MgCaTiO<sub>2</sub> thermoplastic composites, which is loaded with MgCaTiO<sub>2</sub> micro-fillers sintered at 1200°C. As shown by a top-view SEM image of 3D-printed cylindrical specimens in Figure 7.1(a), the COP-based sample is embedded with densified MgCaTiO<sub>2</sub> microspheres with an average size of 5 μm or smaller.

### 7.3 Measured Properties of 3D-printed Samples

#### 7.3.1 Millimeter-Wave Performance Assessment

The mm-wave dielectric characterization was performed using a model 200 circular cavity from Damaskos Inc. and 3D-printed cylindrical specimens of 10 mm diameter and 5 mm thickness

manufactured by FDM process using ceramic-loaded and unloaded COP based feedstock filaments following the methodology reported in Section 5.4.3 and Section 5.4.5. The model 200 circular cavity is a Z-axis tester designed for room temperature measurements. Figure 7.2 depicts the measured dielectric and loss properties up to the V-band frequencies of both pure COP and 30 vol. % COP-MgCaTiO<sub>2</sub> composites based on FDM 3D-printed specimens. Please note the frequency dependence of dielectric loss tangent is more evident in the ceramic filler loaded composite sample.

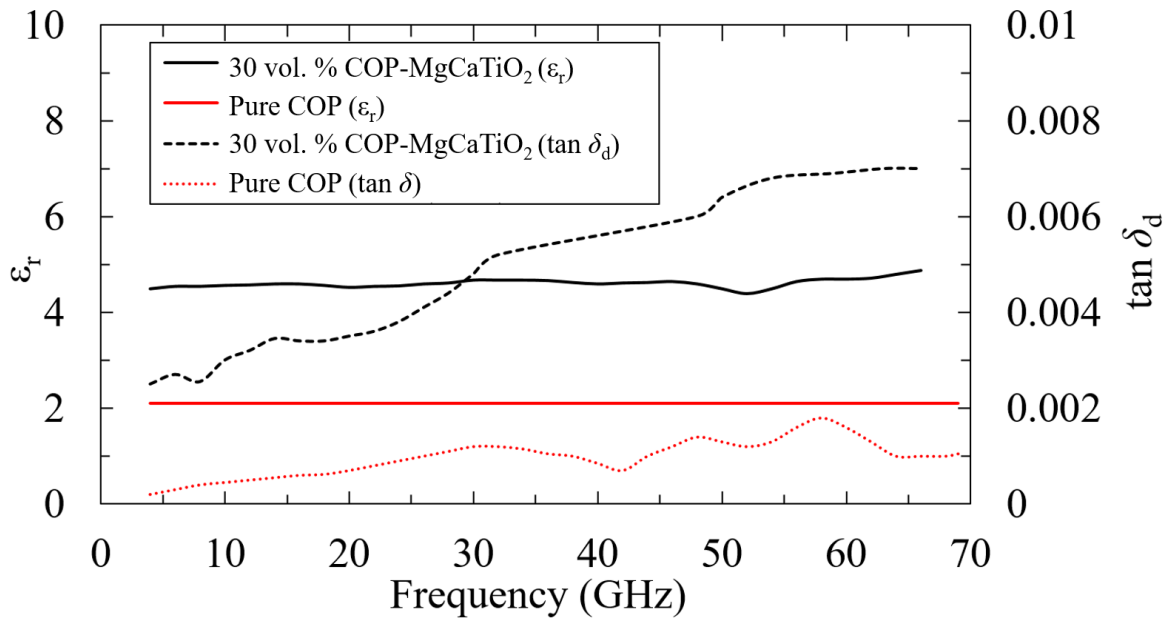


Figure 7.2 – Comparison of measured dielectric and loss properties up to 69 GHz of both a pure COP (ZEONEX® RS420) and a 30 vol. % COP-MgCaTiO<sub>2</sub> EM composites based FDM-printed cylindrical specimens.

In 2014, Bisognin *et al.* reported the dielectric properties of ABS-30<sup>TM</sup> from Stratasys, Ltd. at 60 GHz by using an open Fabry-Perot cavity resonator [83]. The material was used for lens antenna applications instead of RF/microwave substrate. In 2015, Vera *et al.* reported the characterization of ABS at 30 GHz by using an in-house cavity resonator [9] as summarized in Table 7.1.

Table 7.1 presents the comparison of the millimeter-wave dielectric performance of the two types of FDM composite materials studied in this dissertation (pure COP and loaded 30 vol. % COP-MgCaTiO<sub>2</sub> with fillers sintered 1200°C). Three data points for each material from the mm-wave characterization are shown in Table 7.1. The EM composites are compared with Laser Direct Structureable (LDS)-Molded Interconnect Device (MID) materials and high-performance microwave laminates from Rogers Corporation. For instance, as compared to the dielectric properties of LDS- MID materials reported by Dao *et al.* [13], the EM composites developed by this work not only showed higher relative dielectric permittivity but also exhibited lower dielectric losses tangent than all of these materials as seen in Table 7.1. As compared to the dielectric performance with the ABS-30™ material from Stratasy, Ltd., the 30 vol. % COP-MgCaTiO<sub>2</sub> with fillers sintered at 1200°C is 2x higher regarding relative permittivity while exhibiting much lower losses across the whole frequency range up to 66 GHz.

The dielectric properties of the laminate materials by Rogers Corporation are reported in Table 7.1, which were measured by using a cylindrical cavity resonator from Damaskos Inc. and an HP 8510C network analyzer. These measurements were reported by Horn [27]. These values as shown in Table 7.1 were calculated by using the normalized results multiplied by the nominal values of each of these high-performance microwave laminates in the technical report. The engineered FDM-printed composites by this work exhibited better relative dielectric permittivity than all these commercial products from Rogers Corporation, such as RO3003<sup>®</sup>, RT/duroid<sup>®</sup> 5870, RT/duroid<sup>®</sup> 5880, RO4350B<sup>®</sup>, RO4003C<sup>®</sup>, TMM3<sup>®</sup>, and RT/duroid<sup>®</sup> 6002 laminates, despite slightly higher losses. Nevertheless the 30 vol. % COP-MgCaTiO<sub>2</sub> composites (with fillers sintered 1200°C) exhibit losses on par with those of RO4003C<sup>®</sup>, RO4350B<sup>®</sup>, and TMM3<sup>®</sup> tested at 50 GHz as shown in Figure 7.4. Table 7.1 also shows the mm-wave performance of the FDM-printed pure

COP ZEONEX<sup>®</sup> (RS420) material, which exhibited better dielectric losses than most of the laminates from Rogers Corporation with only slightly higher losses than RT/duroid<sup>®</sup> 5880 laminate at 50 GHz, so far, this seems to be the microwave material from industry with the lowest loss tangent. 3D-printed COP also exhibited about 4x lower dielectric losses than the ABS-30<sup>™</sup> material from Stratasys, Ltd. while showing very similar relative permittivity  $\epsilon_r$ . Figure 7.3 depicts the measured dielectric permittivity up to the V-band frequencies for both pure COP and 30 vol. % COP-MgCaTiO<sub>2</sub> composites based on 3D-printed specimens, which are compared with other materials shown in Table 7.1.

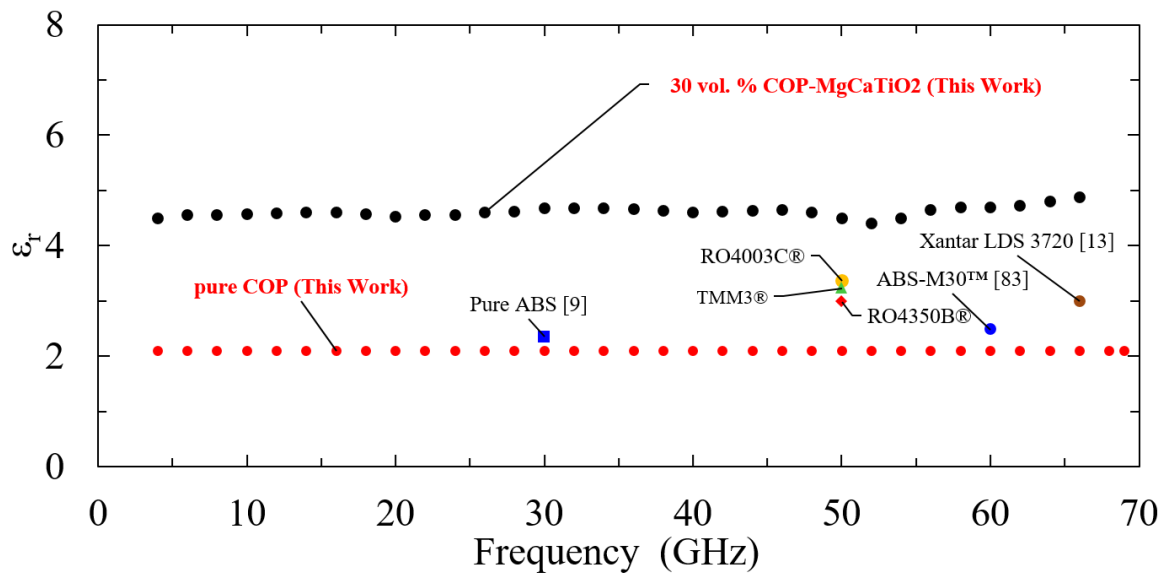


Figure 7.3 – Comparison of measured dielectric permittivity up to 69 GHz of both a pure COP (ZEONEX<sup>®</sup> RS420) and a 30 vol. % COP-MgCaTiO<sub>2</sub> EM composites with commercial microwave laminates from Rogers Corporation [27]. Other materials are shown in Table 7.1.

Figure 7.4 depicts the measured dielectric loss up to the V-band frequencies of both pure COP and 30 vol. % COP-MgCaTiO<sub>2</sub> composites based on 3D-printed specimens, which are compared with other materials shown in Table 7.1.

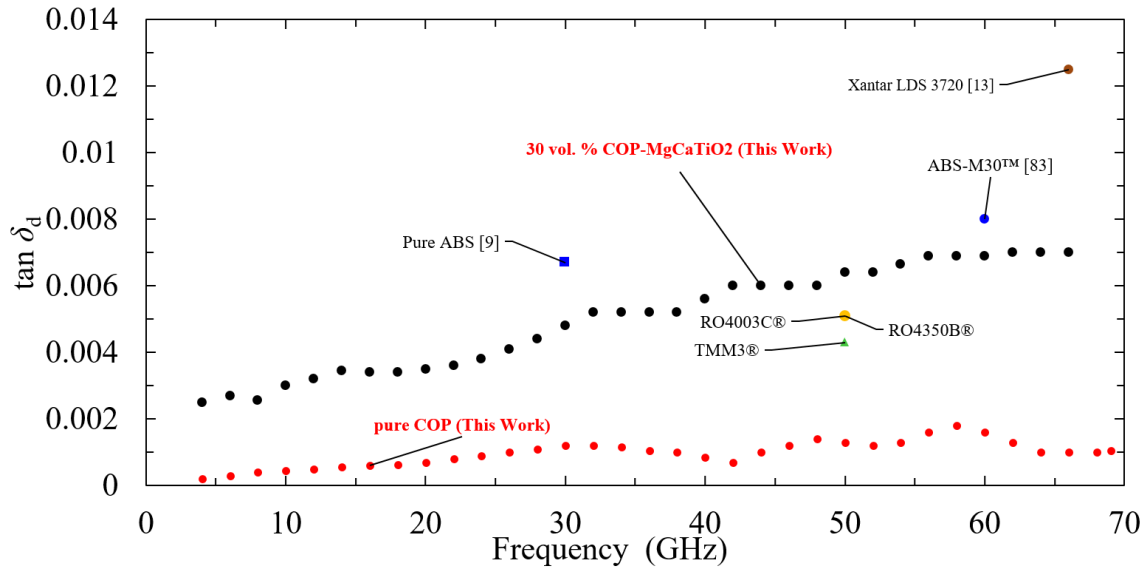


Figure 7.4 – Comparison of measured dielectric loss properties up to 69 GHz of both a pure COP (ZEONEX® RS420) and a 30 vol. % COP-MgCaTiO<sub>2</sub> EM composites with commercial microwave laminates from Rogers Corporation [27]. Other materials are shown in Table 7.1.



Table 7.1 – Comparison of measured EM properties of composite materials vs. prior works in the mm-wave spectrum up to V-band

Composites or Laminates	Year	Technology	Filler	F. (GHz)	$\epsilon_r$	$\tan \delta_d$	Reference
Grilamid 1SVX-50H LDS ‡					4.20	0.0240	
Vestamid HTplus LDS1031 ‡					4.30	0.0210	
Xantar LDS 3720	2014	LDS-MID	N/A	66	3.00	0.0125	[13]
Xantar LDS 3732					3.60	0.0140	
Vectra 840i LDS					4.00	0.0125	
Pure ABS	2015	FDM	N/A	30	2.35	0.0067	[9]
Pure ABS-M30™	2014	FDM	N/A	60	2.48	0.0080	[83]
				69	2.10	0.0011	
Pure COP ZEONEX® (RS420)			N/A	50	2.10	0.0013	
				30	2.10	0.0012	
	2017	FDM		66	4.88	0.0070	<b>This Work</b>
COP-MgCaTiO <sub>2</sub> (sintered 1200°C)			30 vol. %	50	4.50	0.0064	
				30	4.68	0.0048	
RO4003C®					3.36	0.0051	
RO3003®					2.99	0.0017	
RT/duroid® 5870					2.32	0.0015	
RT/duroid® 5880					2.19	0.0009	
RO4350B®	2003	Laminate	N/A	50	2.99	0.0051	[27], Rogers Corp. ‡
TMM3®					3.23	0.0043	
RT/duroid® 6002					2.93	0.0027	
RT/duroid® 6010LM					10.18	0.0033	
RO3006®					6.14	0.0028	

‡Laser Direct Structureable (LDS)-Molded Interconnect Device (MID), LDS-MID materials.

‡For all the Rogers Corporation microwave laminates. These are the reported values in technical report 5788 by using a Damaskos Inc. cylindrical cavity resonator and a HP 8510C network analyzer [27].

### 7.3.2 Thermal Assessment of Pure Thermoplastics and Ceramic-Thermoplastic Composites

Thermal stability plays a critical role while choosing materials for some applications such as space, aerospace, etc. The coefficient of thermal expansion (CTE) gauges how a material changes its dimensions during heating or cooling. Typically, most materials shrink while cooling and expand when heated. The CTE value should be as low as possible or as close as possible to the value of conductive materials in a laminated microwave substrate (e.g., 17 ppm/°C for copper) [84].

Thermal expansion measurements were performed on FDM 3D-printed cylindrical and rectangular specimens with the use of a thermomechanical analyzer (TMA) system Q400 (TA Instruments, New Castle, DE, USA). Table 7.1 shows the glass-transition temperature ( $T_g$ ), the linear CTE from -25°C to 100°C, CTE at 20°C, melting temperature, and heat deflection temperature (HDT) for EM composites based on COP matrix, which are compared with other widely used thermoplastic materials. The materials based on ABS and COP were characterized from -25°C to 200°C, while ULTEM™ 9085 and PPSF from Stratasys, Ltd. were characterized from -25°C to 300°C. Figure 7.5 depicts the comparison of the measured CTEs of some of the FDM-ready thermoplastics explored in this work as compared with COP (ZEONEX® RS420).

The glass-transition temperature  $T_g$  decreased about 13°C when reinforcing the COP matrix with the MgCaTiO<sub>2</sub> ceramic fillers sintered at 1200°C, the measured  $T_g$  of pure COP is 133°C while the measured  $T_g$  for 30 vol. % COP-MgCaTiO<sub>2</sub> 1200°C is roughly 120°C. On the other hand, the  $T_g$  decreased about 10°C when loading the COP matrix with the TiO<sub>2</sub> ceramic fillers sintered at 1200°C. The measured  $T_g$  for 30 vol. % COP-TiO<sub>2</sub> composite is 123°C. Figure 7.6 depicts the comparison of three variations of COP, including ZEONEX® RS420, ZEONEX® RS420-LDS and ZEONOR® 1420R, which are compared with the 30 vol. % COP-MgCaTiO<sub>2</sub> and

30 vol. % COP-TiO<sub>2</sub> composites made of filters sintered at 1200°C. Also the CTE at 20°C decreased about 13 ppm/°C when reinforcing the COP matrix with the MgCaTiO<sub>2</sub> ceramic fillers sintered at 1200°C, the measured CTE of pure COP is 97.7 ppm/°C while the measured CTE for 30 vol. % COP-MgCaTiO<sub>2</sub> 1200°C is roughly 85 ppm/°C.

As observed in Table 7.2, the  $T_g$  of COP is 20°C higher than that of comparing ABS. Meanwhile, the CTE's of COP such as ZEONEX<sup>®</sup> (RS420) and ABS from SABIC Cycolac<sup>™</sup> (MG47) are very similar. It was observed that ZEONOR<sup>®</sup> (1420R) exhibited the lowest linear CTE of 62 ppm/ °C amongst the three variations of 3D-printed COP, which indicate it is an excellent choice as a thermoplastic matrix for the next generation of FDM EM composites. Moreover, due to the ZEONOR<sup>®</sup> (1420R)'s low CTE, it has been used as polymer matrix for PMCs improving the composite's CTE as reported by Takahashi *et al.* [86].

It was observed that the reinforced 30 vol. % COP-MgCaTiO<sub>2</sub> composites show a linear CTE from -25°C to 100°C, which is about 30 ppm/ °C lower as compared to that of the unloaded COP ZEONEX<sup>®</sup> (RS420). Similarly, the measured CTE of 30 vol. % COP-MgCaTiO<sub>2</sub> composite is about 20 ppm/°C, 30ppm/°C and 10ppm/°C lower than that of the ABS White, ABS from SABIC Cycolac<sup>™</sup> (MG47), and ULTEM<sup>™</sup> 9085, respectively, while approaching the low linear CTE of PPSF.

Also, it was observed that the CTE from the 30 vol. % COP-MgCaTiO<sub>2</sub> (sintered 1200°C) is about 20 ppm/°C lower when compared with the ABS white from ultimachine widely used by the research community working in 3D printed RF/microwave devices [1]-[9]. Also ZEONOR<sup>®</sup> (1420R) CTE is 61.4 ppm/°C very close to the CTE values of high-performance and high-temperature ULTEM<sup>™</sup> 9085 resin (polyetherimide (PEI)) and PPSF/PPSU (polyphenylsulfone).

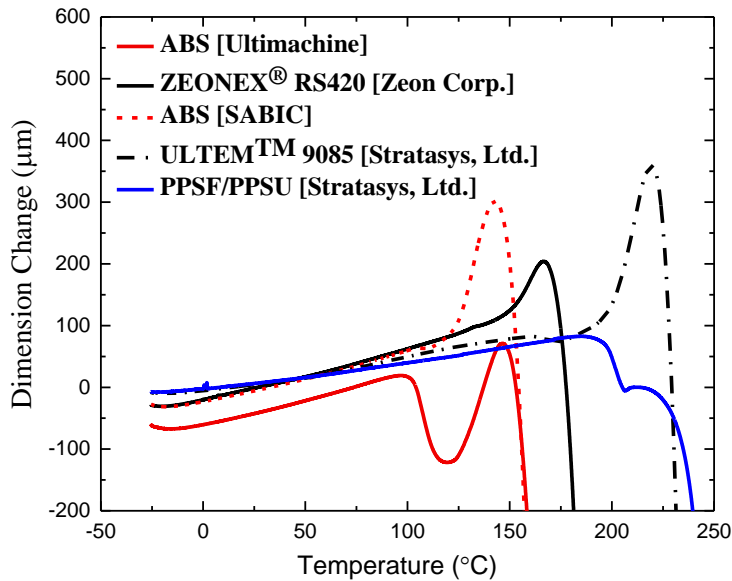


Figure 7.5 – Comparison of measured CTEs of 3D-printed pure (unloaded) thermoplastics. Materials are shown in Table 7.2.

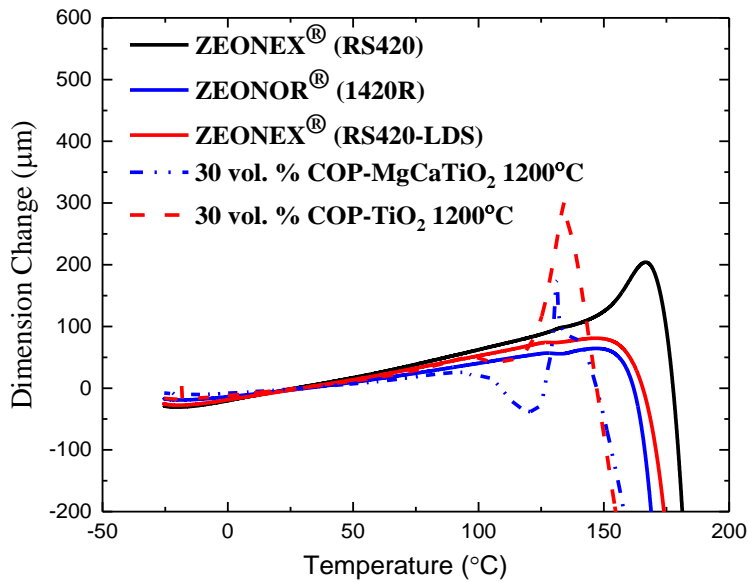


Figure 7.6 – Comparison of measured CTEs of 3D-printed three variations of COP and COP-ceramic based composites. Materials are shown in Table 7.2.

## 7.4 Conclusion

Two types of low-loss FDM composite materials for direct digital manufacturing (DDM) technologies are developed and characterized at V-band frequencies. Pure COP thermoplastic exhibits a relative permittivity of 2.1 and a loss tangent below 0.0011 at 69 GHz, whereas 30 vol. % COP-MgCaTiO<sub>2</sub> composites show a relative permittivity of 4.88 and a loss tangent below 0.0070 at 66 GHz. This new class of high-*k*, low-loss composite materials has shown some promising attributes for enabling the next generation of high-performance 3D-printed RF and microwave devices and antennas operating at the mm-wave frequencies.

Table 7.2 – Measured thermal properties of FDM materials tested in this dissertation with a TMA Q400 instrument

Thermoplastic / Composite	Material	Vendor	$T_g$ (°C)	Linear CTE (-25°C to 100°C) $\mu\text{m}/(\text{m}\cdot^\circ\text{C})$	CTE At 20°C (ppm/°C)	Melting Temp. (°C)	(HDT) @264 psi <sup>†</sup>
ULTEM™ 9085	(PEI)	Stratasys,	193	75.99	61.9	350-400	153
Polyphenylsulfone	(PPSF/PPSU)	Ltd.	202	58.04	55.8	N/A	189
ULTEM™ (1000)	(PEI)	SABIC	217 <sup>†</sup>	N/A	N/A	350-400	201
Cycolac™ (MG47)	(ABS)	SABIC	110	95.69	97.1	216-260	176
ZEONEX® (RS420)			133	96.55	97.7		134
ZEONOR® (1420R)	(COP)	ZEON	126	61.86	61.4	250-300	N/A
ZEONEX® (RS420-LDS)		Corp.	121	83.88	86.4		134
ABS White	(ABS)	Ultimachine	103	86.69	103	216-260	N/A
30 vol. % COP-MgCaTiO <sub>2</sub> (sintered 1200°C) <sup>‡</sup>			120	64.42	84.8	250	N/A
30 vol. % COP-TiO <sub>2</sub> (sintered 1200°C) <sup>‡</sup>	<b>EM Composite</b>	<b>This Work</b>	123	104.2	90.9		N/A
25 vol. % COP-Ba <sub>3</sub> Co <sub>2</sub> Fe <sub>24</sub> O <sub>41</sub> (sintered 1200°C) <sup>‡</sup>			129	65.91	92.9	240	N/A
30 vol. % COP/MgO	Composite	[86]	N/A	N/A	35	N/A	N/A

<sup>†</sup> Reported in datasheets

Heat Deflection Temperature (HDT)

<sup>‡</sup> ZEONEX® (RS420) [COP] was used as polymer matrix in these composites.

## CHAPTER 8 : CONCLUSIONS AND FUTURE WORK

### 8.1 Future Work and Recommendations

Based on the results gained by this dissertation research work, there are a few remaining aspects listed as the following that need further research investigations:

- Explore new methodologies for increasing filler volume loading concentrations by using solvent assisted dispersion processes via a solvent such as xylene or cyclohexane that dissolves the thermoplastic COP while forming the final EM composites in the solvent suspension;
- Explore powder binder jetting techniques to increase the volume fraction of ceramic fillers by not using a thermoplastic or polymer matrix for 3D-printing of microwave structures and components;
- Investigate micro-dispensing of filler-loaded composite pastes/slurries to further extend highest achievable volume fraction ratio of ceramic fillers that increase permittivity for printable dielectrics;
- Conduct more detailed studies on the effect of the surface coating materials at the interface between inorganic fillers and organic matrix by exploring new kinds of hyperdispersants, plasticizers, or another type of surface coating layers;
- Study adhesion methods to improve the bonding between the COP and COP-ceramic composites and the silver paste (CB028) layer after the micro-dispensing processes followed by the curing/drying process such as introducing groups into polymer chains as recommended by Cui et al. [85] or other methodologies. Similarly exploring

adhesion promoters for cyclic olefin resin compositions as suggested by Cruce et al. [87];

- Also for practical electronic/microwave applications and to improve reliability, the CTE of the FDM-printed EM composite and the silver paste (CB028) should be as close as possible, hence CTE characterization of CB028 from  $-25^{\circ}\text{C}$  to  $200^{\circ}\text{C}$  is recommended to be performed, if there is a significant mismatch, it is recommended to explore a new metal paste, or develop a new FDM EM composite;
- Demonstrate the low-loss characteristics of a printed 30 vol. % COP-TiO<sub>2</sub> composite substrate through the design of hairpin filters for Ku-band, which results in a simulated insertion loss of 6 dB at a center frequency of 13 GHz. The preliminary design was rigorously compared with a design based on a commercial laminate core (Rogers RT/duroid® 5870), demonstrating 45% smaller size;
- Based on the measured dielectric performance of ZEONOR® (1420R) with  $\epsilon_r$  of 2.15 and a  $\tan \delta_d$  lower than 0.0016 (as shown in Table 5.3 and Figure 5.13), along with the measured superb thermal properties (e.g., T<sub>g</sub> of  $126^{\circ}\text{C}$  and the lowest CTE of 61.4 ppm/ $^{\circ}\text{C}$  at  $20^{\circ}\text{C}$  amongst the three variations of 3D-printed COPs), which are better than most of the thermoplastics shown in Table 7.2 and very close to the measured values of ULTEM™ 9085 and (PPSF/PPSU) from Stratasys, Ltd., it is an excellent candidate as a thermoplastic matrix for the next generation of FDM EM composites.

## 8.2 Conclusions

A variety of high-permittivity (high- $k$ ) and low-loss ceramic-thermoplastic composite materials as fused deposition modeling (FDM) feedstocks, based on cyclo-olefin polymer (COP) embedded with sintered ceramic fillers, have been developed and investigated for direct digital



manufacturing (DDM) of microwave components. The composites presented in this dissertation use a high-temperature sintering process up to 1500°C to further enhance the dielectric properties of the ceramic fillers. The electromagnetic (EM) properties of these newly developed FDM composites were characterized up to the Ku-band by the cavity perturbation technique. Several models for prediction of the effective relative dielectric permittivity of composites based on the filler loading volume fraction have been evaluated, among which Hanai-Bruggeman and Maxwell models have shown the best accuracy with less than 2% and 5% discrepancies, respectively.

The 30 vol. % COP-TiO<sub>2</sub> FDM-ready composites with fillers sintered at 1200°C have exhibited a relative permittivity ( $\epsilon_r$ ) of 4.78 and a dielectric loss tangent ( $\tan \delta_d$ ) lower than 0.0012 at 17 GHz. Meanwhile, the 30 vol. % COP-MgCaTiO<sub>2</sub> composites with fillers sintered at 1200°C have exhibited an  $\epsilon_r$  of 4.82 and a  $\tan \delta_d$  lower than 0.0018. The DDM approach combines FDM of the engineered EM composites and micro-dispensing for deposition of conductive traces to fabricate by 3D-printing edge-fed patch antennas operating at 17.2 GHz and 16.5 GHz. These antenna devices were demonstrated by employing a 25 vol. % COP-MgCaTiO<sub>2</sub> composite FDM filament with the fillers sintered at 1100°C and a pure COP filament, which were both prepared and extruded following the process described in this dissertation. The low dielectric loss of the 25 vol. % COP-MgCaTiO<sub>2</sub> composite material ( $\tan \delta_d$  lower than 0.0018) has been leveraged to achieve a peak realized gain of 6 dBi. Also, the high-permittivity ( $\epsilon_r$  of 4.74), which corresponds to an index of refraction of 2.17, results in a patch area miniaturization of 50% when compared with an antenna designed and DPAM-printed over a Rogers RT/duroid® 5870 laminate core through micro-dispensing of CB028 silver paste. This reference antenna exhibited a measured peak realized gain of 6.27 dBi, which is on par with the printed 25 vol. % COP-MgCaTiO<sub>2</sub> based antenna.

Also, two low-loss FDM composite materials for DDM technologies are presented and characterized at V-band (mm-wave) frequencies. Pure COP thermoplastic exhibits a dielectric permittivity  $\epsilon_r$  of 2.1 and a low tangent  $\tan \delta_d$  below 0.0011 at 69 GHz, whereas 30 vol. % COP-MgCaTiO<sub>2</sub> composites with fillers sintered at 1200°C show an  $\epsilon_r$  of 4.88 and a  $\tan \delta_d$  below 0.0070 at 66 GHz. To the best of my knowledge, these EM properties (combination of high-permittivity and low-loss) are superior to other 3D-printable microwave materials reported by the scientific microwave community and are on par with materials developed for high-performance microwave laminates by RF/microwave industry as shown in Chapter 7 and summarized in Table 7.1. Meanwhile, the linear coefficient of thermal expansion (CTE) from -25°C to 100°C of the reinforced 30 vol. % COP-MgCaTiO<sub>2</sub> composite with fillers sintered at 1200°C is 64.42 ppm/°C, which is about 20 ppm/°C lower when compared with pure ABS and 10 ppm/°C lower as compared to high-temperature polyetherimide (PEI) ULTEM™ 9085 from Stratasys, Ltd. The CTE at 20°C of the same composite material is 84.8 ppm/°C which is about 20 ppm/°C lower when compared with pure ABS that is widely used by the research community for 3D printed RF/microwave devices by FDM. The electromagnetic (EM) composites with tailored EM properties studied by this work have a great potential for enabling the next generation of high-performance 3D-printed RF/microwave devices and antennas operating at the Ku-band, K-band, and mm-wave frequencies.

### 8.3 Acknowledgments for Sponsors and Facilities

I'd like to thank Rogers corp., isola group, Ferro corp., Trans-Tech, Inc., Premix group, ZEON corp. for providing samples or technical support in some experiments in this chapter. All the SEM, XRD, EDS, AFM, 3D-printing process and 2D surface profile measurements were conducted at the Nanotechnology Research and Education Center, (NREC-USF)<sup>3</sup> facility in

---

<sup>3</sup> NREC: <http://www.nrec.usf.edu/>

Tampa, FL. The nanocomposite fabrication processes were carried out at the RF-MEMS Transducers Laboratory<sup>4</sup>, IDR-USF Research Park in Tampa, FL., the complex permittivity and permeability measurements in Ku-band and K-band, NFMM measurements were performed at the Center for Wireless and Microwave Information Systems (WAMI)<sup>5</sup>, USF in Tampa, FL. High-temperature sintering processes from (1340°C to 1500°C) in some samples were conducted at Dr. Yoon, Yong-Kyu, Interdisciplinary Microsystems Lab, University of Florida (UF)<sup>6</sup>, Gainesville, FL.

I'd like to thank Dr. Mike Hill from (Trans-Tech, Inc. a division of Skyworks) for providing some recommendations in some experiments. Likewise Mark Nevitt from (ZEON Corporation) for providing ZEONEX<sup>®</sup> RS420-LDS samples and others materials, similarly Charles Douglas from Lubrizol Corporation for providing hyperdispersant samples. Moreover, I would like to thank Art Perez, Ana Lopez Marcano and Benjamin Rice for their support in some experiments. Additionally, I'd like to thank Janice Casagrande, Dr. Peter Krenz, Dr. David Rolando and Dr. Jeff Tharp all of them from (ANSYS, Inc.), for their support related to EM simulations. Similarly, I'd like to thank Dr. Nick Damaskos and team from Damaskos, Inc. in Chadds Ford, PA<sup>7</sup> for the mm-wave dielectric characterization in two samples presented in this dissertation. Also, I'd like to thank Gail Borden and John Coonrod from Rogers Corporation for providing me with the technical report 5788 for Rogers microwave laminates mm-wave characterization. Furthermore, I am very grateful to Daniel Harshbarger, Tomas Lopez Lauterio, and Meenal R Vaidya, all of them from Cummins Inc. for the opportunity to work with them in summer 2016.

---

<sup>4</sup> RF-MEMS Transducers Laboratory: <http://transducers.eng.usf.edu/>

<sup>5</sup> WAMI Center: <http://wami.eng.usf.edu/>

<sup>6</sup> IMG-UF: <http://www.img.ufl.edu/>

<sup>7</sup> Damaskos, Inc.: <http://www.damaskosinc.com/>

## REFERENCES

- [1] K. H. Church, N. B. Crane, P. I. Defenbaugh, T. P. Ketterl, C. G. Neff, P. B. Nesbitt, J. T. Nussbaum, C. Perkowski, H. Tsang, J. Castro, J. Wang, and T. M. Weller, "Multimaterial and Multilayer Direct Digital Manufacturing of 3-D Structural Microwave Electronics," *Proceedings of the IEEE*, vol. 105, no.4, pp. 688–701, March 2017.
- [2] T. P. Ketterl, Y. Vega, N. C. Arnal, J. W. I. Stratton, E. A. Rojas-Nastrucci, M. F. Cordoba-Erazo, M. M. Abdin, C. W. Perkowski, P. I. Deffenbaugh, K. H. Church, and T. M. Weller, "A 2.45 GHz Phased Array Antenna Unit Cell Fabricated Using 3-D Multi-Layer Direct Digital Manufacturing," *IEEE Trans. Microwave Theory Techn.*, vol. 63, no. 12, pp. 4382–4394, Dec. 2015.
- [3] P.I. Deffenbaugh, R.C. Rumpf, and K.H. Church, "Broadband Microwave Frequency Characterization of 3-D Printed Materials," *IEEE Transactions on Components, Packaging and Manufacturing Technology*, vol. 3, no. 12, pp. 2147–2155, Dec. 2013.
- [4] N. Delhote, D. Baillargeat, S. Verdeyme, C. Delage, and C. Chaput, "Ceramic Layer-By-Layer Stereolithography for the Manufacturing of 3-D Millimeter-Wave Filters," *IEEE Transactions on Microwave Theory and Techniques*, vol. 55, no. 3, pp. 548–554, Mar. 2007.
- [5] J. O'Brien, M.Córdoba-Erazo, E. Rojas, J. Castro, M. Abdin, G. Mumcu, J. Wang, K. Church, P. Deuffenbaugh, and T. Weller, "Miniaturization of Microwave Components and Antennas Using 3D Manufacturing," *9<sup>th</sup> European Conference on Antennas and Propagation (EuCAP 2015)*, pp.1-4, Lisbon Portugal, Apr. 2015.
- [6] P. Deffenbaugh, K. Church, J. Goldfarb, and X. Chen, "Fully 3D-printed 2.4 GHz Bluetooth/Wi-Fi Antenna," *International Symposium on Microelectronics, IMAPS*, vol. 2013, no. 1, pp. 914–920, Jan. 2013.
- [7] I.T. Nassar, T.M. Weller, and H. Tsang, "A 3D-printed Miniaturized Log-Periodic Dipole Antenna," *IEEE Antennas and Propagation Society International Symposium (APSURSI)*, pp. 11-12, Memphis, TN, July 2014.
- [8] P. I. Deffenbaugh, T. M. Weller, and K. H. Church, "Fabrication and Microwave Characterization of 3-D Printed Transmission Lines," *IEEE Microwave and Wireless Components Letters*, vol. 25, no. 12, pp. 823–825, Dec. 2015.
- [9] A.L.Vera-Lopez, E. Rojas, M.C-Erazo T. Weller, and J. Papapolymerou, "Ka-Band Characterization and RF Design of Acrylonitrile Butadiene Styrene (ABS)," *IEEE MTT-S International Microwave Symposium (IMS)*, pp. 1-4, May 2015.

- [10] J. Castro, E. Rojas, A. Ross, T. Weller, and J. Wang, "High-k and low-loss thermoplastic composites for Fused Deposition Modeling and their application to 3D-printed Ku-band antennas," *IEEE MTT-S International Microwave Symposium (IMS)*, pp.1-4, May 2016.
- [11] M. Vaezi, H. Seitz, and S. Yang, "A review on 3D micro-additive manufacturing technologies," *The International Journal of Advanced Manufacturing Technology*, vol. 67, no. 5–8, pp. 1721–1754, Nov. 2012.
- [12] A. Friedrich, B. Geck, O. Klemp, and H. Kellermann, "On the design of a 3D LTE antenna for automotive applications based on MID technology," *European Microwave Conference (EuMC)*, Nuremberg, pp. 640-643, Oct. 2013.
- [13] Q. H. Dao, A. Friedrich, and B. Geck, "Characterization of Electromagnetic Properties of MID Materials for High-Frequency Applications up to 67 GHz," *Advanced Materials Research*, vol. 1038, pp. 63–68, Sep. 2014.
- [14] M. M. Abdin, J. Castro, J. Wang, and T. Weller, "Miniaturized 3D printed balun using high-k composites," *2015 IEEE 16th Annual Wireless and Microwave Technology Conference (WAMICON)*, pp. 1-3, Apr. 2015.
- [15] J. M. O'Brien, J. E. Grandfield, G. Mumcu, and T. M. Weller, "Miniaturization of a Spiral Antenna Using Periodic Z-Plane Meandering," *IEEE Transactions on Antennas and Propagation*, vol. 63, no. 4, pp. 1843–1848, Apr. 2015.
- [16] J. O'Brien, "Medium Power, Compact Periodic Spiral Antenna," Thesis, M.S. EE, Dept. Elect. Eng., University of South Florida, Tampa, FL., USA, 2013.
- [17] J. Castro, E. Rojas, A. Ross, T. Weller, and J. Wang, "Fabrication, Modeling, and Application of Ceramic-Thermoplastic Composites for Fused Deposition Modeling of Microwave Components," *IEEE Trans. On Microwave Theory and Techniques*, vol. PP, issue. 99, pp. 1-12, February 2017.
- [18] M. D'Auria, W. J. Otter, J. Hazell, B. T. W. Gillatt, C. Long-Collins, N. M. Ridler, and S. Lucyszyn, "3-D printed metal-pipe rectangular waveguides," *IEEE Transactions on Components, Packaging and Manufacturing Technology*, vol. 5, no. 9, pp. 1339-1349, Sept. 2015.
- [19] J. Kimionis, M. Isakov, B. S. Koh, A. Georgiadis and M. M. Tentzeris, "3D-printed origami packaging with inkjet-printed antennas for RF harvesting sensors," *IEEE Transactions on Microwave Theory and Techniques*, vol. 63, no. 12, pp. 4521-4532, Dec. 2015.
- [20] S. Scott Crump, Stratasys, Inc., "Apparatus and method for creating three-dimensional objects," U.S. Patent 5,121,329, June 9<sup>th</sup>, 1992.
- [21] S. Scott Crump, Stratasys, Inc., "Modeling Apparatus for three-dimensional objects," U.S. Patent 5,340,433 A, August 8<sup>th</sup>. 1994.

- [22] S. Scott Crump, J.W. Comb, W.R. Priedeman, Jr. and R.L. Zinniel, Stratasys, Inc., "Process of support removal for fused deposition modeling," U.S. Patent 5,503,785 A, April, 2<sup>nd</sup>, 1996.
- [23] P.I. Deffernbaugh, 3D-printed Electromagnetic Transmission and Electronic Structures Fabricated on a Single Platform Using Advanced Process Integration Techniques, Ph.D. Dissertation, The University of Texas at El Paso, Texas, USA, 2014.
- [24] U. Robles, "3D Printed Impedance Elements by Micro-Dispensing," Thesis, M.S. EE, Dept. Elect. and Comp. Eng., The University of Texas at El Paso, Texas, USA, 2013.
- [25] M. F. Cordoba-Erazo, E. A. Rojas-Nastrucci, and T. Weller, "Simultaneous RF electrical conductivity and topography mapping of smooth and rough conductive traces using microwave microscopy to identify localized variations," *IEEE 16th Annual Wireless and Microwave Technology Conference*, (WAMICON), pp.1-4, Apr. 2015.
- [26] Z.-M. Dang, J.-K. Yuan, J.-W. Zha, T. Zhou, S.-T. Li, and G.-H. Hu, "Fundamentals, processes, and applications of high-permittivity polymer-matrix composites," *Progress in Materials Science*, vol. 57, no. 4, pp. 660–723, May 2012.
- [27] A. Horn, "Dielectric constant and loss of selected grades of Rogers high-frequency circuit substrates from 1-50 GHz," Rogers Corp., Corporate Headquarters, One Technology Drive, Rogers, CT 06263, Tech. Rep. 5788 (1-18), Sep. 2003.
- [28] C. Gray, A. Roach, S. Rappaport, A. Dineen, R. Irion, "High Dielectric Constant, Low Loss Additive Manufacturing Materials for RF/Microwave Applications", *IMAPS New England*, May 2016.
- [29] S. Havriliak and S. Negami, "A complex plane representation of dielectric and mechanical relaxation processes in some polymers," *Polymer*, vol. 8, pp. 161–210, Jan. 1967.
- [30] W. Wersing, "Microwave ceramics for resonators and filters," *Current Opinion in Solid State and Materials Science*, vol. 1, no. 5, pp. 715–731, Oct. 1996.
- [31] L. Li, X. M. Chen, and X. C. Fan, "Characterization of MgTiO<sub>3</sub>-CaTiO<sub>3</sub>-Layered Microwave Dielectric Resonators with TE<sub>01</sub>delta Mode," *Journal of the American Ceramic Society*, vol. 89, no. 2, pp. 557–561, Feb. 2006.
- [32] J. Castro, C. Morales, T. Weller, J. Wang, H. Srikanth, "Synthesis and characterization of low-loss Fe<sub>3</sub>O<sub>4</sub>-PDMS magneto-dielectric polymer nanocomposites for RF applications," *IEEE MTT-S Wireless and Microwave Technology Conference 2014, WAMICON 2014*, pp.1-5, Jun. 2014.
- [33] Y. Shirakata, N. Hidaka, M. Ishitsuka, A. Teramoto, and T. Ohmi, "High Permeability and Low Loss Ni-Fe Composite Material for High-Frequency Applications," *IEEE Transactions on Magnetics*, vol. 44, no. 9, pp. 2100-2106, Sep. 2008.

- [34] C. Morales, J. Dewdney, S. Pal, S. Skidmore, K. Stojak, H. Srikanth, T. Weller, and J. Wang, "Tunable Magneto-Dielectric Polymer Nanocomposites for Microwave Applications," *IEEE Trans. Microwave Theory Techn.*, vol. 59, no. 2, pp. 302–310, Feb. 2011.
- [35] C. Morales, J. Dewdney, S. Pal, K. Stojak, H. Srikanth, J. Wang, and T. Weller, "Magnetically tunable nanocomposites for microwave applications," *2010 IEEE MTT-S International Microwave Symposium*, May 2010.
- [36] K. Stojak, S. Pal, H. Srikanth, C. Morales, J. Dewdney, T. Weller, and J. Wang, "Polymer nanocomposites exhibiting magnetically tunable microwave properties," *Nanotechnology*, vol. 22, no. 13, p. 135602, Feb. 2011.
- [37] H. Mosallaei, and K.Sarabandi, "Engineered meta-substrates for antenna miniaturization," *Proc. of URSI EMTS*, vol.1, pp.191-193, 2004.
- [38] J. Castro, E. Rojas, T. Weller, J. Wang, "High- $k$  and Low-Loss Polymer Composites with Sintered Nd and Mg-Ca Titanates for 3D RF and Microwave Printed Devices: Fabrication and Characterization," *IEEE MTT-S Wireless and Microwave Technology Conference (WAMICON 2015)*, pp. 1-5, Cocoa, Beach FL., April. 2015.
- [39] S. Koulouridis, G. Kiziltas, Y. Zhou, D. J. Hansford, and J. L. Volakis, "Polymer-Ceramic Composites for Microwave Applications: Fabrication and Performance Assessment," *IEEE Trans. Microwave Theory Techn.*, vol. 54, no. 12, pp. 4202–4208, Dec. 2006.
- [40] J. Castro, T. Weller, J. Wang "An Improved Fabrication Method of High- $k$  and Low-Loss Polymer Composites with Sintered Ceramic Fillers for Microwave Applications," *IEEE MTT-S International Microwave Symposium (IMS 2015)*, pp.1-4, May 2016.
- [41] D. Cure, "Reconfigurable Low Profile Antennas Using Tunable High Impedance Surfaces", Ph.D. Dissertation, Dept. Elect. Eng., University of South Florida, Tampa FL., USA, Jan. 2013.
- [42] Y. Shi, L. M. Bhowmik, A. K. Amert, and K. W. Whites, "An effective method for fabrication of 3-D dielectric materials using polymer-ceramic composites," *2014 IEEE Antennas and Propagation Society International Symposium (APSURSI)*, pp. 225-226, Jul. 2014.
- [43] G. Kiziltas, C. Yilmaz, J. L. Volakis, N. Kikuchi, and J. Halloran, "Design of metamaterial textures for microwave applications," *IEEE Antennas and Propagation Society International Symposium* (IEEE Cat. No.02CH37313), 2002.
- [44] G. Kiziltas, J. L. Volakis, and N. Kikuchi, "Metamaterial design via the density method," *IEEE Antennas and Propagation Society International Symposium* (IEEE Cat. No.02CH37313), 2002.



- [45] G. Kiziltas, D. Psychoudakis, J. L. Volakis, and N. Kikuchi, "Topology design optimization of dielectric substrates for bandwidth improvement of a patch antenna," *IEEE Trans. Antennas Propagat.*, vol. 51, no. 10, pp. 2732–2743, Oct. 2003.
- [46] Y.-H.Koh, A. Knapp, J. W. Halloran, H.-W. Kim, and H.-E. Kim, "Co-Firing of Spatially Varying Dielectric Ca-Mg-Silicate and Bi-Ba-Nd-Titanate Composite," *Journal of the American Ceramic Society*, vol. 88, no. 10, pp. 2690–2695, Oct. 2005.
- [47] B. Zhang, F. Ye, S. Liu, Q. Liu, and Y. Gao, "High- $k$  and ultra-low-loss BADCy/Ni<sub>0.5</sub>Ti<sub>0.5</sub>NbO<sub>4</sub> composites for PCB application fabricated by cold isostatic pressing and vacuum assisted infiltration processes," *Journal of Materials Science: Materials in Electronics*, Jul. 2015.
- [48] J. Zhang, Y. Zhou, B. Peng, Z. Xie, X. Zhang, and Z. Yue, "Microwave Dielectric Properties and Thermally Stimulated Depolarization Currents of MgF<sub>2</sub>-Doped Diopside Ceramics," *Journal of the American Ceramic Society*, vol. 97, no. 11, pp. 3537–3543, Aug. 2014.
- [49] J. Castro, E. Rojas, T. Weller, and J. Wang, "Engineered Nanocomposites for Additive Manufacturing of Microwave Electronics," *International Symposium on Microelectronics*, vol. 2015, no. 1, pp. 189–196, Jan. 2015.
- [50] J. Castro, E.Rojas, T. Weller, and J. Wang, "High-permittivity and Low-Loss Electromagnetic Composites based in Sintered Ba<sub>0.55</sub>Sr<sub>0.45</sub>TiO<sub>3</sub> and MgCaTiO<sub>2</sub> Fillers for Additive Manufacturing and their Application to 3D-printed K-Band Antennas," *Journal of Microelectronics and Electronic Packaging*, vol. 13, no. 3, pp. 102–112, Jul. 2016.
- [51] Q. Zhang and P. J. McGinn, "Imaging of oxide dielectrics by near-field microwave microscopy," *Journal of the European Ceramic Society*, vol. 25, pp. 407-416, 4, Apr. 2005.
- [52] C. Gao, B.Hu, I. Takeuchi, K.-S. Chang, X.-D. Xiang, and G. Wang, "Quantitative scanning evanescent microwave microscopy and its applications in characterization of functional materials libraries," *Measurement Science and Technology*, vol. 16, no.1, p. 248-260, Dec. 2004.
- [53] Z. N. Wing, J. W. Halloran, Q. Zhang, and P. J. McGinn, "Variable Dielectrics in the Calcium Magnesium Titanate System Characterized with Scanning Microwave Microscopy," *Journal of the American Ceramic Society*, vol. 89, no. 5, pp. 1610-1614, May 2006.
- [54] V.V. Talanov, A. Scherz, and A. R. Schwartz, "A Microfabricated Near-Field Scanned Microwave Probe for Noncontact Dielectric Constant Metrology of Low- $k$  Films," in *Microwave Symposium Digest, 2006. IEEE MTT-S International*, pp. 1618-1621, 2006.
- [55] C. Gao, and X.-D. Xiang, "Quantitative microwave near-field microscopy of dielectric properties," *Review of Scientific Instruments*, vol. 69, pp. 3846-3851, Nov. 1998.



- [56] M. F. Córdoba-Erazo, and T. M. Weller, "Near-Field Microwave Microscopy for Non-Destructive Characterization of Polymer-Coated Samples," Submitted to *Review of Scientific Instruments*, 2015.
- [57] A.D. Vyas, V. A.Rana, D. H. Gadani, and A. N. Prajapati, "Cavity perturbation technique for complex permittivity measurement of dielectric materials at X-band microwave frequency," 2008 *International Conference on Recent Advances in Microwave Theory and Applications*, Nov. 2008.
- [58] W. Che, Z. Wang, Y. Chang, and P. Russer, "Permittivity Measurement of Biological Materials with Improved Microwave Cavity Perturbation Technique," 2008 38<sup>th</sup>. *European Microwave Conference*, Oct. 2008.
- [59] David Pozar, (2011, November 22<sup>nd</sup>), *Microwave Engineering*, (4th. edition), Wiley, New York, NY.
- [60] G. Bruggeman, "Calculation of Various Physics Constants in Heterogeneous Substances I Dielectricity Constants and Conductivity of Mixed Bodies from Isotropic Substances," *Annalen der Physik*, Berlin, vol. 416, no. 7, pp. 636-664, 1935.
- [61] T. Hanai, "Theory of the dielectric dispersion due to the interfacial polarization and its application to emulsions," *Kolloid-Zeitschrift*, vol. 171, no. 1, pp. 23-31, Jul. 1960.
- [62] W. Zhou, B.B.Hinojosa, and J. C. Nino, "Applicability of the Bruggeman Equation for Analyzing Dielectric Slurries Containing Ceramic Powders with High Permittivity," *Journal of the American Ceramic Society*, vol. 95, no. 2, pp. 457-460, Dec. 2011.
- [63] G. Raju, (2016, May), *Dielectrics in Electric Fields*, (2<sup>nd</sup>. edition), CRC Press, Taylor & Francis Group, Boca Raton, FL.
- [64] P. Barber, S. Balasubramanian, Y. Anguchamy, S. Gong, A. Wibowo, H. Gao, H. J. Ploehn, and H.-C. zur Loye, "Polymer Composite and Nanocomposite Dielectric Materials for Pulse Power Energy Storage," *Materials*, vol. 2, no. 4, pp. 1697-1733, Oct. 2009.
- [65] C. Brosseau, "Modelling and simulation of dielectric heterostructures: a physical survey from a historical perspective," *J. Phys. D: Appl. Phys.*, vol. 39, no. 7, pp. 1277-1294, Mar. 2006.
- [66] V. Myroshnychenko and C. Brosseau, "Finite-element modeling method for the prediction of the complex effective permittivity of two-phase random statistically isotropic heterostructures," *Journal of Applied Physics*, vol. 97, no. 4, p. 044101, 2005.
- [67] C. P. Wong, T. Marinis, Jianmin Qu, and Yang Rao, "A precise numerical prediction of an effective dielectric constant for polymer-ceramic composite based on effective-medium theory," *IEEE Trans. Comp. Packag. Technol.*, vol. 23, no. 4, pp. 680-683, 2000.

- [68] K.-L. Ying and T.-E. Hsieh, "Sintering behaviors and dielectric properties of nanocrystalline barium titanate," *Materials Science and Engineering: B*, vol. 138, no. 3, pp. 241–245, Apr. 2007.
- [69] D.-H. Yoon, J. Zhang, and B. I. Lee, "Dielectric constant and mixing model of BaTiO<sub>3</sub> composite thick films," *Materials Research Bulletin*, vol. 38, no. 5, pp. 765–772, Apr. 2003.
- [70] R. Piagai, I.-T. Kim, J.-G. Park, and Y.-H. Kim, "Preparation of Magnesium-Calcium Titanate Powders by Alkoxide Precursor Method," *Journal of the American Ceramic Society*, vol. 81, no. 5, pp. 1361–1364, May 1998.
- [71] G. S.Swei, and D.J. Arthur, Rogers Corporation, "Particulate Filled Composite Film and Method of Making Same," U.S. Patent 5,374,453, Dec. 20, 1994.
- [72] D.J. Arthur, G. S.Swei, and P. X. Nguyen, Rogers Corporation, "Dielectric Composite," U.S. Patent 5,354,611, Oct. 11, 1994.
- [73] P. S. Grant, F. Castles, Q. Lei, Y. Wang, J. M. Janurudin, D. Isakov, S. Speller, C. Dancer, and C. R. M. Grovenor, "Manufacture of electrical and magnetic graded and anisotropic materials for novel manipulations of microwaves," *Philosophical Transactions of the Royal Society A: Mathematical, Physical and Engineering Sciences*, vol. 373, no. 2049, pp. 1-14, Jul. 2015.
- [74] D. V. Isakov, Q. Lei, F. Castles, C. J. Stevens, C. R. M. Grovenor, and P. S. Grant, "3D-printed anisotropic dielectric composite with meta-material features," *Materials & Design*, vol. 93, pp. 423–430, Mar. 2016.
- [75] F. Castles, D. Isakov, A. Lui, Q. Lei, C. E. J. Dancer, Y. Wang, J. M. Janurudin, S. C. Speller, C. R. M. Grovenor, and P. S. Grant, "Microwave dielectric characterization of 3D-printed BaTiO<sub>3</sub>/ABS polymer composites," *Scientific Reports*, vol. 6, pp.1-8, Mar. 2016.
- [76] J. Castro, M. Cordoba, T. Weller, and J. Wang, "Enhancement of Microwave Dielectric Properties of Polymer-Ceramic Electromagnetic Composites with MgCaTiO<sub>2</sub> and TiO<sub>2</sub> Micro-fillers through a High-Temperature Sintering Process," *Journal of American Ceramic Society*, submitted to be submitted to external peer-review on April 2017.
- [77] T. Nakatsuka, "Polylactic acid-coated cable," *Fujikura Tech. Rev.*, pp. 39–45, 2011, Rev. 40.
- [78] D. Espalin, D. Muse, E. MacDonald, and R. Wicker, "3-D printing multifunctionality: Structures with electronics," *Int. J. Adv. Manuf. Tech.*, vol. 72, no. 5, pp. 963–978, Mar. 2014.
- [79] Y. Sakabe, N. Wada, and Y. Hamaji, "Grain Size Effects on Dielectric Properties and Crystal Structure of Fine-grained BaTiO<sub>3</sub> Ceramics," *1998 Journal of the Korean Physical Society*, vol. 32, pp. S260-S264, Feb. 1998.

- [80] Constantine A. Balanis. (2005, April 4th.) *Antenna Theory: Analysis and Design*, (3rd Edition), Wiley-Interscience, New Jersey.
- [81] Y. Arbaoui, P. Agaciak, A. Chevalier, V. Laur, A. Maalouf, J. Ville, P. Roquefort, T. Aubry, and P. Queffelec, “3D-printed ferromagnetic composites for microwave applications,” *Journal of Materials Science*, vol. 52, no. 9, pp. 4988–4996, Jan. 2017.
- [82] J. Castro, E.Rojas, T. Weller, and J. Wang, “High- $k$  and Low-Loss Electromagnetic Composites for Direct Digital Manufacturing of mm-wave Devices,” *IEEE Antennas and Propagation Society International Symposium (APSURSI)*, accepted, March 2017.
- [83] A. Bisognin, D. Titz, F. Ferrero, R. Pilard, C. A. Fernandes, J. R. Costa, C. Corre, P. Calascibetta, J.-M. Riviere, A. Poulain, C. Badard, F. Gianesello, C. Luxey, P. Busson, D. Gloria, and D. Belot, “3D printed plastic 60 GHz lens: Enabling innovative millimeter wave antenna solution and system,” *IEEE MTT-S International Microwave Symposium (IMS2014)*, pp. 1-4, Jun. 2014.
- [84] Coonrod, John. “PCB Materials Keep Demanding Satellite Communications On Track,” ROG Blog. N.P., 2017. Web. 10 Mar. 2017.
- [85] J. Cui, J.-X. Yang, Y.-G. Li, and Y.-S. Li, “Synthesis of High Performance Cyclic Olefin Polymers (COPs) with Ester Group via Ring-Opening Metathesis Polymerization,” *Polymers*, vol. 7, no. 8, pp. 1389–1409, Aug. 2015.
- [86] S. Takahashi, Y. Imai, A. Kan, Y. Hotta, and H. Ogawa, “High-frequency dielectric and mechanical properties of cyclo-olefin polymer/MgO composites,” *Polymer Bulletin*, vol. 72, no. 7, pp. 1595–1601, Mar. 2015.
- [87] C.J. Cruce, B. Edgecombe, P.W. Boothe, and M.A. Giardello, Materia, Inc., “Storage Stable Adhesion Promoter Compositions for Cyclic Olefin Resin Compositions,” U.S. Patent 20,150,166,767 A1, June, 18<sup>th</sup>, 2015.

## APPENDICES

## Appendix A: Copyright Permissions

The permission below is for the use of Figure 2.1, and Figure 2.4 in Chapter 2.



RightsLink®

Home

Account Info

Help



**Title:** Multimaterial and Multilayer Direct Digital Manufacturing of 3-D Structural Microwave Electronics  
**Author:** Kenneth H. Church  
**Publication:** Proceedings of the IEEE  
**Publisher:** IEEE  
**Date:** Feb 13, 2017  
Copyright © 2017, IEEE

Logged in as:  
Juan Castro  
Account #:  
3001120566

LOGOUT

### Thesis / Dissertation Reuse

**The IEEE does not require individuals working on a thesis to obtain a formal reuse license, however, you may print out this statement to be used as a permission grant:**

*Requirements to be followed when using any portion (e.g., figure, graph, table, or textual material) of an IEEE copyrighted paper in a thesis:*

- 1) In the case of textual material (e.g., using short quotes or referring to the work within these papers) users must give full credit to the original source (author, paper, publication) followed by the IEEE copyright line © 2011 IEEE.
- 2) In the case of illustrations or tabular material, we require that the copyright line © [Year of original publication] IEEE appear prominently with each reprinted figure and/or table.
- 3) If a substantial portion of the original paper is to be used, and if you are not the senior author, also obtain the senior author's approval.

*Requirements to be followed when using an entire IEEE copyrighted paper in a thesis:*

- 1) The following IEEE copyright/ credit notice should be placed prominently in the references: © [year of original publication] IEEE. Reprinted, with permission, from [author names, paper title, IEEE publication title, and month/year of publication]
- 2) Only the accepted version of an IEEE copyrighted paper can be used when posting the paper or your thesis on-line.
- 3) In placing the thesis on the author's university website, please display the following message in a prominent place on the website: In reference to IEEE copyrighted material which is used with permission in this thesis, the IEEE does not endorse any of [university/educational entity's name goes here]'s products or services. Internal or personal use of this material is permitted. If interested in reprinting/republishing IEEE copyrighted material for advertising or promotional purposes or for creating new collective works for resale or redistribution, please go to [http://www.ieee.org/publications\\_standards/publications/rights/rights\\_link.html](http://www.ieee.org/publications_standards/publications/rights/rights_link.html) to learn how to obtain a License from RightsLink.

If applicable, University Microfilms and/or ProQuest Library, or the Archives of Canada may supply single copies of the dissertation.

The permission below is for the use of Figure 2.2(a).

**From:** Brian Schieman [mailto:bschieman@imaps.org]  
**Sent:** Thursday, March 9, 2017 10:55 AM  
**To:** Castro, Juan <jcastro10@usf.edu>  
**Subject:** RE: Copyright release Journal of Microelectronics and Electronic Packaging Publication and IMAPS 2015 Conference proceeding, J.Castro USF Tampa (PhD Dissertation)

You are able to use that photo. Please reference the source paper in our journal though.

**From:** Castro, Juan [mailto:jcastro10@usf.edu]  
**Sent:** Wednesday, March 8, 2017 8:59 PM  
**To:** Brian Schieman <bschieman@imaps.org>  
**Subject:** RE: Copyright release Journal of Microelectronics and Electronic Packaging Publication and IMAPS 2015 Conference proceeding, J.Castro USF Tampa (PhD Dissertation)

Hello Brian,

I hope you can help me with the copyright letter to be able to use Fig. 8 in my dissertation.

This is the publication:

[1] P. Deffenbaugh, K. Church, J. Goldfarb, and X. Chen, "Fully 3D Printed 2.4 GHz Bluetooth/Wi-Fi Antenna," *International Symposium on Microelectronics*, vol. 2013, no. 1, pp. 000914–000920, Jan. 2013.

Thank you very much in advance.

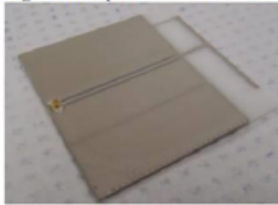
--

My Best Regards!.

Juan Castro,

**From:** Castro, Juan  
**Sent:** Sunday, March 5, 2017 3:59 PM  
**To:** 'Brian Schieman' <bschieman@imaps.org>  
**Subject:** RE: Copyright release Journal of Microelectronics and Electronic Packaging Publication and IMAPS 2015 Conference proceeding, J.Castro USF Tampa (PhD Dissertation)  
Figure 8.

Figure 8 Fully-3D Printed Antenna



Thank you

--

My Best Regards!

Juan

The permission below is for the use of Figure 2.2(b).



RightsLink®

Home

Account Info

Help



**Title:** Miniaturization of a Spiral Antenna Using Periodic Z-Plane Meandering  
**Author:** Jonathan M. O'Brien  
**Publication:** Antennas and Propagation, IEEE Transactions on  
**Publisher:** IEEE  
**Date:** April 2015  
Copyright © 2015, IEEE

Logged in as:  
Juan Castro  
Account #:  
3001120566

LOGOUT

### Thesis / Dissertation Reuse

**The IEEE does not require individuals working on a thesis to obtain a formal reuse license, however, you may print out this statement to be used as a permission grant:**

*Requirements to be followed when using any portion (e.g., figure, graph, table, or textual material) of an IEEE copyrighted paper in a thesis:*

- 1) In the case of textual material (e.g., using short quotes or referring to the work within these papers) users must give full credit to the original source (author, paper, publication) followed by the IEEE copyright line © 2011 IEEE.
- 2) In the case of illustrations or tabular material, we require that the copyright line © [Year of original publication] IEEE appear prominently with each reprinted figure and/or table.
- 3) If a substantial portion of the original paper is to be used, and if you are not the senior author, also obtain the senior author's approval.

*Requirements to be followed when using an entire IEEE copyrighted paper in a thesis:*

- 1) The following IEEE copyright/ credit notice should be placed prominently in the references: © [year of original publication] IEEE. Reprinted, with permission, from [author names, paper title, IEEE publication title, and month/year of publication]
- 2) Only the accepted version of an IEEE copyrighted paper can be used when posting the paper or your thesis on-line.
- 3) In placing the thesis on the author's university website, please display the following message in a prominent place on the website: In reference to IEEE copyrighted material which is used with permission in this thesis, the IEEE does not endorse any of [university/educational entity's name goes here]'s products or services. Internal or personal use of this material is permitted. If interested in reprinting/republishing IEEE copyrighted material for advertising or promotional purposes or for creating new collective works for resale or redistribution, please go to [http://www.ieee.org/publications\\_standards/publications/rights/rights\\_link.html](http://www.ieee.org/publications_standards/publications/rights/rights_link.html) to learn how to obtain a License from RightsLink.

If applicable, University Microfilms and/or ProQuest Library, or the Archives of Canada may supply single copies of the dissertation.



The permission below is for the use of Figure 2.3 in Chapter 2.



RightsLink®

Home

Account Info

Help



**Title:** Miniaturized 3D printed balun using high-*k* composites  
**Conference Proceedings:** Wireless and Microwave Technology Conference (WAMICON), 2015 IEEE 16th Annual  
**Author:** Mohamed M. Abdin  
**Publisher:** IEEE  
**Date:** April 2015  
Copyright © 2015, IEEE

Logged in as:  
Juan Castro  
Account #:  
3001120566

LOGOUT

### Thesis / Dissertation Reuse

**The IEEE does not require individuals working on a thesis to obtain a formal reuse license, however, you may print out this statement to be used as a permission grant:**

*Requirements to be followed when using any portion (e.g., figure, graph, table, or textual material) of an IEEE copyrighted paper in a thesis:*

- 1) In the case of textual material (e.g., using short quotes or referring to the work within these papers) users must give full credit to the original source (author, paper, publication) followed by the IEEE copyright line © 2011 IEEE.
- 2) In the case of illustrations or tabular material, we require that the copyright line © [Year of original publication] IEEE appear prominently with each reprinted figure and/or table.
- 3) If a substantial portion of the original paper is to be used, and if you are not the senior author, also obtain the senior author's approval.

*Requirements to be followed when using an entire IEEE copyrighted paper in a thesis:*

- 1) The following IEEE copyright/ credit notice should be placed prominently in the references: © [year of original publication] IEEE. Reprinted, with permission, from [author names, paper title, IEEE publication title, and month/year of publication]
- 2) Only the accepted version of an IEEE copyrighted paper can be used when posting the paper or your thesis on-line.
- 3) In placing the thesis on the author's university website, please display the following message in a prominent place on the website: In reference to IEEE copyrighted material which is used with permission in this thesis, the IEEE does not endorse any of [university/educational entity's name goes here]'s products or services. Internal or personal use of this material is permitted. If interested in reprinting/republishing IEEE copyrighted material for advertising or promotional purposes or for creating new collective works for resale or redistribution, please go to [http://www.ieee.org/publications\\_standards/publications/rights/rights\\_link.html](http://www.ieee.org/publications_standards/publications/rights/rights_link.html) to learn how to obtain a License from RightsLink.

If applicable, University Microfilms and/or ProQuest Library, or the Archives of Canada may supply single copies of the dissertation.



The permission below is for the use of Figure 2.4 in Chapter 2.



RightsLink®

Home

Account Info

Help



**Title:** A 2.45 GHz Phased Array Antenna Unit Cell Fabricated Using 3-D Multi-Layer Direct Digital Manufacturing  
**Author:** Thomas P. Ketterl  
**Publication:** Microwave Theory and Techniques, IEEE Transactions on  
**Publisher:** IEEE  
**Date:** Dec. 2015  
Copyright © 2015, IEEE

Logged in as:  
Juan Castro  
Account #:  
3001120566

LOGOUT

### Thesis / Dissertation Reuse

**The IEEE does not require individuals working on a thesis to obtain a formal reuse license, however, you may print out this statement to be used as a permission grant:**

*Requirements to be followed when using any portion (e.g., figure, graph, table, or textual material) of an IEEE copyrighted paper in a thesis:*

- 1) In the case of textual material (e.g., using short quotes or referring to the work within these papers) users must give full credit to the original source (author, paper, publication) followed by the IEEE copyright line © 2011 IEEE.
- 2) In the case of illustrations or tabular material, we require that the copyright line © [Year of original publication] IEEE appear prominently with each reprinted figure and/or table.
- 3) If a substantial portion of the original paper is to be used, and if you are not the senior author, also obtain the senior author's approval.

*Requirements to be followed when using an entire IEEE copyrighted paper in a thesis:*

- 1) The following IEEE copyright/ credit notice should be placed prominently in the references: © [year of original publication] IEEE. Reprinted, with permission, from [author names, paper title, IEEE publication title, and month/year of publication]
- 2) Only the accepted version of an IEEE copyrighted paper can be used when posting the paper or your thesis on-line.
- 3) In placing the thesis on the author's university website, please display the following message in a prominent place on the website: In reference to IEEE copyrighted material which is used with permission in this thesis, the IEEE does not endorse any of [university/educational entity's name goes here]'s products or services. Internal or personal use of this material is permitted. If interested in reprinting/republishing IEEE copyrighted material for advertising or promotional purposes or for creating new collective works for resale or redistribution, please go to [http://www.ieee.org/publications\\_standards/publications/rights/rights\\_link.html](http://www.ieee.org/publications_standards/publications/rights/rights_link.html) to learn how to obtain a License from RightsLink.

If applicable, University Microfilms and/or ProQuest Library, or the Archives of Canada may supply single copies of the dissertation.

The permission below is for the use of Figure 3.8 and Figure 3.9 in Chapter 3.

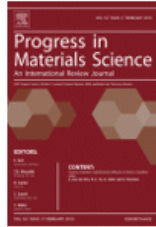


RightsLink®

Home

Account Info

Help



**Title:** Fundamentals, processes and applications of high-permittivity polymer-matrix composites  
**Author:** Zhi-Min Dang, Jin-Kai Yuan, Jun-Wei Zha, Tao Zhou, Sheng-Tao Li, Guo-Hua Hu  
**Publication:** Progress in Materials Science  
**Publisher:** Elsevier  
**Date:** May 2012  
 Copyright © 2011 Elsevier Ltd. All rights reserved.

Logged in as:

Juan Castro

Account #:

3001120566

LOGOUT

**Order Completed**

Thank you for your order.

This Agreement between Juan Castro ("You") and Elsevier ("Elsevier") consists of your license details and the terms and conditions provided by Elsevier and Copyright Clearance Center.

Your confirmation email will contain your order number for future reference.

[Printable details.](#)

License Number	4063430612226
License date	Mar 07, 2017
Licensed Content Publisher	Elsevier
Licensed Content Publication	Progress in Materials Science
Licensed Content Title	Fundamentals, processes and applications of high-permittivity polymer-matrix composites
Licensed Content Author	Zhi-Min Dang, Jin-Kai Yuan, Jun-Wei Zha, Tao Zhou, Sheng-Tao Li, Guo-Hua Hu
Licensed Content Date	May 2012
Licensed Content Volume	57
Licensed Content Issue	4
Licensed Content Pages	64
Type of Use	reuse in a thesis/dissertation
Portion	figures/tables/illustrations
Number of figures/tables/illustrations	8
Format	electronic
Are you the author of this Elsevier article?	No
Will you be translating?	No
Order reference number	
Original figure numbers	Fig. 4, Fig. 5, Fig. 6, Fig. 7, Fig. 8, Fig. 9, Fig. 49
Title of your thesis/dissertation	Engineered Nanocomposite Materials for Microwave/Millimeter-Wave Applications of Fused Deposition Modeling
Expected completion date	Apr 2017
Estimated size (number of pages)	180
Elsevier VAT number	GB 494 6272 12
Requestor Location	Juan Castro 4202 E. Fowler Ave. ENB118 TAMPA, FL 33620 United States Attn: Juan Castro
Publisher Tax ID	98-0397604

The permission below is for the use of material in Chapter 3 and Chapter 4, and Figure 5.7(a).

February 20, 2017

Juan Castro  
Ph.D Candidate in Electrical Engineering  
Center for Wireless and Microwave Information Systems (WAMI)  
Electrical Engineering Department  
University of South Florida  
4202 E.Fowler Avenue, ENB 118  
Tampa, FL 33620

Dear Juan,

Per our email discussions, IMAPS does authorize you to reference or otherwise use the following articles in your upcoming Ph.D dissertation:

- [1] **J. Castro**, E.Rojas, T. Weller, and J. Wang, "High-Permittivity and Low-Loss Electromagnetic Composites Based on Co-Fired  $Ba_{0.55}Sr_{0.45}TiO_3$  or  $MgCaTiO_2$  Micro-Fillers for Additive Manufacturing and Their Application to 3D-Printed K-Band Antennas," *Journal of Microelectronics and Electronic Packaging*, July 20<sup>th</sup>. (2016). DOI: [HTTP://DX.DOI.ORG/10.4071/IMAPS.509](http://dx.doi.org/10.4071/IMAPS.509)
- [2] **J.Castro**, E.Rojas, T. Weller, and J. Wang, "Engineered Nanocomposites for Additive Manufacturing of Microwave Electronics," 48th. International Symposium on Microelectronics (*IMAPS 2015*), Orlando FL., October (2015). DOI: [HTTP://DX.DOI.ORG/10.4071/ISOM-2015-WA12](http://dx.doi.org/10.4071/ISOM-2015-WA12)

Best of luck and contact me with any questions please.

Brian Schieman  
IMAPS Director of Program Development and Technology  
919-293-5000 | [bschieman@imaps.org](mailto:bschieman@imaps.org)

---

International Microelectronics Assembly and Packaging Society & The Microelectronics Foundation  
PO Box 110127, RTP, NC 27709 USA • Tel: (919)293-5000 • eFax: (919)287-2339 • [www.imaps.org](http://www.imaps.org)

The permission below is for the use of material in Chapter 3 and Chapter 4.



RightsLink®

Home

Account Info

Help



**Title:** High-k and low-loss polymer composites with co-fired Nd and Mg-Ca titanates for 3D RF and microwave printed devices: Fabrication and characterization

**Conference Proceedings:** Wireless and Microwave Technology Conference (WAMICON), 2015 IEEE 16th Annual

**Author:** Juan Castro

**Publisher:** IEEE

**Date:** April 2015

Copyright © 2015, IEEE

Logged in as:

Juan Castro

Account #: 3001120566

LOGOUT

### Thesis / Dissertation Reuse

**The IEEE does not require individuals working on a thesis to obtain a formal reuse license, however, you may print out this statement to be used as a permission grant:**

*Requirements to be followed when using any portion (e.g., figure, graph, table, or textual material) of an IEEE copyrighted paper in a thesis:*

- 1) In the case of textual material (e.g., using short quotes or referring to the work within these papers) users must give full credit to the original source (author, paper, publication) followed by the IEEE copyright line © 2011 IEEE.
- 2) In the case of illustrations or tabular material, we require that the copyright line © [Year of original publication] IEEE appear prominently with each reprinted figure and/or table.
- 3) If a substantial portion of the original paper is to be used, and if you are not the senior author, also obtain the senior author's approval.

*Requirements to be followed when using an entire IEEE copyrighted paper in a thesis:*

- 1) The following IEEE copyright/ credit notice should be placed prominently in the references: © [year of original publication] IEEE. Reprinted, with permission, from [author names, paper title, IEEE publication title, and month/year of publication]
- 2) Only the accepted version of an IEEE copyrighted paper can be used when posting the paper or your thesis on-line.
- 3) In placing the thesis on the author's university website, please display the following message in a prominent place on the website: In reference to IEEE copyrighted material which is used with permission in this thesis, the IEEE does not endorse any of [university/educational entity's name goes here]'s products or services. Internal or personal use of this material is permitted. If interested in reprinting/republishing IEEE copyrighted material for advertising or promotional purposes or for creating new collective works for resale or redistribution, please go to [http://www.ieee.org/publications\\_standards/publications/rights/rights\\_link.html](http://www.ieee.org/publications_standards/publications/rights/rights_link.html) to learn how to obtain a License from RightsLink.

If applicable, University Microfilms and/or ProQuest Library, or the Archives of Canada may supply single copies of the dissertation.

The permission below is for the use of material in Chapter 3 and Chapter 4.



RightsLink®

Home

Account Info

Help



**Title:** An improved fabrication method of high-k and low-loss polymer composites with sintered ceramic fillers for microwave applications

**Conference Proceedings:** Microwave Symposium (IMS), 2015 IEEE MTT-S International

**Author:** Juan Castro

**Publisher:** IEEE

**Date:** May 2015

Copyright © 2015, IEEE

Logged in as:  
Juan Castro  
Account #:  
3001120566

LOGOUT

### Thesis / Dissertation Reuse

**The IEEE does not require individuals working on a thesis to obtain a formal reuse license, however, you may print out this statement to be used as a permission grant:**

*Requirements to be followed when using any portion (e.g., figure, graph, table, or textual material) of an IEEE copyrighted paper in a thesis:*

- 1) In the case of textual material (e.g., using short quotes or referring to the work within these papers) users must give full credit to the original source (author, paper, publication) followed by the IEEE copyright line © 2011 IEEE.
- 2) In the case of illustrations or tabular material, we require that the copyright line © [Year of original publication] IEEE appear prominently with each reprinted figure and/or table.
- 3) If a substantial portion of the original paper is to be used, and if you are not the senior author, also obtain the senior author's approval.

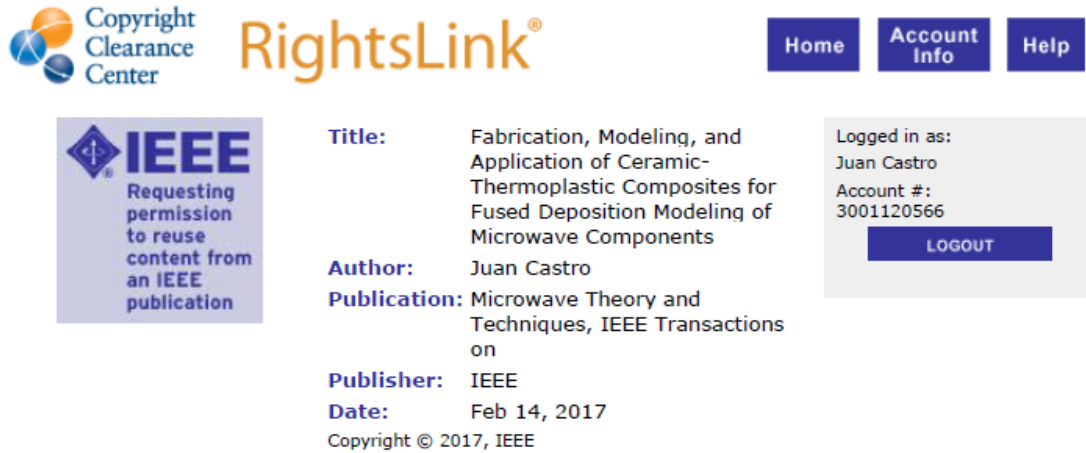
*Requirements to be followed when using an entire IEEE copyrighted paper in a thesis:*

- 1) The following IEEE copyright/ credit notice should be placed prominently in the references: © [year of original publication] IEEE. Reprinted, with permission, from [author names, paper title, IEEE publication title, and month/year of publication]
- 2) Only the accepted version of an IEEE copyrighted paper can be used when posting the paper or your thesis on-line.
- 3) In placing the thesis on the author's university website, please display the following message in a prominent place on the website: In reference to IEEE copyrighted material which is used with permission in this thesis, the IEEE does not endorse any of [university/educational entity's name goes here]'s products or services. Internal or personal use of this material is permitted. If interested in reprinting/republishing IEEE copyrighted material for advertising or promotional purposes or for creating new collective works for resale or redistribution, please go to [http://www.ieee.org/publications\\_standards/publications/rights/rights\\_link.html](http://www.ieee.org/publications_standards/publications/rights/rights_link.html) to learn how to obtain a License from RightsLink.

If applicable, University Microfilms and/or ProQuest Library, or the Archives of Canada may supply single copies of the dissertation.



The permission below is for the use of material in Chapter 5 and Chapter 6, and Figure 5.7(b).



The screenshot shows the IEEE RightsLink interface. On the left is the Copyright Clearance Center logo. The main content area displays the IEEE logo with the text 'Requesting permission to reuse content from an IEEE publication'. To the right, the following information is shown:

- Title:** Fabrication, Modeling, and Application of Ceramic-Thermoplastic Composites for Fused Deposition Modeling of Microwave Components
- Author:** Juan Castro
- Publication:** Microwave Theory and Techniques, IEEE Transactions on
- Publisher:** IEEE
- Date:** Feb 14, 2017

At the bottom of this section, it says 'Copyright © 2017, IEEE'. On the right side of the page, there are navigation buttons for 'Home', 'Account Info', and 'Help'. Below these, a user is logged in as 'Juan Castro' with account number '3001120566' and a 'LOGOUT' button.

#### Thesis / Dissertation Reuse

**The IEEE does not require individuals working on a thesis to obtain a formal reuse license, however, you may print out this statement to be used as a permission grant:**

*Requirements to be followed when using any portion (e.g., figure, graph, table, or textual material) of an IEEE copyrighted paper in a thesis:*

- 1) In the case of textual material (e.g., using short quotes or referring to the work within these papers) users must give full credit to the original source (author, paper, publication) followed by the IEEE copyright line © 2011 IEEE.
- 2) In the case of illustrations or tabular material, we require that the copyright line © [Year of original publication] IEEE appear prominently with each reprinted figure and/or table.
- 3) If a substantial portion of the original paper is to be used, and if you are not the senior author, also obtain the senior author's approval.

*Requirements to be followed when using an entire IEEE copyrighted paper in a thesis:*

- 1) The following IEEE copyright/ credit notice should be placed prominently in the references: © [year of original publication] IEEE. Reprinted, with permission, from [author names, paper title, IEEE publication title, and month/year of publication]
- 2) Only the accepted version of an IEEE copyrighted paper can be used when posting the paper or your thesis on-line.
- 3) In placing the thesis on the author's university website, please display the following message in a prominent place on the website: In reference to IEEE copyrighted material which is used with permission in this thesis, the IEEE does not endorse any of [university/educational entity's name goes here]'s products or services. Internal or personal use of this material is permitted. If interested in reprinting/republishing IEEE copyrighted material for advertising or promotional purposes or for creating new collective works for resale or redistribution, please go to [http://www.ieee.org/publications\\_standards/publications/rights/rights\\_link.html](http://www.ieee.org/publications_standards/publications/rights/rights_link.html) to learn how to obtain a License from RightsLink.

If applicable, University Microfilms and/or ProQuest Library, or the Archives of Canada may supply single copies of the dissertation.

The permission below is for the use of material in Chapter 5 and Chapter 6.



RightsLink®

Home

Account Info

Help



**Title:** High-*k* and low-loss thermoplastic composites for Fused Deposition Modeling and their application to 3D-printed Ku-band antennas

**Conference Proceedings:** Microwave Symposium (IMS), 2016 IEEE MTT-S International

**Author:** Juan Castro

**Publisher:** IEEE

**Date:** May 2016

Copyright © 2016, IEEE

Logged in as:

Juan Castro

Account #:  
3001120566

LOGOUT

### Thesis / Dissertation Reuse

**The IEEE does not require individuals working on a thesis to obtain a formal reuse license, however, you may print out this statement to be used as a permission grant:**

*Requirements to be followed when using any portion (e.g., figure, graph, table, or textual material) of an IEEE copyrighted paper in a thesis:*

- 1) In the case of textual material (e.g., using short quotes or referring to the work within these papers) users must give full credit to the original source (author, paper, publication) followed by the IEEE copyright line © 2011 IEEE.
- 2) In the case of illustrations or tabular material, we require that the copyright line © [Year of original publication] IEEE appear prominently with each reprinted figure and/or table.
- 3) If a substantial portion of the original paper is to be used, and if you are not the senior author, also obtain the senior author's approval.

*Requirements to be followed when using an entire IEEE copyrighted paper in a thesis:*

- 1) The following IEEE copyright/ credit notice should be placed prominently in the references: © [year of original publication] IEEE. Reprinted, with permission, from [author names, paper title, IEEE publication title, and month/year of publication]
- 2) Only the accepted version of an IEEE copyrighted paper can be used when posting the paper or your thesis on-line.
- 3) In placing the thesis on the author's university website, please display the following message in a prominent place on the website: In reference to IEEE copyrighted material which is used with permission in this thesis, the IEEE does not endorse any of [university/educational entity's name goes here]'s products or services. Internal or personal use of this material is permitted. If interested in reprinting/republishing IEEE copyrighted material for advertising or promotional purposes or for creating new collective works for resale or redistribution, please go to [http://www.ieee.org/publications\\_standards/publications/rights/rights\\_link.html](http://www.ieee.org/publications_standards/publications/rights/rights_link.html) to learn how to obtain a License from RightsLink.

If applicable, University Microfilms and/or ProQuest Library, or the Archives of Canada may supply single copies of the dissertation.

The permission below is for the use of ZEONEX® and ZEONOR® trademarks in all the dissertation.

**From:** Mark Nevitt [mailto:Nevitt@zeonchemicals.com]  
**Sent:** Monday, February 27, 2017 8:42 AM  
**To:** Castro, Juan <jcastro10@usf.edu>  
**Subject:** RE: Copyright release Zeon Corporation

Hello Juan,  
Zeon Corporation has approved the use of its name in your research dissertation with following requests for proper trademarked acknowledgements.

For dissertation, please incorporate: "ZEONEX® and ZEONOR® are registered trademarks of ZEON CORPORATION"

And, if possible, please revise the material tradename in the literature to use the following:

(Wrong)

Zeonex®

Zeonor®

(Correct)

ZEONEX®

ZEONOR®

Please let me know if you have any questions. And thank you again for consideration to use ZEONEX COP in your research.

Kind regards,

Mark

Mark Nevitt

Zeon Chemicals L.P.

p: +1.502.775.2131

m: +1.502.500.6293

[www.zeonex.com](http://www.zeonex.com)

**From:** Castro, Juan [mailto:jcastro10@usf.edu]  
**Sent:** Thursday, February 23, 2017 1:39 AM  
**To:** Mark Nevitt <Nevitt@zeonchemicals.com>  
**Subject:** RE: Copyright release Zeon Corporation

Hi Mark

The IEEE Transactions on MTT paper related to the ceramic-thermoplastic composites for FDM is in IEEE Xplore early access, you can download the final version in this link.

<http://ieeexplore.ieee.org/stamp/stamp.jsp?arnumber=7855799>

<http://ieeexplore.ieee.org/document/7855799/>

I attached the two publications and the letter. I need to submit my dissertation draft next march 1<sup>st</sup>. I hope to be able to get a letter from Zeon or email, just to add it to the appendix section in my dissertation.

Thank you very much in advance.

--

My Best Regards!.

Juan Castro, M.Sc.E.E.

Ph.D Candidate in Electrical Engineering

Center for Wireless and Microwave Information Systems ([WAMI](#))

Electrical Engineering Department

University of South Florida

4202 E.Fowler Avenue, ENB 118,

Tampa, FL 33620.

Ph. (813) 748-9408

[jcastro10@usf.edu](mailto:jcastro10@usf.edu)



## ABOUT THE AUTHOR

Juan Castro received a B.S. degree in Electrical Engineering (*summa cum laude*) and a M.B.A degree from the Autonomous University of Baja California, Mexicali, Mexico, in 2005 and 2011, respectively. And he got a M.S. degree in Electrical Engineering from the University of South Florida, Tampa, FL. USA, in 2014, where he is currently pursuing the Ph.D. degree in Electrical Engineering. Juan has authored or coauthored over 12 professional journals and conference publications in the RF/microwave field, and he has one provisional disclosure. His current research interests include 3D-printed RF/microwave circuits and antennas based on engineered electromagnetic nanocomposite materials.

Juan was the recipient of the 2017 dissertation fellowship of the honors society of Phi Kappa Phi and the 2016 IEEE Microwave Theory and Techniques Society (IEEE MTT-S) graduate fellowship. He was also the recipient of the 2016 SHPE engineering science symposium “Best Student Paper Award” under the applied physics/electrical and computer engineering category, he also received the “Best of Track” and “Outstanding Student Paper” awards under the IoT & advanced applications track during the 48<sup>th</sup> International Symposium on Microelectronics (IMAPS 2015). In addition, he received the 2015 USF research day poster competition award and 2014 HENAAC graduate STEM category technical poster award, and the 2012 doctorate fellowship by CONACYT (the Mexican National Council for Science and Technology).

Juan has worked for several companies, including Panasonic in 2007, Medtronic (formerly COVIDIEN) from 2008-2011, Nypro Healthcare (a Jabil company) from 2011-2012, and Cummins Inc. in Columbus, IN in summer 2016.